ISSN 0368-0797
eISSN 2410-2091

МИСИС
УНИВЕРСИТЕТ НАУКИ И ТЕХНОЛОГИЙ

СибГИУ
Сибирский государственный индустриальный университет

# ИЗВЕСТИЯ ВЫСШИХ УЧЕБНЫХ ЗАВЕДЕНИЙ ЧЕРНАЯ МЕТАЛЛУРГИЯ

# IZVESTIYA. FERROUS METALLURGY

fermet.misis.ru

2023 Том Vol. 66 № No. 6

МИСИС УНИВЕРСИТЕТ

СибГИУ
Сибирский государственный индустриальный университет

ISSN 0368-0797
eISSN 2410-2091

# ИЗВЕСТИЯ ВЫСШИХ УЧЕБНЫХ ЗАВЕДЕНИЙ ЧЕРНАЯ МЕТАЛЛУРГИЯ

Научно-технический журнал

Издается с января 1958 г. Выпускается 6 раз в год

2023 Том Vol. 66 № No. 6

# IZVESTIYA FERROUS METALLURGY

Scientific and Technical Journal

Published since January 1958. Issued 6 times a year

# IZVESTIYA FERROUS METALLURGY

www.fermet.misis.ru

ISSN 0368-0797 *(Print)* ISSN 2410-2091 *(Online)*

**Alternative title:**

Izvestiya vuzov. Chernaya metallurgiya

**Founders:**

MISIS
UNIVERSITY OF SCIENCE AND TECHNOLOGY

SibSIU
Siberian State Industrial University



**Publisher:**

National University of Science and Technology "MISIS"

**Editorial Office Address:**

***in Moscow***
4 Leninskii Ave., Moscow 119049, Russian Federation
National University of Science and Technology "MISIS"
*Tel.*: +7 (495) 638-44-11
*E-mail*: fermet.misis@mail.ru, ferrous@misis.ru

***in Novokuznetsk***
42 Kirova Str., Novokuznetsk, Kemerovo Region – Kuzbass
654007, Russian Federation
Siberian State Industrial University
Tel.: +7 (3843) 74-86-28 *E-mail*: redjizvz@sibsiu.ru



*In accordance with paragraph 5 of the Rules for the formation of the Higher Attestation Comission list journal "Izvestiya. Ferrous metallurgy" is included in the list of leading peer-reviewed scientific journals, publication in which is taken into account in the defense of candidate and doctoral dissertations, as indexed in internatonal data bases.*

***Indexed:*** Scopus, Russian Science Citation Index (RSCI), Research Bible, Chemical Abstracts, OCLC and Google Scholar

Registered in Federal Service for Supervision in the Sphere of Mass Communications **PI number FS77-35456**.

# ИЗВЕСТИЯ
## ВЫСШИХ УЧЕБНЫХ ЗАВЕДЕНИЙ
# ЧЕРНАЯ МЕТАЛЛУРГИЯ

www.fermet.misis.ru

ISSN 0368-0797 *(Print)* ISSN 2410-2091 *(Online)*

**Варианты названия:**

Известия вузов. Черная металлургия

Izvestiya. Ferrous Metallurgy

**Учредители:**

МИСИС
УНИВЕРСИТЕТ НАУКИ И ТЕХНОЛОГИЙ

СибГИУ
Сибирский государственный индустриальный университет





**Издатель:**

Национальный исследовательский технологический университет «МИСИС»

**Адреса подразделений редакций:**

***в Москве***
Россия, 119049, Москва, Ленинский просп., д. 4, стр. 1
Национальный исследовательский технологический университет «МИСИС»
*Тел.*: +7 (495) 638-44-11 *E-mail*: ferrous@misis.ru

***в Новокузнецке***
Россия, 654007, Новокузнецк,
Кемеровская обл. – Кузбасс, ул. Кирова, зд. 42
Сибирский государственный индустриальный университет
*Тел.*: +7 (3843) 74-86-28 *E-mail:* redjizvz@sibsiu.ru




*В соответствии п. 5 Правил формирования перечня ВАК журнал «Известия вузов. Черная металлургия» входит в перечень ведущих рецензируемых научных журналов и изданий, публикация в которых учитывается при защитах кандидатских и докторских диссертаций как индексируемый в МБД.*


***Индексирование:*** Scopus, Russian Science Citation Index (RSCI), Research Bible, Chemical Abstracts, OCLC и Google Scholar

Зарегистрирован Федеральной службой по надзору в сфере связи и массовых коммуникаций **ПИ № ФС77-35456**.

Izvestiya. Ferrous Metallurgy.
2023;66(6)

Известия вузов. Черная металлургия.
2023;66(6)

CONTENTS / СОДЕРЖАНИЕ

## METALLURGICAL TECHNOLOGIES



## MATERIALS SCIENCE



## МЕТАЛЛУРГИЧЕСКИЕ ТЕХНОЛОГИИ



## МАТЕРИАЛОВЕДЕНИЕ

CONTENTS *(Continuation)* / СОДЕРЖАНИЕ *(продолжение)*



## INNOVATIONS IN METALLURGICAL INDUSTRIAL AND LABORATORY EQUIPMENT, TECHNOLOGIES AND MATERIALS

## ИННОВАЦИИ В МЕТАЛЛУРГИЧЕСКОМ ПРОМЫШЛЕННОМ И ЛАБОРАТОРНОМ ОБОРУДОВАНИИ, ТЕХНОЛОГИЯХ И МАТЕРИАЛАХ



## PHYSICO-CHEMICAL BASICS OF METALLURGICAL PROCESSES

## ФИЗИКО-ХИМИЧЕСКИЕ ОСНОВЫ МЕТАЛЛУРГИЧЕСКИХ ПРОЦЕССОВ



## BASED ON THE MATERIALS OF THE INTERNATIONAL CONFERENCE "SCIENTIFIC AND PRACTICAL SCHOOL FOR YOUNG METALLURGISTS"

## ПО МАТЕРИАЛАМ МЕЖДУНАРОДНОЙ КОНФЕРЕНЦИИ «НАУЧНО-ПРАКТИЧЕСКАЯ ШКОЛА ДЛЯ МОЛОДЫХ МЕТАЛЛУРГОВ»



## INFORMATION TECHNOLOGIES AND AUTOMATIC CONTROL IN FERROUS METALLURGY

## ИНФОРМАЦИОННЫЕ ТЕХНОЛОГИИ И АВТОМАТИЗАЦИЯ В ЧЕРНОЙ МЕТАЛЛУРГИИ

**UDC** 669.1:001.89
**DOI** 10.17073/0368-0797-2023-6-638-644



***Original article***
***Оригинальная статья***

# Prediction of carbon content in the metal of final blow period in BOF using neural network

**M. K. Shakirov** ✉, **E. V. Protopopov, A. V. Zimin, E. B. Turchaninov**

**Siberian State Industrial University** (42 Kirova Str., Novokuznetsk, Kemerovo Region – Kuzbass, 654007, Russian Federation)

✉ shakirov.maxim@mail.ru

***Abstract***. Prediction and control of the carbon content after the end of oxygen blow in BOF converter are key points of steel production efficiency. One of the most accurate methods is the dynamic predicting method based on the use of intermediate sublance measurement (TSC probe) when about 85 – 90 % of total oxygen is consumed and on the final period model. Models of the final period are traditionally based on exponential or cubic functions, currently there are developments based on neural network technologies. We investigated the possibility of using a neural network to predict the final carbon content using the results of intermediate sublance measurement (TSO probe) when about 95 % of total oxygen is consumed. As a model of the final period, a two-layer neural network with one hidden layer and an activation function of the Softplus type for all neurons was implemented in software. The input vectors contain initial carbon content and oxygen consumption for the second blow values. The output vector contains the predicted final carbon content, the output training vector - actual final carbon content values. The network was trained on 700 heats data of the training set. The model trained in this way was tested on 232 heats data of the testing set. The prediction errors distribution and values of the mean absolute error and root mean square error for the training and testing sets are correspondingly close. They are also comparable with similar indicators of the heats, the final period of which was carried out without oxygen blow (only flux additions and/or nitrogen blow), and this indicates a high accuracy of the prediction.

***Keywords:*** BOF, carbon content, sublance, mathematical simulation, prediction, final period, neural network

***For citation:*** Shakirov M.K., Protopopov E.V., Zimin A.V., Turchaninov E.B. Prediction of carbon content in the metal of final blow period in BOF using neural network. *Izvestiya. Ferrous Metallurgy*. 2023;66(6):638–644. https://doi.org/10.17073/0368-0797-2023-6-638-644

# Прогнозирование содержания углерода в металле заключительного периода продувки в кислородном конвертере с использованием нейронной сети

**М. К. Шакиров** ✉, **Е. В. Протопопов, А. В. Зимин, Е. Б. Турчанинов**

**Сибирский государственный индустриальный университет** (Россия, 654007, Кемеровская обл. – Кузбасс, Новокузнецк, ул. Кирова, 42)

✉ shakirov.maxim@mail.ru

***Аннотация***. Прогнозирование и управление содержанием углерода в металле по окончании продувки в кислородном конвертере являются ключевыми моментами в обеспечении эффективности производства стали. Наиболее точным методом является метод динамического прогнозирования, основанный на использовании информации промежуточного замера фурмой-зондом (блок типа TSC) в период израсходования порядка 85 – 90 % общего расхода кислорода на плавку и принятой модели заключительного периода продувки. Для прогнозирования традиционно используются модели заключительного периода на основе экспоненциальных или кубических функций, существуют разработки на основе нейросетевых технологий. В настоящем исследовании заключительный период плавки определили как период между первым и последним (перед выпуском плавки) замерами фурмой-зондом. В зависимости от результатов первого замера и требуемых параметров металла в этот период может производиться продувка кислородом, присадка флюсов, а также усреднительная продувка азотом. Была исследована возможность использования нейросети для прогнозирования конечного содержания углерода с использованием результатов промежуточного замера фурмой–зондом (блок типа TSO) в период израсходования порядка 95 % общего расхода кислорода на плавку. В качестве модели заключительного периода была программно реализована двухслойная нейросеть с одним скрытым слоем и активационной функцией типа Softplus для всех нейронов. Входные данные - содержание углерода промежуточного замера и расход кислорода на заключительный период продувки. Выходные данные – прогнозируемое конечное содержание углерода. Для обучения использовались данные по фактическому конечному содержанию углерода в металле. Нейронная сеть была настроена

по данным 700 плавок обучающей выборки. Настроенная таким образом модель была дополнительно протестирована на данных 232 плавок, не использовавшихся при обучении. Получены близкие значения ошибок прогноза для обучающей и тестирующей выборок. Кроме того, полученные значения ошибок сопоставимы с изменениями содержания углерода для плавок без использования кислорода в заключительный период, что говорит о высокой точности прогноза.

***Ключевые слова:*** кислородный конвертер, содержание углерода, измерительная фурма, математическое моделирование, прогнозирование, заключительный период, нейронная сеть

***Для цитирования:*** Шакиров М.К., Протопопов Е.В., Зимин А.В., Турчанинов Е.Б. Прогнозирование содержания углерода в металле заключительного периода продувки в кислородном конвертере с использованием нейронной сети. *Известия вузов. Черная металлургия*. 2023;66(6):638–644. https://doi.org/10.17073/0368-0797-2023-6-638-644

## Introduction

The accumulated operational experience with converters employing upper oxygen blow has compellingly demonstrated the process's advantages. These include high productivity, sufficiently durable unit lining, simple equipment design and operation, and technological flexibility regarding the composition of processed pigments [1 – 3]. However, achieving stable technological melting indicators and overall process efficiency depends significantly on the accuracy and correctness of determining the completion moment of the operation [4].

In the practice of organizing blowing, addressing this challenge typically involves using indirect characteristics to gauge the progress of blowing and the bath's behavior. Examples include:

– determining the completion moment of the blowing operation based on the oxygen consumption amount;

– observing the luminosity intensity of the exhaust gas plume above the converter;

– analyzing the chemical composition of exhaust gases;

– examining changes in indirect characteristics such as the bath's behavior (acoustic phenomena, lance vibration), observing the temperature of the water cooling the lance, and measuring the electrical conductivity of the bath, among others.

Simultaneously, the enumerated elements and methods for controlling the blowing process can be categorized as subjective factors, assuming a high level of competence among the process personnel. However, the rapidity of oxidative refining processes within the BOF, coupled with intense dust and gas emissions, and the fluctuating bath level with the potential for emissions or, conversely, slag coagulation, all contribute to the substantial complexity in managing the smelting process.

The scrutinized predictive models assume particular significance in the production of specialty steels, especially low-carbon steels, including void-free steels with minimal impurities (≤0.003 % C and 0.004 % N). In this context, the accurate prediction and control of carbon content in the metal during the final phase of the blowing operation emerge as a critical task. Effectively addressing this challenge facilitates an improvement and stabilization of technological performance.

Incorporating additional information for predicting smelting characteristics, the well-established methods for calculating residual carbon content in metal prior to release can be classified as follows [4; 5]:

– prediction through static models;

– prediction through dynamic models;

– intelligent prediction.

### 1. Static prediction

Static prediction employs what are known as static melt models, relying on calculations of thermal and material balances or statistical descriptions of the entire melt. Initial data include the chemical composition and temperature of the iron, the chemical composition of the solid metal charge and additional materials, along with results from previous melts and the required values of metal indicators at the end of blowing – primarily the chemical composition and temperature. This method facilitates the determination of the quantity of charge and additional materials, including assessment of the amount of oxygen consumed during the blowing period necessary to achieve the desired carbon content in the metal [6 – 8].

However, the accuracy of this method in predicting post-blowing melt parameters is not consistently stable due to the influence of numerous uncontrolled factors [9]. These factors may encompass variations in the chemical composition and physical properties of the metal charge, fluctuations in properties and quantities of additives, uncontrolled heat losses, losses of oxygen during different blowing periods, and more [7]. Theoretical [10 – 12] or static [13 – 15] models, including those based on neural networks, are the most commonly used approaches for static forecasting.

### 2. Dynamic prediction

It is established that the use of a sublance in combination with models for the final blowing period serves as a dynamic control tool, leading to a reduction in the melting cycle by significantly minimizing the time required for corrective operations (turndown, metal cooling) [15].

Models for the final period are constructed on a statistical description of the relationships between the ultimate values of melting parameters – primarily carbon content and temperature – their initial values, and the quantity of consumed oxygen [16]. In this scenario, the decarburization rate can be expressed as follows

$$-\frac{\partial C}{\partial \tau} = k(C - C_0), \quad (1)$$

where $k$ is the decarburization reaction rate constant, $s^{-1}$; $C$ is the current concentration of carbon in the liquid metal, %; $C_0$ is the minimum achievable carbon concentration in liquid metal, characterizing mass and rate of carbon oxidation in the region of its low values, %; $\tau$ is the duration of oxygen blowing, s.

The use of a sublance facilitates the measurement and sampling of metal for chemical analysis without the need for tilting, which typically involves interrupting oxygen purge and tilting the converter. In this scenario, two measurements are usually conducted for each melting operation: one during oxygen blowing (after 85 – 90 % of the estimated total oxygen amount has been consumed) and another at the conclusion of the oxygen blowing process.

The first measurement uses TSC probes (*temperature*, *sample*, *carbon*): metal temperature and carbon content are determined based on the liquidus temperature of the melt, and a sample is taken. To enhance result reliability, the oxygen blowing intensity is reduced during this measurement period. The first "dynamic" measurement serves as input for the final period model, which calculates the necessary amount of oxygen and potential coolant required to achieve the desired temperature and carbon content during metal tapping.

Following the oxygen blowing phase, measurements are conducted using TSO probes (*temperature*, *sample*, *oxygen*): the metal's temperature is determined, its oxidation is assessed, carbon content is calculated, and a metal sample is taken.

However, in domestic converter shops, TSC probes are currently not employed, and measurements are instead carried out using TSO probes during the blowing period, corresponding to a lower (less than 0.15 %) carbon content in the metal.

The use of a measuring sublance helps eliminate the influence of fluctuations in the properties of charge materials, thereby enhancing the accuracy of predicting the final carbon content for converter smelting compared to static prediction methods. Some Japanese manufacturers have achieved predicting accuracy of over 90 % within an interval of ±0.02 % C [17].

Another variation of dynamic carbon content prediction involves an approach based on utilizing indirect indicators of the decarbonization process, such as the results of exhaust gas composition analysis. The primary drawback of this option, coupled with the impact on the results of analyzing the amount of air drawn from the atmosphere in the gas discharge tract operation mode with partial combustion of exhaust gases, is the presence of a delay (time delay) in the initial information for calculation.

## 3. Intelligent prediction

Intelligent prediction of carbon content in the melt, as per the aforementioned characteristics, involves employing additional indirect information about the progress of the process, such as the vibration of the oxygen lance, the level of slag-metal emulsion, acoustic characteristics of the blowing progress, and more.

The initial application of this approach includes the development of a model for the final blowdown period based on a neural network [18].

Specifically, to predict carbon content, a network is employed with input neurons corresponding to carbon content measured by the sublance of the probe, the amount of oxygen, and coolant consumed during the final period. The positive results obtained allow for conclusions regarding the effectiveness of the method used.

The development and implementation of such approaches underscore the advantages of predicting carbon content in the final blowing period using neural networks compared to exponential, cubic, and carbon oxidation models based on analysis of the chemical composition of exhaust gases. Notably, these studies were conducted using experimental data from intermediate measurements employing only TSC probes [17; 19 – 21].

Therefore, it appears pertinent to evaluate the suitability of neural networks for describing the final period of blowing, particularly for predicting the final carbon content in the metal based on intermediate measurement data from TSO probes commonly used in the industry.

## Research methodology

In this current study, the final blowing period was defined as the conditional interval between the first and last (prior to heat release) sublance measurements. Depending on the outcomes of the first measurement and the required final parameters of the metal, activities such as oxygen blowing, flux addition, and averaging nitrogen blowing can be conducted during this period.

The study aimed to assess the accuracy of predicting the final carbon content in the metal using intermediate measurements by TSO probes, accounting for approximately 95 % of the estimated total oxygen consumption for melting. Additionally, the results obtained were compared with similar ones derived from technology utilizing TSC probes.

The data analyzed in this study were derived from ongoing production heats conducted in a 350-ton converter equipped with a measuring lance under the direct supervision of the authors.

The melts chosen for training and testing the carbon content prediction specifically involved cases where only oxygen blowing was employed in the final period.

The determination of initial carbon content relies on sublance measurements conducted before the commencement of the final period, while the final content is ascertained through chemical analysis of a metal sample taken with a sublance at the end of blowing. Table 1 provides the initial ($C_1$) and final ($C_2$) carbon content, along with the change in carbon concentration resulting from the final period ($\Delta C^{\text{final}} = C_2 - C_1$) and the oxygen consumption for the operation. The values are presented in Table 1 as a ratio of the range of change in the numerator to the average value in the denominator.

To predict the carbon content at the end of the final blowing period, a two-layer neural network with one hidden layer was employed. The input data included the actual carbon content in the metal before the start of the final period C1 and the actual oxygen consumption in the final period $O_2^{\text{final}}$. The output data consisted of the predicted carbon content in the metal $C_2^{\text{predict}}$ at the end of the final period. Training utilized data on the actual final carbon content from the metal sample. The activation function for the network was defined by the equation

$$Y = \ln(1 + e^x). \quad (2)$$

The initial and final carbon content, along with oxygen consumption data, were normalized using the following equation

$$C_i^* = \frac{C_i - C_{\min}}{C_{\max} - C_{\min}}, \quad (3)$$

where $C_i$ is the actual parameter value; $C_{\min}$ and $C_{\max}$ are the minimum and the maximum values of the parameter, respectively.

A training set comprising data from 700 melts was used, with the results tested on data from 232 subsequent melts that followed the training set in chronological order. Of these, 56 melts were conducted under the direct supervision of the authors.

The network was trained using a backpropagation algorithm, specifically the gradient descent method. Throughout the training process, the sum of squared deviations between the actual $C_2$ and the predicted carbon content $C_2^{\text{predict}}$ in the metal was minimized.

The accuracy of prediction was evaluated using the following indicators:

– *mean error*, calculated as

$$ME = \frac{1}{N}\sum_{i=1}^{N}\left(Y_i - \hat{Y}_i\right), \quad (4)$$

where $N$ is the number of observations; $Y_i$, $\hat{Y}_i$ are the actual and the predicted values of the parameter, respectively;

– *mean absolute error*, calculated as

$$MAE = \frac{1}{N}\sum_{i=1}^{N}\left|Y_i - \hat{Y}_i\right|, \quad (5)$$

– *root mean square error*, calculated as

$$RMSE = \sqrt{\frac{1}{N}\sum_{i=1}^{N}\left(Y_i - \hat{Y}_i\right)^2}. \quad (6)$$

## Results and discussion

As a result of training and subsequent testing of the neural network on the corresponding experimental data arrays, a distribution of prediction errors of the final carbon content in metal $C_2 - C_2^{\text{predict}}$ was obtained (see Fig.).

It's noteworthy that the distribution of prediction errors for the testing set closely aligns with that of the training set. The indication that over 90 % of errors fall within the range of ±0.010 %, and approximately 70 % of melts fall within the range of ±0.005 %, suggests a sufficiently high accuracy in predicting the final carbon content in the metal.

For a comprehensive comparison, the achieved prediction accuracy indices for both the training and testing sets were contrasted with similar indices obtained from melts that did not involve the use of oxygen in the final period of blowing. In these comparative melts, lime and/or limestone additives were employed, and averaging nitrogen blowing occurred through an oxygen lance. The initial values of $C_1$, derived from the results of the first sublance probe measurement, were used as the predicted values for the final carbon content $C_2^{\text{predict}}$ (Table 2). Accuracy indicators were then calculated according to Eqs. (4) – (6).

The results indicate that the accuracy indicators characterizing the prediction for both the training and

Table 1

**Parameters of the final oxygen blow period**

*Таблица 1.* **Параметры заключительного периода продувки с использованием кислорода**

| $C_1$, % | $C_2$, % | $\Delta C^{\text{final}}$, % | $O_2^{\text{зп}}$, nm$^3$ |
|---|---|---|---|
| 0.026 – 0.168 | 0.017 – 0.117 | 0 – 0.099 | 411 – 4012 |
| 0.055 | 0.039 | 0.016 | 1156 |

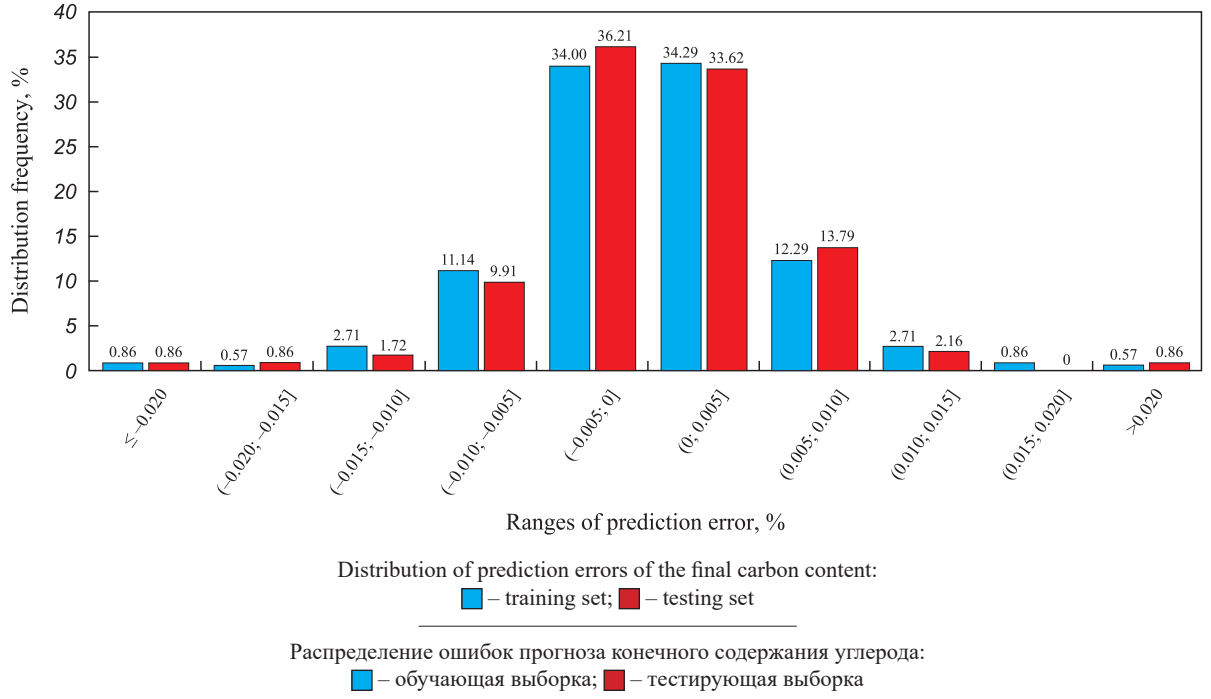


testing sets have close values. Additionally, these values are comparable with those observed in melts conducted without the use of oxygen in the final period. Changes in carbon content ($C_2 - C_1 = C_2 - C_2^{predict}$) for such melts are evidently associated with the heterogeneity of the chemical composition throughout the bulk of the metal bath. In other words, the data obtained (Table 2) suggest that the achieved prediction accuracy is on par with changes in the carbon content in the metal, potentially linked to the heterogeneity of the bath and, possibly, errors in determining the carbon content during measurements using sublance. The prediction accuracy of the proposed model for the final period, within the ranges of ±0.005 and ±0.010 % for the testing set, was reported as 70 and 94 %, respectively.

The authors in [22] demonstrated, for technology employing TSC probes, that a final period model based on a neural network allows achieving a prediction error for the carbon content in the metal within the ranges of ±0.005, ±0.010, ±0.015 and ±0.020 %, corresponding to 25, 54 71 and 91 % of cases. The analysis conducted indicates that these indicators outperform those for exponential, cubic models, and the carbon oxidation model based on an analysis of the chemical composition of exhaust gases.

However, it's worth noting that in this case, the average initial value of carbon content was 0.244 % which is significantly higher than that in the present study.

To optimize the obtained results, future research can explore options and assess the impact of updating the training set to adapt the model to changing conditions during the converter campaign.

## Conclusions

The accurate prediction of carbon content in the metal is crucial for effective management during the final smelting period in a BOF. The findings of this study align with the results reported in works [21; 22], affirming the feasibility of employing a neural network for predicting the carbon content in the metal during the final blowing period in a BOF.

Table 2

**Comparison of parameters of training, testing sets and heats without oxygen in the final period**

*Таблица 2*. **Сравнение показателей плавок обучающей, тестирующей выборок и плавок без использования кислорода в заключительный период**

| Set | Number of melts | *ME*, % | *MAE*, % | *RMSE*, % |
|---|---|---|---|---|
| Training set | 700 | $-1.36 \cdot 10^{-7}$ | 0.0044 | 0.0060 |
| Testing set | 232 | $-1.09 \cdot 10^{-5}$ | 0.0043 | 0.0060 |
| Without $O_2$ | 330 | $2.53 \cdot 10^{-4}$ | 0.0040 | 0.0048 |

## References / Список литературы


1. Lyakishev N.P., Shalimov A.G. *Comparative Characteristics of the State of Oxygen-Converter Steel Production in Russia and Abroad*. Moscow: Eliz; 2000:64. (In Russ.).

   Лякишев Н.П., Шалимов А.Г. *Сравнительная характеристика состояния кислородно-конвертерного производства стали в России и за рубежом*. Москва: Элиз; 2000:64.
2. Kolpakov S.V., Starov R.V., Smoktii V.V., Lebedev V.I., Ryabov V.V. *Technology of Steel Production in Modern Converter Shops*. Moscow: Mashinostroenie; 1991:464. (In Russ.).

   *Технология производства стали в современных конвертерных цехах* / С.В. Колпаков, Р.В. Старов, В.В. Смоктий, В.И. Лебедев, В.В. Рябов. Москва: Машиностроение; 1991:464.
3. Afonin S.Z. Current state, prospects and challenges facing the metallurgical industry of Russia. *Stal'*. 1995;(7):1–4. (In Russ.).

   Афонин С.З. Современное состояние, перспективы и задачи стоящие перед металлургической промышленностью России. *Сталь*. 1995;(7):1–4.
4. Baptizmansii V.I. *Theory of Oxygen Converter Process*. Moscow: Metallurgiya; 1975:375. (In Russ.).

   Баптизманский В.И. *Теория кислородно-конвертерного процесса*. Москва: Металлургия; 1975:375.
5. Baptizmanskii V.I., Medzhibozhskii M.Ya., Okhotskii V.B. *Converter Processes in Steel Production*. Kiev-Donetsk: Vishcha shkola; 1984:344. (In Russ.).

   Баптизманский В.И., Меджибожский М.Я., Охотский В.Б. *Конвертерные процессы производства стали*. Киев-Донецк: Вища школа; 1984:344.
6. Turkenich D.I. *Control of Steel Melting in a Converter.* Moscow: Metallurgiya; 1971:360. (In Russ.).

   Туркенич Д.И. *Управление плавкой стали в конвертере*. Москва: Металлургия; 1971:360.
7. Boichenko B.M., Nizyaev K.G., Stoyanov A.N., Molchanov L.S., Sinegin E.V. Parametrization of steel production in an oxygen converter. *Sistemnye Tekhnologii*. 2017;(3(110)):10–15. (In Russ.).

   Бойченко Б.М., Низяев К.Г., Стоянов А.Н., Молчанов Л.С., Синегин Е.В. Параметризация процесса выплавки стали в кислородном конвертере. *Системные технологии*. 2017;(3(110)):10–15.
8. Bigeev A.M. *Mathematical Description and Calculations of Steelmaking Processes*. Moscow: Metallurgiya; 1982:160. (In Russ.).

   Бигеев А.М. *Математическое описание и расчеты сталеплавильных процессов*. Москва: Металлургия; 1982:160.
9. Wang Z., Xie F., Wang B., Liu Q., Lu X.C., Hu L.N., Cai F. The control and prediction of end-point phosphorus content during BOf steelmaking process. *Steel Research International*. 2014;85(4):599–606. https://doi.org/10.1002/srin.201300194
10. Mochalov S.P., Aizatulov R.S., Shakirov K.M. Predicting dynamic model of converter process. *Izvestiya. Ferrous Metallurgy*. 1979;22(4):128–131. (In Russ.).

    Мочалов С.П., Айзатулов Р.С., Шакиров К.М. Прогнозирующая динамическая модель конвертерного процесса. *Известия вузов. Черная металлургия*. 1979;22(4):128–131.
11. Chen J.D., Zhang C.J., Feng J.H. Static mechanics model in loading converter and energy saving. *Journal of Hebei Institute of Technology*. 2007;29(1):32–35.
12. Rozhkov I.M., Travin O.V., Turkenich D.I. *Mathematical Models of Converter Process*. Moscow: Metallurgiya; 1978:184. (In Russ.).

    Рожков И.М., Травин О.В., Туркенич Д.И. *Математические модели конверторного процесса*. Москва: Металлургия; 1978:184.
13. Pal J., Singh S., Ghose A.K., Mohan S. A mathematical model for end point control of basic oxygen steel making furnace. *Journal of Metallurgy and Materials Science*. 2002;44(1):39–49.
14. Cunha A.P., Pacianotto T.A., Frottini Fileti A.M. Steelmaking process: neural models improve end-point predictions. *Computer Aided Chemical Engineering*. 2004;18(4):631–636. https://doi.org/10.1016/S1570-7946(04)80171-8
15. Apeldoorn G.J., Gootjes P. Sublances for BOf steelmaking. In: *Millennium Steel*. 2006;97–101.
16. Bigeev A.M., Baitman V.V. Adaptation of mathematical model of BOf blowing end to conditions of BOf shop of Magnitogorsky Iron and Steel Works. *Metallurg*. 2006;(9):47–49. (In Russ.).

    Бигеев А.М., Байтман В.В. Адаптация математической модели окончания продувки конвертерной плавки к условиям кислородно-конвертерного цеха Магнитогорского металлургического комбината. *Металлург*. 2006;(9):47–49.
17. Vortrefflich W., Vries J. Maximizing BOf production capacity and producing cost efficient by using sublance based process control. *Iron & Steel Review*. 2010;10:94–100.
18. Koshelev A.E., Voronin N.I., Petrunin M.V., Kiseleva T.V., Turchaninov E.B. On indirect control of carbon content in converter bath. *Izvestiya. Ferrous Metallurgy*. 1981;24(12):105–110. (In Russ.).

    Кошелев А.Е., Воронин Н.И., Петрунин М.В., Киселева Т.В., Турчанинов Е.Б. О косвенном контроле содержания углерода в конвертерной ванне. *Известия вузов. Черная металлургия*. 1981;24(12):105–110.
19. Wu M., Wu F. Application of using dynamic control with offgas analysis for making medium-high carbon steel. *Iron and Steel*. 2007;42(12):38–41.
20. Avdeev V.P., Aizatulov R.S., Myshlyaev L.P., Petrunin M.V., Sarapulov Yu.A. *Methods of Calculating the Masses of Materials in Converter Production*. Moscow: Metallurgiya; 1994:192. (In Russ.).

    *Способы расчета масс материалов конверторного производства* / В.П. Авдеев, Р.С. Айзатулов, Л.П. Мышляев, М.В. Петрунин, Ю.А. Сарапулов. Москва: Металлургия; 1994:192.
21. Jun T., Xin W., Tianyou C., Shuming X. Intelligent control method and application for BOf steelmaking process. *IFAC Proceedings Volumes*. 2002;35(1):439–444. https://doi.org/10.3182/20020721-6-ES-1901.00726
22. Gu M., Xu A., Wang H., Wang Z. Real-time dynamic carbon content prediction model for second blowing stage in BOf based on CBR and LSTM. *Processes*. 2021;9(11):1987. https://doi.org/10.3390/pr9111987

## Information about the Authors

***Maksim K. Shakirov,*** *Cand. Sci. (Eng.), Assist. Prof. of the Chair of Automation and Information Systems,* Siberian State Industrial University
***ORCID:*** 0009-0007-4938-5975
***E-mail:*** shakirov.maxim@mail.ru

***Evgenii V. Protopopov,*** *Dr. Sci. (Eng.), Prof. of the Chair of Ferrous Metallurgy,* Siberian State Industrial University
***ORCID:*** 0000-0002-7554-2168
***E-mail:*** protopopov@sibsiu.ru

***Aleksei V. Zimin,*** *Dr. Sci. (Eng.), Head of the Chair of Automation and Information Systems,* Siberian State Industrial University
***ORCID:*** 0000-0002-0485-9846
***E-mail:*** zimin.0169@yandex.ru

***Evgenii B. Turchaninov,*** *Cand. Sci. (Eng.), Assist. Prof. of Chair of Automation and Information Systems,* Siberian State Industrial University
***E-mail:*** evgen52.turchaninov@gmail.com

## Сведения об авторах

***Максим Кимович Шакиров,*** *к.т.н., доцент кафедры автоматизации и информационных систем,* Сибирский государственный индустриальный университет
***ORCID:*** 0009-0007-4938-5975
***E-mail:*** shakirov.maxim@mail.ru

***Евгений Валентинович Протопопов,*** *д.т.н., профессор кафедры металлургии черных металлов,* Сибирский государственный индустриальный университет
***ORCID:*** 0000-0002-7554-2168
***E-mail:*** protopopov@sibsiu.ru

***Алексей Валерьевич Зимин,*** *д.т.н., заведующий кафедрой автоматизации и информационных систем,* Сибирский государственный индустриальный университет
***ORCID:*** 0000-0002-0485-9846
***E-mail:*** zimin.0169@yandex.ru

***Евгений Борисович Турчанинов,*** *к.т.н., доцент кафедры автоматизации и информационных систем,* Сибирский государственный индустриальный университет
***E-mail:*** evgen52.turchaninov@gmail.com

## Contribution of the Authors

***M. K. Shakirov*** – statement of the research tasks, development and realization of the algorithm, analysis of the results.
***E. V. Protopopov*** – technological description of the task, justification of the research direction, analysis of the results.
***A. V. Zimin*** – statement of the research tasks, formulation of conclusions.
***E. B. Turchaninov*** – statement of the research tasks, data analysis.

## Вклад авторов

***М. К. Шакиров*** – постановка задач исследования, разработка и реализация алгоритма, анализ полученных результатов.
***Е. В. Протопопов*** – технологическое описание поставленной задачи, обоснование направления исследований, анализ полученных результатов.
***А. В. Зимин*** – постановка проблемы, формирование выводов.
***Е. Б. Турчанинов*** – постановка задач исследования, анализ данных.

Received 25.04.2023
Revised 11.09.2023
Accepted 25.09.2023

Поступила в редакцию 25.04.2023
После доработки 11.09.2023
Принята к публикации 25.09.2023

**UDC** 621.771.65
**DOI** 10.17073/0368-0797-2023-6-645-652



*Original article*
*Оригинальная статья*

# Formation of microstructure in rail steel grinding balls depending on quenching medium parameters

**A. A. Umanskii** ✉, **V. V. Baidin, A. S. Simachev,**
**L. V. Dumova, S. O. Safonov**

**Siberian State Industrial University** (42 Kirova Str., Novokuznetsk, Kemerovo Region – Kuzbass 654007, Russian Federation)

✉ umanskii@bk.ru

***Abstract***. Studies of the formation of microstructure of grinding balls from the rejects of rail steel were carried out during their quenching in various polymer media. At the first stage, based on studies of the cooling capacity of solutions of polymers PCM and Thermovit with varying concentrations and temperatures, the authors constructed the cooling curves of grinding balls made of K76F rail steel. It was found that at concentration of these polymers in an aqueous solution of 2 and 4 %, cooling rate of grinding balls made of K76F steel is almost identical at solution temperatures of 20 and 30 °C and significantly decreases when the temperature of the polymer solution increases to 40 °C. At the same time, the most noticeable decrease in the cooling rate is characteristic of PCM polymer with its concentration at the level of 2 %. At the second stage, the authors carried out metallographic studies of the microstructure of grinding balls made of K76F rail steel, which were quenched in laboratory conditions using polymers PCM and Thermovit with concentrations of 2 – 4 % and temperature of 20 – 40 °C. As a result, it was determined that the use of the PCM solution for quenching balls provides a significantly higher quality of microstructure and hardness of heat-treated balls compared to the use of the Thermovit polymer. At the same time, varying the concentration and temperature of the PCM polymer quenching medium allows one to obtain grinding balls with different performance characteristics that determine the potential areas of their application. Thus, quenching of balls in a solution of the specified polymer with concentration of 2 % and temperature of 20 – 30 °C ensures the production of balls with high hardness (corresponding to the IV hardness group according to the state standard GOST 7524 – 2015), and the use of a solution of the same polymer with concentration of 4 % and temperature of 20 – 30 °C for quenching creates the possibility of producing balls with lower hardness, but potentially high impact resistance.

***Keywords:*** microstructure, grinding balls, rail steel, polymers, heat treatment, quenching medium, impact resistance

***Acknowledgements:*** The research was supported by the Russian Science Foundation, grant No. 22-29-20170, and by the Kemerovo Region – Kuzbass.

***For citation:*** Umanskii A.A., Baidin V.V., Simachev A.S., Dumova L.V., Safonov S.O. Formation of microstructure in rail steel grinding balls depending on quenching medium parameters. *Izvestiya. Ferrous Metallurgy*. 2023;66(6):645–652.
https://doi.org/10.17073/0368-0797-2023-6-645-652

# Исследования процессов формирования микроструктуры мелющих шаров из рельсовой стали в зависимости от параметров закалочной среды

**А. А. Уманский** ✉, **В. В. Байдин, А. С. Симачев,**
**Л. В. Думова, С. О. Сафонов**

**Сибирский государственный индустриальный университет** (Россия, 654007, Кемеровская обл. – Кузбасс, Новокузнецк, ул. Кирова, 42)

✉ umanskii@bk.ru

***Аннотация***. Проведены исследования формирования микроструктуры мелющих шаров из отбраковки рельсовой стали при их закалке в различных полимерных средах. На первом этапе, на основании исследований охлаждающей способности растворов полимеров «ПКМ» и «Термовит» при варьировании их концентраций и температуры построены кривые охлаждения мелющих шаров из рельсовой стали марки К76Ф. При концентрации указанных полимеров в водном растворе 2 и 4 % скорость охлаждения мелющих шаров из стали К76Ф практически идентична при температурах раствора 20 и 30 °С и значимо снижается в случае увеличении температуры раствора полимера до 40 °С. При этом наиболее заметное снижение скорости охлаждения характерно для полимера «ПКМ» при его концентрации на уровне 2 %. На втором этапе проведены металлографические исследования микроструктуры мелющих шаров из рельсовой стали К76Ф, закалка которых проводилась в лабораторных условиях с использованием полимеров «ПКМ» и «Термовит»

с концентраций 2 – 4 % и температурой 20 – 40 °С. Использование раствора «ПКМ» для закалки шаров обеспечивает значительно более высокие качество микроструктуры и твердость термообработанных шаров по сравнению с применением полимера «Термовит». Варьирование концентрации и температуры полимерной закалочной среды «ПКМ» позволяет получать мелющие шары с различными эксплуатационными характеристиками, определяющими потенциальные области их применения. Закалка шаров в растворе указанного полимера с концентрацией 2 % и температурой 20 – 30 °С обеспечивает получение шаров с высокой твердостью (соответствующей IV группе твердости по ГОСТ 7524 – 2015), а использование для закалки раствора этого же полимера с концентрацией 4 % и температурой 20 – 30 °С создает возможность производства шаров с более низкой твердостью, но потенциально высокой ударной стойкостью.

***Ключевые слова:*** микроструктура, мелющие шары, рельсовая сталь, полимеры, термообработка, закалочная среда, ударная стойкость

***Благодарности:*** Исследование выполнено за счет гранта Российского научного фонда № 22-29-20170, гранта Кемеровской области – Кузбасса.

***Для цитирования:*** Уманский А.А., Байдин В.В., Симачев А.С., Думова Л.В., Сафонов С.О. Исследования процессов формирования микроструктуры мелющих шаров из рельсовой стали в зависимости от параметров закалочной среды. *Известия вузов. Черная металлургия*. 2023;66(6):645–652. https://doi.org/10.17073/0368-0797-2023-6-645-652

## Introduction

In recent years, there has been a noticeable trend towards the intensive development of domestic ball rolling production. Several modern ball rolling mills have been commissioned [1; 2], and significant efforts are underway at various operational mills to enhance the technological processes for grinding ball production [3 – 6]. This phenomenon is attributed to the growing demand for grinding balls with superior performance characteristics, specifically hardness, wear resistance, and resistance to shock loads. This demand arises from the desire to extend the service life of grinding balls used in the metallurgical, mining, and cement industries. Prolonging the service life significantly reduces the cost of the final product and enhances its quality [7 – 9]. Cost reduction is achieved through a decrease in the specific consumption of balls, while quality improvement results from minimizing the entry of broken ball particles into the crushed materials [10].

An analysis of materials from both domestic and foreign researchers indicates that the enhancement of hardness and impact resistance in balls is primarily achieved through the optimization of the chemical composition of steels employed in ball production [11 – 13]. Additionally, improvements in heat treatment modes play a crucial role in achieving these properties [14 – 16]. It is noteworthy that, aside from the mentioned characteristics, the impact resistance of grinding balls is significantly affected by the quality of their macrostructure [17; 18].

The steels used for the production of grinding balls can be categorized into two main groups based on their chemical composition [19; 20]:

– specialized ball steel;

– steels initially designed for the production of other types of rolled products (either carbon or alloyed).

It's worth noting that within the second group of steels, a substantial portion consists of rejected rail steel blanks [21 – 23].

The technologies for the heat treatment of grinding balls can be categorized into three main organizational options:

1) hardening followed by self-tempering of the balls in the air;

2) hardening followed by low tempering;

3) "interrupted hardening" (hardening in several stages), followed by low tempering.

The second and third options for the heat treatment of balls are deemed more preferable, as they facilitate the alleviation of quenching stresses [24; 25]. However, implementing the third option is more challenging.

Irrespective of the chosen heat treatment option for grinding balls, the development of their high-quality quenching microstructure is largely influenced by the cooling capacity of the quenching medium employed. Polymers emerge as the most promising type of quenching medium, as their cooling ability can be effectively regulated across a wide range by adjusting water dilution at different concentrations.

In summary, it can be affirmed that investigations into the processes governing the formation of the quenching microstructure in grinding balls made of rail steel using polymer quenching media are currently of significant scientific and practical interest.

## Materials and methods

The research focused on grinding balls that had not undergone heat treatment, selected from the mill line after rolling but before hardening, sourced from the current production of JSC Guryev Metallurgical Plant and made from rejected rail steel grade K76F.

The research was carried out in two stages:

*1* – examination of the cooling effectiveness of PCM and Thermovit polymer quenching media on the Kompaton facility, with variations in polymer concentration and temperature;

*2* – investigation of the microstructure of grinding balls after quenching using PCM and Thermovit polymer quenching media, with variations in their concentration and temperature.

The temperature of the cooling medium varied in the range of 20 – 40 °C with increments of 10 °C, and the concentration of each studied polymer was set at 2 and 4 %.

The Kompaton facility used in the research is equipped with a digital thermometer featuring a temperature sensor.

The temperature was recorded at specified intervals in automatic mode, and the TC Soft program was employed for data processing, enabling the construction of cooling curves.

To assess the cooling effectiveness of polymer quenching media, grinding balls were heated in a laboratory furnace to the quenching temperature and subsequently cooled in a tank filled with the respective quenching medium. The hardening temperature was maintained 30 °C higher than the $Ac_3$ point, taking into account the actual chemical composition factoring in the actual chemical composition of the samples, as determined by *X*-ray spectral analysis using the Shimadzu XRF-1800 spectrometer. The actual heating temperature of the samples for quenching fell within the range of 790 – 802 °C, with a low tempering temperature ranging between 195 – 215 °C.

Microstructure and hardness studies of the balls were conducted on samples that underwent heat treatment. For each ball, one portion underwent quenching, while the other underwent quenching followed by low tempering. The microstructure analysis utilized an OLYMPUS GX-51 optical metallographic microscope, and hardness was determined using a TK-2M hardness tester.

## Results and discussion

The analysis of the obtained cooling curves for grinding balls made of K76F rail steel suggests that, with both PCM and Thermovit polymer quenching media, the cooling rate remains practically identical at solution temperatures of 20 and 30 °C, regardless of their concentrations (2 or 4 %). However, a noticeable decrease in the cooling rate is observed when the polymer solution temperature is increased to 40 °C (Figs. 1 and 2). Notably, the most pronounced decrease in the cooling rate is observed with the PCM polymer at a concentration of 2 %.

Examination of the microstructure of grinding balls after a complete heat treatment cycle (quenching + low tempering) reveals that the most optimal microstructure, comprising martensite + carbides with some residual austenite, is achieved under specific quenching medium parameters:

1) at a PCM concentration of 2 % and a solution temperature of 20 and 30 °C (Fig. 3, *a*, *b*);

2) at a PCM concentration of 4 % and a polymer temperature of 40 °C (Fig. 3, *c*);

3) at a Thermovit polymer concentration of 4 % and a temperature of 20 °C (Fig. 3, *d*).

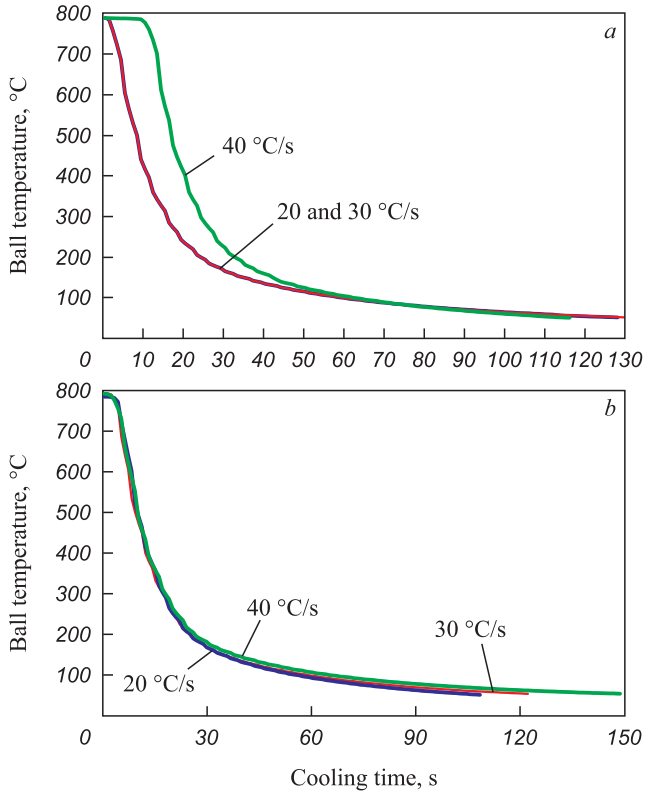


Fig. 1. Cooling curves of K76F rail steel during quenching in an aqueous solution of polymers PCM (*a*) and Thermovit (*b*) with concentration of 2 % depending on the quenching medium temperature

Рис. 1. Кривые охлаждения рельсовой стали К76Ф при закалке в водном растворе полимеров «ПКМ» (*a*) и «Термовит» (*b*) с концентрацией 2 % в зависимости от температуры закалочной среды

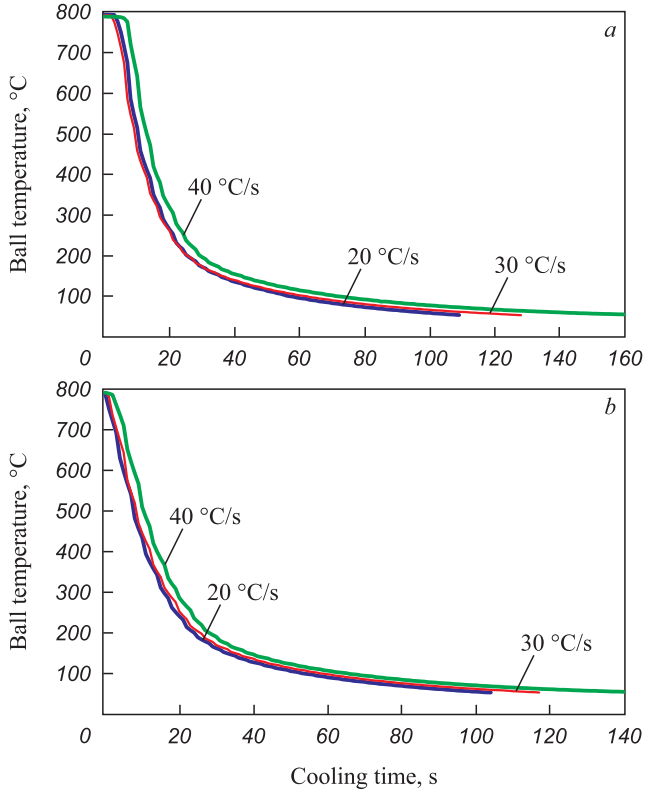


Fig. 2. Cooling curves of K76F rail steel during quenching in an aqueous solution of polymers PCM (*a*) and Thermovit (*b*) with concentration of 4 % depending on the quenching medium temperature

Рис. 2. Кривые охлаждения рельсовой стали К76Ф при закалке в водном растворе полимеров «ПКМ» (*a*) и «Термовит» (*b*) с концентрацией 4 % в зависимости от температуры закалочной среды

Simultaneously, the highest hardness, aligning with hardness group IV as per the state standard GOST 7524–2015 (refer to the Table), is exhibited by balls hardened using the first set of hardening medium parameters (PCM concentration 2 %, solution temperature 20 and 30 °C). Grinding balls hardened by employing the parameters of the quenching medium according to the second and third options only meet the criteria for hardness group II, as per GOST 7524–2015 (PCM concentration 4 %, temperature 40 °C; Thermovit concentration 4 %, temperature 20 °C).

When a 4 % PCM polymer solution is utilized for hardening balls at temperatures of 20 and 30 °C, a microstructure in the form of troostomartensite + carbides + residual austenite is formed (Fig. 4). Although the hardness of such balls falls within hardness group II according

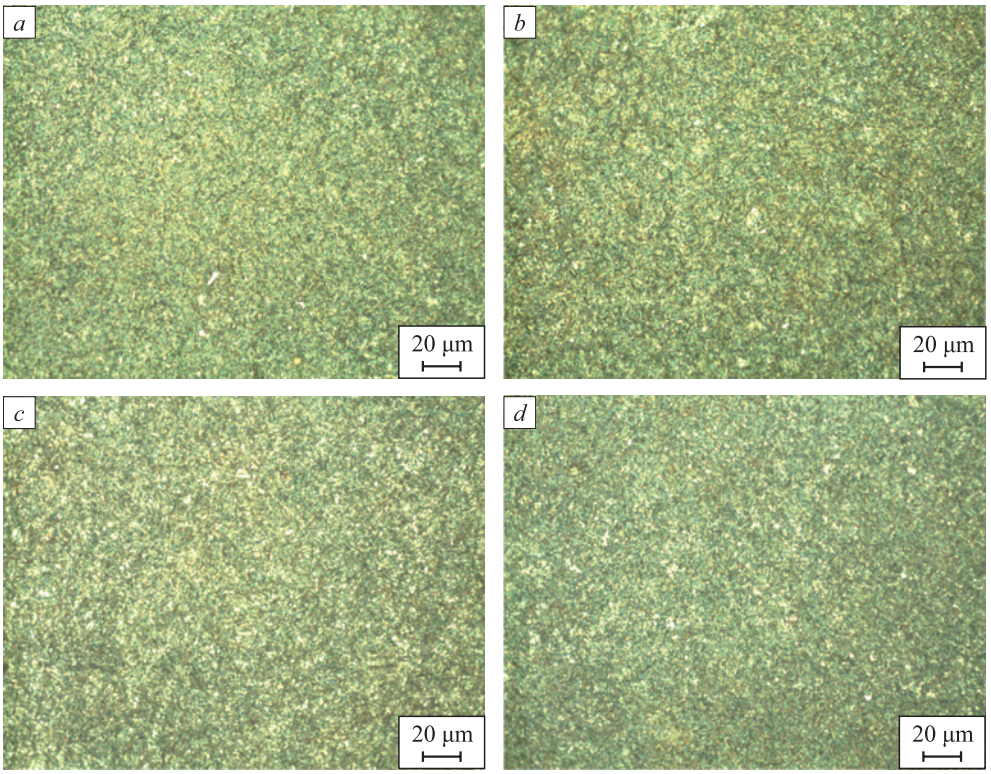


Fig. 3. Microstructure of grinding balls made of K76F rail steel after quenching with subsequent low tempering:
*a*, *b* – PCM polymer concentration of 2 % at 20 and 30 °C; *c* – PCM polymer concentration of 4 % at 40 °C;
*d* – Thermovit polymer concentration of 2 % at 20 °C

Рис. 3. Микроструктура мелющих шаров из рельсовой стали К76Ф после закалки с последующим низким отпуском:
*a*, *b* – концентрация полимера «ПКМ» 2 %, температура 20 и 30 °С; *c* – концентрация полимера «ПКМ» 4 %, температура 40 °С;
*d* – концентрация полимера «Термовит» 2 %, температура 20 °С

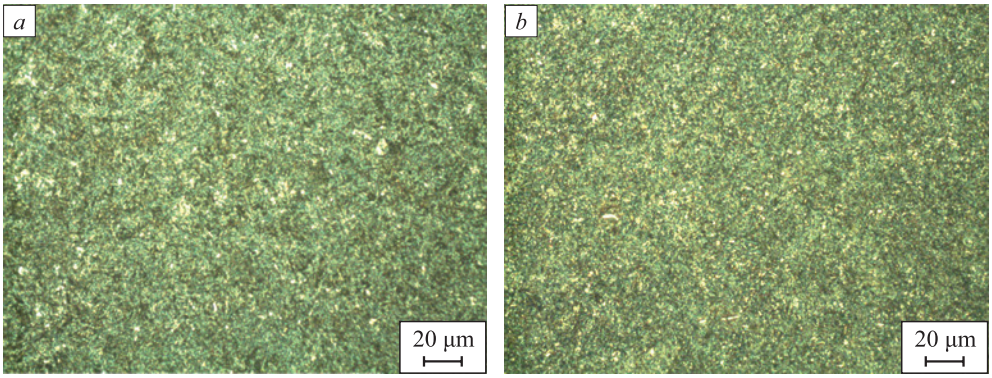


Fig. 4. Microstructure of grinding balls made of K76F rail steel after quenching in a solution of PCM polymer
with concentration of 4 % at 20 (*a*) and 30 °C (*b*)

Рис. 4. Микроструктура мелющих шаров из рельсовой стали К76Ф после закалки в растворе полимера «ПКМ»
с концентрацией 4 %, температура 20 °С (*a*) и 30 °С (*b*)

**Comparative analysis of hardness of the balls after heat treatment using various quenching media**

**Сравнительный анализ твердости шаров после термообработки при использовании различных закалочных сред**

| Temperature of quenching medium, °C | Ball hardness after heat treatment using various quenching media and their concentrations, HRC | | | |
|---|---|---|---|---|
| | PCM | | Thermovit | |
| | 2 % | 4 % | 2 % | 4 % |
| Surface | | | | |
| 20 | 54 – 56 | 48 – 51 | 48 – 50 | 43 – 45 |
| 30 | 53 – 55 | 47 – 49 | 44 – 46 | 38 – 45 |
| 40 | 50 – 52 | 48 – 50 | 44 – 45 | 46 – 48 |
| Requirements of GOST 7524–2015 for balls 60 mm in diameter by groups | | | | |
| Group I | at least 43 HRC | | | |
| Group II | at least 48 HRC | | | |
| Groups III, IV | at least 53 HRC | | | |
| At the depth of 1/2 ball radius | | | | |
| 20 | 52 – 54 | 48 – 51 | 48 – 50 | 39 – 41 |
| 30 | 51 – 53 | 47 – 49 | 44 – 46 | 38 – 45 |
| 40 | 50 – 51 | 48 – 50 | 44 – 45 | 38 – 42 |
| Requirements of GOST 7524–2015 for balls 60 mm in diameter by groups | | | | |
| Groups I, II, III | – | | | |
| Group IV | at least 43 HRC | | | |

to GOST 7524–2015 (refer to the Table), they exhibit potentially higher impact strength owing to the properties of the troostomartensite phase.

However, quenching balls according to other combinations of quenching medium parameters results in a defective microstructure. In addition to martensite, there is the presence of quenching troostite in various forms: acicular, spheroidal, and in the form of a network (Fig. 5). The existence of troostite in the structure indicates a lower cooling rate, signifying inadequate cooling capacity of the quenching medium. Regardless of the type of troostite, its negative impact on the hardness of the grinding balls is evident (refer to the table). Notably, the more pronounced negative influence is naturally exerted by the spheroidal troostite and the form of a grid.

In general, it is noteworthy that the quality of the microstructure in balls hardened with PCM solution is significantly superior compared to those hardened with Thermovit polymer solution. For instance, balls hardened in a PCM solution with a 2 % concentration at a temperature of 40 °C exhibit only acicular troostite in the structure (Fig. 5, *a*); balls hardened with Thermovit polymer at a similar concentration and temperature display spheroidal troostite and troostite in the form of a grid (Fig. 5, *c*). Moreover, the hardness of balls hardened using PCM polymer with the specified concentration and temperature, both on the surface and in the core, is, on average, 6 – 7 HRC higher than the hardness of balls hardened in Thermovit polymer medium (refer to the Table).

In conclusion, it can be inferred that altering the parameters of the polymer quenching medium enables the variation of performance characteristics in grinding balls made of rail steel, thus determining potential applications. For example:

• quenching balls in a PCM polymer solution with a 2 % concentration at a temperature of 20 – 30 °C ensures the production of balls with high hardness (hardness group IV as per GOST 7524–2015).

• employing the same polymer solution for quenching with a 4 % concentration and a temperature of 20 – 30 °C creates the possibility of producing balls with lower hardness but potentially high impact resistance.

However, caution is advised as certain combinations of PCM and Thermovit polymer concentrations and temperatures may lead to a high risk of obtaining a defective microstructure.

## Conclusions

Based on laboratory experimental studies, cooling curves were constructed for hardening of the balls made of K76F rail steel in solutions of PCM and Thermovit polymers, each with a concentration of 2 and 4 % and temperature ranging from of 20 to 40 °C. The experimental research in the laboratory has elucidated the patterns

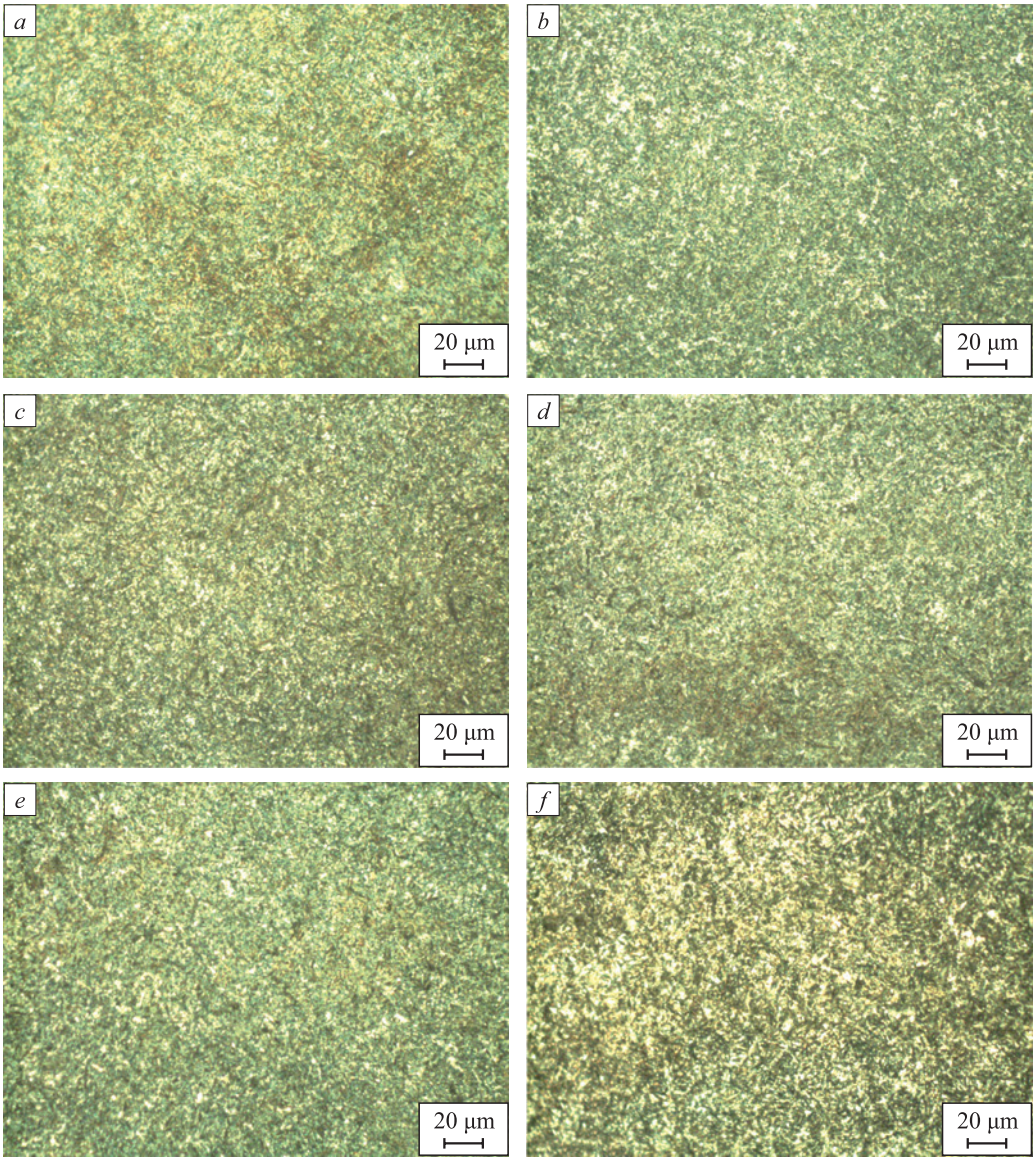


Fig. 5. Defective microstructure of grinding balls made of K76F rail steel after quenching and low tempering:
*a* – PCM polymer concentration of 2 % at 40 °C;
*b*, *c* – Thermovit polymer concentration of 2 % at 30 and 40 °C;
*d*, *e*, *f* – Thermovit polymer concentration of 4 % at 20, 30 and 40 °C

Рис. 5. Дефектная микроструктура мелющих шаров из рельсовой стали К76Ф после закалки и низкого отпуска:
*a* – концентрация полимера «ПКМ» 2 %, температура 40 °C;
*b*, *c* – концентрация полимера «Термовит» 2 %, температура 30 и 40 °C;
*d*, *e*, *f* – концентрация полимера «Термовит» 4 %, температура 20, 30 и 40 °C

governing the formation of the microstructure in grinding balls from the specified steel when utilizing PCM and Thermovit polymer quenching media with varying heat treatment parameters.

Notably, the use of PCM solution for ball hardening ensures a significantly higher quality of the microstructure and hardness of the balls compared to utilization of Thermovit polymer. As a result, recommendations have been developed for optimal combinations of concentration and temperature of PCM polymer. These recommendations aim to ensure the production of balls with increased hardness as well as the production of balls with lower hardness but with a heightened level of impact resistance.

## References / Список литературы

**1.** Ulegin K.A., Shvedov K.N., Borodin A.N., Rubtsov V.Yu. The new ball-rolling mill of EVRAZ NTMK – new possibilities for customers. *Ferrous Metallurgy. Bulletin of Scientific, Technical and Economic Information*. 2020;76(6):602–608. (In Russ.). https://doi.org/10.32339/0135-5910-2020-6-602-608

Улегин К.А., Шведов К.Н., Бородин А.Н., Рубцов В.Ю. Новый шаропрокатный стан ЕВРАЗ НТМК – новые воз-

можности для потребителей. *Черная металлургия. Бюллетень научно-технической и экономической информации*. 2020;76(6):602–608. https://doi.org/10.32339/0135-5910-2020-6-602-608

2. Shvedov K.N., Galim'yanov I.K., Kazakovtsev M.A. Production of grinding balls of high surface and normalized volume hardness. *Metallurgist*. 2020;64(5–6):499–507. http://dx.doi.org/10.1007/s11015-020-01019-3
3. Stalinskii D.V., Rudyuk A.S., Solenyi V.K., Yudin A.V., Volkov K.V., Atkonova O.P. Improving the production of steel grinding balls at AO EVRAZ ZSMK. *Steel in Translation*. 2016;46(7):525–528. https://doi.org/10.3103/S0967091216070135
4. Lam M.M., Serov A.I., Smyrnov Y.N., Ternavskii A.N., Mykheiev V.V. Production of hard (class V) grinding balls at PJSC "DMPZ". *Steel in Translation*. 2017;47(5):325–329. https://doi.org/10.3103/S0967091217050072
5. Adigamov R.R., Nikishin I.A., Zhitelev P.S., Andreev A.R., Karlina A.R. Experience in mastering the production of steel grinding balls in PJSC SEVER-STAL. *Stal'*. 2022;(3):13–18. (In Russ.).

   Адигамов Р.Р., Никишин И.А., Жителев П.С., Андреев А.Р., Карлина А.Р. Опыт освоения производства стальных мелющих шаров в ПАО «СЕВЕРСТАЛЬ». *Сталь*. 2022;(3):13–18.
6. Lam M.M., Serov A.I., Smirnov E.N., Ternavskii A.A., Bazarova G.S. Mastering the production of 40- and 60-mm-diam. grinding balls in hardness classes III and IV at the Donetsk Metal-Rolling Plant. *Metallurgist*. 2016;60(3-4): 440–446. http://dx.doi.org/10.1007/s11015-016-0311-x
7. Aldrich C. Consumption of steel grinding media in mills – A review. *Minerals Engineering*. 2013;49:77–91. http://dx.doi.org/10.1016/j.mineng.2013.04.023
8. Umucu Y., Deniz V. The effect of ball type in fine particles grinding on kinetic breakage parameters. *Inzynieria Mineralna*. 2015;16(1):197–203.
9. Song Z., Pu Y., Liu Z., Wang B. Analysis of failure of grinding balls during service. *Metal Science and Heat Treatment*. 2022;64(1-2):127–133. https://doi.org/10.1007/s11041-022-00772-3
10. Rakhutin M., Boiko P. Ways to improve assessment methods of the main characteristics of grinding balls. *Ugol'*. 2017;(12):49–52. http://dx.doi.org/10.18796/0041-5790-2017-12-49-52

    Рахутин М.Г., Бойко П.Ф. Пути совершенствования методов оценки основных характеристик мелющих шаров. *Уголь*. 2017;12:49–52. http://dx.doi.org/10.18796/0041-5790-2017-12-49-52
11. Naizabekov A.B., Mukhametkaliev B.S., Arbuz A.S., Lezhnev S.N. Reducing the consumption of steel grinding balls by improving their production technology. *Vesti vysshikh uchebnykh zavedenii Chernozem'ya*. 2016;4(46): 78–86. (In Russ.).

    Найзабеков А.Б., Мухаметкалиев Б.С., Арбуз А.С., Лежнев С.Н. Снижение расхода стальных мелющих шаров путем улучшения технологии их производства. *Вести высших учебных заведений Черноземья*. 2016;(4(46)):78–86.
12. Sychkov A.B., Steblov A.B., Bereznov S.N. The choice of material and heat treatment regimes of steel grinding balls, meeting the requirements of the modern global market. *Lit'e i metallurgiya*. 2013;(3(71)):30–32. (In Russ.).

    Сычков А.Б., Стеблов А.Б., Березнов С.Н. О выборе материала и режимов термической обработки стальных мелющих шаров, отвечающих требованиям современного мирового рынка. *Литье и металлургия*. 2013;(3(71)):30–32.
13. Umansky A.A., Golovatenko A.V., Prudnikov A N. Analysis of the main trends in the development of the production of grinding balls in Russia and abroad. *IOP Conference Series: Materials Science and Engineering*. 2020;866(1):012032. http://dx.doi.org/10.1088/1757-899X/866/1/012032
14. Bai X., Jin Y. Heat treatment of wear resistant steel ball for large ball mill. *Jinshu Rechuli/Heat Treatment of Metals*. 2017;42(5):193–196. https://doi.org/10.13251/j.issn.0254-6051.2017.05.040
15. Bouhamla K., Bourebia M., Gharbi A., Maouche H., Chaour M., Belhadi S. Effect of heat treatment on tribological behavior of forged steel balls. *AIP Conference Proceedings*. 2019;2123(1):030004. https://doi.org/10.1063/1.5117035
16. Titov S.S., Meshcheryakov V.N., Leushin I.O., Fedorov O.V. Development of technology and equipment for induction axisymmetric hardening of grinding steel balls. *Chernye metally*. 2020;(6):11–16. (In Russ.).

    Титов С.С., Мещеряков В.Н., Леушин И.О., Федоров О.В. Разработка технологии и оборудования для индукционной осесимметричной закалки мелющих стальных шаров. *Черные металлы*. 2020;(6):11–16.
17. Smirnov E.N., Smirnov A.N., Mikheev V.V., Sklyar V.A., Belevitin V.A., Verzilov A.P., Orlov G.A. The exploration of the possibility of using continuous-cast 55 grade steel in the manufacturing of 40-mm-in-diameter grinding balls of IV and V hardness class. *Steel in Translation*. 2020;50(4): 270–276. https://doi.org/10.3103/S0967091220040099
18. Stalinskii D.V., Rudyuk A.S., Solenyi V.K. Development of production and estimation of the efficiency of using high-quality grinding balls. Report 1. Mastering the production of balls from chromium–molybdenum steel. *Steel in Translation*. 2021;51(11):822–826. https://doi.org/10.3103/S0967091221110127
19. Efremenko V.G. Metallographic analysis of the causes of destruction of steel rolled bodies for drum mills. *Vestnik Priazovskogo gosudarstvennogo tekhnicheskogo universiteta*. 2000;(9):89–91. (In Russ.).

    Ефременко В.Г. Металлографический анализ причин разрушения стальных катаных тел для барабанных мельниц. *Вестник Приазовского государственного технического университета*. 2000;(9):89–91.
20. Umanskii A.A., Temlyantsev M.V., Oskolkova T.N., Simachev A.S., Golovatenko A.V. Study of grinding ball quality properties during manufacture in a screw rolling mill. *Metallurgist*. 2019;63(5-6):578–584. http://dx.doi.org/10.1007/s11015-019-00863-2
21. Pater Z., Tomczak J., Bulzak T., Andrietti S., Barbelet M. An innovative method for producing balls from scrap rail heads. *The International Journal of Advanced Manufacturing Technology*. 2018;97(1-4):893–901. https://doi.org/10.1007/s00170-018-2007-9
22. Tomczak J., Pater Z., Bulzak T. The flat wedge rolling mill for forming balls from heads of scrap railway rails. *Archives of Metallurgy and Materials*. 2018;63(1):5–12. http://dx.doi.org/10.24425/118901

**23.** Umanskiy A.A., Simachev A.S., Dumova L.V. Development of technology for production of grinding bodies with improved performance properties from the rail steels rejection. *Chernye Metally*. 2021;(5):57–61.
http://doi.org/10.17580/chm.2021.05.10

Уманский А.А., Симачев А.С., Думова Л.В. Разработка технологии производства мелющих тел с повышенными эксплуатационными свойствами из отбраковки рельсовых сталей. *Черные металлы*. 2021;(5):57–61.
http://doi.org/10.17580/chm.2021.05.10

**24.** Efremenko V.G., Popov E.S., Kuz'min S.O., Trufanova O.I., Efremenko A.V. Introduction of three-stage thermal hardening technology for large diameter grinding balls. *Metallurgist*. 2014;57(9-10):849–854.
http://doi.org/10.1007/s11015-014-9812-7

**25.** Zurnadzhy V.I., Efremenko V.G., Wu K.M., Lekatou A.G, Shimizu K., Chabak Yu.G., Zotov D.S., Dunayev E.V. Quenching and partitioning–based heat treatment for rolled grinding steel balls. *Metallurgical and Materials Transactions A*. 2020;51(1-4):3042–3053.
https://doi.org/10.1007/s11661-020-05737-w

## Information about the Authors

***Aleksandr A. Umanskii,*** *Dr. Sci. (Eng.), Prof. of the Chair of Ferrous Metallurgy,* Siberian State Industrial University
***ORCID:*** 0000-0003-4403-9006
***E-mail:*** umanskii@bk.ru

***Vadim V. Baidin,*** *Candidates for a degree of Cand. Sci. (Eng.) of the Chair of Ferrous Metallurgy,* Siberian State Industrial University
***E-mail:*** 5745426@gmail.com

***Artem S. Simachev,*** *Cand. Sci. (Eng.), Assist. Prof. of the Chair "Metal Forming and Metal Science. "EVRAZ ZSMK",* Siberian State Industrial University
***ORCID:*** 0000-0002-9712-3757
***E-mail:*** simachev_as@mail.ru

***Lyubov' V. Dumova,*** *Candidates for a degree of Cand. Sci. (Eng.) of the Chair of Ferrous Metallurgy,* Siberian State Industrial University
***E-mail:*** doumova@bk.ru

***Sergei O. Safonov,*** *Assistant of the Chair of Ferrous Metallurgy,* Siberian State Industrial University
***E-mail:*** sergey.safonov.1950@mail.ru

## Сведения об авторах

***Александр Александрович Уманский,*** *д.т.н., профессор кафедры металлургии черных металлов,* Сибирский государственный индустриальный университет
***ORCID:*** 0000-0003-4403-9006
***E-mail:*** umanskii@bk.ru

***Вадим Викторович Байдин,*** *соискатель степени к.т.н. кафедры металлургии черных металлов,* Сибирский государственный индустриальный университет
***E-mail:*** 5745426@gmail.com

***Артем Сергеевич Симачев,*** *к.т.н., доцент кафедры «Обработка металлов давлением и металловедение. ЕВРАЗ ЗСМК»*, Сибирский государственный индустриальный университет
***ORCID:*** 0000-0002-9712-3757
***E-mail:*** simachev_as@mail.ru

***Любовь Валерьевна Думова,*** *соискатель степени к.т.н. кафедры металлургии черных металлов,* Сибирский государственный индустриальный университет
***E-mail:*** doumova@bk.ru

***Сергей Олегович Сафонов,*** *ассистент кафедры металлургии черных металлов,* Сибирский государственный индустриальный университет
***E-mail:*** sergey.safonov.1950@mail.ru

## Contribution of the Authors

***A. A. Umanskii*** – development of a research plan, analysis of mechanisms of formation of the microstructure and mechanical properties of grinding balls, formulation of conclusions.
***V. V. Baidin*** – generalization of the results of experimental studies on cooling capacity of polymer quenching media and microstructure of grinding balls.
***A. S. Simachev*** – metallographic studies of microstructure and hardness analysis of grinding balls before and after heat treatment.

***L. V. Dumova*** – conducting an analytical review on the article topic, design of the article.
***S. O. Safonov*** – conducting studies of cooling capacity of polymer quenching media with varying concentrations and temperatures.

## Вклад авторов

***А. А. Уманский*** – разработка плана исследований, анализ механизмов формирования микроструктуры и механических свойств мелющих шаров, формулирование основных выводов.
***В. В. Байдин*** – обобщение результатов экспериментальных исследований охлаждающей способности полимерных закалочных сред и микроструктуры мелющих шаров.
***А. С. Симачев*** – проведение металлографических исследований микроструктуры и анализа твердости мелющих шаров до и после термообработки.
***Л. В. Думова*** – проведение аналитического обзора по тематике исследования, оформление материалов статьи.
***С. О. Сафонов*** – проведение исследований охлаждающей способности полимерных закалочных сред при варьировании их концентраций и температуры.

Received 28.08.2023
Revised 11.09.2023
Accepted 29.09.2023

Поступила в редакцию 28.08.2023
После доработки 11.09.2023
Принята к публикации 29.09.2023

**UDC** 669.187.2
**DOI** 10.17073/0368-0797-2023-6-653-658



***Original article***
***Оригинальная статья***

# Evaluating the efficiency of metallized siderite concentrate electric melting

**A. S. Vusikhis[1] ✉, L. I. Leont'ev[1, 2, 3], Yu. A. Chesnokov[4]**

[1] **Institute of Metallurgy, Ural Branch of the Russian Academy of Science** (101 Amundsena Str., Yekaterinburg 620016, Russian Federation)
[2] **National University of Science and Technology "MISIS"** (4 Leninskii Ave., Moscow 119049, Russian Federation)
[3] **Scientific Council on Metallurgy and Metal Science of Russian Academy of Sciences (Department of Chemistry and Material Sciences)** (32a Leninskii Ave., Moscow 119991, Russian Federation)
[4] **LLC "NPVP TOREKS"** (8 Osnovinskaya Str., Yekaterinburg 620041 Russian Federation)

✉ vas58@mail.ru

***Abstract***. The Bakal siderites belong to low-grade refractory carbonate iron ores. The low content of phosphorus and non-ferrous metals makes siderites a valuable raw material for obtaining highly metallized concentrate suitable for use in steelmaking processes. Reduction of siderites in a rotary furnace at 1300 – 1350 °C followed by magnetic separation of waste rock allows to obtain a concentrate with metallization degree over 90 % and a content of waste rock of about 5 % suitable for steelmaking as raw materials. The purpose of this work is to evaluate the efficiency of the process aimed at obtaining metal from siderite ore including obtaining of highly metallized siderite concentrate in a recovery furnace, as well as its hot loading into ore-thermal furnace and melting process itself. To do this, the electric melting was calculated in the electric ore melting furnace providing for determination of a large number of parameters including the electricity consumption required for melting. As raw materials we used a highly metallized siderite concentrate ($\varphi_{met}$ = 92.3 %) containing 35 % of waste rock and, for comparison, a briquetted metallized siderite concentrate obtained from a lump concentrate in which a significant amount of waste rock was removed by wet magnetic separation. The results analysis shows that increase in concentrate temperatures from 25 to 1000 °C decreases specific energy consumption and at the same time increases the furnace productivity to values comparable to the parameters of melting briquetted concentrate. This confirms the efficiency of the developed process. To reduce the melting point of high-magnesium slag, it is proposed to use colemanite as flux.

***Keywords:*** iron ore raw materials, Bakal siderites, ore benefication, metallization, concentrate, electric melting, colemanite

***Acknowledgements:*** The work was supported by the Russian Science Foundation, project No. 22-29-00400.

***For citation:*** Vusikhis A.S., Leont'ev L.I., Chesnokov Yu.A. Evaluating the efficiency of metallized siderite concentrate electric melting. *Izvestiya. Ferrous Metallurgy*. 2023;66(6):653–658. https://doi.org/10.17073/0368-0797-2023-6-653-658

# Оценка эффективности электроплавки металлизованного сидеритового концентрата

**А. С. Вусихис[1] ✉, Л. И. Леонтьев[1, 2, 3], Ю. А. Чесноков[4]**

[1] **Институт металлургии Уральского отделения РАН** (Россия, 620016, Екатеринбург, ул. Амундсена, 101)
[2] **Национальный исследовательский технологический университет «МИСИС»** (Россия, 119049, Москва, Ленинский пр., 4)
[3] **Президиум РАН** (Россия, 119991, Москва, Ленинский пр., 32а)
[4] **ООО «НПВП ТОРЭКС»** (Россия, 620041, Екатеринбург, ул. Основинская, 8)

✉ vas58@mail.ru

***Аннотация***. Бакальские сидериты относятся к бедным, труднообогатимым карбонатным железным рудам. Низкое содержание фосфора и цветных металлов делает сидериты ценным сырьем для получения высокометаллизированного концентрата, пригодного для использования в сталеплавильных процессах. Восстановление сидеритов во вращающейся печи при 1300 – 1350 °C с последующим отделением пустой породы методом магнитной сепарации позволяет получить в качестве сырья концентрат со степенью металлизации более 90 % и содержанием пустой породы около 5 %, пригодный для выплавки стали. Цель данной работы – оценить эффективность процесса получения металла из сидеритовой руды, включающего получение высокометаллизованного сидеритового концентрата в восстановительной печи, а также его горячую загрузку в руднотермическую печь и сам процесс плавки. Для этого произведен расчет электроплавки в электрической руднотермической печи, позволяющий определить большое количество параметров, в том числе расход

электроэнергии, необходимый для плавки. В качестве исходных материалов использовали кусковой металлизированный сидеритовый концентрат ($\varphi_{мет}$ = 92,3 %), содержащий 35 % пустой породы. Для сравнения взят брикетированный металлизированный сидеритовый концентрат, полученный из кускового концентрата, в котором значительное количество пустой породы удалено методом мокрой магнитной сепарации. Анализ результатов показывает, что повышение температуры кускового концентрата от 25 до 1000 °С снижает удельные энергозатраты и одновременно увеличивает производительность печи до значений, сравнимых с параметрами плавки брикетированного концентрата. Это подтверждает эффективность предлагаемого процесса. Для снижения температуры плавления высокомагнезиальных шлаков в качестве флюса предложено использовать колеманит.

***Ключевые слова:*** железорудное сырье, бакальские сидериты, обогащение руды, металлизация, концентрат, электроплавка, колеманит

***Благодарности:*** Работа выполнена при поддержке Российского научного фонда, проект № 22-29-00400.

***Для цитирования:*** Вусихис А.С., Леонтьев Л.И., Чесноков Ю.А. Оценка эффективности электроплавки металлизованного сидеритового концентрата. *Известия вузов. Черная металлургия*. 2023;66(6):653–658. https://doi.org/10.17073/0368-0797-2023-6-653-658

## Introduction

The Bakal group of deposits, situated in the Chelyabinsk region, holds siderites categorized as low-grade refractory carbonate iron ores. Predominantly composed of sideroplesite and pistomesite, these ores comprise iron, magnesium, and manganese carbonate solid solutions. Complementing these minerals are barren components such as quartz-clay slates, dolomites, dolomitized limestones, diabases, and quartzites [1 – 4].

Siderites, characterized by their low phosphorus content, absence of non-ferrous metals like copper and zinc, and inclusion of manganese, stand as valuable resources for yielding high-metal concentrates suitable for steelmaking processes [5; 6]. Various process solutions have been devised for their production.

Pyrometallurgical techniques for processing low-grade iron ores, involving metallization with a solid reducing agent within rotary furnaces followed by waste rock separation through grinding and magnetic procedures, are widely employed in global industrial practice [7 – 11]. The refractory nature of siderite waste rock permits operation at temperatures ranging from 1300 to 1350 °C. This facilitates the enlargement of iron grains and significantly enhances their extraction into the concentrate through magnetic separation. In this process, a product boasting a metallization degree exceeding 90 % is achieved, containing approximately 5 % waste rock primarily composed of magnesium oxide [12; 13]. The preliminary removal of easily fusible slates enables processing in heavy media [14], where during separation, the lighter fraction of waste rock floats atop the suspension and is subsequently removed.

The metallurgical plants in the Ural region are currently facing a severe shortage of iron ore resources, necessitating their importation from other regions of the country [15 – 17]. Consequently, ensuring steelmaking production with a high-quality metal charge becomes a crucial objective. Therefore, there is an urgent need to evaluate the potential utilization of metallized concentrate derived from Bakal siderites through direct reduction as a resource for electric steelmaking furnaces.

In the majority of coke-free metallurgy technologies, the final product designated for electric steelmaking typically consists of 90 – 93 % iron with a metallization degree ranging from 92 – 95 %, alongside 3 – 5 % waste rock [18; 19]. As the proportion of waste rock increases, furnace yield and productivity decline, while power consumption rises. However, it is recognized that elevating the temperature of the loaded resources leads to a significant reduction in power consumption of the arc furnace, electrodes, and refractory materials, while simultaneously enhancing furnace productivity [19].

Hence, the objective of this study is to assess the efficiency of utilizing metallized siderite concentrate within an ore-thermal furnace.

## Materials and methods

The methodology for calculation and the software module developed for determining the technical and economic indicators of smelting in an ore-thermal furnace comprise a data input block, encompassing:

– chemical composition of charge materials;

– fluxing and fuel additives;

– furnace operation settings.

The electric smelting calculation in an ore-thermal furnace entails:

– determining metal and slag yield;

– assessing the chemical composition of the final slag with specified basicity or iron monoxide content;

– estimating the final metal temperature;

– designing sulfur content in the metal;

– analyzing the composition of flue gas;

– calculating mass and heat balances of the process;

– evaluating process production costs.

The developed software module, accessible in interactive mode, enables the user to:

– enter and edit information, as well as input data for calculations, with the ability to select and sort based on displayed edit fields;

Table 1

**Chemical composition of metallized siderites, wt. %**

*Таблица 1*. **Химический состав металлизованных сидеритов, % (по массе)**

| Description | C | $Fe_{met}$ | S | P | CaO | $SiO_2$ | MgO | MnO | FeO | $Al_2O_3$ | $\varphi_{met}$ |
|---|---|---|---|---|---|---|---|---|---|---|---|
| Metallized concentrate (lump) | 0.90 | 57.07 | 0.14 | 0.03 | 3.49 | 12.89 | 14.34 | 3.28 | 6.12 | 1.77 | 92.3 |
| Metallized concentrate (briquette) | 0.21 | 83.58 | 0.12 | 0.04 | 0.44 | 0.92 | 3.01 | 0.38 | 11.06 | 0.24 | 90.7 |

– quickly add new input data by copying and editing existing records;

– archive and print both input data and calculation results, while also providing authorized access to the software module.

To determine the chemical composition of the initial materials used in the calculations, experimental modeling of the siderite metallization process in a rotary furnace was conducted. A graphite crucible containing raw siderite lumps ranging from 10 to 40 mm in size, along with breeze coke filler sized between 0 and 5 mm, was placed in a Tamman furnace heated to a temperature of 1300 °C. The setup was maintained under specified conditions for 2 h before being cooled down with the furnace. This process resulted in the formation of a metallized concentrate (in lump form). Subsequently, a portion of the metallized concentrate lumps underwent grinding and wet magnetic separation to produce a product suitable for smelting in an electric furnace in the form of briquettes, referred to as metallized concentrate (briquette). The compositions of these materials are outlined in Table 1.

The temperature at which the concentrate (metallized concentrate in lump form) was loaded into the furnace after reducing roasting varied within the range of 25 to 1000 °C. The concentrate (metalized concentrate in briquette from) was loaded at 25 °C.

## Results and discussion

Variants of calculations of melting indicators in an ore-thermal furnace with the use of lump metallized siderite concentrate loaded into the furnace at temperatures of 25 – 1000 °C as an initial resource, all other conditions being equal, are given in Table 2.

Graphical interpretation of the effect of temperature of the lump metallized siderite concentrate loaded into a furnace on the productivity and specific power consumption for melting is given in the Figure.

The analysis of the obtained results shows that the use of highly heated lump metallized siderite concentrate is one of the important process measures to increase the efficiency of its electric smelting. When the temperature of the material increases in the range from 25 to 1000 °C, the specific power consumption decreases and the furnace productivity increases.

Table 3 presents calculations comparing the melting indicators in an ore-thermal furnace using a briquetted metallized siderite concentrate loaded at a temperature

Table 2

**Indicators of melting in ore-thermal furnace**

*Таблица 2*. **Показатели плавки в руднотермической печи**

| Indicator | 25 °C | 100 °C | 500 °C | 1000 °C |
|---|---|---|---|---|
| Furnace capacity, MVA | 16.5 | | | |
| Consumption of iron-ore components, kg/t metal | 1681.8 | 1681.8 | 1681.8 | 1681.8 |
| Metallized concentrate (lump), kg/t metal | 1681.8 | 1681.8 | 1681.8 | 1681.8 |
| Dust output, kg/t metal | 46.8 | 46.8 | 46.8 | 46.8 |
| Metal losses, kg/t metal | 10.0 | 10.0 | 10.0 | 10.0 |
| Electrode consumption, kg/t metal | 20.2 | 20.2 | 20.2 | 20.2 |
| Metal composition, % | | | | |
| Si | 0.40 | 0.40 | 0.40 | 0.40 |
| Mn | 1.24 | 1.24 | 1.24 | 1.24 |
| P | 0.03 | 0.03 | 0.03 | 0.03 |
| S | 0.005 | 0.005 | 0.005 | 0.005 |
| C | 0.10 | 0.10 | 0.10 | 0.10 |
| Metal temperature, °C | 1600 | 1600 | 1600 | 1600 |
| Slag output, kg/t metal | 579.8 | 579.8 | 579.8 | 579.8 |
| Slag composition, % | | | | |
| $SiO_2$ | 34.58 | 34.58 | 34.58 | 34.58 |
| MgO | 40.36 | 40.36 | 40.36 | 40.36 |
| $Al_2O_3$ | 4.89 | 4.89 | 4.89 | 4.89 |
| MnO | 5.32 | 5.32 | 5.32 | 5.32 |
| FeO | 5.00 | 5.00 | 5.00 | 5.00 |
| Basicity of slag, $CaO/SiO_2$ | 0.28 | 0.28 | 0.28 | 0.28 |
| Heat losses, % | 35.0 | 35.0 | 35.0 | 35.0 |
| Material balance, kg | | | | |
| Receipt | 1678.2 | 1678.2 | 1678.2 | 1678.2 |
| Consumption | 1678.1 | 1678.1 | 1678.1 | 1678.1 |
| Power consumption, kW·h/t sold | 1271.2 | 1229.2 | 1005.2 | 725.1 |
| Throughput capacity, t/day metal | 231.3 | 239.2 | 292.5 | 405.5 |

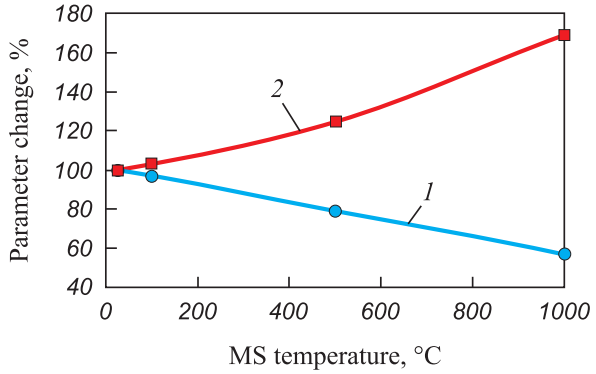


Influence of initial temperature of metallized siderite (MS) on parameters of ore-thermal smelting:
*1* – power consumption; *2* – furnace performance

Влияние начальной температуры металлизованного сидерита (МС) на параметры руднотермической плавки:
*1* – расход электроэнергии; *2* – производительность печи

of 25 °C as feedstock, with all other conditions held constant. Additionally, the data obtained, along with the calculated melting indicators of the lump metallized siderite concentrate loaded at 1000 °C, are provided.

An analysis of the data reveals that feeding a lump metallized siderite concentrate directly into an ore-thermal furnace immediately after discharge from the rotary furnace at temperatures exceeding 1000 °C (similar to the technology employed in processing titanomagnetites of the Bushveld complex in roasting furnaces with loading of a hot stub end into the ore-thermal furnace [20]), proves to be more efficient compared to melting a briquetted metallized siderite concentrate produced through the pyrometallurgical processing of siderites as described in [6; 12; 13].

Consequently, the pyrometallurgical processing technology eliminates the need for operations such as grinding, magnetic separation for waste rock removal, as well as drying and briquetting, thereby significantly reducing the product's overall cost.

The calculations demonstrate that the melting process yields slag with a high magnesium oxide content, characterized by a high melting temperature. However, the addition of material containing boron, such as colemanite [21], to high-magnesia steelmaking slags significantly reduces their melting point.

## Conclusions

The direct loading of lump metallized siderite concentrate into the electric furnace from the reducing furnace in a hot state (at temperatures exceeding 1000 °C) proves to be an effective method for melting and producing metal – a semi-product suitable for subsequent steel production. To ensure adequate fluidity of the high-magnesia slag at outlet temperatures, the addition of boron-containing materials, such as colemanite, to the charge becomes necessary.

Table 3

**Comparative indicators of melting in ore-thermal furnace**

*Таблица 3*. **Сравнительные показатели плавки в руднотермической печи**

| Indicator | 1000 °C | 25 °C |
|---|---|---|
| Furnace capacity, MVA | 16.5 | |
| Consumption of iron-ore components, kg/t metal | 1681.8 | 1114.1 |
| Metallized concentrate (lump), kg/t metal | 1681.8 | 0 |
| Metallized concentrate (briquette), kg/t metal | 0 | 1114.1 |
| Dust output, kg/t metal | 46.8 | 27.2 |
| Metal losses, kg/t metal | 10.0 | 10.0 |
| Electrode consumption, kg/t metal | 20.2 | 20.2 |
| Metal composition, % | | |
| Si | 0.40 | 0.20 |
| Mn | 1.24 | 0.18 |
| P | 0.03 | 0.02 |
| S | 0.005 | 0.008 |
| C | 0.10 | 0.10 |
| Metal temperature, °C | 1600 | 1600 |
| Slag output, kg/t metal | 579.8 | 45.7 |
| Slag composition, % | | |
| $SiO_2$ | 34.58 | 12.30 |
| MgO | 40.36 | 66.07 |
| $Al_2O_3$ | 4.89 | 4.29 |
| MnO | 5.32 | 0.76 |
| FeO | 5.00 | 5.01 |
| Basicity of slag, $CaO/SiO_2$ | 0.28 | 0.89 |
| Heat losses, % | 35.0 | 35.0 |
| Material balance, kg | | |
| Receipt | 1678.2 | 1132.1 |
| Consumption | 1678.1 | 1132.0 |
| Power consumption, kW·h/t sold | 725.1 | 773.4 |
| Throughput capacity, t/day metal | 405.5 | 380.2 |

## References / Список литературы

1. Akhlyustina A.I. Crystal-chemical changes in sideroplesite during firing of Bakal iron ore. *Gornyi zhurnal*. 1968;(8): 60–61. (In Russ.).
Ахлюстина А.И. Кристаллохимические изменения сидероплезита при обжиге бакальской железной руды. *Горный журнал*. 1968;(8):60–61.

**2.** Khokhlov D.G., Akhlyustina A.I. Technology of Bakal carbonate iron ores preparation for blast furnace smelting. *Stal'*. 1968;(4):289–294. (In Russ.).

Хохлов Д.Г., Ахлюстина А.И. Технология подготовки бакальских карбонатных железных руд к доменной плавке. *Сталь*. 1968;(4):289–294.

**3.** Akhlyustina A.I., Zhukovskii G.V., Kvaskov A.P. Technological classification of iron ores of the Bakal deposit. *Trudy "Uralmekhanobr"*. 1972;18:37–43. (In Russ.).

Ахлюстина А.И., Жуковский Г.В., Квасков А.П. Технологическая классификация железных руд Бакальского месторождения. *Труды «Уралмеханобр»*. 1972;18:37–43.

**4.** Krasnoborov V.A., Yaroshevskii S.L., Denisov A.A., etc. *Efficiency and Prospects of Application of Siderite Ore in Blast Furnace Smelting*. Donetsk; 1996:87. (In Russ.).

Красноборов В.А., Ярошевский С.Л., Денисов А.А. и др. *Эффективность и перспективы применения сидеритовой руды в доменной плавке*. Донецк; 1996:87.

**5.** Yur'ev B.P., Melamud S.G., Spirin N.A., Shatsillo V.V. *Technological and Thermal Engineering Bases of Siderite Ore Preparation for Metallurgical Processing: Monograph*. Yekaterinburg: Den' RA; 2016:428. (In Russ.).

Юрьев Б.П., Меламуд С.Г., Спирин Н.А., Шацилло В.В. *Технологические и теплотехнические основы подготовки сидеритовых руд к металлургическим переделам: Монография*. Екатеринбург: ООО АМК «День РА»; 2016:428.

**6.** Vusikhis A.S., Leont'ev L.I. *Application of Siderite Ores in Iron and Steel Production: Monograph*. Moscow; Vologda: Infra-Inzheneriya; 2022:116. (In Russ.).

Вусихис А.С., Леонтьев Л.И. *Применение сидеритовых руд при производстве чугуна и стали: Монография*. Москва, Вологда: Инфра-Инженерия; 2022:116.

**7.** Tatsienko P.A. *Preparation of Refractory Iron Ores*. Moscow: Nedra; 1979:208. (In Russ.).

Тациенко П.А. *Подготовка труднообогатимых железных руд*. Москва: Недра; 1979:208.

**8.** Tulin N.A., Kudryavtsev V.S., Pchelkin S.A., etc. *Development of Coke-Free Metallurgy*. Moscow: Metallurgiya; 1987:228. (In Russ.).

Тулин Н.А., Кудрявцев В.С., Пчелкин С.А. и др. *Развитие бескоксовой металлургии*. Москва: Металлургия; 1987:228.

**9.** Kurunov I.F., Savchuk N.A. *State and Prospects of Direct Metallurgy of Iron*. Moscow: Chermetinformatsiya; 2002:186. (In Russ.).

Курунов И.Ф., Савчук Н.А. *Состояние и перспективы бездоменной металлургии железа*. Москва: Черметинформация; 2002:186.

**10.** Bondarenko B.I., Shapovalov V.A., Garmash N.I. *Theory and Technology of Coke-Free Metallurgy*. Kiev: Naukova Dumka; 2003:536. (In Russ.).

Бондаренко Б.И., Шаповалов В.А., Гармаш Н.И. *Теория и технология бескоксовой металлургии*. Киев: Наукова думка; 2003:536.

**11.** Shumakov N.S. Production of metallized concentrate from siderite ores of the Bakal deposit. *Kompleksnoe ispol'zovanie mineral'nogo syr'ya*. 1990;(4):52–55. (In Russ.).

Шумаков Н.С. Получение металлизованного концентрата из сидеритовых руд Бакальского месторождения. *Комплексное использование минерального сырья*. 1990;(4):52–55.

**12.** Vusikhis A.S., Dvinin V.I., Dmitriev A.N., Kashin V.V., Leont'ev L.I., Nafikov R.A., Chentsov A.V., Shavrin S.V. Evaluating the efficiency of producing highly metallized concentrate from Bakal siderites by hot reduction in a rotary kiln. *Metallurgist*. 2001;45(1-2):14–19. https://doi.org/10.1023/A:1010495309806

Вусихис А.С., Двинин В.И., Дмитриев А.Н., и др. Оценка эффективности получения высокометаллизованного концентрата из бакальских сидеритов методом прямого восстановления во вращающейся печи. *Металлург*. 2001;(1):37–40. https://doi.org/10.1023/A:1010495309806

**13.** Vusikhis A.S., Sheshukov O.Yu., Leont'ev L.I. *Method of metallization of magnesium-containing carbonate iron ore materials*. Patent RF no. 2489494, MPK B21C 1/00. *Bulleten' izobretenii*. 2013;(22). (In Russ.).

Патент RU 2489494 C1. *Способ металлизации магнийсодержащих карбонатных железорудных материалов* / Вусихис А.С., Шешуков О.Ю., Леонтьев Л.И., заявл. 05.12.2011; опубл. 10.08.2013. *Бюллетень изобретений*. 2013;(22).

**14.** Zhunev A.G., Yur'ev B.P., Blank M.E. Intensification of firing and agglomeration of siderite ores. *Ferrous Metallurgy. Bulletin of Scientific, Technical and Economic Information*. 1988;(3):2–13. (In Russ.).

Жунев А.Г., Юрьев Б.П., Бланк М.Э. Интенсификация процессов обжига и агломерации сидеритовых руд. *Черная металлургия. Бюллетень научно-технической информации*. 1988;3:2–13.

**15.** Pakhomov V.P., Dushin A.V. Analysis of the mineral-raw material safety in the Ural Federal District. *Ekonomika regiona*. 2008;(3(15)):129–143. (In Russ.).

Пахомов В.П., Душин А.В. Оценка минерально-сырьевой безопасности УрФО. *Экономика региона*. 2008;(3(15)):129–143.

**16.** Valiev N.G., Slavikovskii O.V., Slavikovskaya Yu.O. Features of development of mineral resource base in the Urals urbanized territories. *Gornyi informatsionno-analiticheskii byulleten' (nauchno-tekhnicheskii zhurnal)*. 2012;(6):344–347. (In Russ.).

Валиев Н.Г., Славиковский О.В., Славиковская Ю.О. Особенности освоения минерально-сырьевой базы на урбанизированных территориях Урала. *Горный информационно-аналитический бюллетень (научно-технический журнал)*. 2012;(6):344–347.

**17.** Kornilkov S.V., Kantemirov V.D. Iron ore deposits of the Nether-Urals as a prospective raw materials base for the Urals metallurgy. *Izvestiya vuzov. Gornyi zhurnal*. 2015;(8);22–28. (In Russ.).

Корнилков С.В., Кантемиров В.Д. Железорудные месторождения Приполярного Урала как перспективная сырьевая база уральской металлургии. *Известия вузов. Горный журнал*. 2015;(8);22–28.

**18.** Soifer V.M. The use of products of direct iron reduction in electric furnaces. *Novosti chernoi metallurgii za rubezhom*. 2007;(8):33–35. (In Russ.).

Сойфер В.М. Использование продуктов прямого восстановления железа в электросталеплавильных печах. *Новости черной металлургии за рубежом*. 2007;(8):33–35.

**19.** Timoshpol'skii V.I., Trusova I.A., Plushchevskii I.N., Korneev S.V. Prospects for production and use of metallized raw materials for obtaining high-quality steel grades. Message 1. Analysis of modern schemes for obtaining metallized raw materials. *Lit'ye i metallurgiya*. 2009;(1(50)):134–138. (In Russ.).

Тимошпольский В.И., Трусова И.А, Плющевский И.Н., Корнеев С.В. Перспективы производства и использования металлизованного сырья для получения высококачественных марок стали. Сообщение 1. Анализ современных схем получения металлизованного сырья. *Литье и металлургия*. 2009;(1(50)):134–138.

**20.** Rohmann B., Raper A.G. Recovery of vanadium from hot metal using the shaking ladle process a preliminary report. *Journal of Iron and Steel Research International*. 1970;208(4):336–342.

**21.** Vusikhis A.S., Agafonov S.N., Tyushnyakov S.N., Sergeeva S.V., Leont'ev L.I. Influence of boric anhydride on viscosity and melting point of high-magnesium steelmaking slags. In: *Fundamental Research and Applied Development of Processing and Disposal of Technogenic Formations: Proceedings of the VI Congress with Int. Part. TECHNOGEN 2023*. Yekaterinburg: Ural Branch of the RAS; 2023: 351–353. (In Russ.).
https://doi.org/10.34923/technogen-ural.2023.15.21.001

Вусихис А.С., Агафонов С.Н., Тюшняков С.Н., Сергеева С.В., Леонтьев Л.И. Влияние борного ангидрида на вязкость и температуру плавления высокомагнезиальных сталеплавильных шлаков. В кн.: *Фундаментальные исследования и прикладные разработки процессов переработки и утилизации техногенных образований: Труды VI Конгресса с международным участием «ТЕХНОГЕН 2023»*. Екатеринбург: УрО РАН; 2023:351–353.
https://doi.org/10.34923/technogen-ural.2023.15.21.001

## Information about the Authors / Сведения об авторах

***Aleksandr S. Vusikhis***, *Cand. Sci. (Eng.), Senior Researcher of the Laboratory of Pyrometallurgy of Non-Ferrous Metals,* Institute of Metallurgy, Ural Branch of the Russian Academy of Science
***ORCID:*** 0000-0002-6395-0834
***E-mail:*** vas58@mail.ru

***Leopol'd I. Leont'ev***, *Academician, Adviser,* Russian Academy of Sciences, *Dr. Sci. (Eng.), Prof.,* National University of Science and Technology "MISIS", *Chief Researcher,* Institute of Metallurgy, Ural Branch of the Russian Academy of Science
***ORCID:*** 0000-0002-4343-914X
***E-mail:*** leo@presidium.ras.ru

***Yurii A. Chesnokov***, *Cand. Sci. (Eng.), Chief Specialist,* LLC "NPVP TOREKS"
***E-mail:*** garlic@torex-npvp.ru

***Александр Семенович Вусихис***, *к.т.н., старший научный сотрудник лаборатории пирометаллургии цветных металлов,* Институт металлургии Уральского отделения РАН
***ORCID:*** 0000-0002-6395-0834
***E-mail:*** vas58@mail.ru

***Леопольд Игоревич Леонтьев***, *академик, советник,* Президиум РАН, *д.т.н., профессор,* Национальный исследовательский технологический университет «МИСиС», *главный научный сотрудник,* Институт металлургии Уральского отделения РАН
***ORCID:*** 0000-0002-4343-914X
***E-mail:*** leo@presidium.ras.ru

***Юрий Анатольевич Чесноков***, *к.т.н., главный специалист,* ООО «НПВП ТОРЭКС»
***E-mail:*** garlic@torex-npvp.ru

## Contribution of the Authors / Вклад авторов

***A. S. Vusikhis*** – setting the research task, performing calculations, writing the text, formation of the conclusions.
***L. I. Leont'ev*** – scientific guidance, analysis of the research results, editing.
***Yu. A. Chesnokov*** – calculations.

***А. С. Вусихис*** – постановка задачи исследования, проведение расчетов, подготовка текста, формулирование выводов.
***Л. И. Леонтьев*** – научное руководство, анализ результатов исследований, редактирование статьи.
***Ю. А. Чесноков*** – проведение расчетов.

Received 31.08.2023
Revised 20.09.2023
Accepted 04.11.2023

Поступила в редакцию 31.08.2023
После доработки 20.09.2023
Принята к публикации 04.11.2023

MATERIALS SCIENCE / МАТЕРИАЛОВЕДЕНИЕ

**UDC** 621.771:620.186.5
**DOI** 10.17073/0368-0797-2023-6-659-665



*Original article*
*Оригинальная статья*

# Structure and properties of low-alloy steel 10G2FBYu after rolling in embossed rolls under conditions of electroplasticity

**Yu. I. Pochivalov**

**Institute of Strength Physics and Materials Science, Siberian Branch of the Russian Academy of Sciences** (2/4 Akademicheskii Ave., Tomsk 634055, Russian Federation)

pochiv@ispms.ru

***Abstract***. The article describes the features of grain structure formation and mechanical properties of low-alloy steel 10G2FBYu after rolling in flat and embossed rolls under the conditions of ordinary and electroplastic deformation. When rolling in embossed rolls, a significant non-uniformity of deformation is achieved over the rolling cross-section, expressed in localized macroshifts directed at an angle of 45° to the rolling plane. It is shown that local shear deformation during rolling in embossed rolls leads to an increase in the ultimate strength of the steel under study with a decrease in plasticity of the rolled material. Rolling 10G2FBYu steel in embossed rolls under conditions of electroplasticity provides maximum strength characteristics with a high hardening coefficient at the stage of macrodeformation. At the same time, the plasticity is maintained at a level sufficient for technological purposes. Structural metallographic and electron microscopic studies showed that increase in strength of steel when rolling in embossed rolls under conditions of electroplastic effect is caused by the refinement of ferrite grains to sizes less than 0.5 μm. Fractographic studies revealed changes in the nature of fracture in steel during rolling in embossed rolls, which is expressed in appearance of areas of brittle fracture in the rolled samples. Rolling under conditions of electroplasticity increases the proportion of ductile fracture and ductility of 10G2FBYu steel.

***Keywords:*** 10G2FBYu steel, rolling, embossed rolls, electroplastic deformation, fracture, structure

***Acknowledgements:*** The work was performed within the framework of the state task of the Institute of Strength Physics and Materials Science, Siberian Branch of the Russian Academy of Sciences, subject no. FWRW-2021-0009.

***For citation:*** Pochivalov Yu.I. Structure and properties of low-alloy steel 10G2FBYu after rolling in embossed rolls under conditions of electroplasticity. *Izvestiya. Ferrous Metallurgy*. 2023;66(6):659–665. https://doi.org/10.17073/0368-0797-2023-6-659-665

# Структура и свойства малолегированной стали 10Г2ФБЮ после прокатки в рельефных валках в условиях электропластичности

**Ю. И. Почивалов**

**Институт физики прочности и материаловедения Сибирского отделения РАН** (Россия, 634055, Томск, пр. Академический, 2/4)

pochiv@ispms.ru

***Аннотация***. Исследованы особенности формирования зеренной структуры и механические свойства малолегированной стали 10Г2ФБЮ после прокатки в плоских и рельефных валках в условиях обычной и электропластической деформации. При прокатке в рельефных валках достигается существенная неравномерность деформации по сечению проката, что выражается в локализованных макросдвигах, направленных под углом 45° к плоскости проката. Локальная сдвиговая деформация при прокатке в рельефных валках приводит к возрастанию предела прочности исследуемой стали при снижении пластичности прокатанного материала. Прокатка стали 10Г2ФБЮ в рельефных валках в условиях электропластичности обеспечивает максимальные прочностные характеристики с высоким коэффициентом упрочнения на стадии макродеформации. Пластичность при этом сохраняется на достаточном для технологических целей уровне. Структурные металлографические и электронно-микроскопические исследования показали, что повышение прочности стали при прокатке в рельефных валках в условиях электропластического эффекта обусловлены измельчением зерен феррита до размеров менее 0,5 мкм. Фрактографические исследования выявили изменения характера разрушения в стали при прокатке в рельефных валках, которое выражается в появлении областей хрупкого разрушения в прокатанных образцах. Переход к прокатке в условиях электропластичности повышает долю вязкого разрушения и пластичность стали 10Г2ФБЮ.

***Ключевые слова:*** сталь 10Г2ФБЮ, прокатка, рельефные валки, электропластическая деформация, разрушение, структура

***Благодарности:*** Работа выполнена в рамках государственного задания Института физики прочности и материаловедения Сибирского отделения РАН, тема номер FWRW-2021-0009.

***Для цитирования:*** Почивалов Ю.И. Структура и свойства малолегированной стали 10Г2ФБЮ после прокатки в рельефных валках в условиях электропластичности. *Известия вузов. Черная металлургия*. 2023;66(6):659–665. https://doi.org/10.17073/0368-0797-2023-6-659-665

## Introduction

Improving the quality of rolled sheets stands as the paramount objective in rolling production. Attaining enhanced strength in low-alloy steels, crucial for construction, oil and gas equipment manufacturing, and oil and gas pipeline production, can be achieved through various methods: targeted alloying [1], controlled rolling [1; 2], asymmetric rolling [3], and other techniques [4 – 6]. To produce high-strength fine-grained rolled products, the suggestion is to employ deformation rolling processes featuring local macroshifts. These macroshifts are facilitated by rolling sheet material in rolls with annular grooves [7 – 9]. In [10], it is demonstrated that rolling 09G2BT steel in such rolls results in a 10 % increase in tensile strength and a 17 – 47 MJ/m$^2$ boost in impact strength, while decreasing anisotropy ($r$) from 2.8, observed during rolling in smooth rolls, to 1.9 when using rolls with annular grooves.

In [11 – 13], the study explores rolling in rolls with a corrugated or wavy surface as a form of intense plastic deformation. This induces local macroshifts, influencing the rolled metal through localized deformation effects. Such macroshifts play a crucial role in processing the entire thickness of the sheet, refining the grain structure, and forming a fine-crystalline grain structure. This overall enhancement leads to improved strength characteristics in the rolled metal, including an increase in impact strength.

The quality of rolled metal can undergo substantial improvement through the application of specialized rolling methods combined with additional impact on the metal via low-duty impulses of high-density electric current (up to 1000 A/mm$^2$) [14 – 16]. This approach is grounded in the electroplastic effect, which entails an augmentation in the plasticity of materials under the influence of an electric current. Notably, higher deformations have been achieved through rolling in the electroplastic deformation mode, eliminating the need for intermediate high-temperature annealing [17 – 19]. In a related study [20], it was demonstrated that rolling with current could lead to the formation of a nanocrystalline structure in titanium-based alloys and titanium nitride, significantly enhancing their strength characteristics.

The current investigation encompasses an examination of the combined method involving rolling in embossed rolls with the additional impact of electric current pulses on the structure and mechanical properties of low-alloy steel 10G2FBYu. This is compared to rolling in flat rolls, encompassing the electroplastic deformation (EPD) mode.

## Materials and methods

This study focused on low-alloy low-carbon steel 10G2FBYu. The steel composition includes, wt. %: C 0.10; Mn 1.58; Si 0.38; S 0.005; P 0.015; Ti 0.019; Al 0.034; V 0.076; Nb 0.048; $N_2$ 0.008.

The investigation involved steel in its as-delivered state, specifically a 56 mm thick sheet after hot rolling. Billets for rolling, in the form of rectangular section rods measuring 15×10 mm with a length of 200 mm, were cut from the original sheet along the rolling direction. Four rolling modes were employed. Mode *1*: rolling billets in flat rolls, reducing thickness from 10 mm to 1 mm without intermediate annealing in multiple passes with a reduction per pass of 0.2 mm (referred to as rolling in flat rolls). Mode *2*: rolling samples from 10 mm to 3 mm in flat rolls, from 3 mm to 1.6 mm in embossed rolls, and from 1.6 mm to 1 mm in flat rolls without intermediate annealing in multiple passes with a reduction per pass of 0.2 mm (referred to as rolling in embossed rolls). Modes *3* and *4* differed from modes *1* and *2* by applying electrical current pulses, with a frequency of 4 kHz and a duration of 100 μs, from a specialized pulse generator with a power of 600 W (referred to as rolling with EPD).

The rolling of steel samples took place on a VEM 3 laboratory mill.

Mechanical tests for uniaxial tension were conducted using an Instron-5582 universal testing machine at a speed of $10^{-4}$ s$^{-1}$ at room temperature. Samples of 10G2FBYu steel for mechanical testing were cut into double-sided blades with a working length of 25 mm and a cross-section of 1×5 mm.

Metallographic studies utilized a Zeiss Axiovert 25 CA optical microscope.

Fractographic studies of the destroyed samples were carried out using the raster electron microscopy with a Tesla BS-300 scanning microscope.

Electron microscopic analysis was conducted utilizing a JEM–100 CXII transmission electron microscope operating at an accelerating voltage of 100 kV. To prepare samples for this analysis, sections were precisely cut using an electrical discharge machine, ground to a thickness of 100 μm, and discs with a diameter of 3 mm were

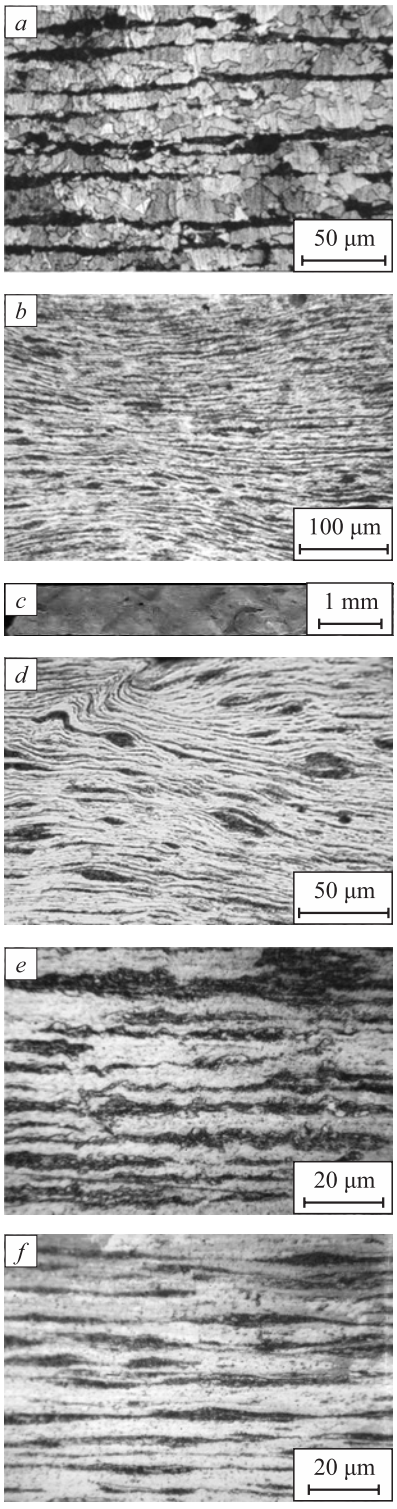


Fig. 1. Structure of 10G2FBYu steel in the state of delivery and after rolling under different conditions:
*a* – in the state of delivery; *b* – after rolling in flat rolls;
*c*, *d* – after rolling in embossed rolls;
*e* – after rolling in flat rolls with eloctroplastic deformation (EPD);
*f* – after rolling in embossed rolls with EPD

Рис. 1. Структура стали 10Г2ФБЮ в состоянии поставки и после прокатки в разных условиях:
*a* – в состоянии поставки; *b* – после прокатки в плоских валках;
*c*, *d* – после прокатки в рельефных валках;
*e* – после прокатки в плоских валках с ЭПД;
*f* – после прокатки в рельефных валках с ЭПД

subsequently cut. The samples were further polished until a hole emerged through jet electropolishing in an electrolyte composed of 125 ml $CH_3COOH$, 25 g $GrO_3$, and 5 ml $H_2O$.

## Results and discussion

In Fig. 1, *a*, the structure of 10G2FBYu steel is depicted in its as-delivered state after pickling in a 4 % nitric acid solution.

The steel exhibits a typical two-phase grain structure characterized by grains elongated along the rolling direction, displaying ferrite-pearlite banding (Fig. 1, *a*). Ferrite grain sizes range from 5 to 15 μm, and the width of pearlite strips is 3 – 7 μm. The tensile diagram of the steel in its as-delivered state is illustrated in Fig. 2, curve *1*, with a tensile strength of 563 ± 12 MPa and a ductility of approximately 15 % (refer to the Table).

Following rolling in flat rolls, 10G2FBYu steel develops a structure with grains elongated along the rolling direction (Fig. 1, *b*). During the rolling process, pearlite colonies undergo substantial crushing and transformation into small particles, measuring 3 – 5 μm in size and exhibiting irregular shapes. The ultimate strength of the steel experiences a notable increase (Fig. 2, Table). However, concurrently, the ductility undergoes a significant reduction, almost halving in comparison.

The structure of 10G2FBYu steel after rolling in embossed rolls is presented in Fig. 1, *c*, *d*. Notably, rolling in embossed rolls achieves significant, uneven deformation across the cross-section of the rolled product, evident in localized macroshifts directed at a 45° angle to the plane of the rolled product (Fig. 1, *c*). These shifts result

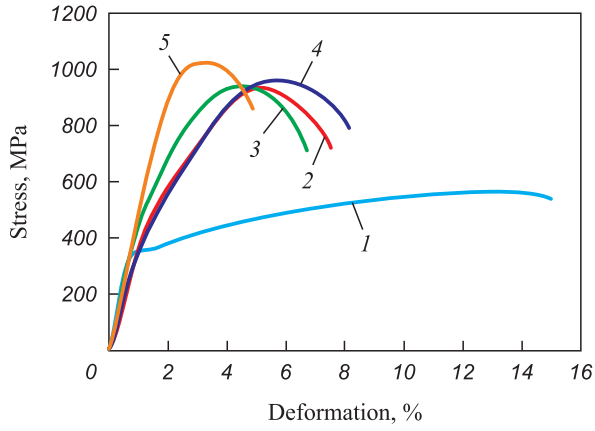


Fig. 2. Stretching diagrams of 10G2FBYu steel:
*1* – in the state of delivery; *2* – after rolling;
*3* – after rolling in embossed rolls; *4* – after rolling with EPD;
*5* – after rolling in embossed rolls with EPD

Рис. 2. Диаграммы растяжения стали 10Г2ФБЮ:
*1* – в состоянии поставки; *2* – после прокатки;
*3* – после прокатки в рельефных валках; *4* – после прокатки с ЭПД;
*5* – после прокатки в рельефных валках с ЭПД

**Mechanical properties of 10G2FBYu steel samples in the state of delivery and after rolling without and with EPD**

**Механические свойства образцов стали 10Г2ФБЮ в состоянии поставки и после прокатки без ЭПД и с ЭПД**

| State (type of treatment) | Elastic strength $\sigma_0$, MPa | Yield strength $\sigma_{0.2}$, MPa | Ultimate strength $\sigma_u$, MPa | Relative elongation, % |
|---|---|---|---|---|
| As delivered | 265 ± 22 | 353 ± 2 | 563 ± 12 | 15.0 ± 2 |
| After rolling | 307 ± 27 | 502 ± 47 | 934 ± 14 | 7.5 ± 0.1 |
| After rolling in embossed rolls | 321 ± 15 | 540 ± 29 | 938 ± 4 | 6.8 ± 0.1 |
| After rolling with EPD | 278 ± 9 | 423 ± 24 | 958 ± 2 | 8.3 ± 0.1 |
| After rolling in embossed rolls with EPD | 511 ± 16 | 905 ± 17 | 1024 ± 12 | 5.0 ± 0.1 |

from local shear deformation during the rolling process in embossed rolls. Post-rolling, the grain structure undergoes significant refinement, and a less pronounced banded ferrite–pearlite structure is formed (Fig. 1, *d*) compared to the original steel sample (Fig. 1, *a*). Strength characteristics after rolling in embossed rolls are nearly identical to those of 10G2FBYu steel rolled in flat rolls (Fig. 2, Table). Notably, there is a noticeable increase in the elastic limit, the hardening coefficient at the macrodeformation stage, and, consequently, an elevation in the conditional yield strength $\sigma_{0.2}$.

Rolling in flat rolls in the electroplasticity mode marginally enhances the tensile strength and ductility of the steel compared to conventional rolling (Fig. 2, Table). The structure of the steel rolled in the electroplasticity mode remains consistent with that observed during conventional rolling in flat rolls.

The structures of 10G2FBYu steel after rolling in flat and embossed rolls in the electroplastic deformation mode are depicted in Fig. 1, *d*, *f*. Notably, the size and morphology of cementite particles exhibit marked variations depending on the rolling method applied. Cementite particles in 10G2FBYu steel after rolling in flat rolls with EPD (Fig. 1, *e*) are larger in size, with an average width of 3.5 μm, compared to rolling in embossed rolls with EPD (Fig. 1, *f*) where the average width of cementite plates is 2.2 μm. In both rolling scenarios, highly dispersed carbide particles are observed inside the ferrite grains (Fig. 1, *e*, *f*).

The aforementioned mechanical test results for 10G2FBYu steel, following various rolling schemes, underscore the significant influence of the rolling scheme and additional impact on the strength properties of the rolled material. During rolling in embossed rolls, where plastic flow occurs in both longitudinal and transverse directions with significant local macroshifts, the strength of 10G2FBYu steel surpasses that achieved through conventional rolling in flat rolls. Rolling the steel samples with the application of powerful electric current pulses in the electroplastic deformation mode also leads to an increase in its strength characteristics. The peak strength for 10G2FBYu steel is achieved after rolling in embossed rolls while simultaneously subjecting it to shear deformation and electric current pulses. In this scenario, the tensile strength reaches 1000 MPa, accompanied by a substantial increase in the hardening coefficient at the macrodeformation stage, rising from 200 MPa during conventional rolling to 500 MPa when rolling in embossed rolls in the EPD mode.

An examination of the microstructure of 10G2FBYu steel through transmission electron microscopy reveals that in the as-delivered state, the predominant component is ferrite (Fig. 3, *a*), with an average grain size of 5 – 10 μm. Deposits of iron carbide $Fe_3C$ of lamellar or spherical type are observed inside and along the grain boundaries. After rolling, a fine-grained structure with an average grain size of 5 – 7 μm forms in the steel, featuring a cellular dislocation structure with misorientation between cells ranging from 2 to 10°. It's worth noting that the post-rolling structure is highly heterogeneous.

Following rolling in embossed rolls, the average grain size further decreases to 2 – 3 μm, and the grains become fragmented into cells with sizes less than 0.5 μm. This reduction in grain size during embossed roll rolling is attributed to shear stresses, contributing to grain refinement. Rolling under conditions of electroplastic deformation, influenced by electric current pulses, leads to an even more significant reduction in the average grain size (less than 1 μm) and the formation of a cellular structure with dimensions less than 0.3 μm. This rolling mode corresponds to the highest strength achieved for the studied steel.

Similar findings were reported in [21], where it was observed that rolling L80 brass in rolls with grooves led to a reduction in the average size of the initial grain from 22 to 3 μm. In contrast, traditional rolling only resulted in a decrease in grain size to 9 μm. The formation of a fine-crystalline structure, as demonstrated in both studies, contributes to an enhancement in the strength properties of the rolled material.

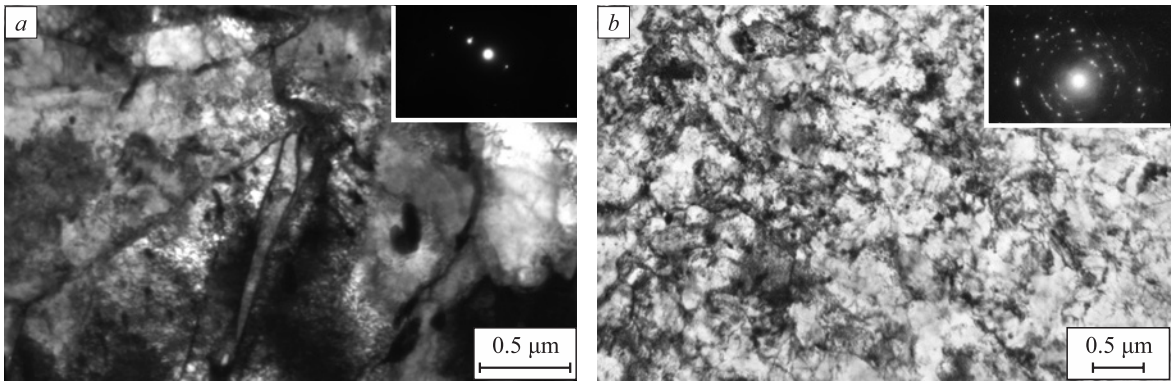


Fig. 3. Electron microscopic images of structure of 10G2FBY steel:
*a* – in the state of delivery; *b* – after rolling in embossed rolls

Рис. 3. Электронно-микроскопические изображения структуры стали 10Г2ФБЮ:
*a* – в состоянии поставки; *b* – после прокатки в рельефных валках

The analysis of fracture patterns in 10G2FBYu steel samples subjected to active tension reveals distinctive characteristics. In the as-delivered state, fractures result in knife-like patterns, with the fracture surface characterized by plastic materials featuring a cup-shaped appearance (Fig. 4, *a*, *c*). The size of pits on the fracture surface ranges from 0.5 to 15 μm. Some pits contain small (≈2 μm) non-metallic inclusions. Tensile testing in this state demonstrates the maximum ductility of 10G2FBYu steel. The elongation of fracture pits indicates the presence of a shear stress component during fracture.

Following rolling in flat rolls, fractures in 10G2FBYu steel exhibit delaminations along the rolled planes, significantly elongated fracture pits, and the emergence of quasi-cleavage areas (Fig. 4, *b*, *d*). The ductility of the steel sharply decreases after rolling. These fracture features persist during rolling in relief rolls and in the electroplastic deformation mode. After rolling in embossed

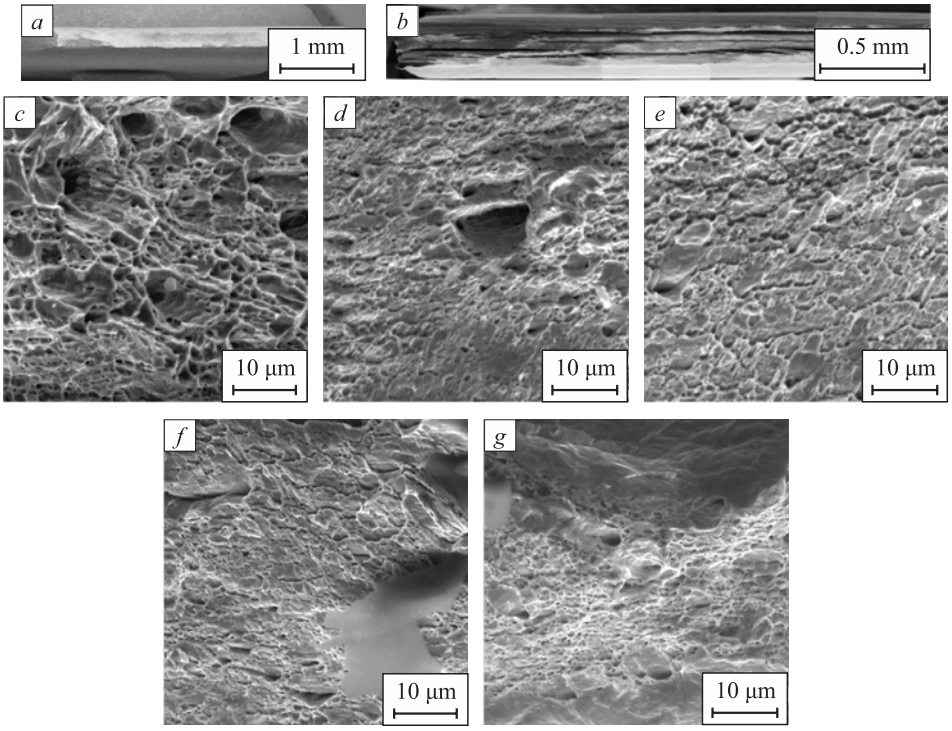


Fig. 4. Fracture factors of 10G2FBYu steel samples:
*a*, *c* – in the state of delivery; *b*, *d* – after rolling in flat rolls; *e* – after rolling in embossed rolls;
*f* – after rolling in flat rolls with EPD; *g* – after rolling in embossed rolls with EPD

Рис. 4. Фрактуры разрушения образцов стали 10Г2ФБЮ:
*a*, *c* – в состоянии поставки; *b*, *d* – после прокатки в плоских валках; *e* – после прокатки в рельефных валках;
*f* – после прокатки в плоских валках с ЭПД; *g* – после прокатки в рельефных валках с ЭПД

rolls, the proportion of quasi-cleavage increases, and the fractograms of the fracture surface show large areas with a quasi-brittle type of fracture (Fig. 4, *e*). Samples rolled in the electroplastic deformation mode exhibit a decrease in the proportion of brittle fracture. Fig. 4, *f*, *g* display fractograms of the destruction of samples rolled in flat and embossed rolls in the electroplastic deformation mode.

## Conclusions

The local shear plastic deformation occurring during rolling in embossed rolls induces the formation of localized deformation bands. These bands play a crucial role in effectively refining the grain structure and pearlite plates. Structural investigations have demonstrated that, particularly during such rolling under conditions of electroplastic deformation, a submicrocrystalline structure with a grain size of less than 0.5 μm is established.

The development of a submicrocrystalline structure results in a significant enhancement of the strength characteristics of the studied steel, including an increase in the hardening coefficient at the stage of macrodeformation. In this scenario, ductility experiences a reduction but remains at a sufficient level for practical applications. Fractographic studies have revealed alterations in the nature of fracture in the steel during rolling, manifested in the emergence of areas featuring brittle fracture in the rolled samples. The shift to rolling under electroplastic deformation conditions increases the proportion of ductile fracture and enhances the ductility of 10G2FBYu steel.

## References / Список литературы

1. Efron L.I. *Metals Science in "Big" Metallurgy. Pipe Steels*. Moscow: Metallurgiya; 2012:696. (In Russ.).

   Эфрон Л.И. *Металловедение в «большой» металлургии. Трубные стали*. Москва: Металлургия; 2012:696.
2. Derevyagina L.S., Pochivalov Y.I., Gordienko A.I. Structural modification of heat treated steel 10Mn2VNbAl and its properties under tension. *AIP Conference Proceedings*. 2016;1783:020038. https://doi.org/10.1063/1.4966331
3. Kawałek A. The theoretical and experimental analysis of the effect of asymmetrical rolling on the value of unit pressure. *Journal of Materials Processing Technology*. 2004;157-158:531–535. https://doi.org/10.1016/j.jmatprotec.2004.07.142
4. Saito Y., Utsunomiya H., Tsuji N., Sakai T. Novel ultra-high straining process for bulk materials – development of the accumulative roll-bonding (ARB) process. *Acta Materialia*. 1999;47(2):579–583. https://doi.org/10.1016/S1359-6454(98)00365-6
5. Richert M., Stüwe H.P., Zehetbauer M.J., Richert J., Pippan R., Motz Ch., Schafler E. Work hardening and microstructure of AlMg5 after severe plastic deformation by cyclic extrusion and compression. *Materials Science and Engineering: A*. 2003;355(1-2):180–185. https://doi.org/10.1016/S0921-5093(03)00046-7
6. Korotovskaya S.V. *Development of a thermomechanical treatment technology ensuring unification of shipbuilding and pipe steels by chemical composition due to formation of ultrafine-grained and submicrocrystalline structure: Extended Abstract of Cand. Sci. Diss*. St. Petersburg; 2014:24. (In Russ.).

   Коротовская С.В. *Разработка технологии термомеханической обработки, обеспечивающей унификацию судостроительных и трубных сталей по химическому составу за счет формирования ультрамелкозернистой и субмикрокристаллической структуры: автореф… дис. канд. техн. наук*. Санкт-Петербург; 2014:24.
7. Meandrov L.V., Vorontsov V.K., Pogorzhel'skii V.I., etc. Improving the conditions for deformation of continuously cast slabs in order to improve the quality of rolled products. *Stal'*. 1982;(3):43−45. (In Russ.).

   Меандров Л.В., Воронцов В.К., Погоржельский В.И. и др. Совершенствование условий деформирования непрерывнолитых слябов с целью улучшения качества проката. *Сталь*. 1982;(3):43−45.
8. Demchuk N.N. *Simulation of plates rolling with additional local deformation effect: Extended Abstract of Cand. Sci. Diss*. Moscow: MISiS; 2000:25. (In Russ.).

   Демчук Н.Н. *Моделирование процесса прокатки толстых листов с дополнительным локальным деформационным воздействием: автореф. дис. канд. техн. наук*. Москва: МИСиС; 2000:25.
9. Mashekov S.A., Absadykov B.N., Tusupkalieva E.A., Mashekova A.S., Akimbekova M.M., Maulenova M.R. Structure and properties of aluminum alloy AD31 after rolling in helical rolls and longitudinal-wedge mill. *Sistemy. Metody. Tekhnologii*. 2018;(1(37)):36–44. (In Russ.). https://doi.org/10.18324/2077-5415-2018-1-36-44

   Машеков С.А., Абсадыков Б.Н., Тусупкалиева Э.А., Машекова А.С., Акимбекова М.М., Мауленова М.Р. Структура и свойства алюминиевого сплава АД31 после прокатки в волнистых валках и продольно-клиновом стане. *Системы. Методы. Технологии*. 2018;(1(37)):36–44. https://doi.org/10.18324/2077-5415-2018-1-36-44
10. Naizabekov A., Lezhnev S., Koinov T., Mazur I., Panin E. Research and development of technology for rolling of high-quality plates of non-ferrous metals and alloys in relief rolls. *Journal of Chemical Technology and Metallurgy*. 2016;51(4):363–370.
11. Naizabekov A.B., Lezhnev S.N., Ashkeev Zh.A. Study of rolling in embossed rolls. *Izvestiya. Ferrous Metallurgy*. 2001;44(2):25–26. (In Russ.).

    Найзабеков А.Б., Лежнев С.Н., Ашкеев Ж.А. Исследование процесса прокатки в рельефных валках. *Известия вузов. Черная металлургия*. 2001;44(2):25–26.
12. Brinza V.V., Demchuk N.N., Yarmak G.M. Study of regularities of plastic forming of rolls with a complex cross-sectional configuration. *Izvestiya. Ferrous Metallurgy*. 1996;39(11):29–33. (In Russ.).

    Бринза В.В., Демчук Н.Н., Ярмак Г.М. Исследование закономерностей пластического формоизменения раскатов со сложной конфигурацией поперечного сечения. *Известия вузов. Черная металлургия*. 1996;39(11):29–33.

**13.** Traino A.I., Polukhin V.P., Nikolaev V.A. Macro shears as non-traditional aid for provision of sheet products high quality. *Metallurg*. 2011;(5):57–62. (In Russ.).

Трайно А.И., Полухин В.П., Николаев В.А. Интенсивные макросдвиги как нетрадиционное средство обеспечения высокого качества листового проката. *Металлург*. 2011;(5):57–62.

**14.** Spitsyn V.I., Troitskii O.A. *Electroplastic Deformation of Metals*. Moscow: Nauka; 1985:160. (In Russ.).

Спицын В.И., Троицкий О.А. *Электропластическая деформация металлов*. Москва: Наука; 1985:160.

**15.** Gromov V.E., Zuev L.B., Kozlov E.V., Zellermaer V.Ya. *Electrostimulated Plasticity of Metals and Alloys*. Moscow: Nedra; 1996:290. (In Russ.).

Громов В.Е., Зуев Л.Б., Козлов Э.В., Целлермайер В.Я. *Электростимулированная пластичность металлов и сплавов*. Москва: Недра; 1996:290.

**16.** Conrad H., White J., Cao W.D., Lu X.P., Sprecher A.F. Effect of electric current pulses on fatigue characteristics of polycrystalline copper. *Materials Science and Engineering: A*. 1991;145(1):1–12. https://doi.org/10.1016/0921-5093(91)90290-4

**17.** Stolyarov V.V. Features of electroplastic effect in alloys with martensite transformation. *Acta Metallurgica Sinica (English Letters)*. 2018;31:1305–1310. https://doi.org/10.1007/s40195-018-0747-z

**18.** Baranov Yu.V., Troitsky O.A., Avraamov Yu.S., Shlyapin A.D. *Physical Foundations of Electropulse and Electroplastic Treatments and New Materials*. Moscow: MSIU; 2001:844. (In Russ.).

Баранов Ю.В., Троицкий О.А., Аврамов Ю.С., Шляпин А.Д. *Физические основы электроимпульсной и электропластической обработок и новые материалы*. Москва: МГИУ; 2001:844.

**19.** Ruszkiewicz B.J., Grimm T., Ragai I., Mears L., Roth J.T. A review of electrically-assisted manufacturing with emphasis on modeling and understanding of the electroplastic effect. *Journal of Manufacturing Science and Engineering*. 2017;139(11):110801. https://doi.org/10.1115/1.4036716

**20.** Stolyarov V. Deformation behavior at rolling and tension under current in TiNi alloy. *European Symposium on Martensitic Transformations (ESOMAT)*. 2009:06033. https://doi.org/10.1051/esomat/200906033

**21.** Naizabekov A.B., Lezhnev S.N., Volokitina I.E., Panin E.A. Evolution of the brass microstructure during rolling in relief and smooth rolls. *IOP Conference Series: Materials Science and Engineering*. 2021;1100:012005. https://doi.org/10.1088/1757-899X/1100/1/012005

## Information about the Author / Сведения об авторе

***Yurii I. Pochivalov,*** *Cand. Sci. (Phys.-Math.), Leading Researcher of the Laboratory of Physical Mesomechanics and Non-Destructive Testing,* Institute of Strength Physics and Materials Science, Siberian Branch of the Russian Academy of Sciences
***ORCID:*** 0000-0003-0236-816X
***E-mail:*** pochiv@ispms.ru

***Юрий Иванович Почивалов,*** *к.ф-м.н. ведущий научный сотрудник лаборатории физической мезомеханики и неразрушающих методов контроля,* Институт физики прочности и материаловедения Сибирского отделения РАН
***ORCID:*** 0000-0003-0236-816X
***E-mail:*** pochiv@ispms.ru

Received 01.11.2022
Revised 07.09.2023
Accepted 11.09.2023

Поступила в редакцию 01.11.2022
После доработки 07.09.2023
Принята к публикации 11.09.2023

**Материаловедение / Materials science**

**УДК** 536.625:539.25:539.651
**DOI** 10.17073/0368-0797-2023-6-666-672



***Оригинальная статья***
***Original article***

# Analysis of contact zone of coating-substrate system exposed to irradiation with a pulse electron beam

**M. O. Efimov[1], Yu. F. Ivanov[2], V. E. Gromov[1] ✉,**
**Yu. A. Shlyarova[1], I. A. Panchenko[1]**

[1] **Siberian State Industrial University** (42 Kirova Str., Novokuznetsk, Kemerovo Region – Kuzbass 654007, Russian Federation)
[2] **Institute of High Current Electronics, Siberian Branch of the Russian Academy of Sciences** (2/3 Academicheskii Ave., Tomsk 634055, Russian Federation)

✉ gromov@physics.sibsiu.ru

***Abstract***. Using the wire-arc additive manufacturing method (WAAM) on a 5083 aluminum alloy substrate, a non-equiatomic Mn – Cr – Fe – Co – Ni high-entropy alloy (HEA) coating was formed. By scanning and transmission electron diffraction microscopy we analyzed the structure, phase and elemental composition of the contact zone after irradiation with high-current low-energy electron beams with the following parameters: accelerated electron energy 18 keV, electron beam energy density 30 J/cm$^2$, electron beam pulse duration 200 μs, number of pulses 3, pulse repetition rate 0.3 s$^{-1}$. Multiphase multielement submicro- and nanocrystalline structures are formed predominantly in the substrate, which has a lower melting temperature compared to HEAs. Mutual doping of the coating – substrate system occurs in the contact layer, which has sinuous boundaries. The contact layers adjacent to the substrate and coating have the structure of high-speed cellular crystallization. In the layer adjacent to the substrate, the cells are formed by a solid solution of magnesium in aluminum. Interlayers of the second phase, enriched in atoms of the coating and substrate, are revealed along the cell boundaries. In the layer adjacent to the coating, the cells are formed by an alloy of composition 0.17Mg – 20.3Al – 4.3Cr – 16.7Fe – 9.3Co – 49.2Ni corresponding to the coating. Interlayers of the second phase, enriched mainly in magnesium and, to a lesser extent, in atoms of the HEA coating, are located along the cell boundaries. Central region of the contact zone with a thickness of ~1700 μm is formed by lamellar crystallites, which indicates the eutectic nature of its formation. Its main element is aluminum (≈77 at. %).

***Keywords:*** high-entropy alloy, 5083 alloy, wire-arc additive manufacturing method, pulsed electron beam, elemental and phase composition, structure, contact zone

***Acknowledgements:*** The work was supported by the Russian Science Foundation, project no. 20-19-00452 and grant no. 19-19-00183, https://rscf.ru/project/19-19-00183/.

***For citation:*** Efimov M.O., Ivanov Yu.F., Gromov V.E., Shlyarova Yu.A., Panchenko I.A. Analysis of contact zone of coating-substrate system exposed to irradiation with a pulse electron beam. *Izvestiya. Ferrous Metallurgy*. 2023;66(6):666–672. https://doi.org/10.17073/0368-0797-2023-6-666-672

# Анализ зоны контакта системы покрытие – подложка, подвергнутой облучению импульсным электронным пучком

**М. О. Ефимов[1], Ю. Ф. Иванов[2], В. Е. Громов[1] ✉,**
**Ю. А. Шлярова[1], И. А. Панченко[1]**

[1] **Сибирский государственный индустриальный университет** (Россия, 654007, Кемеровская обл. – Кузбасс, Новокузнецк, ул. Кирова, 42)
[2] **Институт сильноточной электроники Сибирского отделения РАН** (Россия, 634055, Томск, пр. Академический, 2/3)

✉ gromov@physics.sibsiu.ru

***Аннотация***. Методом проволочно-дугового аддитивного производства (WAAM – *wire arc additive manufacturing*) на подложке из алюминиевого сплава 5083 сформировано покрытие из высокоэнтропийного сплава Mn – Cr – Fe – Co – Ni неэквиатомного состава. Методами сканирующей и просвечивающей электронной дифракционной микроскопии выполнен анализ структуры, фазового и элементного состава зоны контакта после облучения сильноточными низкоэнергетическими электронными пучками с параметрами: энергия ускоренных электронов 18 кэВ; плотность энергии пучка электронов 30 Дж/см$^2$; длительность импульса пучка электронов 200 мкс; количество импульсов 3; частота следования импульсов 0,3 с$^{-1}$. Многофазная многоэлементная субмикро- и нанокристал-

лическая структуры формируются преимущественно в подложке, которая имеет более низкую температуру плавления по сравнению с ВЭС. В контактном слое, имеющем извилистые границы, происходит взаимное легирование системы покрытие – подложка. Контактные слои, примыкающие к подложке и покрытию, имеют структуру высокоскоростной ячеистой кристаллизации. В слое, примыкающем к подложке, ячейки образованы твердым раствором магния в алюминии. По границам ячеек находятся прослойки второй фазы, обогащенные атомами покрытия и подложки. В слое, примыкающем к покрытию, ячейки сформированы сплавом состава 0,17 % Mg – 20,3 % Al – 4,3 % Cr – 16,7 % Fe – 9,3 % Co – 49,2 % Ni, соответствующего покрытию. По границам ячеек располагаются прослойки второй фазы, обогащенные преимущественно магнием и в меньшей степени атомами покрытия ВЭС. Центральная область зоны контакта толщиной примерно 1700 мкм сформирована кристаллитами пластинчатой формы, что свидетельствует об эвтектической природе ее образования. Ее основным элементом является алюминий (примерно 77 % (ат.)).

***Ключевые слова:*** высокоэнтропийный сплав, сплав 5083, метод проволочно-дугового аддитивного производства, импульсный электронный пучок, элементный и фазовый состав, структура, зона контакта

***Благодарности:*** Работа выполнена при финансовой поддержке Российского научного фонда, грант № 20-19-00452 и грант № 19-19-00183, https://rscf.ru/project/19-19-00183/.

***Для цитирования:*** Ефимов М.О., Иванов Ю.Ф., Громов В.Е., Шлярова Ю.А., Панченко И.А. Анализ зоны контакта системы покрытие – подложка, подвергнутой облучению импульсным электронным пучком. *Известия вузов. Черная металлургия*. 2023;66(6):666–672. https://doi.org/10.17073/0368-0797-2023-6-666-672

## Introduction

Over the past two decades, there has been a notable surge in scientific interest regarding the development and investigation of high-entropy alloys (HEAs) owing to their distinctive microstructure, composite composition, and exceptional mechanical and functional properties [1; 2]. The pioneering materials in this category were alloys within the Al – Co – Cr – Fe – Ni systems and the Cantor alloy Mn – Co – Cr – Fe – Ni [3; 4]. HEAs, beyond possessing characteristics typical of conventional metal alloys, exhibit unique and unconventional properties reminiscent of metal-ceramics. These include high hardness and resistance to temperature hardening, dispersion hardening, a positive temperature hardening coefficient, elevated temperature strength, high wear and corrosion resistance, among other attributes [5 – 8].

Various reviews [8 – 11] have comprehensively analyzed the structural-phase states, properties, simulation, production methods, and application areas of the most promising HEAs. It has been emphasized that the advent of HEAs represents a significant leap forward in the advancement of metal alloys.

Currently, there is a wealth of information being actively accumulated on high-entropy alloys (HEAs), encompassing structural-phase states, defect substructure, stability, deformation behavior over a broad temperature range, the impact of doping and other factors, as well as novel methods for HEA production [12 – 17]. In the realm of HEA physics, there is a distinct focus on enhancing surface properties through various treatments, including irradiation with low-energy high-current electron beams. Electron-beam processing offers ultrahigh surface heating rates (up to $10^8$ K/s) and subsequent cooling through heat-water transfer to the material's bulk. This leads to the formation of nonequilibrium submicro- and nanocrystalline structural-phase states, the development of a columnar structure, and the homogenization of chemical composition [18].

The primary objective of the current study is to analyze the structural-phase states within the contact zone of the HEA layer (coating) formed by wire-arc additive manufacturing on alloy 5083 (substrate) and subjected to electron-beam treatment.

## Materials and methods

The material under investigation in this study comprised a coating – substrate system. The coating was a high-entropy alloy with the elemental composition Mn – Cr – Fe – Co – Ni, fabricated onto the substrate using wire-arc additive manufacturing [1; 2]. The substrate material employed was alloy 5083. The contact zone of the coating–substrate system underwent irradiation with an intense pulsed electron beam using the SOLO installation. The process parameters for the irradiation were as follows: accelerated electrons' energy $U = 18$ keV, electron beam energy density $E_S = 30$ J/cm$^2$, electron beam pulse duration $t = 200$ μs, number of pulses $N = 3$, and pulse repetition rate $f = 0.3$ s$^{-1}$. The irradiation took place in a vacuum at a residual gas pressure (argon) in the installation chamber of $p = 0.02$ Pa. To investigate the structural phase states of the contact zone between the coating and the substrate, scanning electron microscopy (SEM 515 Philips with EDAX ECON IV *X*-ray spectral microanalyzer) and transmission diffraction electron microscopy (JEM-2100) were employed [19 – 21]. Foils for the transmission electron microscope were prepared through ion thinning (Ion Slicer EM-091001S, utilizing argon ions) of plates obtained from bulk samples using an Isomet Low Speed Saw unit. The cutting was performed perpendicular to the surface of the HEA deposited layer, extending from the interface between the substrate and the deposit. This method facilitated the observation of structural and phase composition changes in the material with distance from the contact zone of the coating with the substrate.

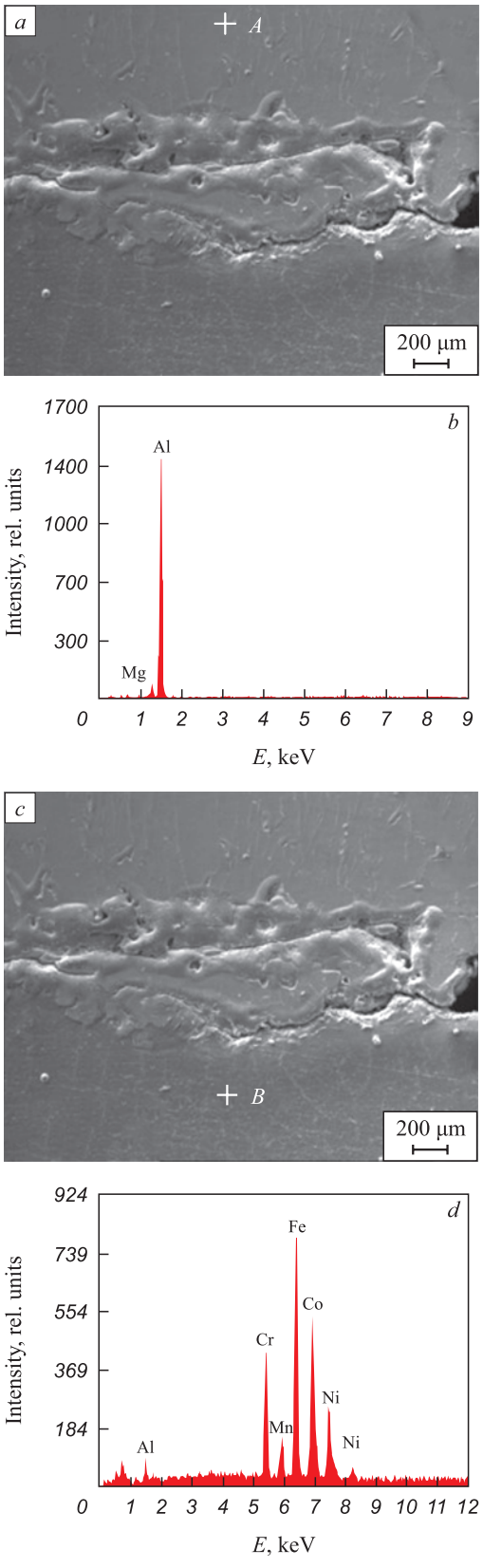


Fig. 1. Structure of the contact zone of HEA surfacing and substrate (AMg5) irradiated with a pulsed electron beam (*a*, *c*) and energy spectra obtained from regions *A* (*b*) and *B* (*d*)

Рис. 1. Структура области контакта наплавки ВЭС и подложки (АМг5), облученной импульсным электронным пучком (*a*, *c*) и энергетические спектры, полученные с области *A* (*b*) и области *B* (*d*)

## Results and discussion

In Fig. 1, an electron microscopic image displays the cross-section of the contact zone between the coating (HEA) and the substrate (alloy 5083). An extended layer, up to 700 μm thick, is evident, characterized by microcracks along the contact boundary on the substrate side. The sinuous boundaries of the contact layer suggest a high degree of fusion between the substrate and deposited material.

*X*-ray spectral microanalysis revealed mutual diffusion of atoms from the substrate and coating, as indicated in Table 1. Notably, the near-contact layer of the coating shows aluminum doping (Fig. 1, *a*, *b*, analysis region *A*), while the near-contact layer of the substrate exhibits doping with HEA elements (Fig. 1, *c*, *d*, analysis region *B*). Significantly, aluminum is more pronounced as a dopant in the coating, likely attributed to its lower melting point compared to HEA. Fig. 2 illustrates the change in elemental composition in the contact layer of the film – substrate system during the transition from the surfacing metal to the substrate metal (Fig. 2, *b*). A smooth transition in the elemental composition of the contact zone suggests the absence of vortex flows in the employed method of coating deposition on the substrate and subsequent irradiation with a pulsed electron beam.

Under the conditions of irradiation with a pulsed electron beam, mutual doping of the coating and substrate is expected to result in a significant alteration of the phase composition in the contact zone. The elemental and phase compositions were investigated using thin foil methods in layers (Fig. 2, *b*).

The examination revealed that the structure of layer *I* is characterized by cells displaying high-speed crystallization (Fig. 3, *a*). As it moves away from the contact zone with the coating, the cellular structure transforms into a layered structure (Fig. 3, *b*). The majority of cells constitute a solid solution of magnesium in aluminum, consistent with alloy 5083 (Table 2, analysis regions *1* and *2* are indicated in Fig. 3). Second-phase layers

Table 1

**Results of microrentgenospectral analysis of elemental composition of the coating in *A* region and the substrate in *B* region**

*Таблица 1.* **Результаты микрорентгеноспектрального анализа элементного состава покрытия в области *A* и подложки в области *B***

| Region | Content, at. % | | | | | | |
|---|---|---|---|---|---|---|---|
| | Mg | Al | Cr | Mn | Fe | Co | Ni |
| *A* | 5.7 | 92.4 | 0.3 | 0.5 | 0.5 | 0.3 | 0.3 |
| *B* | 0 | 12.3 | 12.6 | 2.7 | 32.5 | 25.3 | 14.6 |

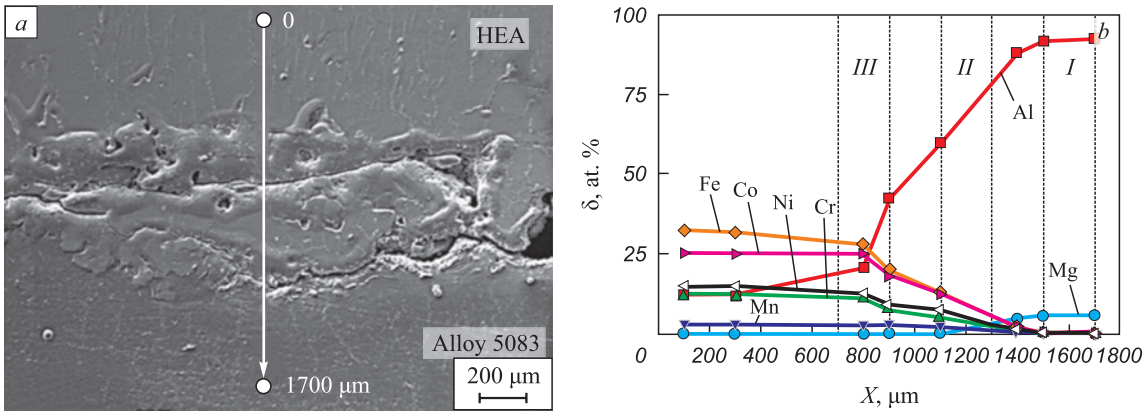


Fig. 2. Dependences of alloying elements concentration (*b*) of the contact zone of coating and substrate identified along the line (0 – 1700) shown on *a* (*I*, *II*, *III* – layers in which the analysis of structural-phase states was carried out by TEM and STEM methods)

Рис. 2. Зависимости концентрации легирующих элементов (*b*) зоны контакта покрытия и подложки, выявленные вдоль линии (0 – 1700), приведенной на поз. *a* (цифрами *I*, *II*, *III* обозначены слои, в которых осуществлялся анализ структурно-фазовых состояний методами TEM и STEM)

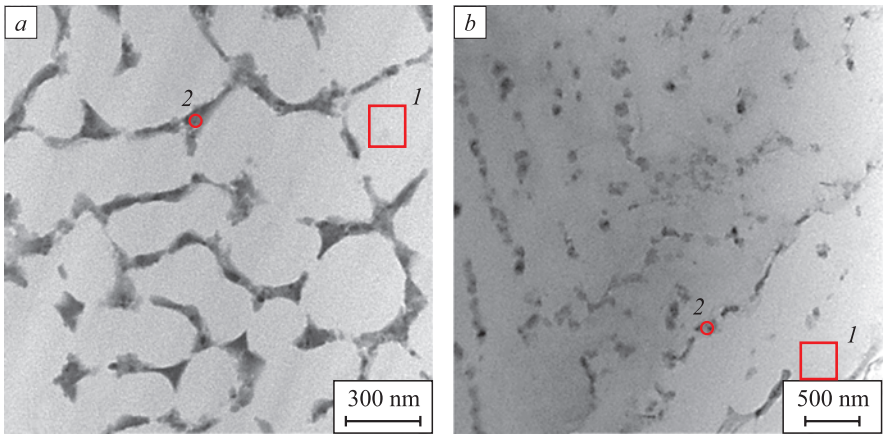


Fig. 3. Structure of layer *I* of the surfacing – substrate system irradiated by a pulsed electron beam (*1* and *2* – areas of microrentgenospectral analysis of the alloy elemental composition)

Рис. 3. Структура слоя *I* системы «наплавка – подложка», облученной импульсным электронным пучком (цифрами *1* и *2* обозначены области микрорентгеноспектрального анализа элементного состава сплава)

at the cell boundaries are enriched with atoms from both the surfacing and substrate.

Through darkfield analysis with subsequent microelectronogram identification, it was determined that the majority of high-speed crystallization cells were formed by a solid solution based on aluminum. These cells are separated by layers of the $Mg_2Si$ phase.

Layer *II* exhibits a lamellar structure seemingly arising from eutectic transformation during high-speed heat treatment initiated by the pulsed electron beam (Fig. 4, *a*). *X*-ray spectral microanalysis of the foil indicates that the predominant element in layer *II* is aluminum (76.8 %), accompanied by smaller amounts of Mg (4.1 %), Cr (2.2 %), Mn (0.3 %), Fe (4.9 %), Co (1.6 %), Ni (10.1 %) (at. %).

Darkfield analysis, coupled with subsequent microelectronogram identification, revealed that this layer is composed of plates corresponding to the follo-

Table 2

**Results of micro-X-ray spectral analysis of the elemental composition of the surfacing – substrate system irradiated with a pulsed electron beam**

*Таблица 2*. **Результаты микрорентгеноспектрального анализа элементного состава системы «наплава – подложка», облученной импульсным электронным пучком**

| Spectrum | Content, % | | | | | | | |
|---|---|---|---|---|---|---|---|---|
| | Mg | Al | Si | Cr | Mn | Fe | Co | Ni |
| Region *A* | | | | | | | | |
| *1* | 3.55 | 96.45 | 0 | 0 | 0 | 0 | 0 | 0 |
| *2* | 5.69 | 83.06 | 3.95 | 0.27 | 0.38 | 1.44 | 0.41 | 4.79 |
| Region *B* | | | | | | | | |
| *1* | 3.00 | 97.00 | 0 | 0 | 0 | 0 | 0 | 0 |
| *2* | 10.73 | 80.65 | 2.43 | 0.29 | 0.31 | 1.25 | 0.33 | 4.02 |

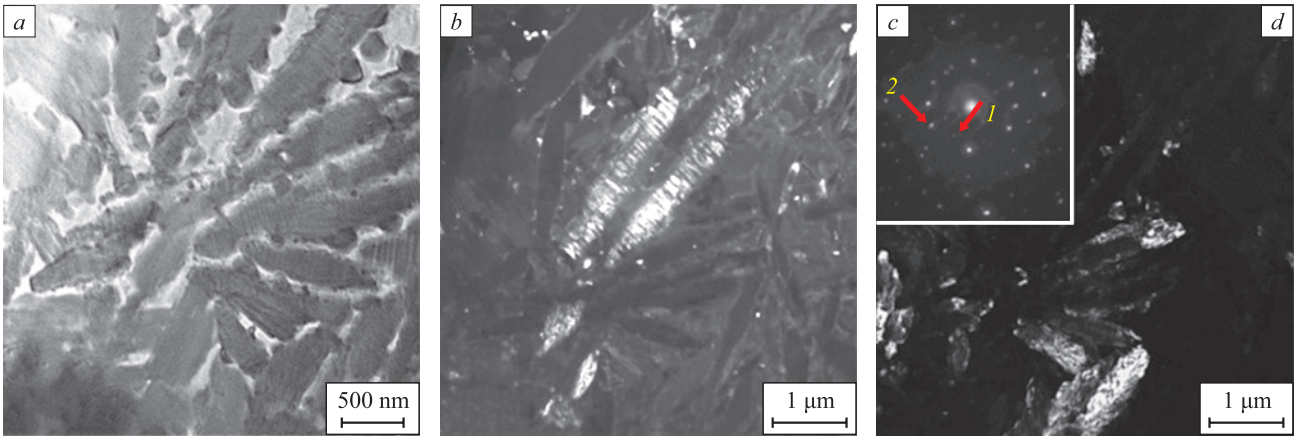


Fig. 4. Structure of layer *II* of the surfacing – substrate system:
*a* – light–field image; *b*, *d* – dark-field images; *c* – microelectronic image from the foil section (*a*).
Image (*b*) was obtained in reflex [113]$Al_{13}Fe_4$; image (*d*) was obtained in reflexes [101]Cr–Ni–Fe + [114]$Al_6Fe$;
on (*c*) the reflexes are indicated in which the dark fields *1* (*b*) and *2* (*d*) are obtained

Рис. 4. Структура слоя *II* системы «наплавка – подложка»:
*a* – светлопольное изображение; *b*, *d* – темнопольные изображения; *c* – микроэлектронограмма с участка фольги (*a*).
Изображение (*b*) получено в рефлексе [113]$Al_{13}Fe_4$; изображение (*d*) получено в рефлексах [101]Cr–Ni–Fe + [114]$Al_6Fe$;
на поз. (*c*) обозначены рефлексы, в которых получены темные поля *1* (*b*) и *2* (*d*)

wing phases: $Al_{13}Fe_4$ (Fig. 4, *b*), Cr – Ni – Fe and $Al_6Fe$ (Fig. 4, *d*).

Layer *III*, akin to layer *I*, consists of cells displaying high-speed crystallization (Fig. 5, *a*). The majority of these cells constitute an alloy with the composition 0.17 % Mg – – 20.3 % Al – 4.3 % Cr – 16.7 % Fe – 9.3 % Co – 49.2 % Ni, aligning with a HEA doped with substrate elements. Interlayers of the second phase, situated along the boundaries of the cells, are also formed by elements from the surfacing and substrate (41.5 % Mg – 10.9 % Al – – 9.0 % Cr – 1.0 % Mn – 15.2 % Fe – 4.1 % Co – 18.4 % Ni).

Darkfield analysis, along with microelectronogram indication, revealed that the bulk of high-speed crystallization cells in layer *III* is constituted by a solid solution based on HEA, doped with aluminum and magnesium (Fig. 5, *b*). These crystallization cells are separated by interlayers of the $Al_{18}Cr_2Mg_3$ phase (Fig. 5, *c*).

## CONCLUSIONS

The wire-arc additive manufacturing method was employed to create a HEA coating with a non-equi-

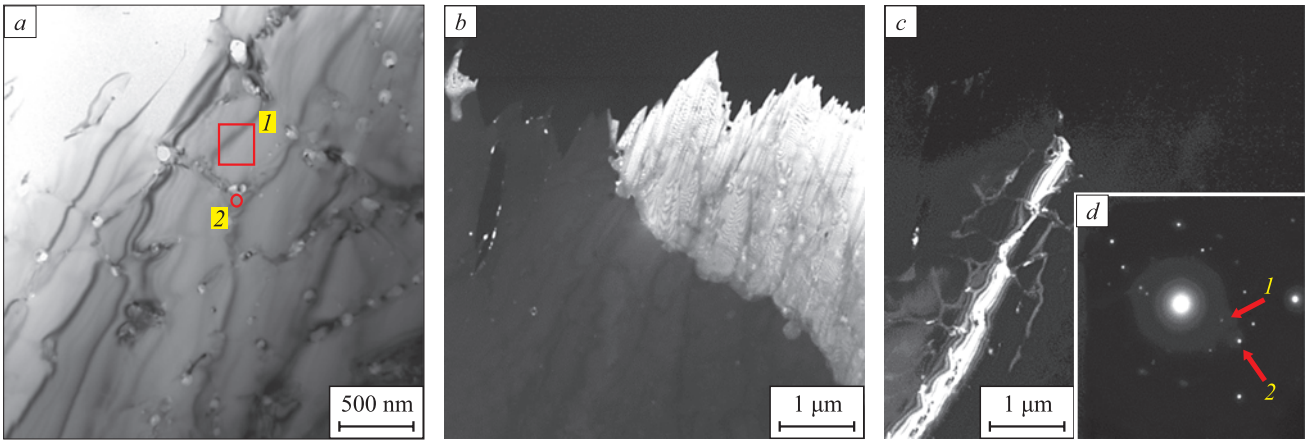


Fig. 5. Structure of layer *III* of the surfacing – substrate system after electron beam processing:
*a* – light–field image; *b*, *c* – dark-field images and microelectronogram (*d*) obtained from the foil section (*a*).
Image (*b*) was obtained in the reflex [210]Cr–Ni–Fe; image (*c*) was obtained in reflexes [222]Cr–Ni–Fe + [880]$Al_{18}Cr_2Mg_3$;
on (*d*) the reflexes are indicated in which dark fields *1* (*b*) and *2* (*c*) are obtained

Рис. 5. Структура слоя *III* системы «наплавка – подложка» после электронно-пучковой обработки:
*a* – светлопольное изображение; *b*, *c* – темнопольные изображения и микроэлектронограмма (*d*), полученные с участка фольги (*a*).
Изображение (*b*) получено в рефлексе [210]Cr–Ni–Fe; изображение (*c*) получено в рефлексах [222]Cr–Ni–Fe + [880]$Al_{18}Cr_2Mg_3$;
на поз. *d* обозначены рефлексы, в которых получены темные поля *1* (*b*) и *2* (*c*)

atomic elemental composition Mn – Cr – Fe – Co – Ni on alloy 5083. The contact zone of the coating – substrate system underwent irradiation with an intense pulsed electron beam. Through advanced techniques in physical materials science, investigations into the elemental and phase compositions, as well as the state of the defective substructure of the alloy formed in the contact zone of the substrate – coating system, were conducted. The analysis revealed mutual doping of the coating and substrate in a layer with an approximate thickness of 1700 μm. The high-speed cooling of the contact zone in the coating – substrate system, occurring under the thermal influence initiated by a pulsed electron beam, resulted in the formation of a multi-element, multi-phase submicro-nanocrystalline structure. The contact layer adjacent to the substrate exhibited a high-speed cellular crystallization structure, with the cell bulk formed by a solid solution of magnesium in aluminum, corresponding to alloy 5083. Interlayers of the second phase, enriched in atoms from both the coating and substrate, were observed along the cell boundaries. In the central region of the contact zone, plate-shaped crystallites were found, suggesting a potential eutectic nature of formation. The primary chemical element in this area was aluminum, constituting approximately 77 at. %. The contact layer adjacent to the coating displayed a high-speed cellular crystallization structure, with the majority of cells formed by an alloy composition (0.17 % Mg – 20.3 % Al – – 4.3 % Cr – 16.7 % Fe – 9.3 % Co – 49.2 % Ni) corresponding to HEA, doped with substrate elements. Interlayers of the second phase, located along the boundaries of the cells, were enriched with magnesium and, to a lesser extent, with atoms forming the coating.

## References / Список литературы


1. Gromov V.E., Konovalov S.V., Ivanov Yu.F., Osintsev K.A. *Structure and Properties of High-Entropy Alloys*. Springer: Advanced Structured Materials; 2021;107:110. https://doi.org/10.1007/978-3-030-78364-8
2. Osintsev K.A., Gromov V.E., Konovalov S.V., Ivanov Yu.F., Panchenko I.A. High-entropy alloys: Structure, mechanical properties, deformation mechanisms and application. *Izvestiya. Ferrous Metallurgy*. 2021;64(4):249–258. (In Russ.). https://doi.org/10.17073/0368-0797-2021-4-249-258

   Осинцев К.А., Громов В.Е., Коновалов С.В., Иванов Ю.Ф., Панченко И.А. Высокоэнтропийные сплавы: структура, механические свойства, механизмы деформации и применение. *Известия вузов. Черная металлургия*. 2021;64(4):249–258. https://doi.org/10.17073/0368-0797-2021-4-249-258
3. Yeh J.-W., Chen S.-K., Lin S.-J., Gan J.-Y., Chin T.-S., Shun T.-T., Tsau C.-H., Chang S.-Y. Nanostructured high entropy alloys with multiple principal elements: Novel alloy design concepts and outcomes. *Advanced Engineering Materials*. 2004;6(5):299–303. https://doi.org/10.1002/adem.200300567
4. Cantor B., Chang I.T.H., Knight P., Vincent A.J.B. Microstructural development in equiatomic multicomponent alloys. *Materials Science and Engineering: A*. 2004;375-377: 213–218. https://doi.org/10.1016/j.msea.2003.10.257
5. Yeh J.-W., Chen Y.-L., Lin S.-J., Chen S.-K. High-entropy alloys – A new era of exploitation. *Materials Science Forum*. 2007;560:1–9. https://doi.org/10.4028/www.scientific.net/MSF.560.1
6. Zhang Y., Yang X., Liaw P.K. Alloy design and properties optimization of high-entropy alloys. *JOM*. 2012;64(7): 830–838. https://doi.org/10.1007/s11837-012-0366-5
7. Yeh J.-W. Recent Progress in high-entropy alloys. *European Journal of Control*. 2006;31(6):633–648. https://doi.org/10.3166/acsm.31.633-648
8. Yeh J.-W. Alloy design strategies and future trends in high-entropy alloys. *JOM*. 2013;65(12):1759–1771. https://doi.org/10.1007/s11837-013-0761-6
9. Zhang L.-S., Ma G.-L., Fu L.-C., Tian J.-Y. Recent progress in high-entropy alloys. *Advanced Materials Research*. 2013;631-632:227–232. https://doi.org/10.4028/www.scientific.net/AMR.631-632.227
10. Zhang Y., Zuo T.T., Tang Z., Gao M.C., Dahmen K.A., Liaw P.K., Lu Z.P. Microstructures and properties of high-entropy alloys. *Progress in Materials Science*. 2014;61:1–93. https://doi.org/10.1016/j.pmatsci.2013.10.001
11. Gali A., George E.P. Tensile properties of high- and medium-entropy alloys. *Intermetallics*. 2013;39:74–78. https://doi.org/10.1016/j.intermet.2013.03.018
12. Li D.Y., Zhang Y. The ultrahigh charpy impact toughness of forged AlCoCrFeNi high entropy alloys at room and cryogenic temperatures. *Intermetallics*. 2016;70:24–28. https://doi.org/10.1016/j.intermet.2015.11.002
13. Cantor B. Multicomponent and high entropy alloys. *Entropy*. 2014;16(9):4749–4768. https://doi.org/10.3390/e16094749
14. Miracle D.B., Senkov O.N. A critical review of high entropy alloys and related concepts. *Acta Materialia*. 2017;122: 448–511. https://doi.org/10.1016/j.actamat.2016.08.081
15. Zhang W., Liaw P.K., Zhang Y. Science and technology in high-entropy alloys. *Science China Materials*. 2018;61(1): 2–22. https://doi.org/10.1007/s40843-017-9195-8
16. Tsai M.-H., Yeh J.-W. High-entropy alloys: a critical review. *Materials Research Letters*. 2014;2(3):107–123. https://doi.org/10.1080/21663831.2014.912690
17. Alaneme K.K., Bodunrin M.O., Oke S.R. Processing, alloy composition and phase transition effect on the mechanical and corrosion properties of high entropy alloys: a review. *Journal of Materials Research and Technology*. 2016;5(4):384–393. https://doi.org/10.1016/j.jmrt.2016.03.004
18. Osintsev K.A., Gromov V.E., Ivanov Yu.F., Konovalov S.V., Panchenko I.A., Vorobyov S.V. Evolution of structure in AlCoCrFeNi high-entropy alloy irradiated by pulsed electron beam. *Metals*. 2021;11(8):1228. https://doi.org/10.3390/met11081228
19. Egerton F.R. *Physical Principles of Electron Microscopy*. Basel; 2016:96.
20. Kumar C.S.S.R. *Transmission Electron Microscopy. Characterization of Nanomaterials*. New York; 2014:717.
21. Carter C.B., Williams D.B. *Transmission Electron Microscopy*. Berlin; 2016:518.

## Information about the Authors

***Mikhail O. Efimov*,** *Postgraduate of the Chair of Science named after V.M. Finkel',* Siberian State Industrial University
***ORCID:*** 0000-0002-4890-3730
***E-mail:*** moefimov@mail.ru

***Yurii F. Ivanov*,** *Dr. Sci. (Phys.-Math.), Prof., Chief Researcher,* Institute of High-Current Electronics, Siberian Branch of the Russian Academy of Sciences
***ORCID:*** 0000-0001-8022-7958
***E-mail:*** yufi55@mail.ru

***Viktor E. Gromov*,** *Dr. Sci. (Phys.-Math.), Prof., Head of the Chair of Science named after V.M. Finkel',* Siberian State Industrial University
***ORCID:*** 0000-0002-5147-5343
***E-mail:*** gromov@physics.sibsiu.ru

***Yuliya A. Shlyarova*,** *Postgraduate of the Chair of Science named after V.M. Finkel', Researcher of Laboratory of Electron Microscopy and Image Processing,* Siberian State Industrial University
***ORCID:*** 0000-0001-5677-1427
***E-mail:*** rubannikova96@mail.ru

***Irina A. Panchenko*,** *Cand. Sci. (Eng.), Head of the Laboratory of Electron Microscopy and Image Processing,* Siberian State Industrial University
***ORCID:*** 0000-0002-1631-9644
***E-mail:*** i.r.i.ss@yandex.ru

## Сведения об авторах

***Михаил Олегович Ефимов*,** *аспирант кафедры естественнонаучных дисциплин им. профессора В.М. Финкеля,* Сибирский государственный индустриальный университет
***ORCID:*** 0000-0002-4890-3730
***E-mail:*** moefimov@mail.ru

***Юрий Федорович Иванов*,** *д.ф.-м.н., профессор, главный научный сотрудник,* Институт сильноточной электроники Сибирского отделения РАН
***ORCID:*** 0000-0001-8022-7958
***E-mail:*** yufi55@mail.ru

***Виктор Евгеньевич Громов*,** *д.ф.-м.н., профессор, заведующий кафедрой естественнонаучных дисциплин им. профессора В.М. Финкеля,* Сибирский государственный индустриальный университет
***ORCID:*** 0000-0002-5147-5343
***E-mail:*** gromov@physics.sibsiu.ru

***Юлия Андреевна Шлярова*,** *аспирант кафедры естественнонаучных дисциплин им. профессора В.М. Финкеля, научный сотрудник лаборатории электронной микроскопии и обработки изображений,* Сибирский государственный индустриальный университет
***ORCID:*** 0000-0001-5677-1427
***E-mail:*** rubannikova96@mail.ru

***Ирина Алексеевна Панченко*,** *к.т.н., заведующий лабораторией электронной микроскопии и обработки изображений,* Сибирский государственный индустриальный университет
***ORCID:*** 0000-0002-1631-9644
***E-mail:*** i.r.i.ss@yandex.ru

## Contribution of the Authors

***M. O. Efimov*** – coating of Mn – Cr – Fe – Co – Ni HEA on the substrate of alloy 5083, writing the text.
***Yu. F. Ivanov*** – conducting electron microscopic studies, analysis of the results.
***V. E. Gromov*** – formation of the research concept, analysis of TEM images, writing the text.
***Yu. A. Shlyarova*** – literary review, preparation of the HEA constituent elements, design of the article.
***I. A. Panchenko*** – irradiation of the samples, analysis of the results, writing the text.

## Вклад авторов

***М. О. Ефимов*** – нанесение покрытия ВЭС состава Mn – Cr – Fe – Co – – Ni на подложку сплава 5083, написание статьи.
***Ю. Ф. Иванов*** – проведение электронно-микроскопических исследований, анализ результатов.
***В. Е. Громов*** – формирование концепции работы, анализ ПЭМ изображений, написание статьи.
***Ю. А. Шлярова*** – обзор литературы, подготовка составляющих элементов ВЭС, оформление статьи.
***И. А. Панченко*** – облучение образцов, анализ результатов, написание статьи.

Received 02.06.2023
Revised 15.07.2023
Accepted 11.09.2023

Поступила в редакцию 02.06.2023
После доработки 15.07.2023
Принята к публикации 11.09.2023

MATERIALS SCIENCE / МАТЕРИАЛОВЕДЕНИЕ

**UDC** 669.046:533.9
**DOI** 10.17073/0368-0797-2023-6-673-680



*Original article*
*Оригинальная статья*

# Lüders and Portevin–Le Chatelier processes in austenitic-martensitic TRIP steel

**V. I. Danilov** ✉, **D. V. Orlova, V. V. Gorbatenko, L. V. Danilova**

**Institute of Strength Physics and Materials Science, Siberian Branch of Russian Academy of Sciences** (2/4 Akademicheskii Ave., Tomsk 634055, Russian Federation)

✉ dvi@ispms.ru

***Abstract***. The authors studied the nature of mobile fronts of localized deformation that generate and propagate during deformation of metastable austenitic-martensitic TRIP steel VNS9-Sh along the entire length of the loading curve from the yield point to fracture. A joint research of the nature of the deformation fronts movement and kinetics of the magnetic phase accumulation made it possible to establish that the fronts under consideration are the fronts of the thermoelastic phase transformation of metastable austenite into martensite. This transformation is realized firstly by formation of the Chernov–Lüders bands and then the Portevin–Le Chatelier bands. Both processes are consistent with staging of the deformation curve, which contains a pseudo-plateau, a section with an increasing hardening coefficient, and a section with a decreasing hardening coefficient. It is shown that the deformation-induced phase transformation corresponds to the fronts propagating on the pseudo-plateau and on the section of loading curve with an increasing hardening coefficient. The Portevin–Le Chatelier bands, which are formed in the section of the loading diagram with a decreasing hardening coefficient, are not associated with "austenite-martensite" transformation and have a twin nature. The kinetics of thermoelastic transformation fronts, as well as deformation fronts in materials with a shear mechanism of shaping, can be described in terms of the autowave concept. On the yield plateaus, the phase transformation occurs through generation and propagation of localized plasticity switching autowaves. In the section with an increasing hardening coefficient, it continues through generation and movement of excitation autowaves. The propagation regions of excitation autowaves are limited in the sample space. They are set by the zones of origin and annihilation of primary switching autowaves which were formed on the yield plateau.

***Keywords:*** TRIP steel, thermoelastic phase transformation, localized deformation fronts, Chernov–Lüders bands, Portevin–Le Chatelier bands, switching autowaves, excitation autowaves

***Acknowledgements:*** The work was supported by the Russian Science Foundation (project No. 22-29-00171, https://rscf.ru/project/22-29-00171/).

***For citation:*** Danilov V.I., Orlova D.V., Gorbatenko V.V., Danilova L.V. Lüders and Portevin–Le Chatelier processes in austenitic-martensitic TRIP steel. *Izvestiya. Ferrous Metallurgy*. 2023;66(6):673–680. https://doi.org/10.17073/0368-0797-2023-6-673-680

# Процессы Людерса и Портевена–Ле Шателье в аустенитно-мартенситной TRIP-стали

**В. И. Данилов** ✉, **Д. В. Орлова, В. В. Горбатенко, Л. В. Данилова**

**Институт физики прочности и материаловедения Сибирского отделения РАН** (Россия, 634055, Томск, пр. Академический, 2/4)

✉ dvi@ispms.ru

***Аннотация***. Исследована природа подвижных фронтов локализованной деформации, которые возникают и распространяются в процессе деформирования метастабильной аустенитно-мартенситной TRIP-стали ВНС9-Ш на всем протяжении кривой нагружения от предела текучести до разрушения. Совместное исследование характера движения деформационных фронтов и кинетики накопления магнитной фазы позволило установить, что рассматриваемые фронты являются фронтами термоупругого фазового превращения метастабильного аустенита в мартенсит. Данное превращение реализуется вначале путем формирования полос Чернова–Людерса, а затем полос Портевена–Ле Шателье. Оба процесса согласованы со стадийностью деформационной кривой, которая содержит вырожденную площадку текучести, участок с возрастающим коэффициентом упрочнения и участок с убывающим коэффициентом упрочнения. Показано, что деформационно-индуцированному фазовому превращению соответствуют фронты, распространяющиеся на площадке текучести и на участке кривой нагружения, с возрастающим коэффициентом упрочнения. Полосы Портевена–Ле Шателье, которые образуются на участке диаграммы нагружения с убывающим коэффициентом упрочнения, с превращением «аустенит – мартенсит» не связаны и имеют двойниковую природу. Кинетика фронтов термоупругого превращения, как и деформационных фронтов в материалах со сдвиговым механизмом формоизменения, может быть описана в рамках автоволновой концепции. На площадках текучести фазовое превращение

происходит путем зарождения и распространения автоволн переключения локализованной пластичности. На участках с возрастающим коэффициентом упрочнения оно продолжается путем зарождения и движения автоволн возбуждения. Области распространения автоволн возбуждения ограничены в пространстве образца. Они задаются зонами зарождения и аннигиляции первичных автоволн переключения, которые были сформированы на площадках текучести.

***Ключевые слова:*** TRIP-сталь, термоупругое фазовое превращение, фронты локализованной деформации, полосы Чернова–Людерса, полосы Портевена–Ле Шателье, автоволны переключения, автоволны возбуждения

***Благодарности:*** Работа выполнена за счет гранта Российского научного фонда (проект № 22-29-00171, https://rscf.ru/project/22-29-00171/.

***Для цитирования:*** Данилов В.И., Орлова Д.В., Горбатенко В.В., Данилова Л.В. Процессы Людерса и Портевена–Ле Шателье в аустенитно-мартенситной TRIP-стали. *Известия вузов. Черная металлургия*. 2023;66(6):673–680.
https://doi.org/10.17073/0368-0797-2023-6-673-680

## Introduction

The utilization of the autowave concept to characterize Lüders deformation in low-carbon steel has proven to be productive [1]. This conceptual framework enabled the establishment of the nonlinear relationship between the speed of Lüders fronts and the deformation rate, shedding light on the underlying reasons for this nonlinearity. It is recognized that, at the microscopic level in low-carbon steel, the emergence of Chernov-Lüders bands (ChLB) is attributed to two competing processes: the thermally activated movement of dislocations, where the primary barriers are "forest" dislocations, and their additional hindrance due to the deposition of impurity atoms on mobile dislocations (effect of dynamic strain aging) [2 – 4]. Nevertheless, certain materials, such as shape memory alloys and certain steels with a metastable phase structure, exhibit ChLB formation at the microlevel not linked to dislocation processes but rather to deformation-induced phase transformation [5 – 8]. This raises the question of how applicable the autowave concept of plastic flow is in such cases.

In response to the demands of technological practice, the advancement of insights into the mechanisms governing thermoelastic phase transformations has contributed to the development of TRIP-steels (*transformation induced plasticity*), characterized by high strength coupled with significant plasticity. This steel class encompasses metastable austenitic–ferritic [8] and austenitic–martensitic steels [9]. The attainment of the TRIP effect is contingent upon the nature of changes in metastable austenite volume fraction during mechanical processing. This process is influenced by various parameters, including the crystal lattice orientation, temperature, deformation rate, degree of hardening, and the heterogeneity of alloying element distribution [10 – 13]. For example, the authors of [12] demonstrated that the disparate stability of austenite in austenitic–ferritic TRIP steels stems from the nonuniform distribution of manganese. Similarly [9], established that the stability of austenite in austenitic–martensitic TRIP steel varies based on the reduction amount during "warm" rolling. When the degree of hardening of the austenite phase is substantial, the transformation occurs at high stresses and is fully completed at the yield point. If the hardening is not significant and the yield strength is low, only a small portion of the austenite transforms into the martensite phase at the yield site. The transition in the remaining austenite grains occurs in subsequent stages of the loading curve through the mechanism of formation and propagation of Portevin–Le Chatelier (PLCh) bands. It was noted in [14] that the fronts of the Chernoff–Lüders bands (ChLB) and the fronts of the PLCh bands represent distinct autowave modes. As the processes of shape change in austenitic–martensitic TRIP steels unfold through the thermoelastic transformation of non-magnetic austenite into a magnetic martensitic phase, the objective of this study is to examine the kinetics of localized plastic deformation fronts concurrently with the characterization of martensite accumulation patterns based on the material's magnetization magnitude.

## Materials and methods

The investigations were conducted on samples of VNS9-Sh (23Kh15N5AM3-Sh) TRIP steel. 1 mm thick plates as delivered underwent austenitization (hardening) with a 1 h exposure at a temperature of $T = 1400$ K, followed by cooling in water. Subsequently, multi-pass warm rolling was performed at a temperature of 620 K with a 40 % reduction. Following austenitization, the steel exhibited a low yield strength ($\sigma_{0.2} = 250$ MPa) and high plasticity ($\delta = 27$ %). Hardening during rolling resulted in an almost threefold increase in yield strength ($\sigma_{0.2} = 735$ MPa), accompanied by a reduction in plasticity to 20 %. The austenitized state is denoted as *1*, and the rolled state as *2*. The chemical composition of VNS9-Sh steel is as follows (by weight): 0.25 % C; 14.5 – 16.0 % Cr; 4.8 – 5.8 % Ni; 2.7 – 3.2 % Mo; 0.03 – 0.07 % N; ≤1 % Mn; ≤0.6 % Si; ≤0.01 % S; ≤0.015 % P.

Using the electric spark method, samples of the "double blade" type with working part dimensions of 40×6 mm were cut from the workpieces. The samples underwent uniaxial tension testing at room temperature using a Walter + Bai AG universal testing machine, LFM 125 series. The moving speed of the movable gripper ($V_{mach}$) was set at 0.4 mm/min, ensuring a deformation rate of $1.67 \cdot 10^{-4}$ $s^{-1}$.

Throughout the stretching process, digital images of the deformed sample were sequentially recorded, following a procedure similar to the one outlined in [1]. The recorded series of images served for the identification of areas with localized deformation, and their kinetics were analyzed using the traditional method of digital image correlation (DIC) [15]. Utilizing the obtained data arrays, chronograms were constructed [1; 16], enabling the detection of regions of origin, movement, and annihilation of localized deformation fronts.

Simultaneously, changes in the martensite content in the samples were determined *in situ* by measuring the magnetization of the material using an MVP-2M multifunctional eddy current device. This magnetic measurement method allows for the quantification of the volume fraction of the magnetic phase without the necessity of interrupting mechanical tests. The magnetic measurement sensor remained in contact with the working part of the sample throughout the entire loading duration, with a sensor probe diameter of 2 mm.

## Results

Fig. 1 depicts the strain curves σ(ε) and the corresponding variations in the strain hardening coefficient $\theta(\varepsilon) = d\sigma/d\varepsilon(\varepsilon)$ for samples in states *1* and *2*. A comprehensive analysis of these dependencies facilitate identification of five distinct areas: *I*, *II*, $III_i$, $III_d$, $III_j$. Section *I* ($0 - t_1$) corresponds to elastic loading and microplasticity (not shown in the θ(ε) dependence for state *1*). Section *II* ($t_1 - t_2$) includes a weakly defined tooth and an imperfect yield plateau (referred to as *a pseudo plateau* in the terminology of [16]). Following section *II*, the nonlinear stage *III* begins with a positive hardening coefficient. In section $III_i$ ($t_2 - t_3$) the hardening coefficient increases from zero to its maximum value. Section $III_d$ ($t_3 - t_\delta$) is characterized by a decline in the hardening coefficient from its maximum value to zero, akin to the traditional parabolic strain curve described by the Hollomon–Ludwik equation $\sigma = \sigma_0 + K\varepsilon^n$ (where *K* is the strain hardening coefficient and n is the strain hardening index, with $n < 1$). In the austenitized state *1*, stress surges are observed against the backdrop of this curve (section $III_j$, $t_j - t_\delta$). The Table provides the values of time and deformation corresponding to the boundaries of the stages and sections.

The magnetic measurements conducted during the tensile tests of the sample enabled the characterization of the process of martensitic phase accumulation and, consequently, a reduction in the volume fraction of metastable austenite. Throughout deformation, the content of the austenite phase in steel decreased from 93 % to approximately 30 % in state *1*, and from 80 % to approximately 40 % in state *2* (Fig. 2).

As established in [17], the deformation of TRIP steels develops locally through the formation and movement of deformation fronts. In the present work, it has been

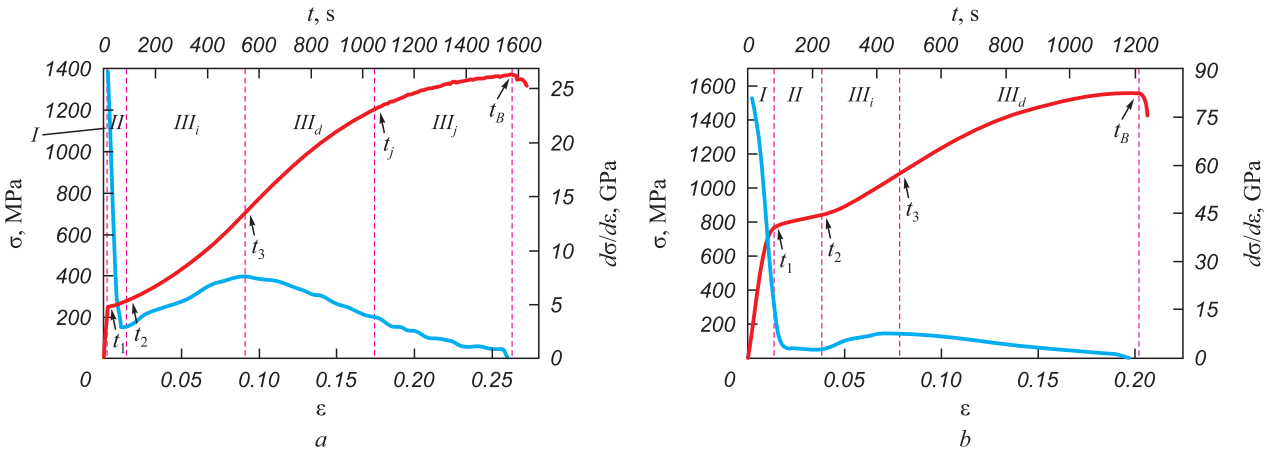


Fig. 1. Stress-strain curve and hardening coefficient of VNS9-Sh steel in states *1* (*a*) and *2* (*b*)

Рис. 1. Деформационная кривая и коэффициент упрочнения стали ВНС9-Ш в состояниях *1* (*a*) и *2* (*b*)

**Duration of loading curve stages**

**Продолжительности стадий кривой нагружения**

| State | $t_1$, s | $\varepsilon_1$ | $t_2$, s | $\varepsilon_2$ | $t_3$, s | $\varepsilon_3$ | $t_j$, s | $\varepsilon_j$ | $t_\delta$, s | δ |
|---|---|---|---|---|---|---|---|---|---|---|
| *1* | 18 | 0.003 | 90 | 0.015 | 545 | 0.090 | 1050 | 0.175 | 1575 | 0.265 |
| *2* | 83 | 0.014 | 227 | 0.078 | 470 | 0.078 | – | – | 1214 | 0.202 |

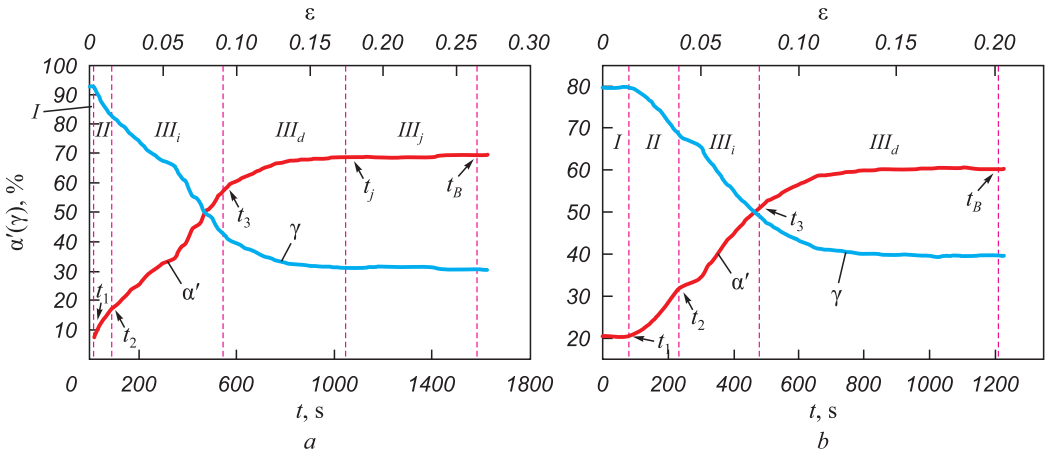


Fig. 2. Variation in phase composition of VNS9-Sh steel during deformation in states *1* (*a*) and *2* (*b*)

Рис. 2. Изменение в процессе деформации фазового состава стали ВНС9-Ш в состояниях *1* (*a*) и *2* (*b*)

demonstrated that the kinetics of deformation fronts align not only with the stages of the hardening curve but also with changes in the phase composition.

Fig. 3 shows the initial section of the chronograms depicting the movement of deformation fronts in TRIP steel in states *1* and *2*. The chronograms are constrained to 810 s (state *1*) and 1150 s (state *2*) due to the significantly higher amplitudes of deformation in the destruction zone compared to the *pseudo plateau*. This sharp inhomogeneity in contrast complicates the perception of fronts in the early stages of deformation. It is evident that in all sections, except for section *I*, localized deformation fronts are in motion. During the *pseudo plateau* stage, ChLBs form in both states, denoted as *A*, *B*, *C*, and *A*, *B*, *C*, *D*, *E* for states *1* and *2*, respectively.

The chronogram in Fig. 3, *a* (state *1*), illustrates that the Lüders band *A* appeared on the yield tooth at time $t_1$. Subsequently, bands *B* and *C* were formed, and their fronts (boundaries) moved in pairs towards each other, culminating in annihilation at time $t_2$. At this juncture, the entire working area of the sample has transitioned into a plastically deformed state. The regions of annihilation of Lüders fronts play a pivotal role in the subsequent stages.

In all sections of nonlinear stage III, there is also the movement of localized deformation fronts (Fig. 3, *a*). However, initially, they originate and spread within the boundaries set by the annihilation zones of the Lüders fronts. The movement of deformation fronts during stage *III* is such that, overall, they traverse the entire

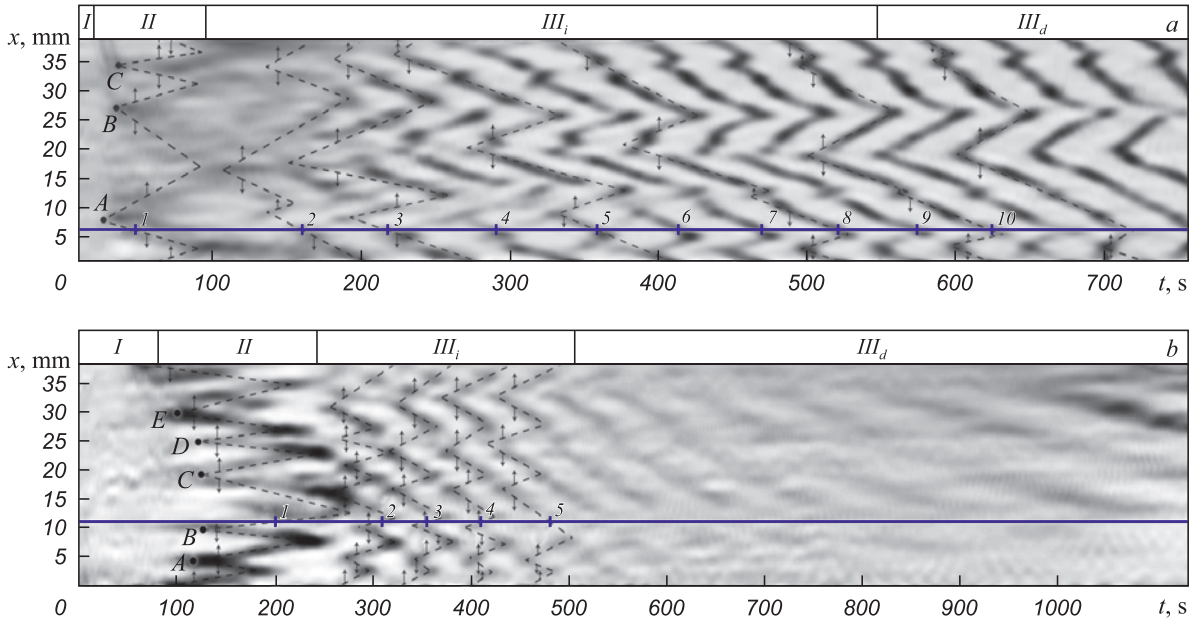


Fig. 3. Chronograms of phase transformation fronts propagation in VNS9-Sh steel in states *1* (*a*) and *2* (*b*)

Рис. 3. Хронограммы распространения фронтов фазового превращения в стали ВНС9-Ш в состояниях *1* (*a*) и *2* (*b*)

sample multiple times. As section $III_j$ commences, the regions of annihilation of Lüders fronts cease to serve as boundaries for the movement of deformation fronts during stage *III*.

In state *2* (Fig. 3, *b*) in the *pseudo plateau* area, the scenario is analogous to that described for state *1*, albeit with a higher generation of Chernov–Lüders bands (ChLB). The regions of annihilation of Lüders fronts continue to act as constraints on the movement of deformation fronts during stage III. However, in this case, such fronts move only up to approximately 700 s. Following this period, macro-level deformation localization is absent until the formation of a fracture neck at $t_\delta$ = 1214 s.

In a previous study [17], it was hypothesized that the observed fronts of localized deformation are attributed to the progression of the γ → α′ phase transformation. If this assumption holds true, the accumulation of the martensite phase should align with the kinetics of deformation fronts. In Fig. 3, horizontal blue lines denote the coordinates where the magnetic measurement sensor is positioned on the working part of the sample; the numbers indicate the instances of the passage of localized deformation fronts through these coordinates. As the deformation front traverses the specified point, the rate of strain accumulation $d\varepsilon/dt$ sharply increases, as evident in Fig. 4. Time instant *1* (state *1*) corresponds (Fig. 4, *a*) to the passage of front *A* of the Lüders band through the magnetic sensor probe, while the subsequent instances (*2 – 10*) denote the passage of localized deformation fronts during stage *III*.

In Fig. 4, *a*, the dependence of the rate of martensite phase accumulation on time in state *1* is also depicted. It is evident that the passage of front *A* of the Lüders band at time *1* corresponds to the maximum rate of formation of the magnetic phase of α′ martensite. It is estimated that up to 10 % of the magnetic phase is formed on the *pseudo plateau*. The remaining transformation γ → α′ primarily occurs in the nonlinear section $III_i$ under conditions of increasing hardening rate. Here, too, the maximum rate of martensite formation aligns with times *2 – 10*, coinciding with the passage of deformation fronts through the probe. The highest transformation rates are observed at times of passage of fronts *5 – 8*. In total, approximately 50 % of the martensite phase is formed in section $III_i$. As section $III_d$ begins ($t_3$ = 545 s), the transformation rate sharply decreases, and the correspondence between the time of passage of deformation fronts and the maximum rates of γ → α′ transformation is disrupted. By the start of section $III_j$ ($t_j$ = 1050 s), the rate of γ → α′ transformation nearly becomes zero (Fig. 4, *a*), and the content of α′ martensite reaches 69 %, remaining almost unchanged (Fig. 2). Simultaneously, the deformation fronts continue to propagate, and their amplitudes even increase (Fig. 3, *a* and 4, *a*).

In state *2* (Fig. 4, *b*) the situation is generally similar. However, *pseudo plateau* (section *II*) produces markedly more martensite (≈15 %). Additionally, even though the duration of section $III_i$ is significantly shorter in state *2*, almost 40 % of martensite has been formed within this section. Here as well, the maximum rate of α′ phase formation corresponds to the passage of deformation fronts through the probe of the magnetic sensor. As the section $III_d$ commences, similar to state *1*, the transformation rate sharply decreases to zero. The synchronicity between the maximum velocities γ → α′ and the times of passage of deformation fronts is disrupted, and the amount of martensite, having reached 60 %, remains unchanged further (Fig. 4, *b* and Fig. 2). It is worth noting that in state *2*, in section $III_d$, there is no movement of deformation fronts, no stress drops, and the σ(ε) diagram remains smooth until failure (Fig. 1, *b* and Fig. 3, *b*).

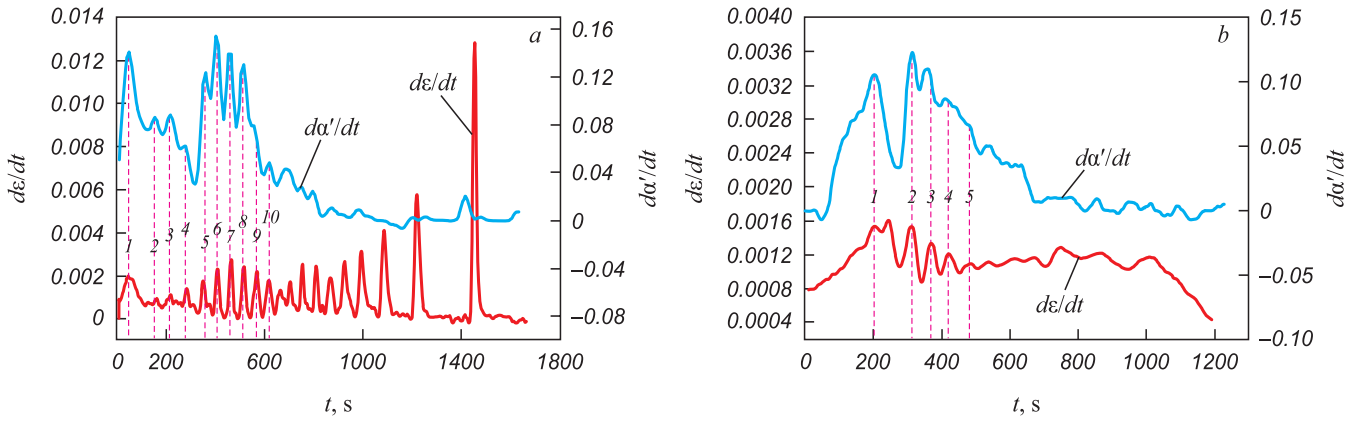


Fig. 4. Accumulation rates of local deformation $d\varepsilon/dt$ and martensite $d\alpha'/dt$ at contact point of the magnetic measurement sensor:
*a* – state *1*; *b* – state *2*

Рис. 4. Скорости накопления локальной деформации $d\varepsilon/dt$ и мартенсита $d\alpha'/dt$ в точке контакта датчика магнитных измерений:
*a* – состояние *1*; *b* – состояние *2*

## Discussion

The thermoelastic martensitic transformation in the TRIP steel under investigation can potentially occur throughout the entire deformation process, spanning from the yield point to fracture. However, the sequence of macroscopic manifestations and the completeness of this process are contingent on various external factors. For instance, as demonstrated by the authors of [10], the $\gamma \rightarrow \alpha'$ transformation in VNS9-Sh steel never reaches completion. As the deformation rate and test temperature increase, a greater quantity of "stable" austenite, as per the authors' terminology, remains. At room temperature and a stretching rate of approximately $10^{-4}$ $s^{-1}$, about 70 % of austenite is retained, aligning with the findings obtained in this study.

It is commonly asserted that the thermoelastic transformation $\gamma \rightarrow \alpha'$ in TRIP steels is primarily facilitated through the formation of ChLB [7; 10], and then continues in the form of the Portevin–Le Chatelier effect [7; 10; 17]. The findings of this study generally align with this concept. However, in a previous investigation [18], it was demonstrated that at a high level of hardening of metastable austenite, the transformation can be entirely completed by the formation of ChLB at the yield site, and further deformation occurs without the involvement of a phase transformation.

Building upon the results of this study (VNS9-Sh in state *1*, low yield strength), it was established that after Lüders deformation, the phase transformation indeed continues through the formation and propagation of PLCh bands, but only while the strain hardening rate increases. Upon transitioning to the section of the deformation curve with a decreasing hardening rate, the transformation diminishes and comes to a complete halt in the region of abrupt deformation. The observed discontinuous flow thereafter is not associated with a phase transformation and appears to be explained, similar to stable austenitic steels, by twinning [19]. When the steel under study was in state *2* (high yield stress), phase transformation also occurred through the formation of both ChLB and PLCh bands. However, the latter were observed only in the section of the loading diagram with an increasing hardening coefficient. Subsequently, the deformation developed monotonically.

As mentioned in [18; 20], the kinetics of deformation fronts in materials undergoing deformation-induced phase transformation can be explained using autowave theory [21; 22]. In this conceptual framework, ChLB fronts are considered autowaves of switching localized plasticity. Switching autowaves traverse the loaded object once, transitioning it from an elastically stressed to a plastically deformed state. These autowaves are formed in media with bistable active elements, that can operate just once.

A deformable body can serve as a medium with excitable active elements that, unlike bistable ones, can return to a state of excitation under external influence and relax again after a refractory period. In this scenario, localized plasticity excitation autowaves are formed, which can pass through the deformable object multiple times. These autowaves represent the fronts of the PLCh bands.

Within the framework of autowave theory, the obtained results can be interpreted as follows. Multiple ChLBs are formed on the *pseudo plateau*, and the moving boundaries of these bands can be considered as switching autowaves. These autowaves partially transition the material from the metastable austenitic state to the stable martensitic state. In the regions of autowave generation and annihilation, the material undergoes a radical change in state, leading to the division of the sample into relatively isolated sections. A notable characteristic of the thermoelastic phase transformation is its self-blocking nature due to internal stresses. However, with a subsequent increase in external stresses, the transformation can resume. Therefore, the regions of origin and annihilation of primary autowaves, where the material's state is significantly distorted, act as sources for new phase transformation fronts, referred to as secondary autowaves of excitation. These secondary waves propagate within the formed isolated areas without crossing their boundaries. This process repeats multiple times as long as there is austenite capable of transformation. As indicated by magnetic measurements, the $\gamma \rightarrow \alpha'$ transformation halts when section $III_d$ begins. Simultaneously, the boundaries of the isolated areas cease to play a role, allowing deformation fronts to freely traverse the entire sample pattern. While these fronts are also autowaves of excitation, their physical nature is different. They do not represent a relay phase transformation but rather shear processes, likely of a twin nature.

## Conclusions

Plastic deformation of VNS9-Sh TRIP steel can occur locally throughout the entire strain curve, spanning from the yield point to fracture. Initially, the process involves the generation and propagation of localized plasticity switching autowaves, induced by the deformation-induced transformation of metastable austenite into α′-martensite. The process persists via propagation of localized plasticity switching autowaves within boundaries determined by primary switching autowaves. Following the depletion of transformable austenite, steel deformation takes place through dislocation or twin mechanisms.

## References / Список литературы

1. Danilov V.I., Gorbatenko V.V., Danilova L.V. Kinetics of Lüders deformation as an autowave process. *Izvestiya.*

*Ferrous Metallurgy*. 2022;65(4):261–267. (In Russ.). https://doi.org/10.17073/0368-0797-2022-4-261-267

Данилов В.И., Горбатенко В.В., Данилова Л.В. Кинетика деформации Людерса как автоволнового процесса. *Известия вузов. Черная металлургия*. 2022;65(4):261–267. https://doi.org/10.17073/0368-0797-2022-4-261-267

2. Friedel J. *Dislocations*. Pergamon, London; Addison-Wesley; 1964.

Фридель Ж. *Дислокации*. Москва: Мир; 1967:626.

3. Hall E.O. *Yield Point Phenomena in Metals and Alloys*. N.Y.: Plenum Press; 1970:296.
4. Pelleg J. *Mechanical Properties of Materials*. Dordrecht: Springer; 2013:634.
5. Show J.A., Kyriakides S. On the nucleation and propagation of phase transformation fronts in NiTi alloy. *Acta Materialia*. 1997;45(2):683–700. http://doi.org/10.1016/S1359-6454(96)00189-9
6. Otsuka K., Ren X. Physical metallurgy of Ti–Ni-based shape memory alloys. *Progress in Materials Science*. 2005; 50(5):511–678. https://doi.org/10.1016/j.pmatsci.2004.10.001
7. Luo H.W., Dong H., Huang M.X. Effect of intercritical annealing on the Lüders strains of medium Mn transformation-induced plasticity steels. *Materials & Design*. 2015;83: 42–48. https://doi.org/10.1016/j.matdes.2015.05.085
8. Wang X.G., Liu C.H., He B.B., Jiang C., Huang M.X. Microscopic strain partitioning in Lüders band of an ultrafine-grained medium Mn steel. *Materials Science and Engineering A*. 2019;761:138050. https://doi.org/10.1016/j.msea.2019.138050
9. Terent'ev V.F., Slizov A.K., Sirotinkin V.P., Prosvirnin D.V., Kobeleva L.I., Eliseev E.A., Rybal'chenko O.V., Ashmarin A.A. Effect of the removal of the surface layer of a TRIP steel sheet on its phase composition after static tension at various strain rates. *Russian Metallurgy (Metally)*. 2016;(1): 34–38. https://doi.org/10.1134/S0036029516010122
10. Terent'ev V.F., Ashmarin A.A., Blinova E.N., Titov D.D., Blinov V.M., Slizov A.K., Seval'neva T.G. Mechanical properties and structure of a VNS9-Sh steel as functions of the tempering temperature. *Russian Metallurgy (Metally)*. 2019; 2019(4):403–408. https://doi.org/10.1134/S0036029519040293

Терентьев В.Ф., Ашмарин А.А., Блинова Е.Н., Титов Д.Д., Блинов В.М., Слизов А.К., Севальнева Т.Г. Исследование зависимости механических свойств и структуры трипстали ВНС9-Ш от температуры отпуска. *Деформация и разрушение материалов*. 2018;(6):20–25.

11. Tilak Kumar J.V., Sudha J., Padmanabhan K.A., Frolova A.V, Stolyarov V.V. Influence of strain rate and strain at temperature on TRIP effect in a metastable austenitic stainless steel. *Materials Science and Engineering: A*. 2020;777:139046. https://doi.org/10.1016/j.msea.2020.139046
12. Cai Z.H., Ding H., Misra R.D.K., Ying Z.Y. Austenite stability and deformation behavior in a cold-rolled transformation-induced plasticity steel with medium manganese content. *Acta Materialia*. 2015;84:229–236. https://doi.org/10.1016/j.actamat.2014.10.052
13. Soleimani M., Kalhor A., Mirzadeh H. Transformation-induced plasticity (TRIP) in advanced steels: A review. *Materials Science and Engineering: A*. 2020;795:140023. https://doi.org/10.1016/j.msea.2020.140023
14. Zuev L.B., Danilov V.I., Danilova L.V., Gorbatenko V.V. Deformable material as a nonlinear active medium. *Izvestiya vuzov. Fizika*. 2022;65(2):89–97. (In Russ.). http://dx.doi.org/10.17223/00213411/65/2/89

Зуев Л.Б., Данилов В.И., Данилова Л.В., Горбатенко В.В. Деформируемый материал как нелинейная активная среда. *Известия вузов. Физика*. 2022;65(2):89–97. http://dx.doi.org/10.17223/00213411/65/2/89

15. Sutton M.A. Digital image correlation for shape and deformation measurements. In: *Springer Handbook of Experimental Solid Mechanics. Springer Handbooks*. Sharpe W. ed. Springer: Boston, MA; 2008:565–600. https://doi.org/10.1007/978-0-387-30877-7_20
16. Sun H.B., Yoshida F., Ohmori M., Ma X. Effect of strain rate on Lüders band propagating velocity and Lüders strain for annealed mild steel under uniaxial tension. *Materials Letters*. 2008;57(29):4535–4539. https://doi.org/10.1016/S0167-577X(03)00358-6
17. Callahan M., Hubert O., Hild F., Perlade A., Schmitt J.-H. Coincidence of strain-induced TRIP and propagative PLC bands in medium Mn steels. *Materials Science and Engineering: A*. 2017;704:391–400. https://doi.org/10.1016/j.msea.2017.08.042
18. Orlova D.V., Danilov V.I., Gorbatenko V.V., Danilova L.V., Shlyakhova G.V., Zuev L.B. The effect of preliminary thermomechanical processing on the kinetics of localized plasticity autowaves in TRIP steel. *Metals*. 2020;10(11):1494. https://doi.org/10.3390/met10111494
19. Karaman I., Sehitoglu H., Maier H.J., Chumlyakov Yu.I. Competing mechanisms and modeling of deformation in austenitic stainless steel single crystals with and without nitrogen. *Acta Materialia*. 2001;49(19):3919–3933. https://doi.org/10.1016/S1359-6454(01)00296-8
20. Danilov V.I., Gorbatenko V.V., Danilova L.V. Switching autowaves in materials with dislocations and martensitic transformations. *Russian Physics Journal*. 2020;63:940–946. https://doi.org/10.1007/s11182-020-02121-4

Данилов В.И., Горбатенко В.В., Данилова Л.В. Автоволны переключения в материалах с дислокационным и мартенситным механизмами пластичности. *Известия вузов. Физика*. 2020;63(6(750)):37–42. https://doi.org/10.1007/s11182-020-02121-4

21. Krinsky V.I. *Self-Organization: Autowaves and Structures Far from Equilibrium*. Berlin: Springer-Verlag; 1984:270.
22. Loskutov A.Yu., Mikhailov A.S. *Foundations of the Theory of Complex Systems*. Moscow-Izhevsk: IKI; 2007:612. (In Russ.).

Лоскутов А.Ю., Михайлов А.С. *Основы теории сложных систем*. Москва-Ижевск: ИКИ; 2007:612.

## Information about the Authors

***Vladimir I. Danilov,*** *Dr. Sci. (Phys.-Math.), Prof., Chief Researcher of the Laboratory of Strength Physics,* Institute of Strength Physics and Materials Science, Siberian Branch Russian Academy of Sciences
***ORCID:*** 0000-0002-5741-7574
***E-mail:*** dvi@ispms.ru

***Dina V. Orlova,*** *Cand. Sci. (Phys.-Math.), Research Associate of the Laboratory of Strength Physics,* Institute of Strength Physics and Materials Science, Siberian Branch of Russian Academy of Sciences
***ORCID:*** 0000-0003-0068-2542
***E-mail:*** dvo@ispms.ru

***Vadim V. Gorbatenko,*** *Cand. Sci. (Phys.-Math.), Senior Researcher of the Laboratory of Strength Physics,* Institute of Strength Physics and Materials Science, Siberian Branch of Russian Academy of Sciences
***ORCID:*** 0000-0001-6464-6159
***E-mail:*** gvv@ispms.ru

***Lidiya V. Danilova,*** *Cand. Sci. (Phys.-Math.), Junior Researcher of the Laboratory of Strength Physics,* Institute of Strength Physics and Materials Science, Siberian Branch of Russian Academy of Sciences
***ORCID:*** 0000-0002-4124-0516
***E-mail:*** dlv@ispms.ru

## Сведения об авторах

***Владимир Иванович Данилов,*** *д.ф.-м.н., профессор, главный научный сотрудник лаборатории физики прочности,* Институт физики прочности и материаловедения Сибирского отделения РАН
***ORCID:*** 0000-0002-5741-7574
***E-mail:*** dvi@ispms.ru

***Дина Владимировна Орлова,*** *к.ф.-м.н., научный сотрудник лаборатории физики прочности,* Институт физики прочности и материаловедения Сибирского отделения РАН
***ORCID:*** 0000-0003-0068-2542
***E-mail:*** dvo@ispms.ru

***Вадим Владимирович Горбатенко,*** *к.ф.-м.н., старший научный сотрудник лаборатории физики прочности,* Институт физики прочности и материаловедения Сибирского отделения РАН
***ORCID:*** 0000-0001-6464-6159
***E-mail:*** gvv@ispms.ru

***Лидия Владиславовна Данилова,*** *к.ф.-м.н., младший научный сотрудник лаборатории физики прочности,* Институт физики прочности и материаловедения Сибирского отделения РАН
***ORCID:*** 0000-0002-4124-0516
***E-mail:*** dlv@ispms.ru

## Contribution of the Authors

***V. I. Danilov*** – formation of the main concept of the article, revising and writing final version of the manuscript.
***D. V. Orlova*** – analysis and discussion of experimental results, writing the draft version of the manuscript.
***V. V. Gorbatenko*** – carrying out mechanical tests and registration of the evolution of patterns of localized plasticity, analysis and discussion of chronograms.
***L. V. Danilova*** – mathematical processing of experimental data, construction and analysis of correlation dependencies.

## Вклад авторов

***В. И. Данилов*** – идея работы, научное руководство, написание окончательного варианта рукописи.
***Д. В. Орлова*** – анализ и обсуждение экспериментальных результатов, написание первичного варианта рукописи.
***В. В. Горбатенко*** – проведение механических испытаний и регистрация эволюции картин локализованной пластичности, анализ и обсуждение хронограмм.
***Л. В. Данилова*** – математическая обработка экспериментальных данных, построение и анализ корреляционных зависимостей.

Received 30.01.2023
Revised 12.06.2023
Accepted 09.10.2023

Поступила в редакцию 30.01.2023
После доработки 12.06.2023
Принята к публикации 09.10.2023

MATERIALS SCIENCE / МАТЕРИАЛОВЕДЕНИЕ

**UDC** 538.951
**DOI** 10.17073/0368-0797-2023-6-681-687



*Original article*
*Оригинальная статья*

# Theoretical strength of austenite in the presence of a pore or vacancies in the crystal: Molecular dynamics study

**I. V. Zorya[1], G. M. Poletaev[2], R. Yu. Rakitin[3]**

[1] **Siberian State Industrial University** (42 Kirova Str., Novokuznetsk, Kemerovo Region – Kuzbass 654007, Russian Federation)
[2] **Polzunov Altai State Technical University** (46 Lenina Ave., Barnaul, Altai Territory 656038, Russian Federation)
[3] **Altai State University** (100 Komsomol'skii Ave., Barnaul, Altai Territory 656038, Russian Federation)

zorya.i@mail.ru

***Abstract***. The molecular dynamics method was used to study the influence of pores of different diameters, as well as the corresponding concentration of individual vacancies, on the theoretical strength of austenite at different temperatures. The deformation in the model was carried out by shear at a constant rate of 20 m/s. We considered a shear along two directions: [$\bar{1}\bar{1}$2] and [111]. The computational austenite cell had the shape of a rectangular parallelepiped 14.0 nm long, 14.0 nm high, and 5.1 nm wide. To describe interatomic interactions, the Lau EAM potential was used, which reproduces well the structural, energy, and elastic characteristics of austenite. The stress-strain curves obtained for both considered shear directions had a similar form. In the absence of dislocation sources, plastic deformation was carried out by the formation of dislocation dipoles (dislocations with opposite Burgers vectors). The presence of a pore significantly reduced the yield strength of austenite. In this case, it was found that single vacancies randomly scattered over the volume of the computational cell also lead to a decrease in the yield strength, but, of course, not as much as the pore. The emission of dislocations during deformation occurred by the formation of dislocation loops, as a rule, in two slip planes at once. The effect of pores and vacancies on the yield strength was stronger at low temperatures. As the temperature increased, the effect of defects on the critical stress at which dislocations were formed decreased. With an increase in the pore size, as well as the concentration of vacancies, the yield strength decreased. In this case, the strongest dependence was observed for pores up to 1 nm in diameter. The influence of the concentration of vacancies in the considered range on the yield strength turned out to be comparatively smoother and almost linear.

***Keywords:*** molecular dynamics, austenite, dislocation, pore, vacancy, theoretical strength

***For citation:*** Zorya I.V., Poletaev G.M., Rakitin R.Yu. Theoretical strength of austenite in the presence of a pore or vacancies in the crystal: molecular dynamics study. *Izvestiya. Ferrous Metallurgy*. 2023;66(6):681–687. https://doi.org/10.17073/0368-0797-2023-6-681-687

# Теоретическая прочность аустенита при наличии в кристалле поры или вакансий: молекулярно-динамическое исследование

**И. В. Зоря[1], Г. М. Полетаев[2], Р. Ю. Ракитин[3]**

[1] **Сибирский государственный индустриальный университет** (Россия, 654007, Кемеровская обл. – Кузбасс, Новокузнецк, ул. Кирова, 42)
[2] **Алтайский государственный технический университет им. И.И. Ползунова** (Россия, 656038, Алтайский край, Барнаул, пр. Ленина, 46)
[3] **Алтайский государственный университет** (Россия, 656038, Алтайский край, Барнаул, Комсомольский пр., 100)

zorya.i@mail.ru

***Аннотация***. Методом молекулярной динамики проведено исследование влияния поры разного диаметра, а также соответствующей концентрации отдельных вакансий на теоретическую прочность аустенита при разной температуре. Деформация в модели осуществляется путем сдвига с постоянной скоростью 20 м/с. Рассматривается сдвиг вдоль двух направлений: [$\bar{1}\bar{1}$2] и [111]. Расчетная ячейка аустенита имеет форму прямоугольного параллелепипеда длиной 14,0 нм, высотой 14,0 нм и шириной 5,1 нм. Для описания межатомных взаимодействий использовался EAM потенциал Лау, хорошо воспроизводящий структурные, энергетические и упругие характеристики аустенита. Кривые напряжение – деформация, полученные для обоих рассматриваемых направлений сдвига, имеют аналогичный вид. В отсутствие источников дислокаций пластическая деформация осуществляется путем формирования дислокационных диполей

(дислокаций с противоположными векторами Бюргерса). Наличие поры существенно снижает предельную прочность аустенита. Обнаружено, что случайно разбросанные по объему расчетной ячейки одиночные вакансии также приводят к снижению предельной прочности, но, естественно, не так сильно, как пора. Испускание дислокаций порой при деформации происходит путем формирования дислокационных петель, как правило, сразу в двух плоскостях скольжения. Сильнее влияние поры и вакансий на предельную прочность наблюдается при низких температурах. При увеличении температуры влияние дефектов на критическое напряжение, при котором происходит образование дислокаций, снижается. С увеличением размера поры, как и концентрации вакансий, прочность уменьшается. При этом наиболее сильная зависимость наблюдается для пор диаметром до 1 нм. Влияние концентрации вакансий в рассматриваемом диапазоне на предельную прочность оказалось сравнительно более плавное и почти линейное.

***Ключевые слова:*** молекулярная динамика, аустенит, дислокация, пора, вакансия, теоретическая прочность

***Для цитирования:*** Зоря И.В., Полетаев Г.М., Ракитин Р.Ю. Теоретическая прочность аустенита при наличии в кристалле поры или вакансий: молекулярно-динамическое исследование. *Известия вузов. Черная металлургия*. 2023;66(6):681–687.
https://doi.org/10.17073/0368-0797-2023-6-681-687

## Introduction

During plastic deformation, in addition to interface boundaries (such as grain boundaries and their triple junctions, interphase boundaries, and surfaces), pores and microvoids play crucial role as sources of dislocations in polycrystalline materials [1 – 3]. However, there has been relatively little research dedicated to studying the mechanisms of plastic deformation at the atomic level involving pores. To date, computer modeling has demonstrated that dislocation emission from pores during deformation is facilitated by the formation of dislocation loops [3 – 6]. The authors of [5; 6] assert that in FCC crystals, loops are formed simultaneously in two slip planes. Moreover, as the pore size increases, the critical stress required for dislocation formation decreases [5; 6].

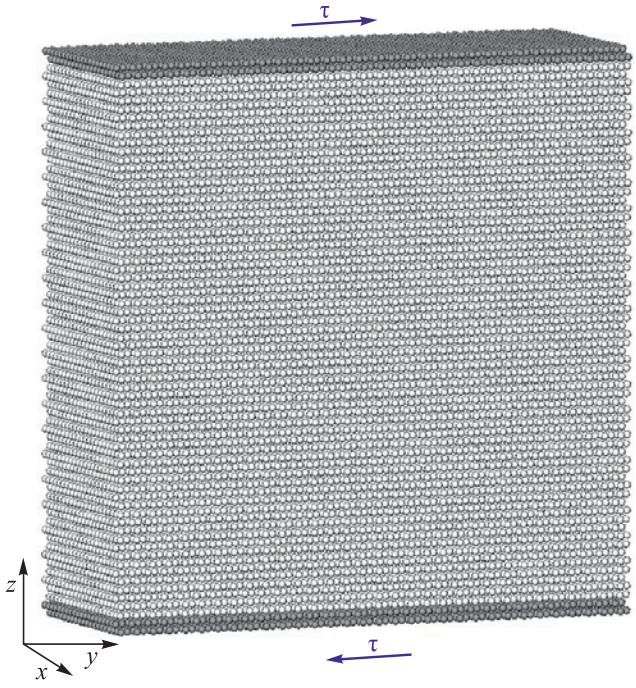


Fig. 1. Calculation cell for modeling the shift along the *y* axis (direction [$\bar{1}\bar{1}$2]) in the FCC iron

Рис. 1. Расчетная ячейка для моделирования сдвига вдоль оси *y* (направления [$\bar{1}\bar{1}$2]) в ГЦК железе

Point defects, for example, vacancies, also contribute significantly to a decrease in theoretical strength, yet the impact of their concentration on strength remains insufficiently explored, especially when compared to the effect of pore accumulations. The present study focuses on conducting a comparative analysis using molecular dynamics to investigate the influence of vacancies and pores on the theoretical strength of austenite, with consideration given to variations in temperature and vacancy concentration or pore size. Austenite garners particular interest as it serves as the foundation for many steels of considerable practical importance, such as Hadfield steel [7; 8]. Furthermore, the qualitative findings derived for austenite in this study can readily be extrapolated to other metals possessing an FCC crystal lattice.

Previously, in [9], the molecular dynamics method was employed to examine the slip velocity of edge and screw dislocations in austenite and Hadfield steel, contingent upon temperature and strain rate. The energy of formation for the aforementioned dislocations was also computed. This investigation serves as a continuation of the research documented in [9].

## Model description

In the molecular dynamics model, the calculation cell representing austenite had the shape of a rectangular parallelepiped (see Fig. 1) with dimensions of 14.0 nm in length, 14.0 nm in height, and 5.1 nm in width. Initially, the cell contained 87,040 atoms. The orientation of the coordinate axes corresponded to specific crystallographic directions within the FCC lattice: *x* – [$\bar{1}$10], *y* – [$\bar{1}\bar{1}$2], *z* – [111]. The study investigated shear deformation along two directions: the *y*-axis (Fig. 1) and the *z*-axis. To induce shear in the model, atoms in the boundary regions (highlighted in dark gray in Fig. 1) were displaced. Atoms on opposite sides of the calculation cell moved in opposite directions at a constant speed of 20 m/s during the computer experiment. In previous research [9], this velocity was determined as optimal for modeling shear using the molecular dynamics method in austenite. The motion of the remaining atoms within

the computational cell was unrestricted and governed by Newton's classical equations of motion. Boundary conditions along the other axes were set as periodic.

Interatomic interactions in austenite were described using Lau's Embedded Atom Method (EAM) potential [10], known for accurately reproducing the structural, energetic, and elastic properties of austenite [10; 11]. The time integration step in the molecular dynamics method was set to 2 fs [12 – 14]. The initial velocities of atoms were assigned according to the Maxwell distribution to achieve the desired temperature. It was essential to consider the thermal expansion of the crystal lattice when setting the temperature [13 – 15]. The interatomic interaction potential employed in this study has a thermal expansion coefficient of $18 \cdot 10^{-6}$ $K^{-1}$, aligning well with reference data [11]. To maintain a constant temperature throughout the modeling, a Nosé–Hoover thermostat was utilized. Throughout the temperature range explored (from 100 to 1500 K), the FCC crystal lattice type remained consistent; polymorphic transformations were not considered in this investigation.

A pore was created in the center of the computational cell by removing atoms in a spherical region. The pore diameter varied from 0.6 to 2.0 nm. Vacancies were introduced by removing random atoms throughout the entire volume of the computational cell, except for the boundary layers (shown in dark gray in Fig. 1). The considered values of vacancy concentration corresponded to the number of removed atoms during the creation of pores. After the introduction of defects, a procedure of relaxation of the structure followed until an equilibrium state was achieved.

## Results and discussion

Fig. 2 depicts the stress–strain dependences for the two shear orientations considered, with a constant speed of 20 m/s at a temperature of 300 K, for three scenarios: a defect-free crystal (*1*), a crystal containing 79 vacancies randomly distributed throughout its volume (*2*), and a crystal containing a pore with a diameter of 1.2 nm (*3*). The number of vacancies equaled the number of atoms removed during creation of the aforementioned pore resulting in a concentration of 0.09 % in this case.

It is widely acknowledged that the theoretical shear strength of metal crystals is exceptionally high, often exceeding 10 GPa [1; 5; 6; 16; 17]. However, introducing just one dislocation into a pristine crystal in the molecular dynamics model reduces the strength to several hundred MPa [18]. As illustrated in Fig. 2, plastic deformation in a pure austenite crystal at 300 K commenced with shear along both the *y* and *z* axes at approximately the same strain values (12.0 – 12.5 %) and stress levels (9.0 – 9.5 GPa). It is crucial to highlight that the initial ideal crystal lacked any sources of dislocation formation, including free surfaces. Consequently, the region of elastic deformation was relatively extensive.

In the absence of dislocation sources, plastic deformation occurred through the creation of dislocation dipoles, consisting of dislocations with opposite Burgers vectors. Complete dislocations promptly emerged as pairs of partial Shockley dislocations separated by a stacking fault. Typically, the distance between partial dislocations was a few nanometers, consistent with modeling findings reported by other researchers [19 – 21]. Additionally, alongside dislocation dipoles, the formation of deformation twins was also prominent during subsequent deformation stages.

As illustrated in Fig. 2, the inclusion of a pore with a diameter of 1.2 nm notably diminishes the theoretical strength: plastic shear and dislocation formation occur at significantly lower strain and stress thresholds (approxi-

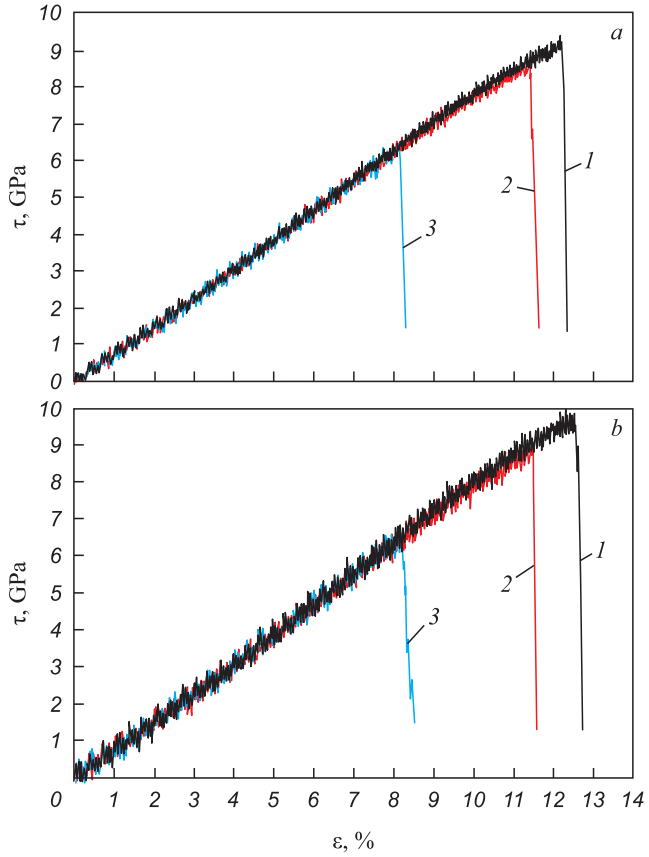


Fig. 2. Stress – strain dependences at a temperature of 300 K when shifted along the *y* axis (direction [$\bar{1}\bar{1}$2]) (*a*) and when shifted along the *z* axis (direction [111]) (*b*): *1* – in a pure FCC iron crystal; *2* – in the presence of 79 vacancies, randomly scattered over the volume of the calculation cell; *3* – in the presence of a pore with a diameter of 1.2 nm

Рис. 2. Зависимости напряжение – деформация при температуре 300 К при сдвиге вдоль оси *y* (направления [$\bar{1}\bar{1}$2]) (*a*) и при сдвиге вдоль оси *z* (направления [111]) (*b*): *1* – в чистом кристалле ГЦК железа; *2* – при наличии 79 вакансий, случайно разбросанных по объему расчетной ячейки; *3* – при наличии поры диаметром 1,2 нм

mately 8.5 % and 6 GPa, respectively). Conversely, vacancies randomly distributed throughout the computational cell, equating in number to those in the pore, exert a comparatively weaker influence on the ultimate strength. However, intriguingly, they still contribute to its reduction, with dislocations forming at a strain of about 11.5 % and a stress of 8.5 GPa. Thus, even basic point defects like vacancies attenuate the theoretical strength of the crystal.

Dislocation emission from a pore during deformation transpired via the formation of dislocation loops, aligning with findings from modeling conducted by other researchers [3 – 6]. Fig. 3 depicts examples of such loop formation from a pore with a diameter of 1.2 nm upon displacement along the *y* and *z* axes. It is evident that loops manifest in two slip planes, consistent with observations made by authors elsewhere [5; 6]. To visualize dislocations within the computational cell, an average distance to the nearest atoms visualizer was utilized, providing insight into local stretching and indirectly indicating the distribution of free volume. For each atom, the average distance to the nearest atoms was computed. If this distance deviated slightly from the distance corresponding to an ideal crystal, the atom remained uncolored; otherwise, it was assigned a color based on the deviation.

As commonly understood, temperature significantly impacts the elastic properties of materials and the likelihood of dislocation formation during deformation. Elastic moduli typically decrease nearly linearly with rising temperatures across a wide range [22 – 24], a trend often attributed to thermal expansion [22]. Plastic deformation in most materials initiates at lower stress levels as temperature increases [24 – 26].

Fig. 4 illustrates the temperature dependence of ultimate strength for shear along the *y* and *z* axes. The dependencies are presented for a defect-free crystal (*1*), a crystal containing 79 randomly scattered vacancies (*2*), and a crystal with a pore diameter of 1.2 nm (*3*). In all instances, strength diminishes with increasing temperature. Notably, as temperature rises, the influence of defects on theoretical strength diminishes. Specifically, the discrepancies in ultimate strength values between the defect-free crystal and those with vacancies or pores decrease with increasing temperature, converging toward the same value. It is pertinent to note that this convergence suggests an anticipated intersection of dependencies at the melting temperature.

Fig. 5 presents the dependencies of ultimate strength at a temperature of 300 K for shear along the *y* and *z* axes (Fig. 5, *b*) concerning the percentage of atoms $c_v$ removed from the calculation cell in the form of individual randomly scattered vacancies or pores (designated as dependencies *1* and *2*, respectively, in Fig. 2, 4). For comparison, with a pore diameter of 1.0 nm, $c_v$ = 0.05 %; with a pore diameter of 1.2 nm, $c_v$ = 0.09 %; and with a pore diameter of 1.6 nm, $c_v$ = 0.23 %.

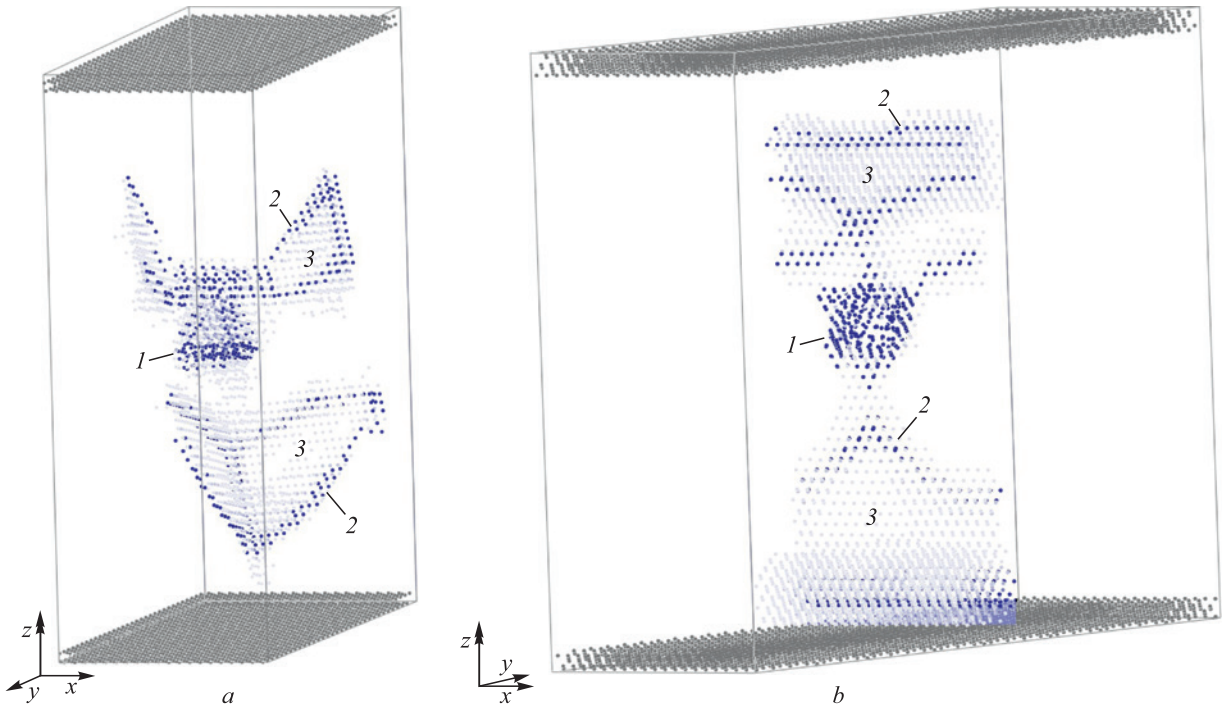


Fig. 3. Emission of dislocations by a pore in the form of dislocation loops when shifted along the *y* axis (*a*) and when shifted along the *z* axis (*b*): *1* – pore; *2* – partial dislocation; *3* – packaging defect

Рис. 3. Испускание дислокаций порой в виде дислокационных петель при сдвиге вдоль оси *y* (*a*) и оси *z* (*b*): *1* – пора; *2* – частичная дислокация; *3* – дефект упаковки

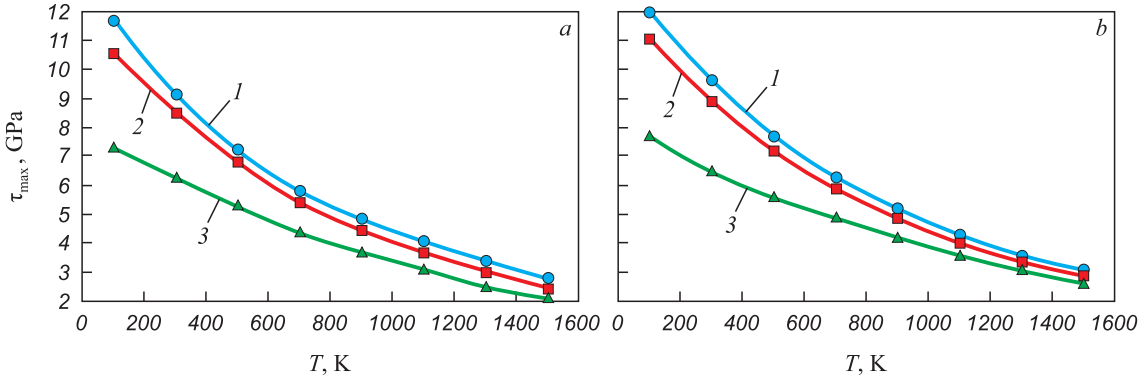


Fig. 4. Dependences of strength on temperature when shifted along the *y* axis (direction [$\bar{1}\bar{1}$2]) (*a*) and when shifted along the *z* axis (direction [111]) (*b*):
*1* – in a pure FCC iron crystal; *2* – in the presence of 79 vacancies randomly scattered over the volume calculation cell; *3* – in the presence of a pore with a diameter of 1.2 nm

Рис. 4. Зависимости прочности от температуры при сдвиге вдоль оси *y* (направления [$\bar{1}\bar{1}$2]) (*a*) и при сдвиге вдоль оси *z* (направления [111]) (*b*):
*1* – в чистом кристалле ГЦК железа; *2* – при наличии 79 вакансий, случайно разбросанных по объему расчетной ячейки; *3* – при наличии поры диаметром 1,2 нм

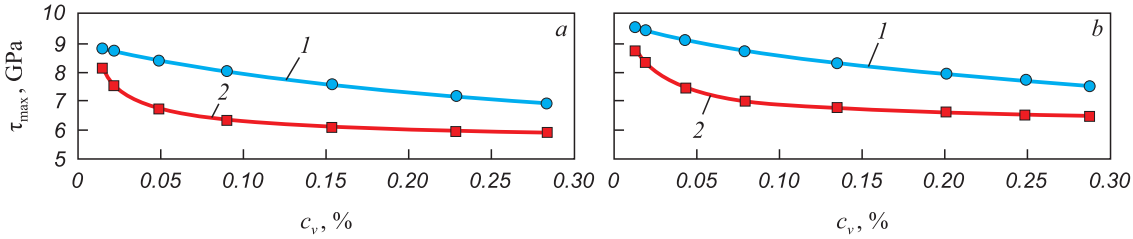


Fig. 5. Dependences of strength at temperature of 300 K on the number of atoms removed from the calculated cell in the form of randomly scattered vacancies (*1*) or pores (*2*) when shifted along the *y* axis (directions [$\bar{1}\bar{1}$2]) (*a*) and when shifted along the *z* axis (directions [111]) (*b*)

Рис. 5. Зависимости прочности при температуре 300 К от количества удаленных из расчетной ячейки атомов в виде случайно разбросанных вакансий (*1*) или поры (*2*) при сдвиге вдоль оси *y* (направления [$\bar{1}\bar{1}$2]) (*a*) и при сдвиге вдоль оси *z* (направления [111]) (*b*)

As evident, an increase in both vacancy concentration and pore radius correlates with a reduction in strength. Notably, the most pronounced dependence is observed for small pore sizes, up to approximately 1 nm. Beyond this range, while strength continues to decrease with increasing pore radius, the rate of decline is notably less pronounced compared to smaller pore sizes. Conversely, the influence of vacancy concentration within the considered range on theoretical strength is more gradual and nearly linear.

## Conclusions

The influence of pores of varying diameters, along with the corresponding concentration of individual vacancies, on the theoretical strength of austenite across different temperatures was investigated using the molecular dynamics method. Deformation in the model was induced by shearing at a constant speed of 20 m/s, considering shifts along two directions: [$\bar{1}\bar{1}$2] and [111]. Stress-strain dependences obtained for both shear directions exhibited similar trends. In the absence of dislocation sources, plastic deformation ensued through the formation of dislocation dipoles characterized by dislocations with opposite Burgers vectors. The presence of pores substantially reduced the ultimate strength of austenite, while single vacancies randomly dispersed throughout the computational cell also contributed to a decrease in ultimate strength, albeit to a lesser extent compared to pores. Dislocation emission from pores during deformation occurred through the formation of dislocation loops, typically manifesting in two slip planes simultaneously. A more pronounced impact of pores and vacancies on ultimate strength was observed at lower temperatures. However, as temperature increased, the influence of defects on the critical stress at which dislocation formation occurred diminished. Moreover, with increasing pore size and vacancy concentration, the strength exhibited a decreasing trend. Notably, the strongest dependence was observed for pores with diameters up to 1 nm. The effect of vacancy concentration within the considered range on ultimate strength was relatively smoother and displayed an almost linear behavior.

## References / Список литературы


1. Seppälä E.T., Belak J., Rudd R.E. Three-dimensional molecular dynamics simulations of void coalescence during dynamic fracture of ductile metals. *Physical Review B*. 2005;71(6):064112. https://doi.org/10.1103/PhysRevB.71.064112
2. Bobylev S.V., Morozov N.F., Ovid'ko I.A. Dislocation emission by pores in nanocrystalline metals. *Physics of the Solid State*. 2007;49(6):1098–1103. https://doi.org/10.1134/S1063783407060133
3. Ruestes C.J., Bringa E.M., Stukowski A., Rodríguez Nieva J.F., Tang Y., Meyers M.A. Plastic deformation of a porous bcc metal containing nanometer sized voids. *Computational Materials Science*. 2014;88:92–102. http://dx.doi.org/10.1016/j.commatsci.2014.02.047
4. Wang Y., Bi W., Deng L., Zhang X., Tang J., Wang L. Study on the relationship between surface and dislocation of nanoporous copper under cyclic shear loading. *AIP Advances*. 2022;12(3):035318. https://doi.org/10.1063/5.0085569
5. Traiviratana S., Bringa E.M., Benson D.J., Meyers M.A. Void growth in metals: Atomistic calculations. *Acta Materialia*. 2008;56(15):3874–3886. https://doi.org/10.1016/j.actamat.2008.03.047
6. Bringa E.M., Traiviratana S., Meyers M.A. Void initiation in fcc metals: Effect of loading orientation and nanocrystalline effects. *Acta Materialia*. 2010;58(13):4458–4477. https://doi.org/10.1016/j.actamat.2010.04.043
7. Zhang F.C., Lv B., Wang T.S., Zheng C.L., Zhang M., Luo H.H., Liu H., Xu A.Y. Explosion hardening of Hadfield steel crossing. *Materials Science and Technology*. 2010; 26(2):223–229. https://doi.org/10.1179/174328408X363263
8. Chen C., Lv B., Ma H., Sun D., Zhang F. Wear behavior and the corresponding work hardening characteristics of Hadfield steel. *Tribology International*. 2018;121:389–399. https://doi.org/10.1016/j.triboint.2018.01.044
9. Zorya I.V., Poletaev G.M., Rakitin R.Yu. Energy and velocity of sliding of edge and screw dislocations in austenite and Hadfield steel: Molecular dynamics simulation. *Izvestiya. Ferrous Metallurgy*. 2022;65(12):861–868. (In Russ.). https://doi.org/10.17073/0368-0797-2022-12-861-868

   Зоря И.В., Полетаев Г.М., Ракитин Р.Ю. Энергия и скорость скольжения краевой и винтовой дислокаций в аустените и стали Гадфильда: молекулярно-динамическое моделирование. *Известия вузов. Черная металлургия*. 2022;65(12):861–868. https://doi.org/10.17073/0368-0797-2022-12-861-868
10. Lau T.T., Forst C.J., Lin X., Gale J.D., Yip S., Van Vliet K.J. Many-body potential for point defect clusters in Fe-C alloys. *Physical Review Letters*. 2007;98(21):215501. https://doi.org/10.1103/PhysRevLett.98.215501
11. Oila A., Bull S.J. Atomistic simulation of Fe-C austenite. *Computational Materials Science*. 2009;45(2):235–239. https://doi.org/10.1016/j.commatsci.2008.09.013
12. Chen C., Zhang F., Xu H., Yang Z., Poletaev G.M. Molecular dynamics simulations of dislocation–coherent twin boundary interaction in face-centered cubic metals. *Journal of Materials Science*. 2022;57:1833–1849. https://doi.org/10.1007/s10853-021-06837-7
13. Poletaev G.M. Self-diffusion in liquid and solid alloys of the Ti–Al system: Molecular-dynamics simulation. *Journal of Experimental and Theoretical Physics*. 2021;133(4): 455–460. https://doi.org/10.1134/S1063776121090041
14. Poletaev G.M., Novoselova D.V., Kaygorodova V.M. The causes of formation of the triple junctions of grain boundaries containing excess free volume in fcc metals at crystallization. *Solid State Phenomena*. 2016;247:3–8. https://doi.org/10.4028/www.scientific.net/SSP.247.3
15. Poletaev G.M., Zorya I.V. Influence of light impurities on the crystal-melt interface velocity in Ni and Ag. Molecular dynamics simulation. *Technical Physics Letters*. 2020;46(6): 575–578. https://doi.org/10.1134/S1063785020060231
16. Bukreeva K.A., Iskandarov A.M., Dmitriev S.V., Umeno Y., Mulyukov R.R. Theoretical shear strength of FCC and HCP metals. *Physics of the Solid State*. 2014;56(3):423–428. https://doi.org/10.1134/S1063783414030081
17. Li P.-T, Yang Y.-Q., Xia Zh., Luo X., Jin N., Gao Y., Liu G. Molecular dynamic simulation of nanocrystal formation and tensile deformation of TiAl alloy. *RSC Advances*. 2017;7:48315–48323. https://doi.org/10.1039/C7RA10010H
18. Krasnikov V.S., Kuksin A.Yu., Mayer A.E., Yanilkin A.V. Plastic deformation under high-rate loading: the multiscale approach. *Physics of the Solid State*. 2010;52(7):1386–1396. https://doi.org/10.1134/S1063783410070115
19. Zhao Sh., Osetsky Yu.N., Zhang Y. Atomic-scale dynamics of edge dislocations in Ni and concentrated solid solution NiFe alloys. *Journal of Alloys and Compounds*. 2017;701: 1003–1008. https://doi.org/10.1016/j.jallcom.2017.01.165
20. Rodney D., Ventelon L., Clouet E., Pizzagalli L., Willaime F. Ab initio modeling of dislocation core properties in metals and semiconductors. *Acta Materialia*. 2017;124:633–659. https://doi.org/10.1016/j.actamat.2016.09.049
21. Hunter A., Beyerlein I.J., Germann T.C., Koslowski M. Influence of the stacking fault energy surface on partial dislocations in fcc metals with a three-dimensional phase field dislocations dynamics model. *Physical Review B*. 2011;84(14):144108. https://doi.org/10.1103/PhysRevB.84.144108
22. Shtremel' M.A. *Strength of Alloys. Part 1. Lattice Defects*. Moscow: Metallurgiya; 1982:280. (In Russ.).

    Штремель М.А. *Прочность сплавов. Ч. 1. Дефекты решетки*. Москва: Металлургия; 1982:280.
23. Киттель Ч. *Введение в физику твердого тела*. Москва: Наука, 1978:792.

    Kittel Ch. *Elementary Solid State Physics*. John Wiley & Sons; 1962:339.
24. Guo J., Wen B., Melnik R., Yao Sh., Li T. Molecular dynamics study on diamond nanowires mechanical properties: Strain rate, temperature and size dependent effects. *Diamond and Related Materials*. 2011;20(4):551–555. https://doi.org/10.1016/j.diamond.2011.02.016
25. Tachibana T., Furuya H., Koizumi M. Dependence on strain rate and temperature shown by yield stress of uranium dioxide. *Journal of Nuclear Science and Technology*. 1976;13(9):497–502. https://doi.org/10.1080/18811248.1976.9734063
26. Cereceda D., Diehl M., Roters F., Raabe D., Perlado J.M., Marian J. Unraveling the temperature dependence of the yield strength in single-crystal tungsten using atomistically-informed crystal plasticity calculations. *International Journal of Plasticity*. 2016;78:242–265. https://doi.org/10.1016/j.ijplas.2015.09.002

## Information about the Authors / Сведения об авторах

***Irina V. Zorya,*** *Dr. Sci. (Phys.-Math.), Assist. Prof., Head of the Chair of Heat-Gas-Water Supply, Water Disposal and Ventilation,* Siberian State Industrial University
***ORCID:*** 0000-0001-5748-813X
***E-mail:*** zorya.i@mail.ru

***Gennadii M. Poletaev,*** *Dr. Sci. (Phys.-Math.), Prof., Head of the Chair of Advanced Mathematics,* Polzunov Altai State Technical University
***ORCID:*** 0000-0002-5252-2455
***E-mail:*** gmpoletaev@mail.ru

***Roman Yu. Rakitin,*** *Cand. Sci. (Phys.-Math.), Assist. Prof., Director of College,* Altai State University
***ORCID:*** 0000-0002-6341-2761
***E-mail:*** movehell@gmail.ru

***Ирина Васильевна Зоря,*** *д.ф.-м.н., доцент, заведующий кафедрой теплогазоводоснабжения, водоотведения и вентиляции,* Сибирский государственный индустриальный университет
***ORCID:*** 0000-0001-5748-813X
***E-mail:*** zorya.i@mail.ru

***Геннадий Михайлович Полетаев,*** *д.ф.-м.н., профессор, заведующий кафедрой высшей математики,* Алтайский государственный технический университет им. И.И. Ползунова
***ORCID:*** 0000-0002-5252-2455
***E-mail:*** gmpoletaev@mail.ru

***Роман Юрьевич Ракитин,*** *к.ф.-м.н., доцент, директор колледжа,* Алтайский государственный университет
***ORCID:*** 0000-0002-6341-2761
***E-mail:*** movehell@gmail.ru

## Contribution of the Authors / Вклад авторов

***I. V. Zorya*** – problem statement, analysis of literary sources, processing of results, writing the main text.
***G. M. Poletaev*** – problem statement, development of a computer model, analysis of literary sources, processing of results, editing the final version of the article.
***R. Yu. Rakitin*** – creating a computer model, performing calculations, obtaining results, obtaining drawings and graphs.

***И. В. Зоря*** – постановка задачи, анализ литературных источников, обработка результатов, написание основного текста статьи.
***Г. М. Полетаев*** – постановка задачи, разработка компьютерной модели, анализ литературных источников, обработка результатов, редактирование финальной версии статьи.
***Р. Ю. Ракитин*** – создание компьютерной модели, проведение расчетов и получение результатов, получение рисунков и графиков для статьи.

Received 06.02.2023
Revised 27.02.2023
Accepted 20.07.2023

Поступила в редакцию 06.02.2023
После доработки 27.02.2023
Принята к публикации 20.07.2023

**МАТЕРИАЛОВЕДЕНИЕ / MATERIALS SCIENCE**

**УДК** 621.373.826:621.78+620.186+620.178.162.4
**DOI** 10.17073/0368-0797-2023-6-688-695



*Оригинальная статья*
*Original article*

# Структура и износные характеристики чугуна после лазерной модификации поверхности

**С. И. Яресько, Г. В. Гусева, В. И. Щербаков, П. В. Казакевич**

**Самарский филиал Физического института им. П.Н. Лебедева РАН** (Россия, 443011, Самара, ул. Ново-Садовая, 221)

yarsi54@gmail.com

***Аннотация***. Представлены результаты исследований макро- и микроструктуры легированного хромованадиевого чугуна после лазерной обработки (ЛО) на воздухе с использованием непрерывного лазерного источника при вариации его мощности от 60 до 100 Вт и скорости сканирования лазерного луча, изменяющейся от 5 до 17 мм/с. Методами металлографии и дюрометрии определены состав и структура зон лазерного воздействия (ЗЛВ). Лазерная обработка с незначительным оплавлением поверхности приводит к существенному росту микротвердости в ЗЛВ. В поверхностном слое ЗЛВ в зоне оплавления основной структурой является мартенсит, а в зоне закалки превалирует ледебуритная структура. Для исследованных режимов ЛО глубина ЗЛВ составляет 220 – 310 мкм. При этом микротвердость более чем в 2,5 – 4,2 раза больше микротвердости основного металла (820 $HV_{0,1}$), что является существенным фактором повышения износостойкости материала. При лазерной обработке без оплавления поверхности существенных изменений структуры не установлено. Для выявления роли ЛО в изнашивании чугуна проводили испытания на трение скольжения по схеме «диск – палец» при давлении в зоне контакта 12,5 МПа и скорости вращения индентора 580 об/мин. По данным испытаний установлено значительное уменьшение линейного износа и интенсивности изнашивания после ЛО с оплавлением поверхности. Интенсивность изнашивания уменьшается более чем в 100 раз, а линейный износ более чем в 50 раз. Характеристики поверхности ЗЛВ обуславливают уменьшение коэффициента трения на 30 % по сравнению с необработанной поверхностью.

***Ключевые слова:*** лазерная обработка, чугун, зона лазерного воздействия, металлография, микротвердость, трибологические испытания, интенсивность изнашивания

***Для цитирования:*** Яресько С.И., Гусева Г.В., Щербаков В.И., Казакевич П.В. Структура и износные характеристики чугуна после лазерной модификации поверхности. *Известия вузов. Черная металлургия*. 2023;66(6):688–695. https://doi.org/10.17073/0368-0797-2023-6-688-695

# Structure and wear characteristics of cast iron after laser surface modification

**S. I. Yares'ko, G. V. Guseva, V. I. Shcherbakov, P. V. Kazakevich**

**Samara Branch of Lebedev Physical Institute, Russian Academy of Sciences** (221 Novo-Sadovaya Str., Samara 443011, Russian Federation)

yarsi54@gmail.com

***Abstract***. The paper presents the results of studies of macro- and microstructure of alloyed chromium-vanadium cast iron after laser treatment (LT) in air using a continuous laser source with a variation in its power from 60 to 100 W and scanning speed of the laser beam varying from 5 to 17 mm/s. Metallography and durometry methods were used to determine composition and structure of the laser exposure zones (LEZ). It is shown that LT with a slight melting of the surface leads to a significant increase in microhardness in LEZ. In this case, martensite is the main structure in the near-surface layer of LEZ in the melting zone, and ledeburite structure prevails in the quenching zone. For the studied LT modes, LEZ depth is 220 – 310 μm. At the same time, microhardness is more than 2.5 – 4.2 times higher than microhardness of the base metal and reaches 820 $HV_{0.1}$, that is a significant factor in increasing the wear resistance of the material. On the contrary, no significant structural changes were found in the case of LT without melting the surface. In order to identify the role of LT in wear of cast iron, sliding friction tests were carried out according to the "disk – finger" scheme at a pressure in the contact zone of 12.5 MPa and indenter rotation speed of 580 rpm. According to the test data, a significant decrease in linear wear and the wear intensity after the surface melting was found. The wear intensity is reduced by more than 100 times, and linear wear – by more than 50 times. The characteristics of LEZ surface cause a decrease in the friction coefficient by 30 % relative to the untreated surface.

***Keywords:*** laser treatment, cast iron, laser exposure zone, metallography, microhardness, tribo-tests, wear intensity

***For citation:*** Yares'ko S.I., Guseva G.V., Shcherbakov V.I., Kazakevich P.V. Structure and wear characteristics of cast iron after laser surface modification. *Izvestiya. Ferrous Metallurgy*. 2023;66(6):688–695. https://doi.org/10.17073/0368-0797-2023-6-688-695

## Введение

Чугуны как конструкционный материал имеют широкий спектр применения (станкостроение, автомобилестроение, машиностроение, судостроение, тракторостроение и ряд других отраслей промышленности). В автотракторостроении основная номенклатура продукции из чугуна – это детали двигателей внутреннего сгорания [1; 2], элементы тормозных систем [3 – 5], корпусные детали различного назначения; в станкостроении – это корпусные детали высокой прочности, жесткости и износостойкости (станины мощных станков и механизмов) [6; 7]; в нефтегазовой промышленности высокопрочные чугуны нашли применение при строительстве нефтепроводов для решения проблемы защиты от коррозии [8]. Известно применение чугунов в инструментальном производстве как при изготовлении режущего инструмента [9; 10], так и при изготовлении вытяжных штампов, применяемых при производстве деталей автомобилей [11; 12].

Из чугуна производят отливки, работающие на износ (шестерни, подшипники, колеса, тормозные колодки, направляющие станков, суппорты, цилиндры или втулки двигателей, поршни и поршневые кольца, валки, катки и другое). Износ этих отливок достаточно велик. Например, износ направляющих токарных станков может достигать 0,2 мм в год [6; 7]. При анализе работоспособности этих изделий особое внимание следует уделять повышению износостойкости наиболее дорогих и трудно сменяемых частей сопрягаемых пар машины, иногда за счет большого износа более дешевых и легче сменяемых частей (подшипники, поршневые кольца и другие), но при этом следует иметь в виду, что большой износ одной детали очень часто вызывает повышенный износ и контртела. Исключительно важно повышение износостойкости деталей из чугуна, используемых в конструкции прецизионных станков и приборов, так как даже сравнительно малый износ делает их непригодными для дальнейшего применения.

Для повышения служебных характеристик деталей из чугунов, отличающихся как по структуре, так и по назначению, используют нанесение покрытий [5; 11], поверхностную закалку токами высокой частоты (ТВЧ) [6], методы поверхностного пластического деформирования [6; 13] и химико-термической обработки (ХТО) [14 – 16], лазерную закалку [1; 2; 6; 17 – 21], плазменную закалку [11; 12; 22 – 24], газотермическое напыление [5; 7; 25; 26] и другие методы.

Лазерная обработка, как и другие методы модификации поверхности, оказывает заметное влияние на трибологические характеристики чугунов разных марок. В частности, при лазерной обработке (ЛО) серого чугуна с использованием 5 кВт $CO_2$ лазера была получена глубина упрочнения до 300 мкм при микротвердости от 800 до 950 $HV_{0,1}$, превышающей микротвердость исходного материала почти в три раза. При этом срок службы упрочненного слоя почти в два раза больше, чем у необработанного, что непосредственно связано с образованием мартенситной микроструктуры [4]. Аналогичная структура с неизменными графитовыми конкрециями образуется при ЛО без оплавления ковкого чугуна на глубине до 150 мкм. В этом случае микротвердость достигает значений 800 HV при мощности излучения до 780 Вт [17]. Уменьшение износных параметров характерно и для ЛО серого чугуна импульсным лазерным излучением. Образующаяся мартенситная структура в зоне плавления при плотности энергии 10 – 12 Дж/мм$^2$ приводит к уменьшению примерно на 78 % потери массы и скорости износа образца после ЛО излучением Nd:YAG лазера [20]. Увеличение твердости в зоне оплавления до 1025 HV почти в шесть раз уменьшает потерю массы для серого чугуна марки СЧ20, снижает скорость износа до 78 % [2] при ЛО излучением волоконного лазера мощностью 5 кВт с длительностью импульса до 1,5 нс и диаметре пятна до 4,4 мм. Лазерная обработка высокопрочного чугуна марки ВЧ60-2 излучением непрерывного $CO_2$-лазера (мощность излучения до 2,5 кВт, скорость сканирования луча до 2000 мм/мин) в 2,1 – 3,3 раза повышает его сопротивление абразивному изнашиванию [19]. Повышение износостойкости закаленного чугуна связано с наличием в зоне лазерного воздействия (ЗЛВ) участков с термостойкой ледебуритной структурой и с положительным влиянием на износостойкость метастабильного остаточного аустенита, обладающего повышенной устойчивостью к распаду при нагреве.

Таким образом, после упрочняющей ЛО чугунов наблюдается повышение их износных и прочностных характеристик. Однако выбор режимов обработки должен осуществляться индивидуально с учетом особенностей эксплуатации изделий и структуры упрочняемого материала.

Целью настоящей работы является экспериментальное определение рациональных режимов поверхностной упрочняющей ЛО хромованадиевого чугуна, используемого для изготовления пуансонов и матриц формообразующих штампов холодной штамповки, изучение их влияния на структуру чугуна в зоне ЛО и трибологические характеристики поверхности ЗЛВ.

## Материалы и методы исследования

В качестве материала для исследований был выбран хромованадиевый чугун марки ХФ следующего состава, % (по массе): 2,90 – 3,10 C; 0,60 – 0,90 Mn; 1,60 – 1,80 Si; менее 0,12 P; 0,12 S; 0,30 – 0,50 Cr; 0,20 – 0,30 V; 0,05 – 10 Ti; остальное – железо. В соответствии со стандартом СТО 06300.0008 – 2021 чугун марки ХФ является одним из самых применяемых материалов для изготовления пуансонов и матриц формообразующих штампов холодной штамповки на АО «АВТОВАЗ».

Лазерную обработку образцов из чугуна марки ХФ размерами 20×20×4 мм проводили с использованием иттербиевого непрерывного волоконного лазера ИЛМ-100-В с длиной волны 1,07 мкм. В экспериментах мощность лазерного излучения ($P$) варьировалась от 60 до 90 Вт, а скорость обработки ($V$) – от 5 до 17 мм/с. Для трибологических испытаний обрабатывали всю поверхность образцов по следующей схеме. Лазерный луч перемещался параллельно одной из сторон, формируя полосы шириной 1,6 – 1,8 мм; расстояние между центрами полос $\Delta l = 0{,}4$ мм, расфокусировка $\Delta F = 40$ мм (обработка за фокусом). Лазерную обработку осуществляли по двум режимам: без оплавления поверхности (при $P = 60$ Вт, $V = 5{,}7$ мм/с) и с оплавлением поверхности материала (при $P = 80$ Вт, $V = 5{,}7$ мм/с).

Микроструктурный анализ выполняли на поперечных шлифах. Наклепанный слой снимали трехкратным чередованием полировки алмазной пастой и травления 4 %-ным раствором $HNO_3$ в этиловом спирте. Для выявления структуры основного металла и ЗЛВ использовали указанный выше реактив. Измерение микротвердости проводили с помощью твердомера ПТМ-3 при нагрузке 0,98 Н; металлографический анализ – с помощью оптического микроскопа NEOPHOT-30 (Carl Zeiss).

Испытания на трение скольжения проводили по схеме «диск – палец». При испытаниях в качестве контртела «палец» был использован полый цилиндр диаметром 6 мм с толщиной стенки 1 мм, изготовленный из закаленной стали марки 40Х. Вращение цилиндра со скоростью 580 об/мин осуществляли без смазывающей жидкости по плоскости образца для двух типов контактных пар (без ЛО поверхности образца и после ЛО). Во всех случаях давление в зоне контакта составляло 12,5 МПа.

В процессе испытаний автоматизированный сбор данных и мониторинг информации с датчиков нормальной нагрузки, момента трения и температуры фрикционного разогрева испытываемой пары трения проводили с помощью многоканальной быстродействующей микроконтроллерной системы сбора данных АЦП E14-140 фирмы L-Card. Для получения и обработки данных, поступающих с АЦП, использовали программный пакет PowerGraph.

После испытаний оценку линейного износа проводили визуально с помощью оптического микроскопа или измерителя шероховатости TR200 (компания Time Group Inc., Китай).

## Результаты и их обсуждение

В исходном состоянии чугун марки ХФ имеет феррито-перлитную структуру, цементит в основном расположен по границам перлитных колоний, форма графитных включений пластинчатая, микротвердость примерно 197 – 296 $HV_{0,1}$.

Внешний вид ЗЛВ на поперечном шлифе чугуна марки ХФ после лазерной обработки с оплавлением поверхности приведен на рис. 1, *а*. В зоне оплавления основной структурой является мартенсит (рис. 1, *б*). В верхней части зоны оплавления шириной около 40 – 50 мкм карбиды растворены, графитовая составляющая отсутствует. Граница между зонами оплавления и закалки неравномерная (рис. 1, *б*), а сама зона закалки из твердой фазы отличается неоднородной структурой. При нагреве ферритная матрица около графитных включений насыщается углеродом, в результате чего температура ее плавления снижается. По этой же причине в верхней части зоны закалки область вокруг феррита оплавляется и насыщается углеродом. Степень насыщения на различном расстоянии от графита отличается, поэтому около графита образуется светлый слой ледебурита (рис. 1, *б*). Эта структура является превалирующей при удалении от поверхности ЗЛВ, наблюдаются

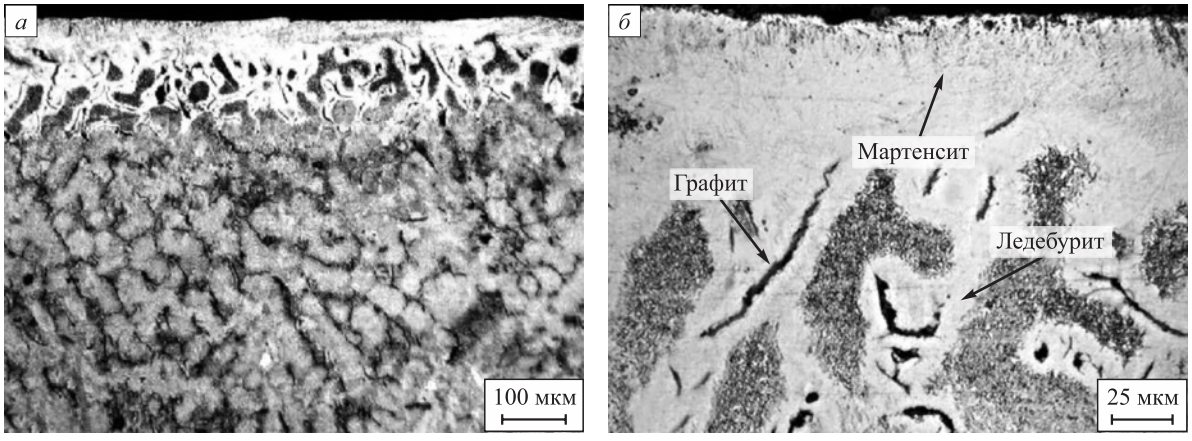


Рис. 1. Микроструктура чугуна марки ХФ после ЛО с оплавлением поверхности:
*а* – общий вид ЗЛВ при обработке с оплавлением поверхности; *б* – граница зоны оплавления и зоны закалки

Fig. 1. Microstructure of KhF cast iron after laser treatment (LT) with surface melting:
*a* – general view of laser exposure zones (LEZ); *б* – boundary between melting and quenching zones

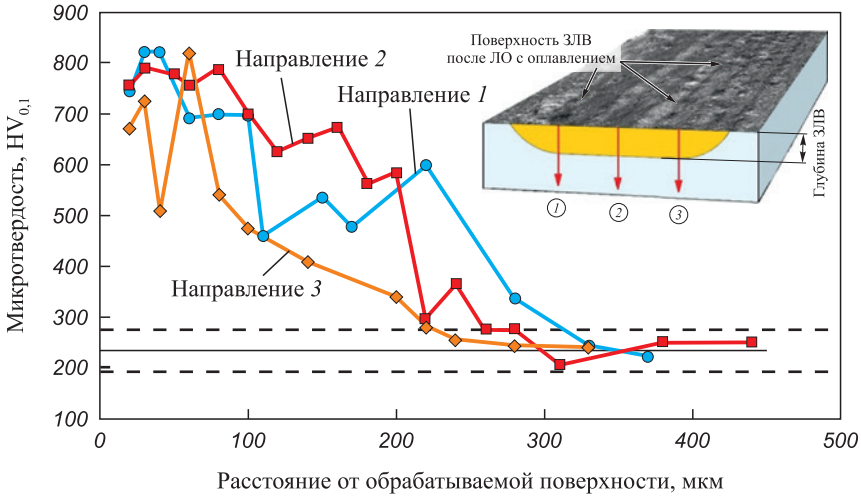


Рис. 2. Изменение микротвердости по глубине ЗЛВ, полученной при обработке чугуна марки ХФ с оплавлением поверхности (на врезке показана схема измерения микротвердости после ЛО)

Fig. 2. Change in microhardness along the depth of LEZ obtained by treatment of KhF cast iron with surface melting (the inset shows a scheme for measuring microhardness after laser treatment)

следы феррита и пластинчатый графит. На границе зоны закалки с основным металлом в структуре чугуна превалирует перлитная составляющая.

Микротвердость по глубине ЗЛВ с оплавлением была измерена по трем направлениям, находящимся на разных расстояниях от центра полосы обработки. Схема измерения показана на врезке к рис. 2. Ширина дорожки обработки на поверхности образца 3,96 мм. Глубина зоны упрочнения с модифицированной структурой при ЛО с оплавлением составила 220 – 310 мкм. Микротвердость мартенситной структуры в зоне оплавления достигает примерно 750 – 820 $HV_{0,1}$ (рис. 2), что в 2,5 – 4,2 раза превышает микротвердость исходной структуры, которая равна 234 ± 41 $HV_{0,1}$ (рис. 2, штриховая линия).

После лазерной обработки без оплавления поверхности образца чугуна марки ХФ структура ЗЛВ на поперечном шлифе в целом подобна структуре чугуна в исходном состоянии. Отличия заключаются в том, что в отдельных участках зоны при ЛО без оплавления поверхности наблюдаются сгруппированные распределенные по ЗЛВ локальные участки карбидной фазы, равномерно расположенные включения пластинчатого графита.

Ближе к поверхности ЗЛВ находятся участки бейнита, с ростом глубины в структуре превалирует ледебуритная составляющая. Измерение микротвердости проводили по той же самой схеме, что и при ЛО с оплавлением поверхности. Ширина зоны измерения 4,38 мм. Микротвердость по глубине ЗЛВ, полученной при обработке чугуна марки ХФ без оплавления поверхности, находится практически на уровне микротвердости исходного материала, только в отдельных очень узких зонах перекрытия лазерных дорожек, где наблюдали незначительное оплавление поверхности, микротвердость превышает исходную и находится на уровне примерно 500 $HV_{0,1}$.

Лазерная обработка хромованадиевого чугуна марки ХФ излучением непрерывного волоконного лазера в режиме с оплавлением поверхности приводит к образованию структур в ЗЛВ, обеспечивающих превышение микротвердости над исходным значением в 2,5 – 4,2 раза при глубине зоны упрочнения 220 – 310 мкм. В то же время при лазерной обработке без оплавления поверхности существенных изменений в ЗЛВ не наблюдается, микротвердость остается на уровне микротвердости исходного материала.

Лазерную обработку поверхности образцов чугуна, предназначенных для проведения трибологических испытаний, проводили как на режиме, при котором обеспечивалось оплавление поверхности, так и на режиме, когда оплавления поверхности ЗЛВ не достигалось.

Было проведено несколько серий трибологических испытаний образцов чугуна при различном времени испытаний. В первой серии опытов после ЛО время испытаний составляло 60 мин, а время испытаний образца в исходном состоянии – 25 мин. При уменьшении времени испытаний износ образцов чугуна без ЛО превышал значение 3,8 мм, равное толщине образца. Во второй серии испытаний образцов после лазерной обработки время испытаний было сокращено до 30 мин, а образца в исходном состоянии – до 15 мин.

Во время испытаний соответствующими датчиками непосредственно измеряли момент трения $M$ (рис. 3, кривая *3*), нормальную нагрузку $N$ (рис. 3, кривая *2*) и температуру $T$ фрикционного разогрева (рис. 3, кривая *1*). Типичные зависимости параметров, контролируемых во время проведения испытаний для времени испытаний 60 мин, приведены на рис. 3 (на врезках

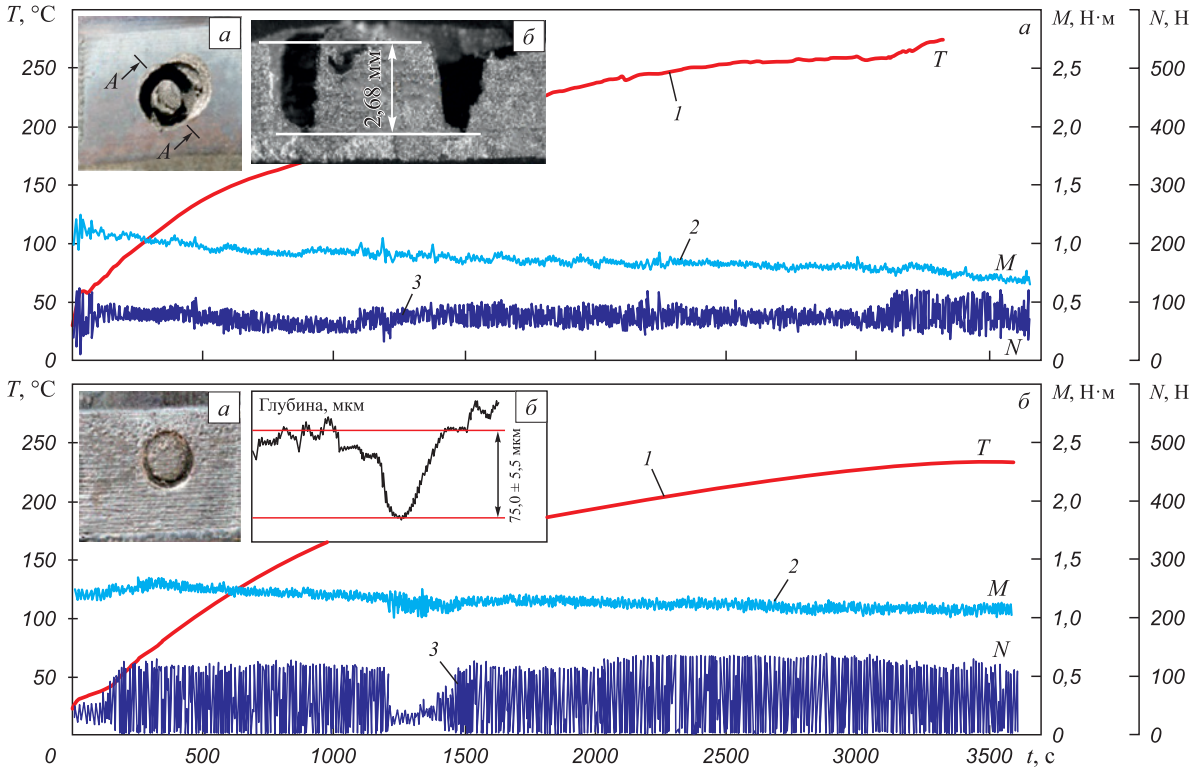


Рис. 3. Изменение параметров, контролируемых при проведении трибологических испытаний:
*а* – ЛО без оплавления; *б* – ЛО с оплавлением

Fig. 3. Change of the parameters controlled during tribotests:
*a* – laser treatment without reflow; *б* – laser treatment with reflow

показан вид поверхности образцов чугуна марки ХФ после окончания процесса трения и профиль лунки износа). Измерение глубины лунки износа образцов после ЛО без оплавления поверхности проводили после приготовления среза по диаметру зоны контакта (сечение *А – А* на врезке *а* к рис. 3, *а*) и наблюдения профиля лунки износа с помощью оптического микроскопа при увеличении 10 крат (врезка *б* к рис. 3, *а*). Измерение линейного износа образцов после ЛО с оплавлением поверхности осуществляли профилометрированием не менее чем в трех местах по зоне контакта, полученные данные обрабатывали методами математической статистики. Фрагмент профиля лунки износа после трибологических испытаний образца, обработанного с оплавлением поверхности, представлен на врезке *б* к рис. 3, *б*.

Кроме измерения линейного износа, равного глубине канавки в месте касания «пальца» (полого цилиндра (врезка *а* к рис. 3)) и поверхности исследуемого образца, определяли интенсивность изнашивания как отношение линейного износа к пути трения. За путь трения принимали относительное перемещение трущихся поверхностей в течение всего цикла измерений. Линейный износ, интенсивность изнашивания и пути трения приведены в таблице.

Силу трения в месте контакта рассчитывали из условия равенства моментов трения в местах приложения силы трения и измерения момента трения. Причем последнее из конструктивных соображений находилось на расстоянии 25 мм от центра вращения «пальца» по поверхности образца. Учитывая геометрические размеры контртела и пространственное расположение места измерения момента трения в эксперименте, получаем

$$F_{\text{тр}} = \frac{M_{\text{тр}}}{2{,}5} \cdot 10^3 \text{ Н·м.}$$

Расчетные значения силы трения для каждого эксперимента приведены в таблице (здесь величина определяется экспериментально).

Анализируя поведение момента трения, можно предположить, что ЛО изменяет характер изнашивания контактирующих поверхностей. В ряде случаев, например, при испытании образцов после ЛО с оплавлением поверхности наблюдается существенное (более чем в три раза) увеличение среднеквадратического отклонения величины (СКО) момента трения, по сравнению с величиной СКО для испытаний образцов без оплавления поверхности (см. таблицу) при уменьшении среднего момента трения. Можно предположить, что наблюдаемое явление связано с истиранием гребешков поверхности ЗЛВ, образующихся при оплавлении поверхности, и попаданием продуктов износа повышенной твердости в зону трибологического контакта.

**Результаты трибологических испытаний**

**Results of tribological tests**

| Состояние поверхности | Время испытаний, мин | *N*, Н | *T*, °С (max) | *M*, Н·м | $F_{тр}$, Н | Линейный износ, мкм | Путь трения, м | Интенсивность изнашивания, мкм/м | Коэффициент трения |
|---|---|---|---|---|---|---|---|---|---|
| С оплавлением | 60 | 228,5 ± 13,1 | 233,3 | 0,277 ± 0,162 | 110,7 | 74,98 | 546,36 | 0,14 | 0,48 |
| Без оплавления | 60 | 173,8 ± 19,4 | 280,9 | 0,364 ± 0,047 | 145,5 | 2680 | 546,36 | 4,94 | 0,84 |
| Исходное | 25 | 211,4 ± 22,3 | 203,7 | 0,365 ± 0,117 | 145,9 | 3800 | 227,65 | 16,69 | 0,69 |
| С оплавлением | 30 | 214,8 ± 13,7 | 237,5 | 0,321 ± 0,086 | 128,5 | 92,33 | 273,18 | 0,34 | 0,60 |
| Без оплавления | 30 | 207,7 ± 22,5 | 238,1 | 0,329 ± 0,058 | 131,6 | 700 | 273,18 | 2,56 | 0,63 |
| Исходное | 15 | 178,0 ± 16,1 | 154,2 | 0,317 ± 0,047 | 127,0 | 2500 | 136,59 | 18,30 | 0,71 |

Вследствие абразивного изнашивания испытываемых образцов наблюдался значительный разброс значений момента трения (силы трения и коэффициента трения). Наблюдаемое высокое сопротивление абразивному изнашиванию при ЛО с оплавлением поверхности связано с наличием в тонком поверхностном слое структуры мартенсита, а с увеличением глубины ЗЛВ – участков с ледебуритной структурой, имеющих повышенную твердость. Положительное влияние на износостойкость оказывает остаточный аустенит вследствие его повышенной устойчивости к распаду при нагреве и возможности перехода в мартенсит деформации при трении.

Структурные изменения после ЛО с оплавлением по данным трибологических испытаний приводят к уменьшению линейного износа более чем в 50 раз, а интенсивности изнашивания – более чем в 100 раз, коэффициент трения при этом снижается почти на 30 %. После ЛО без оплавления уменьшение указанных трибологических характеристик существенно меньше: в 1,42 раза и 3,4 раза соответственно.

## Выводы

Экспериментально показано, что обработка поверхности хромованадиевого чугуна марки ХФ непрерывным лазерным излучением волоконного лазера различного уровня мощности приводит к существенным изменениям в поверхностном слое материала. При ЛО с оплавлением поверхности микротвердость в ЗЛВ возрастает в 2,5 – 4,2 раза при глубине упрочненного слоя 220 – 310 мкм, что является существенным фактором повышения износных характеристик материала. При лазерной обработке без оплавления поверхности наблюдается локальное увеличение микротвердости до 1,9 – 2,7 раза при глубине ЗЛВ 50 – 120 мкм. В результате испытаний на трение скольжения по схеме «диск – палец» установлено, что структурные изменения в ЗЛВ после лазерной обработки непрерывным излучением поверхности контакта приводят к снижению линейного износа и интенсивности изнашивания. После ЛО с оплавлением поверхности линейный износ уменьшается более чем в 50 раз, а интенсивность изнашивания более чем в 100 раз, при этом коэффициент трения снижается почти на 30 %. После ЛО без оплавления поверхности изменение трибохарактеристик менее выражено и составляет 1,42 раза и 3,4 раза соответственно.

## Список литературы / References

1. Кулешов И.И., Ходаковский В.М. Повышение эффективности лазерного упрочнения чугунных деталей судовых энергетических установок. *Вестник государственного университета морского и речного флота им. адмирала С.О. Макарова*. 2017;9(4):814–828.
Kuleshov I.I., Khodakovskii V.M. Improvement efficiency of laser strengthening of iron details ship's power plants. *Vestnik gosudarstvennogo universiteta morskogo i rechnogo flota im. admirala S.O. Makarova*. 2017;9(4):814–828. (In Russ.).
2. Ali A., Khalid E.A., Alwan A.S., Jaddoa A. Effect of fibre laser surface treatment on wear resistance of gray cast iron ASTM A48. *Journal of Mechanical Engineering Research and Developments*. 2021;44(2):141–149.
3. Gigan G.Le, Ekh M., Vernersson T., Lundén R. Modelling of grey cast iron for application to brake discs for heavy vehicles. *Proceedings of the Institution of Mechanical Engineers, Part D: Journal of Automobile Engineering*. 2017;231(1):35–49. https://doi.org/10.1177/0954407016632090
4. Hwang J.-H., Kim D.-Y., Youn J.-G., Lee Y.-S. Laser surface hardening of gray cast iron used for piston ring. *Journal of Materials Engineering and Performance*. 2002;11(3):294–300. https://doi.org/10.1361/105994902770344105
5. Aranke O., Algenaid W., Awe S., Joshi Sh. Coatings for automotive gray cast iron brake discs: A review. *Coatings*. 2019;9(9):552. https://doi.org/10.3390/coatings9090552
6. Минаков А.П., Юшкевич Н.М., Камчицкая И.Д., Ильюшина Е.В., Зайцев Д.Л. Анализ способов повышения износостойкости направляющих станин металлорежущих станков. *Вестник Белорусско-Российского Универ-*

*cumeta*. 2016;(3(52)):40–50.
https://doi.org/10.53078/20778481_2016_3_40

Minakov A.P., Yushkevich N.M., Kamchitskaya I.D., Il'yushina E.V., Zaitsev D.L. Analysis of methods to improve wear resistance of bedways of machine tools. *Vestnik Belorussko-Rossiiskogo Universiteta*. 2016;(3(52)):40–50. (In Russ.). https://doi.org/10.53078/20778481_2016_3_40

7. Кадырметов А.М., Симонова Ю.Э. Особенности применения газотермических и плазменных методов для получения функциональных покрытий. *Воронежский научно-технический вестник*. 2021;1(1(35)):25–32.
https://doi.org/10.34220/2311-8873-2022-25-32

Kadyrmetov A.M., Simonova Yu.E. Features of application of gas-thermal and plasma methods for obtaining functional coatings. *Voronezh Scientific-Technical Bulletin*. 2021;1(1(35)):25–32. (In Russ.).
https://doi.org/10.34220/2311-8873-2022-25-32

8. Антонов Б.Ю., Костин С.Н. Трубы из высокопрочного чугуна в нефтегазовой отрасли. *Нефть. Газ. Новации*. 2018;(5):44–46.

Antonov B.Yu., Kostin S.N. Ductile cast-iron pipes in oil and gas industry. *Neft'. Gaz. Novatsii*. 2018;(5):44–46. (In Russ.).

9. Афанасьев В.К., Кольба А.В. Разработка инструмента из белого чугуна без применения специального легирования. *Металлообработка*. 2011;(2(62)):41–48.

Afanas'ev V.K., Kol'ba A.V. Development of a tool made of white cast iron without special alloying. *Metalloobrabotka*. 2011;(2(62)):41–48. (In Russ.).

10. Алифанов А.В. Применение горячедеформированного хромованадиевого белого чугуна для получения дереворежущего инструмента. *Литье и металлургия*. 2012;(3(67)):157–161.

Alifanov A.V. The use of not-chrome vanadium white iron for wodcutting tools. *Lit'e i metallurgiya*. 2012;(3(67)):157–161. (In Russ.).

11. Аманов С.Р., Кислов А.В., Юков А.В. Влияние поверхностной обработки штампов на коэффициент трения при вытяжке. *Кузнечно-штамповое производство. Обработка материалов давлением*. 2003;(1):35–39.

Amanov S.R., Kislov A.V., Yukov A.V. Effect of stamps surface treatment on friction coefficient at drawing. *Kuznechno-shtampovoe proizvodstvo. Obrabotka materialov davleniem*. 2003;(1):35–39. (In Russ.).

12. Васькин К.Я., Блинов А.А., Блинов А.В. Плазменная закалка чугуна ХФ. *Технические науки – от теории к практике*. 2017;(4(64)):33–37.

Vas'kin K.Ya., Blinov A.A., Blinov A.V. Plasma hardening of HF cast iron. *Tekhnicheskie nauki – ot teorii k praktike*. 2017;(4(64)):33–37. (In Russ.).

13. Silva K.H.S., Carneiro J.R., Coelho R.S., Pinto H., Brito P. Influence of shot peening on residual stresses and tribological behavior of cast and austempered ductile iron. *Wear*. 2019;440–441:203099.
http://doi.org/10.1016/j.wear.2019.203099

14. Веселовский А.А., Немцев А.Е. Способ повышения работоспособности мелкомодульных зубчатых колес из высокопрочного чугуна. *Вестник Курганской ГСХА*. 2022;1(41):59–66.
https://doi.org/10.52463/22274227_2022_41_59

Veselovskii A.A., Nemtsev A.E. Method of improving the performance of small-module gears made of high-strength cast iron. *Vestnik Kurganskoi GSKhA*. 2022;(1(41)):59–66. (In Russ.). https://doi.org/10.52463/22274227_2022_41_59

15. Zhang D., Li Y., Du X., Fan H., Gao F. Microstructure and tribological performance of boride layers on ductile cast iron under dry sliding conditions. *Engineering Failure Analysis*. 2022;134:106080.
https://doi.org/10.1016/j.engfailanal.2022.106080

16. Kondakci E., Solak N. The effect of microstructure on nitriding mechanism of cast iron. *International Journal of Metalcasting*. 202;14(4):1033–1040.
https://doi.org/10.1007/s40962-019-00404-2

17. Zammit A., Abela S., Betts J.C., Grech M. Discrete laser spot hardening of austempered ductile iron. *Surface and Coatings Technology*. 2017;331:143–152.
https://doi.org/10.1016/j.surfcoat.2017.10.054

18. Němeček S. Surface of cast iron after laser hardening. *Advanced Materials Research*. 2013;685:92–96.
https://doi.org/10.4028/www.scientific.net/AMR.685.92

19. Макаров А.В., Малыгина И.Ю., Осинцева А.Л. Влияние лазерной обработки на структуру, износостойкость и усталостные свойства высокопрочного чугуна. *Физика и химия обработки материалов*. 2006;(4):46–55.

Makarov A.V., Malygina I.Yu., Osintseva A.L. The effect of laser treatment on the structure, wear resistance and fatigue properties of high-strength cast iron. *Fizika i khimiya obrabotki materialov*. 2006;(4):46–55. (In Russ.).

20. Aziz S.S., Alwan A.S., Abed K.A. Influence of Nd-YAG laser beam on microstructure and wear characteristics of gray cast iron. *Journal of Biochemical and Cellure Archives*. 2019;19(1):1587–1592.

21. Catalán N., Ramos-Moore E., Boccardo A., Celentano D. Surface laser treatment of cast irons: A review. *Metals*. 2022;12(4):562. https://doi.org/10.3390/met12040562

22. Самотугина Ю.С. Технологические особенности локального упрочнения высокопрочного чугуна. *Автоматическая сварка*. 2005;(5):47–50.

Samotugina Yu.S. Technological features of local hardening of high-strength cast iron. *Avtomaticheskaya svarka*. 2005;(5):47–50. (In Russ.).

23. Pan W.X., Meng X., Li G., Fei Q.X., Wu C.K. Feasibility of laminar plasma-jet hardening of cast iron surface. *Surface & Coatings Technology*. 2005;197(2-3):345–350.
https://doi.org/10.1016/j.surfcoat.2004.06.043

24. Гречнева М.В. Краткий анализ результатов работ в области плазменного поверхностного упрочнения сталей и сплавов. *Вестник Иркутского государственного технического университета*. 2017;21(5):10–23.
https://doi.org/10.21285/1814-3520-2017-5-10-23

Grechneva M.V. A brief analysis of the results of works in the field of steel and alloy plasma surface hardening. *Proceedings of Irkutsk State Technical University*. 2017;21(5):10–23. (In Russ.). https://doi.org/10.21285/1814-3520-2017-5-10-23

25. Ksiazek M., Nejman I., Boron L. Investigation on microstructure, mechanical and wear properties of HVOF sprayed composite coatings (WC–Co+Cr) on ductile cast iron. *Materials*. 2021;14(12):3282. https://doi.org/10.3390/ma14123282

26. Балдаев Л.Х., Борисов В.Н., Вахалин В.А. *Газотермическое напыление*. Москва: Маркет ДС; 2007:344.

## Сведения об авторах / Information about the Authors

***Сергей Игоревич Яресько,*** *д.т.н., заведующий лабораторией лазерно-индуцированных процессов, старший научный сотрудник,* Самарский филиал Физического института им. П.Н. Лебедева РАН
***ORCID:*** 0000-0001-5299-886X
***E-mail:*** yarsi54@gmail.com

***Галина Валентиновна Гусева,*** *инженер-технолог,* Самарский филиал Физического института им. П.Н. Лебедева РАН
***ORCID:*** 0000-0003-4329-3619
***E-mail:*** guseva_g.v@mail.ru

***Владимир Иванович Щербаков,*** *инженер-исследователь,* Самарский филиал Физического института им. П.Н. Лебедева РАН
***ORCID:*** 0000-0003-0602-7717
***E-mail:*** vladimir@fian.smr.ru

***Павел Владимирович Казакевич,*** *к.ф.-м.н., старший научный сотрудник,* Самарский филиал Физического института им. П.Н. Лебедева РАН
***ORCID:*** 0000-0002-7816-9696
***E-mail:*** morteus@yandex.ru

***Sergei I. Yares'ko,*** *Dr. Sci. (Eng.), Head of the Laboratory of Laser-Induced Processes, Senior Researcher,* Samara Branch of Lebedev Physical Institute, Russian Academy of Sciences
***ORCID:*** 0000-0001-5299-886X
***E-mail:*** yarsi54@gmail.com

***Galina V. Guseva,*** *Engineer-Technologist,* Samara Branch of Lebedev Physical Institute, Russian Academy of Sciences
***ORCID:*** 0000-0003-4329-3619
***E-mail:*** guseva_g.v@mail.ru

***Vladimir I. Shcherbakov,*** *Research Engineer,* Samara Branch of Lebedev Physical Institute, Russian Academy of Sciences
***ORCID:*** 0000-0003-0602-7717
***E-mail:*** vladimir@fian.smr.ru

***Pavel V. Kazakevich,*** *Cand. Sci. (Phys.-Math.), Senior Researcher,* Samara Branch of Lebedev Physical Institute, Russian Academy of Sciences
***ORCID:*** 0000-0002-7816-9696
***E-mail:*** morteus@yandex.ru

## Вклад авторов / Contribution of the Authors

***С. И. Яресько*** – разработка концепции исследования, планирование исследований, обобщение и интерпретация результатов исследования, формулировка выводов, подготовка рукописи статьи.
***Г. В. Гусева*** – пробоподготовка образцов (приготовление металлографических шлифов), металлографические исследования структуры, дюрометрия, изготовление фотографий микроструктуры, работа с графическим материалом.
***В. И. Щербаков*** – проведение лазерной обработки образцов исследуемого материала, разработка методики, проведение трибоиспытаний.
***П. В. Казакевич*** – проведение сравнительного анализа результатов исследований, обработка результатов экспериментального исследования.

***S. I. Yares'ko*** – formation of the research concept, research planning, generalization and interpretation of the results, formulation of conclusions, writing the text.

***G. V. Guseva*** – sample preparation (preparation of metallographic grinds), metallographic studies of the structure, durometry, production of microstructure photographs and graphic material.

***V. I. Shcherbakov*** – conducting laser treatment of the samples, developing the methodology, conducting tribotests.

***P. V. Kazakevich*** – conducting a comparative analysis of the results, processing of the experimental results.

Поступила в редакцию 20.03.2023
После доработки 05.06.2023
Принята к публикации 11.09.2023

Received 20.03.2023
Revised 05.06.2023
Accepted 11.09.2023

MATERIALS SCIENCE / МАТЕРИАЛОВЕДЕНИЕ

**UDC** 620.173:539.4.015:622.78
**DOI** 10.17073/0368-0797-2023-6-696-704



*Original article*
*Оригинальная статья*

# Effect of structure of unfluxed burnt titanomagnetite pellets on strength under static compression

**A. N. Dmitriev[1], V. G. Smirnova[1], E. A. Vyaznikova[1], G. Yu. Vit'kina[1] ✉, A. S. Smirnov[2]**

[1] **Institute of Metallurgy, Ural Branch of the Russian Academy of Sciences** (101 Amundsen Str., Yekaterinburg 620016, Russian Federation)
[2] **E.S. Gorkunov Institute of Engineering Science, Ural Branch of the Russian Academy of Sciences** (34 Komsomolskaya Str., Yekaterinburg 620049, Russian Federation)

✉ 20procents@mail.ru

***Abstract***. Burnt pellets must retain their strength from the moment they are taken out of an induration machine until they are loaded into a blast furnace. One of the indicators of the burnt pellets' strength is the compressive strength, i.e. the ultimate force. In experiments to determine compressive strength, the main type of fracture is occurrence and development of cracks that pass through the core center of pellets (where the maximum radial tensile stresses present) or near it. The paper presents the requirements for static compression strength imposed by blast furnace production to iron ore pellets. Using an optical and scanning electron microscope equipped with an energy-dispersive microanalyzer, we analyzed the relationship of structural components and pores in the core of burnt unfluxed iron ore titanomagnetite pellets with the ultimate force under static compression. By scanning electron microscopy and X-ray spectral microanalysis, it was established that the core of pellets is a multiphase material, and its main phases are titanomagnetite, magnetite, titanohematite, hematite and aluminosilicate binder. Optical microscopy made it possible to establish the microstructure of the pellet core, which has three types of microstructures: non-oxidized core (magnetite or titanomagnetite), partially oxidized core – around (magnetite or titanomagnetite) hematite grains (titanohematite) and oxidized core (hematite and titanohematite). The main factors for obtaining pellets with an ultimate force of more than 2.5 kN/pellet according to the requirements of blast furnace production are: the number of closed macropores and the number of large grains in the core. It is shown that with an increase in the number of closed macropores and the number of large grains in the core, the ultimate force is reduced from 3.5 kN to 0.87 kN/pellet.

***Keywords:*** unfluxed pellets, titanomagnetite, magnetite, titanohematite, hematite, aluminosilicate binder, core microstructure, ultimate force, closed pores

***Acknowledgements:*** The research was supported by the State Task of the Institute of Metallurgy, Ural Branch of the Russian Academy of Sciences (122020100125-6) using the equipment of the Center for Collective Use "Ural-M" of the Institute of Metallurgy, Ural Branch of the Russian Academy of Sciences and the Research Center "Plastometry" of the E.S. Gorkunov Institute of Engineering Science, Ural Branch of the Russian Academy of Sciences.

***For citation:*** Dmitriev A.N., Smirnova V.G., Vyaznikova E.A., Vit'kina G.Yu., Smirnov A.S. Effect of structure of unfluxed burnt titanomagnetite pellets on strength under static compression. *Izvestiya. Ferrous Metallurgy*. 2023;66(6):696–704.
https://doi.org/10.17073/0368-0797-2023-6-696-704

# Влияние структуры неофлюсованных обожженных титаномагнетитовых окатышей на их прочность при статическом сжатии

**А. Н. Дмитриев[1], В. Г. Смирнова[1], Е. А. Вязникова[1], Г. Ю. Витькина[1] ✉, А. С. Смирнов[2]**

[1] **Институт металлургии Уральского отделения РАН** (Россия, 620016, Екатеринбург, ул. Амундсена, 101)
[2] **Институт машиноведения имени Э.С. Горкунова Уральского отделения РАН** (Россия, 620049, Екатеринбург, ул. Комсомольская, 34)

20procents@mail.ru

***Аннотация***. Обожженные окатыши должны сохранять прочность от момента схода с обжиговой машины до загрузки в доменную печь. Одним из показателей прочности обожженных окатышей является прочность на сжатие, то есть усилие при разрушении. При испытании окатышей на прочность на сжатие основным видом разрушения является возникновение и развитие трещин, проходящих через центр ядра окатышей (где действуют максимальные радиальные растягивающие напряжения) или в непосредственной близости от него. Представлены требования по прочности на статическое сжатие, предъявляемые при доменном производстве к железорудным окатышам. С использованием оптического и сканирующего электронного микроскопа, оснащенного энергодисперсионным микроанализатором, проанализировали связь структурных составляющих и пор в ядре обожженных неофлюсованных железорудных титаномагнетитовых окатышей с усилием разрушения при статическом сжатии. Методом сканирующей электронной микроскопии и рентгеноспектрального микроанализа установили, что ядро окатышей является многофазным материалом. Основные фазы – титаномагнетит, магнетит, титаногематит, гематит и алюмосиликатное связующее. Оптическая микроскопия позволила установить микроструктуру ядра окатышей. Возможны три типа микроструктуры: неокисленное ядро (магнетит или титаномагнетит), частично окисленное ядро – вокруг (магнетита или титаномагнетита) зерна гематита (титаногематита) и окисленное ядро (гематит и титаногематит). Определяющими факторами для получения окатышей с усилием разрушения более 2,5 кН/окатыш по требованиям доменного производства являются: количество закрытых макропор в ядре и количество зерен крупных размеров в ядре. При увеличении количества закрытых макропор и количества зерен крупных размеров в ядре снижается усилие разрушения от 3,50 до 0,87 кН/окатыш.

***Ключевые слова:*** неофлюсованные окатыши, титаномагнетит, магнетит, гематит, титаногематит, алюмосиликатное связующее, микроструктура ядра, усилие разрушения, закрытые поры

***Благодарности:*** Работа выполнена в рамках реализации Государственного задания ИМЕТ Уральского отделения РАН (№ 122020100125-6) с использованием оборудования ЦКП «Урал-М» ИМЕТ Уральского отделения РАН и ЦКП «Пластометрия» ИМАШ Уральского отделения РАН.

***Для цитирования:*** Дмитриев А.Н., Смирнова В.Г., Вязникова Е.А., Витькина Г.Ю., Смирнов А.С. Влияние структуры неофлюсованных обожженных титаномагнетитовых окатышей на их прочность при статическом сжатии. *Известия вузов. Черная металлургия*. 2023;66(6): 696–704. https://doi.org/10.17073/0368-0797-2023-6-696-704

## Introduction

Iron ore pellets are crucial raw materials for cast iron smelting in blast furnaces. In Russia and abroad, pellet production involves two interrelated processes: the formation of green pellets and their hardening. Green pellets are burned to achieve the necessary metallurgical characteristics, including compressive strength, impact resistance, abrasion resistance, and reduction strength. To enhance the pelletizing process and produce robust pellets, 0.5 – 1.0 % bentonite is added to the finely ground concentrate [1; 2]. Bentonite primarily consists of aluminum and silicon oxides with high moisture absorption capacity [3 – 5]. Bentonite is the most common binder for iron ore pellets [5 – 7]. Green pellets undergo hardening through oxidizing burning on conveyor induration machines. Papers [8 – 10] demonstrate that, in the temperature range of 200 to 1300 °C, moisture is removed, magnetite particles oxidize, magnetite or hematite grains sinter, and pores and the silicate bond are formed, leading to the enhancement of pellet strength properties. As moisture is removed, bentonite forms hard aluminosilicate interstices that contribute to the hardening process [11; 12].

Upon completion of oxidation processes, a uniform pellet structure is achieved [9]. The paper [13] highlights that the key factor influencing the intensity of the oxidation process is the pore size rather than the total porosity. The heightened oxidation characteristics of pellets can be attributed to the larger pore size of pellets with a lower specific surface area of the concentrate. This pertains to the oxidation period, during which the process is primarily governed by oxygen diffusion in the pellet pores. Additionally, when the hematite film forms on the grains, the transformation is contingent on the concentrate grain size.

Magnetite in pellets undergoes oxidation through three distinct mechanisms: complete oxidation across the entire cross-section of the pellet, complete oxidation of the pellet shell with a non-oxidized core, and partial oxidation of the pellet shell with a non-oxidized core [14]. According to findings in [15], introducing oxygen enrichment into the gas atmosphere during the continuous heating of magnetite pellets can result in oxidation throughout their volumes, effectively eliminating non-oxidized cores. The kinetics of magnetite concentrate oxidation suggest that such oxygen enrichment is particularly effective at lower temperatures. Research in [16] revealed that temperatures between 700 and 800 °C, with 21 % $O_2$, or increasing the oxygen content to 60 or 100 % at 800 °C, can achieve complete oxidation across the entire pellet cross-section. The proposed formula for calculating the oxidation reaction rate, as a function of temperature and partial pressure of oxygen in the gas phase, can be found in [17]. Additionally, in [18], observations were made of hematite whiskers growing on the oxidized surface of magnetite concentrate particles at temperatures ranging from 800 to 950 °C. The whisker thickness increased from 30 nm at 800 °C to 200 nm at 950 °C. These whiskers act as bridges between concentrate particles during pellet burning, contributing to the overall strength of the pellets.

The findings in the paper [19] illustrate that when a pellet initiates oxidation, a hematite shell forms around

the pellet while the core remains magnetite. At 1100 °C, the diffusion rate of oxygen was limited by sintering in the magnetite core, taking place before oxidation rather than by the diffusion rate of oxygen through the oxidized hematite shell, as previously asserted in the literature. The oxidation rate peaked at around 1100 °C and substantially decreased at 1200 °C due to heavy sintering in both the hematite shell and the magnetite core. Another study [20] indicated that the hardening of iron ore pellets through sintering begins at 1100 °C. The compressive strength of pellets increases with the heating temperature, although the impact of structure is not considered.

Compressive strength is a crucial metallurgical characteristic of pellets. According to state standard GOST 24765 – 81, ore mining and processing enterprises that produce pellets utilize the results of compressive strength tests to evaluate product quality. Current requirements at most pelletizing plants stipulate a static compression strength of 2.0 kN/pellet, while in blast furnace production, the static compressive strength should exceed 2.5 kN/pellet [21 – 23].

The issue of pellet integrity under mechanical impact has garnered significant attention from researchers employing analytical, numerical, and experimental approaches to predict fracture. Mathematical modeling results [24; 25] indicate that when spherical pellets undergo compression, the most unfavorable stress state occurs in the center due to severe tensile radial stresses. Consequently, the ultimate force is commonly used as a measure to assess pellet strength in compressive strength tests. A study in [26] demonstrated that in compressive strength tests, the primary type of fracture involves the initiation and propagation of cracks passing through the center of the magnetite core, where radial tensile stresses are maximal or in close proximity. Interestingly, it was observed that pellets of both 10 – 12 mm and 14 – 16 mm fractions share a common pattern: the larger the relative size of the magnetite core, the smaller the ultimate force [26].

The scientific and technical literature lacks information on how the core structure influences pellet strength.

This study aims to conduct comprehensive research on the structural components (magnetite, titanomagnetite, hematite, titanohematite, aluminosilicate) and pores in the core of burnt unfluxed titanomagnetite pellets. The primary objective is to determine the dependency of the ultimate force under static compression on the pellet core structure.

## Materials and methods

To investigate how the structure of pellets influences their compressive strength, we examined 13 burnt unfluxed titanomagnetite pellets within the 10 – 16 mm fraction range. These pellets underwent processing under the standard temperature-time burning conditions applied at JSC EVRAZ Kachkanarsky Mining and Processing Plant. Testing was conducted in accordance with ISO 4700 requirements, using the universal machine BT1-FR050THW.A1K (Zwick GmbH, Germany), with hammer heads moving at a speed of 10 mm/min, and the deformation curve was recorded. The total iron content ($Fe_{total}$) in the pellets was determined through titrometry according to GOST 32517.1, and FeO was defined based on GOST 53657. Chemical analysis of CaO, $SiO_2$, $Al_2O_3$, MgO, $TiO_2$ and $V_2O_5$ compounds was conducted using the atomic emission method with inductively coupled plasma on the SpectroBlue device (Spectro, Germany). The chemical composition of the studied pellets is as follows, wt. %: $Fe_{total}$ 60.90; FeO 3.02; CaO 1.00; $SiO_2$ 3.89; $Al_2O_3$ 2.83; MgO 2.59; $TiO_2$ 2.73; $V_2O_5$ 0.59.

Microsections were prepared based on the fractures of the pellets.

The metallographic study was conducted using the Neophot-2 optical microscope, and the obtained images were analyzed with Siams-700 software. Measurements of grain size, closed macropore size, and the binding phase's size in the core were carried out on five fields of vision with 20 line segments. The linear method, following the Cavalieri-Acker principle, was employed to determine the phase fraction, closed macropores, and the binding phase [27]. Grain size was determined according to GOST R ISO 643 – 2015, utilizing the conventional phase number classification: *3 – 8* (large), *9* (medium), *10* (small), *11* and higher (very small). To categorize pores, the following terminology was applied [28]: closed pores are located inside the sample and are completely isolated from neighboring ones, while open pores have an open channel connecting them with the external surface of the body. Pore size was assessed by measuring their maximum size in two perpendicular directions. The classification of pores was based on size criteria [29]: macropores – with a diameter $d_p > 20$ μm; mesopores – $20 \geq d_p \geq 0.2$ μm; micropores – $d_p < 0.2$ μm.

*X*-ray phase analysis (XRF) was performed using the Shimadzu XRD-7000 diffractometer equipped with $CuK_\alpha$ radiation in the air, covering the 2θ range from 10 to 85°. The ICDD PDF4 (International Center for Diffraction Data) database was employed for phase identification and quantification.

*X*-ray spectral microanalysis (XRSM) of the phases was performed on the Tescan Vega II scanning electron microscope, equipped with an Oxford INCA ENERGY 450 energy-dispersive microanalyzer.

## Results and discussion

The optical microscope revealed structures in the microstructure of the pellet core, which can be catego-

rized into three types: type *1* (Table 1, samples *1*, *3*, *4*, *5*, *9*, *10*, *11*) – the non-oxidized core – magnetite or titanium-magnetite; type *2* (Table 1, samples *2*, *6*, *7*, *8*, *12*) – partially oxidized core – grains of hematite or titanohematite around magnetite or titanomagnetite; type *3* (Table 1, sample *13*) – the oxidized core – hematite or titanohematite.

The following phases were detected in the pellets by the XRF method: hematite, magnetite, quartz, magnesium silicate and ferruginous diopside. The XRSM method was used to specify the composition of phases, as diffractograms obtained by the XRF method showed overlapping reflexes for "hematite" and "titanohematite," as well as "magnetite" and "titano-magnetite" (the ratio of intensity lines, angles 2θ of interplanar distances from the reflexes fully coincide with the ICDD PDF 4 (International Center for Diffraction Data)).

The XRSM results (Fig. 1, Table 2) revealed that the pellet core consists of the following phases:

– type *1*: phase at the point *1* – titanomagnetite (70.3 % Fe; 0.4 % Ti); phase at the point *2* – aluminosilicate binder composition, wt. %: FeO 19.28; $SiO_2$ 45.95; CaO 14.7; $Al_2O_3$ 13.8; MgO 2.14; phase at the point *3* – magnetite (72.03 % Fe);

– type *2*: phase at the point *1* – titanohematite (67.1 % Fe; 1.4 % Ti); phase at the point *2* – aluminosilicate binder composition, wt. %: FeO 26.0; $SiO_2$ 40.4; CaO 12.9; $Al_2O_3$ 12.2; MgO 8.9; phase at the point *3* – hematite (60.86 % Fe);

– type *3*: phase at the point *1* – titanohematite (67.5 % Fe; 1.9 % Ti); phase at the point *2* – aluminosilicate binder composition, wt. %: FeO 60.9; $SiO_2$ 23.53; CaO 5.6; $Al_2O_3$ 5.67; MgO 1.3.

The microstructure of the non-oxidized core, type *1* (Fig. 2, *a*) consists of magnetite and titanomagnetite grains (*1*) separated by the aluminosilicate binder (*2*) and closed pores (*3*) of various sizes, ranging from spherical to near-spherical. The magnetite or titanomagnetite grains are interconnected, forming a magnetite or titanomagnetite surface contact during sintering (*4*). The microstructure of the partially oxidized core (type *2*) (Fig. 2, *b*) comprises interconnected structural components of hematite and titanohematite (*1*), titanomagnetite and magnetite (*4*), and the aluminosilicate binder (*2*). Grain shells consisting of hematite (titanohematite) are connected, forming hematite (titanohematite) surface

Table 1

**Results of measuring the ultimate compressive force of pellets depending on their size**

*Таблица 1.* **Результаты измерения усилия разрушения окатышей на сжатие в зависимости от их размера**

| Sample number | Fraction, mm | Ultimate force, kN/pellet |
|---|---|---|
| *1* | 10 – 12 | 3.16 |
| *2* | | 3.06 |
| *3* | | 2.59 |
| *4* | | 2.06 |
| *5* | | 2.01 |
| *6* | | 1.91 |
| *7* | | 1.56 |
| *8* | 14 – 16 | 2.06 |
| *9* | | 1.88 |
| *10* | | 1.33 |
| *11* | | 1.14 |
| *12* | | 0.87 |
| *13* | | 0.70 |

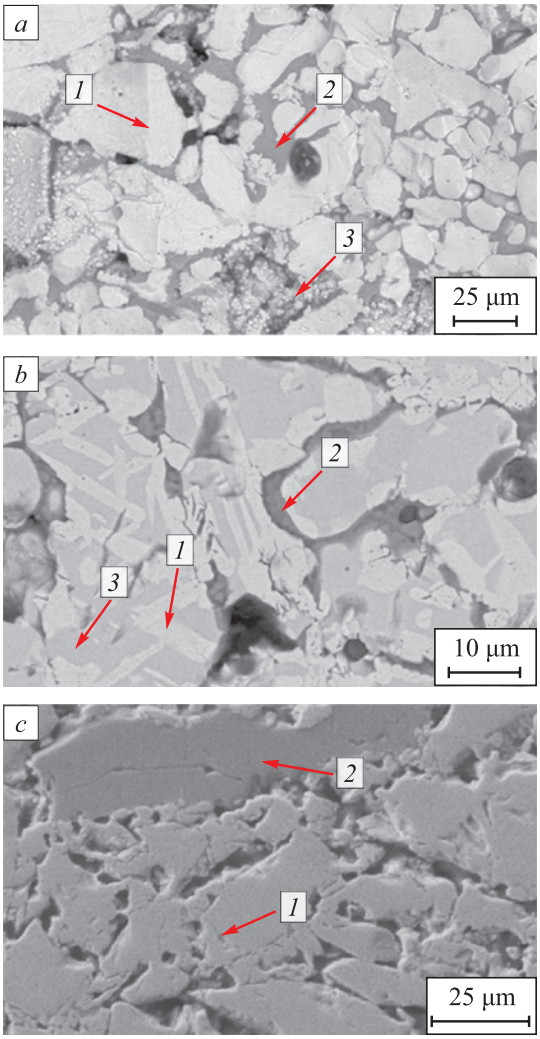


Fig. 1. Electron microscopic image of the pellets' core structure in the plane of ultimate action: *a – c* – type *1 – 3*

Рис. 1. Электронно-микроскопическое изображение структуры ядра окатышей в плоскости действия силы: а – *c* – тип *1 – 3*

Table 2

**Results of X-ray spectral microanalysis of the pellets**

*Таблица 2*. **Результаты рентгеноспектрального микроанализа окатышей**

| Points | Content of elements, wt. %, in the field of analysis | | | | | | | | | |
|---|---|---|---|---|---|---|---|---|---|---|
| | O | Na | Mg | Al | Si | K | Ti | Ca | Fe | V |
| Type *1* | | | | | | | | | | |
| *1* | 27.00 | – | 1.2 | 1.10 | – | – | 0.4 | – | 70.30 | |
| *2* | 50.44 | 1.2 | 1.2 | 7.19 | 21.48 | 0.9 | – | 10.49 | 7.10 | – |
| *3* | 25.07 | – | 1.1 | 1.20 | 0.60 | – | – | – | 72.03 | – |
| Type *2* | | | | | | | | | | |
| *1* | 28.70 | – | 1.2 | 0.90 | 0.70 | – | 1.4 | – | 67.10 | – |
| *2* | 37.14 | – | 5.4 | 6.51 | 18.92 | – | – | 9.31 | 20.22 | 2.5 |
| *3* | 29.64 | – | 7.1 | 1.70 | 0.70 | – | – | – | 60.86 | – |
| Type *3* | | | | | | | | | | |
| *1* | 28.70 | – | 0.4 | 1.00 | – | – | 1.9 | – | 67.50 | 0.5 |
| *2* | 28.70 | 0.4 | 2.0 | 3.00 | 11.00 | 0.1 | 0.8 | 4.00 | 49.50 | 0.5 |

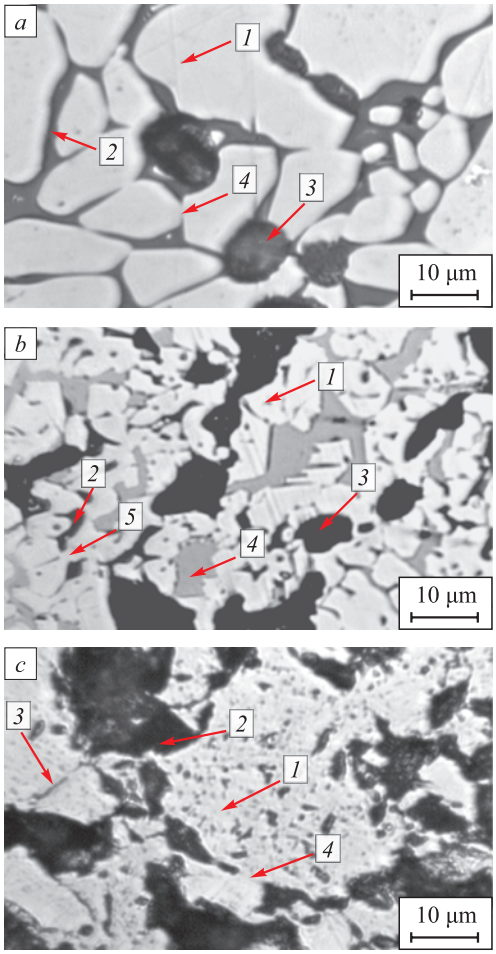


Fig. 2. Typical microstructures of the pellet core in the plane of ultimate action:
*a – c* – type *1 – 3*

Рис. 2. Типичные микроструктуры ядра окатышей в плоскости действия силы:
*a – c* – тип *1 – 3*

contact during sintering (*5*). Some grains are separated by closed pores (*3*). The microstructure of the oxidized core, type *3* (Fig. 2, *c*) consists of titanohematite and hematite grains (*1*) separated by open pores of complex shape (*2*), constituting narrow channels alternating with sharp bulging, aluminosilicate binder (*3*). The hematite (titanohematite) grains, when joined during sintering, form a hematite (titanohematite) surface contact (*4*).

Upon comparing the results from [15 – 20] with the obtained core microstructure, it is assumed that the oxidation of magnetite (titanomagnetite) in type *1*, pellets occurred in the temperature range of 700 – 900 °C, in type *2* pellets in the range of 400 – 600 °C, and in type *3* pellets in the range of 200 – 400 °C.

In Figs. 3 – 5, the research and calculation results are presented in graphical dependencies on the ultimate force.

Fig. 3 depicts the ultimate force as a function of the average size of grains of magnetite (titanomagnetite), hematite (titanohematite), closed macropores, and aluminosilicate binder in pellet cores. The analysis of these dependencies reveals a stable correlation (correlation coefficient $R^2 > 0.7$). Fig. 3, *a* demonstrates that when the average sizes of magnetite (titanomagnetite) are 10 – 15 μm, closed macropores are 12 – 15 μm, and the aluminosilicate binder 1.5 – 2.0 μm, the static compressive strength requirements of 2.5 kN/pellet are met. In the structure under review, both structural components and macropores play a significant role in influencing the ultimate force. However, for type *2* structure (Fig. 3, *b*), no linear relationship was observed among the average grain size of hematite (titanohematite), average sizes of closed macropores, aluminosilicate binder, and ultimate force.

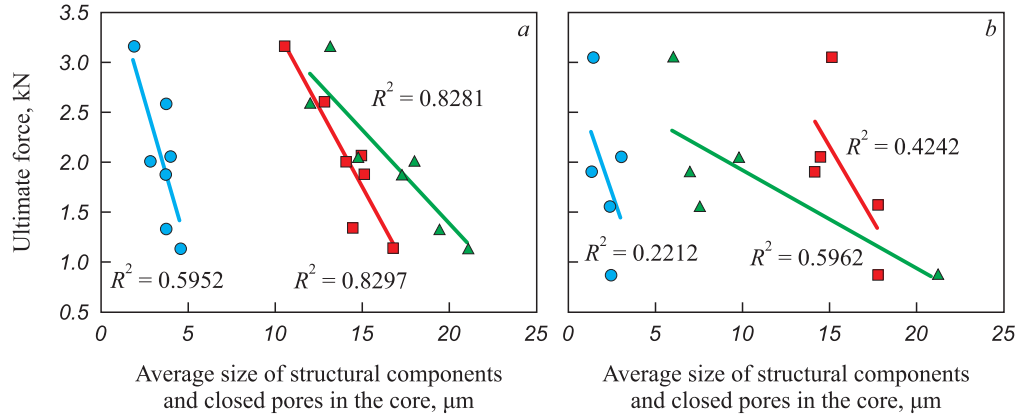


Fig. 3. Effect of the average grain structural components in the core on the ultimate force:
*a* and *b* – type *1* and *2*; ■ – magnetite (titanomagnetite); ▲ – closed macropores; ● – aluminosilicate binder

Рис. 3. Влияние среднего размера структурных составляющих в ядре окатыша на усилие разрушения:
*a* и *b* – тип *1* и *2*; ■ – магнетит (титаномагнетит); ▲ – закрытые макропоры; ● – алюмосиликатное связующее

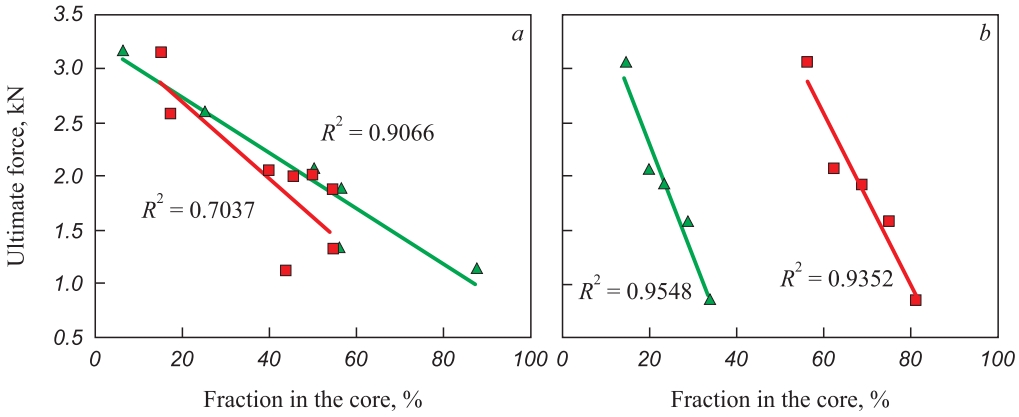


Fig. 4. Effect of the fraction of large grains and closed macropores in the core on the ultimate force:
*a* and *b* – type *1* and *2*; ■ – magnetite (titanomagnetite); ▲ – closed macropores

Рис. 4. Влияние доли зерен крупных размеров и закрытых макропор в ядре окатыша на усилие разрушения:
*a* и *b* – тип *1* и *2*; ■ – магнетит (титаномагнетит); ▲ – закрытые макропоры

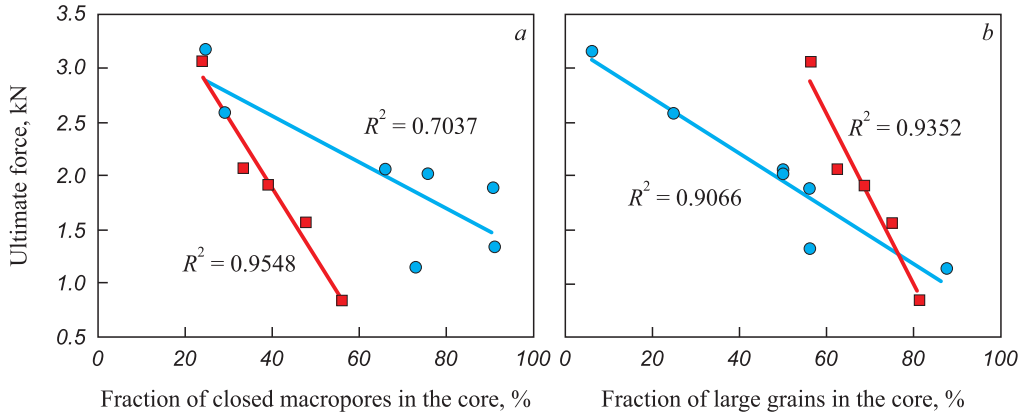


Fig. 5 Effect of the fraction of closed macropores (*a*) and large grains (*b*) in the core
on the ultimate force depending on the type of structure:
● and ■ – type *1* and *2*

Рис. 5. Влияние доли закрытых макропор (*a*) и зерен крупных размеров (*b*) на усилие разрушения
в ядре окатыша в зависимости от типа структуры:
● и ■ – тип *1* и *2*

A linear relationship was identified between the ultimate force in pellet cores and the fraction of large magnetite (titanomagnetite) grains and closed macropores (Fig. 4, *a*). The trend shows that the smaller the fraction of closed macropores and large grains of magnetite (titanomagnetite), the greater the ultimate force. This pattern is also observed in the structure of type *2*.

For all structures (type *1*, *2*), a consistent observation was made: as the number of closed macropores and large grains increased, the ultimate force decreased from 3.5 to 0.87 kN/pellet (Fig. 5).

To produce pellets with an ultimate force exceeding 2.5 kN/pellet, the following conditions should be met: for type *1* structure – the number of closed macropores should be less than 18 %, and the number of large grains should not exceed 25 %; for type *2* structure – these values should be 25 and 60 %, respectively. For pellets with an ultimate force exceeding 2 kN/pellet: for type *1* structure – the number of closed macropores should be less than 40 % and the number of large grains should not exceed 50 %; for type *2* structure – these values should be 25 and 65 %, respectively.

The ultimate force of 0.70 kN/pellet (Type *3*) does not meet the static compressive strength requirements due to the large number of open macropores (47 %) and the number of large grains (75 %).

An important observation is that for both types of structures, pellets with ultimate forces exceeding 2.5 kN/pellet can be obtained.

## Conclusions

The pellet core was found to exhibit three types of structures: type *1* (non-oxidized core): titanomagnetite and magnetite grains, including sintered ones, closed macropores, and aluminosilicate binder; type *2* (partially oxidized core): around magnetite (titanomagnetite), there are hematite and titanohematite grains, including sintered ones, closed macropores, and aluminosilicate binder; type *3* (oxidized core): hematite and titanohematite grains, including sintered ones, open pores, and aluminosilicate binder.

In the manufacturing of pellets capable of withstanding compressive loads exceeding 2.5 kN, it is essential to have the following criteria: for type *1* structure: the number of closed macropores should be less than 18 %, and the number of large grains should exceed 25 %; for type *2* structure: the values should be 25 % for closed macropores and 60 % for large grains.

The ultimate force decreases to 0.70 kN/pellet for the type *3* structure due to the presence of a significant number of open macropores and large grains in the pellet core.

## References / Список литературы

1. Shumakov N.S., Dmitriev A.N., Garaeva O.G. *Raw Materials and Fuel for Blast Furnace Smelting*. Yekaterinburg: UrB RAS; 2007:392. (In Russ.).

   Шумаков Н.С., Дмитриев А.Н., Гараева О.Г. *Сырые материалы и топливо для доменной плавки*. Екатеринбург: УрО РАН; 2007:392.
2. Gul A., Sirkeci A.A., Boylu F., Guldan G., Burat F. Improvement of mechanical strength of iron ore pellets using raw and activated bentonites as binders. *Physicochemical Problems of Mineral Processing*. 2014;51(1):23–36. https://dx.doi.org/10.5277/ppmp150203
3. Bardavelidze G.G., Bragin V.V., Spirin N.A., Pigarev S.P. Research of pellets from concentrate of oxidized ferruginous quartzites of JSC "Mikhailovsky GOK". *Metallurg*. 2021;(12):11–18. (In Russ.). https://doi.org/10.52351/00260827_2021_12_11

   Бардавелидзе Г.Г., Брагин В.В., Спирин Н.А., Пигарев С.П. Исследование окатышей из концентрата окисленных железистых кварцитов АО «Михайловский ГОК». *Металлург*. 2021;(12):11–18. https://doi.org/10.52351/00260827_2021_12_11
4. Shaik M.B., Sekhar C., Dwarapudi S., Gupta N., Paul I., Patel A.K., Tudu S., Kumar A. Characterization of colemanite and its effect on cold compessive strengh and swelling index of iron ore pellets. *Mining, Metallurgy and Exploration*. 2021;38(1):217–231. https://doi.org/10.1007/s42461-020-00331-5
5. Guo H., Shen F.-M., Jiang X., Gao Q.-J., Ding G.-G. Effects of MgO additive on metallurgical properties of fluxed-pellet. *School of Metallurgy, Northeastern University*. 2019;26:3238–3251. https://doi.org/10.1007/s11771-019-4249-6
6. Li W., Fu G., Chu M., Zhu M. Influence of MgO on the oxidation and induration of Hongge vanadium titanomagnetite pellets. *Ironmaking and Steelmaking*. 2019;47(8):837–843. https://doi.org/10.1080/03019233.2019.1615815
7. Yi Y., Li G., Gao P., Zhang X., Zhang Y., Zhang J., Huang J. Effect of humic acid binder on oxidation roasting of vanadium-titanium magnetite pellets via straight-grate process. *Crystals*. 2021;11(11):1–11. https://doi.org/10.3390/cryst11111283
8. Mohamed O.A., Shalabi M.E.H., El-Hussiny N.A., Khedr M.H., Mostafa F. The role of normal and activated bentonite on the pelletization of barite iron ore concentrate and the quality of pellets. *Powder Technology*. 2003; 130(1-3):277–282. https://doi.org/10.1016/S0032-5910(02)00205-X
9. Abzalov V.M., Gorbachev V.A., Evstyugin S.N., Klein V.I., Leont'ev L.I., Yur'ev B.P. *Physicochemical and Thermal Engineering Fundamentals of Iron Ore Pellets Production*. Yekaterinburg: MITs; 2015:335. (In Russ.).

   Абзалов В.М., Горбачев В.А., Евстюгин С.Н., Клейн В.И., Леонтьев Л.И., Юрьев Б.П. *Физико-химические и теплотехнические основы производства железорудных окатышей*. Екатеринбург: МИЦ; 2015:335.
10. Yur'ev B.P., Bruk L.B., Spirin N.A., Sheshukov O.Yu., Gol'tsev V.A., Shevchenko O.I., Metelkin A.A. *Fundamentals of the Theory of Processes in Iron Ore Pellets Firing*. Nizhny Tagil: NTI (Branch) UrFU; 2018:310. (In Russ.).

Юрьев Б.П., Брук Л.Б., Спирин Н.А., Шешуков О.Ю., Гольцев В.А., Шевченко О.И., Метелкин А.А. *Основы теории процессов при обжиге железорудных окатышей*. Нижний Тагил: НТИ (филиал) УрФУ; 2018:310.

11. Bhuiyan I.U., Mouson J., Schröppel B., Kaech A., Dobryden I., Forsmo S.P.E., Hedlund J. Microstructure of bentonite in iron ore green pellets. *Microscopy and Microanalysis*. 2014;20(1):33–41. https://doi.org/10.1017/S1431927613013950
12. Kawatra S.K., Ripke S.J. Effects of bentonite fiber formation in iron ore pelletization. *International Journal of Mineral Processing*. 2002;65(3-4):141–149. https://doi.org/10.1016/s0301-7516(01)00062-x
13. Yur'ev B.P., Dudko V.A. Influence of the pellets' structural characteristics upon their metallurgical properties. *Stal'*. 2021;(4):2–6. (In Russ.).

    Юрьев Б.П., Дудко В.А. Влияние структурных характеристик окатышей на их металлургические свойства. *Сталь*. 2021;(4):2–6.
14. Ericksson A., Andersson C., Ahmed H., Dahlin A., Kumar T.K.S., Semberg P. Effect of varied oxygen levels on the oxidation of a magnetite pellet bed during pot furnace induration. *ISIJ International*. 2021;61(5):1439–1449. https://doi.org/10.2355/isijinternational.ISIJINT-2020-469
15. Tang M., Cho H.J., Pistorius P.C. Early gaseous oxygen enrichment to enhance magnetite pellet oxidation. *Metallurgical and materials Transactions B*. 2014;45(4):1304–1314. https://doi.org/10.1007/s11663-014-0064-5
16. Kumar T.K.S., Viswanathan N.N., Ahmed H., Dahlin A., Andersson C., Bjorkman B. Developing the oxidation kinetic model for magnetite pellet. *Metallurgical and Materials Transactions B*. 2019;50(1):162–172. https://doi.org/10.1007/s11663-018-1423-4
17. Gorbachev V.A., Abzalov V.M., Yu'ev B.P. Conversion of magnetite to hematite in iron-ore pellets. *Izvestiya. Ferrous Metallurgy*. 2007;50(4):27–30.

    Горбачев В.А., Абзалов В.М., Юрьев Б.П. Кристаллохимическое превращение магнетита в гематит в железорудных окатышах. *Известия вузов. Черная металлургия*. 2007;50(4):27–30.
18. Song S., Pistorius P.C. Formation of hematite whiskers during magnetite concentrate oxidation. *ISIJ International*. 2019;59(10):1765–1769. https://doi.org/10.2355/isijinternational.ISIJINT-2018-755
19. Forsmo S.P.E., Forsmo S.-E., Samskog P.-O., Björkman B.M.T. Mechanisms in oxidation and sintering of magnetite iron ore green pellets. *Power Technology*. 2008; 183(2):247–259. https://doi.org/10.1016/j.powtec.2007.07.032
20. Timofeeva A.S., Nikitchenko T.V., Fedina V.V., Akul'shina I.I. Effect of flus on the hardening of pellet during heat treatment. *Metallurgist*. 2017;61(8):700–702. https://doi.org/10.1007/s11015-017-0552-3
21. Gao Q.-J., Shen F.-M., Wei G., Jiang X., Zheng H.-Y. Effects of MgO containing additive on low-temperature metallurgical properties of oxidized pellet. *Journal of Iron and Steel Research International*. 2013;20(7):25–28. https://doi.org/10.1016/S1006-706X(13)60121-1
22. Nikitchenko T.V., Timofeeva A.S., Kozhuhkov A.A. Modification additions influence on the iron ore pellets forming. *Ferrous Metallurgy. Bulletin of Scientific, Technical and Economic Information*. 2018;1(4):67–72. (In Russ.).

    Никитченко Т.В., Тимофеева А.С., Кожухов А.А. Влияние модифицирующих добавок на формирование железорудных окатышей. *Черная металлургия. Бюллетень научно-технической и экономической информации*. 2018;1(4):67–72.
23. Gan M., Sun Y.-F., Fan X.-H., Ji Z.-Y. Lv W., Chen X.-L., Jiang T. Preparing high-quality vanadium titano-magnetite pellets for large-scale blast furnaces as ironmaking burden. *Ironmaking and Steelmaking*. 2018;47(4):1–8. https://doi.org/10.1080/03019233.2018.1492500
24. Gustafsson G., Häggblad H-A., Nishida M., Larsson S., Jonsén P. Fracture probability modelling of impact-loaded iron ore pellets. *International Journal of Impact Engineering*. 2017;102:180–186. http://dx.doi.org/10.1016/j.ijimpeng.2016.12.014
25. Gustafsson G., Häggblad H.-A., Jonsén P. Multi-particle finite element modelling of the compression of iron ore pellets with statistically distributed geometric and material data. *Powder Technology*. 2013;239:231–238. http://dx.doi.org/10.1016/j.powtec.2013.02.005
26. Dmitriev A.N., Smirnova V.G., Vyaznikova E.A., Dolmatov A.V., Vit'kina G.Yu. Influence of structure of burned pellets on strength and destruction in static compression tests. *Izvestiya. Ferrous Metallurgy*. 2021;64(11):785–792. (In Russ.). https://doi.org/10.17073/0368-0797-2021-11-785-792

    Дмитриев А.Н., Смирнова В.Г., Вязникова Е.А., Долматов А.В., Витькина Г.Ю. Влияние структуры обожженных окатышей на прочность и разрушение при испытании на статическое сжатие. *Известия вузов. Черная металлургия*. 2021;64(11):785–792. https://doi.org/10.17073/0368-0797-2021-11-785-792
27. Saltykov S.A. *Stereometric Metallography*. Moscow: Metallurgiya; 1970:376. (In Russ.).

    Салтыков С.А. *Стереометрическая металлография*. Москва: Металлургия; 1970:376.
28. Klobes P., Meyer K. Ronald, Munro R.G. *Porosity and Specific Surface Area Measurements for Solid Materials. NIST Recommended Practice Guide*. U.S. GOVERNMENT Printing Office; Washington: 2006.
29. Abzalov V.M., Klein V.I., Yur'ev B.P. Oxygen diffusion in pores of an iron ore pellet. *Izvestiya. Ferrous Metallurgy*. 2008;51(6):7–9. (In Russ.).

    Абзалов В.М., Клейн В.И., Юрьев Б.П. Диффузия кислорода в порах железорудного окатыша. *Известия вузов. Черная металлургия*. 2008;51(6):7–9.

## Information about the Authors

***Andrei N. Dmitriev,*** *Dr. Sci. (Eng.), Chief Researcher of the Laboratory of Pyrometallurgy of Reduction Processes,* Institute of Metallurgy, Ural Branch of the Russian Academy of Sciences
***ORCID:*** 0000-0001-6446-0215
***E-mail:*** andrey.dmitriev@mail.ru

***Valentina G. Smirnova,*** *Leading Engineer of the Laboratory of Pyrometallurgy of Reduction Processes,* Institute of Metallurgy, Ural Branch of the Russian Academy of Sciences
***ORCID:*** 0000-0002-2285-2509
***E-mail:*** metallography@mail.ru

***Elena A. Vyaznikova,*** *Junior Researcher of the Laboratory of Pyrometallurgy of Reduction Processes,* Institute of Metallurgy, Ural Branch of the Russian Academy of Sciences
***ORCID:*** 0000-0003-2754-1846
***E-mail:*** vjaznikova@mail.ru

***Galina Yu. Vit'kina,*** *Cand. Sci. (Eng.), Senior Researcher, Head of the Laboratory of Pyrometallurgy of Reduction Processes,* Institute of Metallurgy, Ural Branch of the Russian Academy of Sciences
***ORCID:*** 0000-0002-1076-2709
***E-mail:*** 20procents@mail.ru

***Aleksandr S. Smirnov,*** *Cand. Sci. (Eng.), Senior Researcher of the Laboratory of Deformation Mechanics,* E.S. Gorkunov Institute of Engineering Science, Ural Branch of the Russian Academy of Sciences
***ORCID:*** 0000-0002-5826-491X
***E-mail:*** smirnov@imach.uran.ru

## Сведения об авторах

***Андрей Николаевич Дмитриев,*** *д.т.н., главный научный сотрудник лаборатории пирометаллургии восстановительных процессов,* Институт металлургии Уральского отделения РАН
***ORCID:*** 0000-0001-6446-0215
***E-mail:*** andrey.dmitriev@mail.ru

***Валентина Григорьевна Смирнова,*** *ведущий инженер лаборатории пирометаллургии восстановительных процессов,* Институт металлургии Уральского отделения РАН
***ORCID:*** 0000-0002-2285-2509
***E-mail:*** metallography@mail.ru

***Елена Александровна Вязникова,*** *младший научный сотрудник лаборатории пирометаллургии восстановительных процессов,* Институт металлургии Уральского отделения РАН
***ORCID:*** 0000-0003-2754-1846
***E-mail:*** vjaznikova@mail.ru

***Галина Юрьевна Витькина,*** *к.т.н., старший научный сотрудник, заведующий лабораторией пирометаллургии восстановительных процессов,* Институт металлургии Уральского отделения РАН
***ORCID:*** 0000-0002-1076-2709
***E-mail:*** 20procents@mail.ru

***Александр Сергеевич Смирнов,*** *к.т.н., старший научный сотрудник лаборатории механики деформаций,* Институт машиноведения имени Э.С. Горкунова Уральского отделения РАН
***ORCID:*** 0000-0002-5826-491X
***E-mail:*** smirnov@imach.uran.ru

## Contribution of the Authors

***A. N. Dmitriev*** – scientific guidance, formation of the basic concept, goals and objectives of the study.
***V. G. Smirnova*** – writing the text, obtaining and analyzing the data, reviewing publications on the article topic.
***E. A. Vyaznikova*** – obtaining data for analysis.
***G. Yu. Vit'kina*** – visualization of the research results, revision of the text.
***A. S. Smirnov*** – obtaining data for analysis.

## Вклад авторов

***А. Н. Дмитриев*** – научное руководство, формирование основной концепции, цели и задачи исследования.
***В. Г. Смирнова*** – написание текста рукописи, получение и анализ данных, обзор публикаций по теме статьи.
***Е. А. Вязникова*** – получение данных для анализа.
***Г. Ю. Витькина*** – визуализация результатов исследований, доработка текста.
***А. С. Смирнов*** – получение данных для анализа.

Received 21.03.2023
Revised 30.05.2023
Accepted 11.09.2023

Поступила в редакцию 21.03.2023
После доработки 30.05.2023
Принята к публикации 11.09.2023

**Materials science / Материаловедение**

**UDC** 621.791.92:621.727:620.178
**DOI** 10.17073/0368-0797-2023-6-705-708



***Short report***
***Краткое сообщение***

# Influence of tempering on structure of deposited high-speed steel coatings

**L. P. Bashchenko, V. V. Pochetukha, T. A. Mikhailichenko**

**Siberian State Industrial University** (42 Kirova Str., Novokuznetsk, Kemerovo Region – Kuzbass 654007, Russian Federation)

luda.baschenko@gmail.com

***Abstract***. The technology of plasma surfacing in a protective-alloying nitrogen medium with an additive powder wire is characterized by high productivity and the possibility of alloying the deposited metal. Durability of metal products depends on microstructure, chemical composition, production technology, modes of thermal and surface treatments. The article presents the results of a study of structure and microhardness of the high speed alloy R18Yu deposited in nitrogen medium on medium-carbon steel 30KhGSA. There were no differences in structure of the surfacing layer up to 4 mm in depth, but after four times high-temperature tempering at 580 °C, structural and phase changes were revealed. The values of microhardness after surfacing and tempering are consistent with the literature data.

***Keywords:*** plasma surfacing, tempering, high-speed alloy, microstructure, microhardness

***Acknowledgements:*** The study was supported by the Russian Science Foundation (grant No. 23-19-00186 6), https://rscf.ru/project/23-19-00186.

***For citation:*** Bashchenko L.P., Pochetukha V.V., Mikhailichenko T.A. Influence of tempering on structure of deposited high-speed steel coatings. *Izvestiya. Ferrous Metallurgy*. 2023;66(6):705–708. https://doi.org/10.17073/0368-0797-2023-6-705-708

# Влияние отпуска на структуру наплавленных покрытий из быстрорежущей стали

**Л. П. Бащенко, В. В. Почетуха, Т. А. Михайличенко**

**Сибирский государственный индустриальный университет** (Россия, 654007, Кемеровская обл. – Кузбасс, Новокузнецк, ул. Кирова, 42)

luda.baschenko@gmail.com

***Аннотация***. Технология плазменной наплавки в защитно-легирующей среде азота с присадочной порошковой проволокой характеризуется высокой производительностью и возможностью легирования наплавленного металла. Стойкость металлических изделий зависит от микроструктуры, химического состава, технологии получения, режимов термической и поверхностной обработок. В статье приведены результаты исследования структуры и микротвердости плазменно-наплавленного в среде азота быстрорежущего сплава Р18Ю на среднеуглеродистую сталь 30ХГСА. Различий в строении наплавочного слоя до 4 мм по глубине не выявлено, но после четырехкратного высокотемпературного отпуска при 580 °С выявлены структурно-фазовые изменения. Значения микротвердости после наплавки и отпуска согласуются с литературными данными.

***Ключевые слова:*** плазменная наплавка, отпуск, быстрорежущий сплав, микроструктура, микротвердость

***Благодарности:*** Исследование выполнено при поддержке Российского научного фонда (грант № 23-19-00186 6), https://rscf.ru/project/23-19-00186.

***Для цитирования:*** Бащенко Л.П., Почетуха В.В., Михайличенко Т.А. Влияние отпуска на структуру наплавленных покрытий из быстрорежущей стали. *Известия вузов. Черная металлургия*. 2023;66(6):705–708. https://doi.org/10.17073/0368-0797-2023-6-705-708

## Introduction

In recent years, researchers in the field of fundamental materials science have traditionally focused on studying the impact th at structural-phase state of high-speed alloys exerts on the formation of enhanced performance characteristics [1 – 3] and their practical implementation [4; 5].

Heat-resistant, high-hardness steels (R18, R6M5, R2M9, etc.) with excellent service properties are widely employed as surfacing materials in mechanical engi-

neering and metallurgy to protect parts from abrasive wear [6 – 9]. The technology employed is plasma surfacing in a protective-alloying nitrogen medium with an additive powder wire. This technology is highly productive and enables alloying of the deposited metal [6 – 9]. Nitrogen, in the case of wear-resistant coatings, provides increased impact and corrosion resistance [6 – 9]. The resistance of metal products is determined by microstructure, chemical composition, formulation, heat, and surface treatment modes. However, reliable data on enhancing the hardness and wear resistance of high-speed metal obtained by plasma surfacing and subsequent he at treatment is lacking in the literature.

The objective of the present work is to investigate the structure of high-speed steel coating formed by high-temperature plasma in a nitrogen medium and high-temperature tempering.

## Materials and methods

We investigated the deposited high-speed alloy R18Yu, additionally alloyed with aluminum and nitrogen, possessing the following chemical composition, wt. %: C 0.87; Cr 4.41; W 17.00; Mo 0.10; V 1.50; Ti 0.35; Al 1.15; N 0.06. The base material is 30KhGSA steel with the following chemical composition, wt. %: C 0.3; Cr 0.9; Mn 0.8; Si 0.9.

As described in the works [8; 9], ingot deposition was performed using the installation for plasma surfacing of rotation bodies in the thermal cycle with low-temperature heating. The surfacing mode remains consistent with the one outlined in [8].

Samples were cut from the upper layers of the deposited metal using a spark cutting machine and subjected to heat treatment (heating temperature reaching 580 °C, with a 1 h holding time and four tempering cycles). The metallographic study employed the OLYMPUS GX-51 optical microscope. For obtaining EDS mapping images and profiles, the KYKY-EM6900 scanning electron microscope was utilized.

Microhardness was studied using the Vickers method with an HVS-1000 measuring device, employing a 1 N indenter load.

## Results and discussion

According to classical ideas, the structure of the deposited layer forms as outlined in [10]. The carbon-depleted α-solid solution precipitates from the liquid. Subsequently, the peritectic reaction ensues, leading to the formation of γ-mixed crystals. This reaction occurs at the phase interface, and the resulting γ-crystals act to isolate the core of α-crystals from the more carbon-rich liquid. The peritectic reaction can only proceed if carbon and alloying elements diffuse from the liquid solution through the γ-phase. However, this process is rarely observed under real surfacing conditions, where the surface-deposited layers cool down rapidly. Consequently, the structure retains a certain amount of α-phase, a quantity influenced by the cooling rate of the surface layer [10].

Upon subsequent cooling, the eutectoid decomposition of the α-phase takes place, resulting in the formation of an α-eutectoid. This eutectoid comprises a dispersed mixture of austenite and carbides of the $Me_6C$ type, as well as cementite-type carbides.

The inhomogeneity of the structure increases with a higher cooling rate, a phenomenon attributed to the gradually occurring peritectic transformation. Following final solidification, the structure features grains composed of three concentric layers: *1* – a core with a two-phase α-eutectoid structure; *2* – an intermediate light layer (during solidification, γ-crystals form here due to the peritectic reaction, and upon rapid cooling, they transform into martensite and residual austenite); *3* – an outer layer with two-phase eutectics of austenite and carbides, which, after cooling, transforms into martensite and carbides [10].

Microstructure analysis through optical microscopy reveals that the structure of the deposited layer exhibits a typical cast structure, with dispersion that is practically independent of the distance from the surface. This consistency may be attributed to the relatively small thickness of the deposited metal and, consequently, the uniform cooling rates throughout the depth of the layer deposited in a single pass.

A more detailed examination at significant magnification using scanning electron microscopy, which allows a focus on structural elements, also demonstrates no discernible differences in the structure of the deposited layer at various depths from the surface (refer to the Figure).

The distinctive light-colored shell exhibits martensite and residual austenite crystals, formed during accelerated cooling from the γ-phase involved in the peritectic reaction. Inside the light-colored shell, primary carbides of the $Me_6C$ with a skeleton-like shape are situated. The presence of these carbides diminishes the toughness of the steel, prompting exploration into methods for mitigating their impact. Dark areas represent a two-phase eutectic structure, which, after solidification, comprises carbides, martensite, and residual austenite.

Given that the surfacing was conducted in a nitrogen medium, it is expected that nitrogen-containing carbides or carbonitrides must have formed. The works [6; 7] have demonstrated the formation of complex carbides such as $Fe_3(W-Mo-N-V)_3C$. It is possible for $Fe_4N$ nitrides to be formed.

Following four cycles of high-temperature tempering at 580 °C with a 1 h holding time and subsequent air

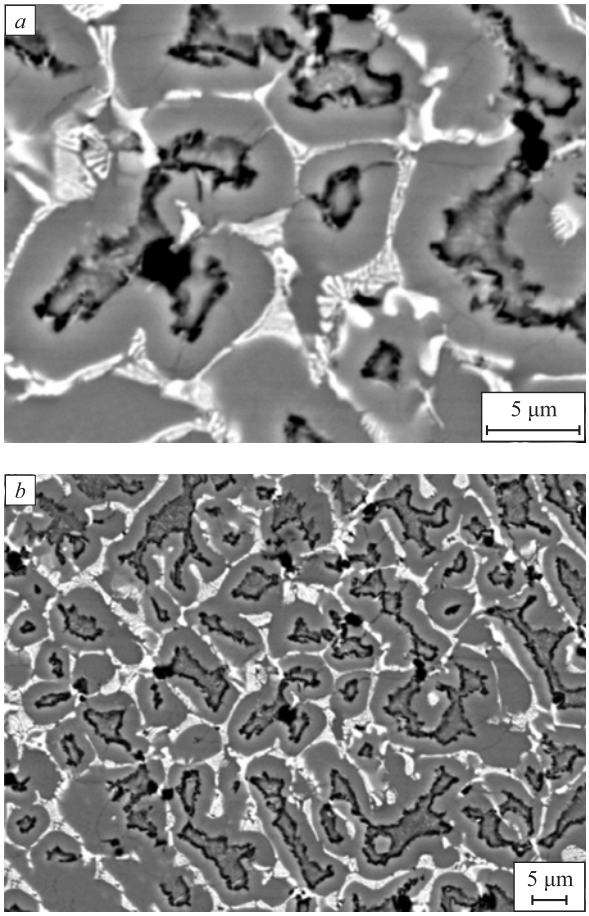


Electron microscopic images of the deposited layer at a distances of 2000 μm (*a*) and 4000 μm (*b*)

Электронно-микроскопические изображения наплавленного слоя на расстоянии 2000 мкм (*a*) и 4000 мкм (*b*)

cooling, structural changes were observed in the deposited layer. In the locations initially comprising martensite and residual austenite, they transformed into tempered martensite with enhanced etchability, releasing dispersed carbides of *Me*C and $Me_6C$ type.

Microhardness on the surface of samples after surfacing and four cycles of high-temperature tempering was automatically measured at 100 μm intervals. The microhardness of the deposited layer was found to be slightly lower than that of the same layer after four cycles of tempering (see the Table).

After four cycles of tempering, as residual austenite decomposed, tempered martensite formed, and dispersed carbides were released. The overall microhardness slightly increased, and its distribution became more homogeneous (see the Table), aligning with data from literary sources [10].

## Conclusions

We employed optical and scanning electron microscopy, along with microhardness measurements, to evaluate the effect of tempering on the structure of the R18Yu high-speed steel coating formed by plasma surfacing in a nitrogen medium with a powder wire.

It was observed th at cells with an austenite-martensitic structure formed, and there was a marginal increase in microhardness.

**Distribution of microhardness in the deposited layer at different distances from the surface of the test material after surfacing and after four-time tempering**

**Распределение микротвердости в наплавленном слое на различном расстоянии от поверхности исследуемого материала после наплавки и после четырехкратного отпуска**

| Microhardness of high-speed steel R18Yu, MPa, at a distance from the sample surface | | | |
|---|---|---|---|
| after surfacing | | after surfacing and high-temperature tempering | |
| 1000 μm | 3000 μm | 1000 μm | 3000 μm |
| 48.20 | 49.82 | 55.15 | 51.72 |
| 46.37 | 45.58 | 53.88 | 52.53 |
| 46.37 | 48.13 | 60.14 | 51.40 |
| 50.45 | 43.96 | 50.15 | 50.52 |
| 46.84 | 47.42 | 55.28 | 51.35 |
| 41.22 | 33.59 | 54.39 | 63.13 |
| 46.99 | 48.63 | 54.26 | 49.30 |
| 34.16 | 44.11 | 49.13 | 55.67 |
| 46.99 | 47.31 | 54.26 | 51.96 |
| 45.43 | 44.39 | 55.26 | 55.25 |

## References / Список литературы

1. Wang Y., Mao B., Chu S., Chen S., Xing H., Zhao H., Wang S., Wang Y., Zhang J., Sun B. Advanced manufacturing of high-speed steels: A critical review of the process design, microstructural evolution, and engineering performance. *Journal of Materials Research and Technology*. 2023;24:8198–8240. https://doi.org/10.1016/j.jmrt.2023.04.269
2. Wang H., Hong D., Hou L., Ou P., Wang Z., Shen L., Zhao H. Influence of tempering temperatures on the microstructure, secondary carbides and mechanical properties of spray-deposited AISI M3:2 high-speed steel. *Materials Chemistry and Physics*. 2020;255:123554. https://doi.org/10.1016/j.matchemphys.2020.123554
3. Lyu C., Zhou J., Zhang X., Yao Y., Zhang Y. Effect of he at treatment on microstructure and impact toughness of a Tungsten-Molybdenum powder metallurgical high-speed steel. *Materials Science and Engineering: A*. 2021;815:141268. https://doi.org/10.1016/j.msea.2021.141268
4. Wang Y., Chu S., Mao B., Xing H., Zhang J., Sun B. Microstructure, residual stress, and mechanical property evolution of a spray-formed vanadium-modified high-speed steel processed by post-he at treatment. *Journal of Materials*

*Research and Technology*. 2022;18:1521–1533. https://doi.org/10.1016/j.jmrt.2022.03.053

5. P an Yu, Pi Z., Liu B., Xu W., Zhang C., Qu X., Lu X. Influence of he at treatment on the microstructural evolution and mechanical properties of W6Mo5Cr4V2Co5Nb (825 K) high speed steel. *Materials Science and Engineering: A*. 2020;787:139480. https://doi.org/10.1016/j.msea.2020.139480
6. Nefediev S.P., Emelyushin A.N. The influence of nitrogen on the formation of the structure and properties of plasma coatings of type 10P6M5. *Bulletin of the Ugra State University*. 2021;(3(62)):33–45. (In Russ.). https://doi.org/10.17816/byusu20210333-45

   Нефедьев С.П., Емелюшин А.Н. Влияние азота на формирование структуры и свойств плазменных покрытий типа 10Р6М5. *Вестник Югорского государственного университета*. 2021;(3(62)):33–45. https://doi.org/10.17816/byusu20210333-45
7. Shaikhutdinova L.R., Khairetdinov E.F., Khusainov Yu.G. Effect of ion nitriding on the structural and phase composition and mechanical properties of high-speed steel R6M5 after SPD. *Metal Science and He at Treatment*. 2020;62(2): 263–268. https://doi.org/10.1007/s11041-020-00546-9
8. Malushin N.N., Gromov V.E., Romanov D.A., Bashchenko L.P., Peregudov O.A. *Hardening of Heat-Resistant Alloys by Plasma in Nitrogen Medium*. Novokuznetsk: Polygraphist; 2022:232. (In Russ.).

   Малушин Н.Н., Громов В.Е., Романов Д.А., Бащенко Л.П., Перегудов О.А. *Упрочнение теплостойких сплавов плазмой в среде азота*. Новокузнецк: Полиграфист; 2022:232.
9. Malushin N.N., Gromov V.E., Romanov D.A., Bashchenko L.P., Kovalev A.P. Development of complex technology of hardening of cold rolling rolls by plasma surfacing. *Zagotovitel'nye proizvodstva v mashinostroenii*. 2023; 21(7):296–302. (In Russ.). https://doi.org/10.36652/1684-1107-2023-21-7-296-302

   Малушин Н.Н., Громов В.Е., Романов Д.А., Бащенко Л.П., Ковалев А.П. Разработка комплексной технологии упрочнения валков холодной прокатки плазменной наплавкой. *Заготовительные производства в машиностроении*. 2023;21(7):296–302. https://doi.org/10.36652/1684-1107-2023-21-7-296-302
10. Geller Yu.A. *Tool Steels*. Moscow: Metallurgiya; 1983:527. (In Russ.).

    Геллер Ю.А. *Инструментальные стали*. Москва: Металлургия; 1983:527.

## Information about the Authors / Сведения об авторах

***Lyudmila P. Bashchenko,*** *Cand. Sci. (Eng.), Assist. Prof. of the Chair "Thermal Power and Ecology",* Siberian State Industrial University
***ORCID:*** 0000-0003-1878-909X
***E-mail:*** luda.baschenko@gmail.com

***Vasilii V. Pochetukha,*** *Cand. Sci. (Eng.), Senior Lecturer of the Chair of Transport and Logistics,* Siberian State Industrial University
***ORCID:*** 0000-0003-0492-6188
***E-mail:*** v.pochetuha@mail.ru

***Tat'yana A. Mikhailichenko,*** *Cand. Sci. (Eng.), Assist. Prof. of the Chair "Thermal Power and Ecology",* Siberian State Industrial University
***E-mail:*** archimih@mail.ru

***Людмила Петровна Бащенко,*** *к.т.н., доцент кафедры теплоэнергетики и экологии,* Сибирский государственный индустриальный университет
***ORCID:*** 0000-0003-1878-909X
***E-mail:*** luda.baschenko@gmail.com

***Василий Витальевич Почетуха,*** *к.т.н., старший преподаватель кафедры транспорта и логистики,* Сибирский государственный индустриальный университет
***ORCID:*** 0000-0003-0492-6188
***E-mail:*** v.pochetuha@mail.ru

***Татьяна Алексеевна Михайличенко,*** *к.т.н., доцент кафедры теплоэнергетики и экологии,* Сибирский государственный индустриальный университет
***E-mail:*** archimih@mail.ru

## Contribution of the Authors / Вклад авторов

***L. P. Baschenko*** – formation of the main concept, writing the text.

***V. V. Pochetuha*** – processing of the results of optical and scanning electron microscopy.
***T. A. Mikhailichenko*** – measurement of microhardness, analysis of structure of the surfacing layer in depth.

***Л. П. Бащенко*** – формулирование общей концепции работы, написание текста.
***В. В. Почетуха*** – обработка результатов оптической и сканирующей электронной микроскопии.
***Т. А. Михайличенко*** – измерение микротвердости, анализ строения наплавочного слоя по глубине.

Received 20.07.2023
Revised 28.08.2023
Accepted 01.09.2023

Поступила в редакцию 20.07.2023
После доработки 28.08.2023
Принята к публикации 01.09.2023

MATERIALS SCIENCE / МАТЕРИАЛОВЕДЕНИЕ

**UDC** 621.791.927.5
**DOI** 10.17073/0368-0797-2023-6-709-717



*Original article*
*Оригинальная статья*

# Structure and mechanical properties anisotropy of a steel product manufactured by layer-by-layer electric arc wire 3D printing

**I. V. Vlasov** ✉, **A. I. Gordienko, A. E. Kuznetsova, V. M. Semenchuk**

**Institute of Strength Physics and Materials Science, Siberian Branch of Russian Academy of Sciences** (2/4 Akademicheskii Ave., Tomsk 634055, Russian Federation)

✉ viv@ispms.ru

***Abstract***. The work presents the study of structure and mechanical properties anisotropy of a metal wall obtained using electric arc wire 3D printing (WAAM) with ER70S-6 wire. The layers were deposited in the protective gases of carbon dioxide and argon. As a result of structural studies, it was found that the internal structure of the model product in form of a wall can be divided into three zones. Repeated heating, cooling cycles and degree of accumulated heat influence the formation of different wall zones. As a result of rapid heat removal to the substrate during deposition of the first layers, the wall base (zone *1*) contains large elongated grains with acicular ferrite structure. The wall middle part (zone *2*) consists of ferrite-pearlite structure, which was formed as a result of recrystallization under conditions of repeated heating and cooling during 3D printing. The size of ferrite grains in zone *2* varies from 11 to 16.3 μm with increasing the number of layers. The gradual accumulation of heat during 3D printing led to the formation of structures in zone *3* under conditions of overheating and a reduced cooling rate. As a result, the wall upper part (zone *3*) consists of large ferrite grains (up to 29.8 μm), sorbite, and a small proportion of Widemanstatten ferrite and acicular ferrite. It is shown that the most uniform level of mechanical characteristics ($\sigma_{0.2}$ = 340 MPa, $\sigma_u$ = 470 MPa, ε = 28 %) correspond to the samples cut from zone *2* in a direction parallel to 3D printing direction. The samples cut in the vertical direction relative to 3D printing and from zone *3* show the lowest level of microhardness and mechanical characteristics ($\sigma_{0.2}$ = 260 MPa, $\sigma_u$ = 425 MPa, ε = 20 %).

***Keywords:*** additive technology, WAAM, GMAW, engineering steel, microstructure, mechanical properties, thermal cycling

***Acknowledgements:*** The work was performed within the framework of the state task of the Institute of Strength Physics and Materials Science, Siberian Branch of Russian Academy of Sciences, project No. FWRW-2021-0009.

***For citation:*** Vlasov I.V., Gordienko A.I., Kuznetsova A.E., Semenchuk V.M. Structure and mechanical properties anisotropy of a steel product manufactured by layer-by-layer electric arc wire 3D printing. *Izvestiya. Ferrous Metallurgy*. 2023;66(6):709–717.
https://doi.org/10.17073/0368-0797-2023-6-709-717

# Исследование структуры и анизотропии механических свойств стального изделия, полученного методом послойной электродуговой проволочной 3D-печати

**И. В. Власов** ✉, **А. И. Гордиенко, А. Е. Кузнецова, В. М. Семенчук**

**Институт физики прочности и материаловедения Сибирского отделения РАН** (Россия, 634055, Томск, пр. Академический, 2/4)

✉ viv@ispms.ru

***Аннотация***. В работе проведено исследование структуры и анизотропии механических свойств металлической стенки, полученной с помощью электродуговой проволочной 3D-печати (WAAM) проволокой ER70S-6. Нанесение слоев проводится в среде защитных газов: углекислого газа и аргона. В результате структурных исследований обнаружено, что внутреннюю структуру сформированного модельного изделия в виде элементарной стенки можно разделить на три зоны. Формирование разных зон стенки обусловлено многократными циклами нагрева и охлаждения участков стенки и степенью накопленного тепла по мере увеличения циклов 3D-печати. В результате быстрого теплоотвода в подложку при нанесении первых слоев основание стенки (зона *1*) содержит крупные вытянутые зерна со структурой игольчатого феррита. Средняя часть стенки (зона *2*) состоит из феррито-перлитной структуры, которая формируется

в результате перекристаллизации в условиях многократного нагрева и охлаждения при 3D-печати. Размер ферритных зерен в зоне *2* изменяется в пределах от 11 до 16,3 мкм по мере увеличения количества слоев. Постепенное накопление тепла при 3D-печати приводит к формированию структур в зоне *3* в условиях перегрева и сниженной скорости охлаждения, вследствие этого верхняя часть стенки (зона *3*) состоит из крупных ферритных зерен (размером до 29,8 мкм), сорбита, небольшой доли виндманштеттового и игольчатого феррита. Однородное распределение микротвердости и оптимальные механические характеристики ($\sigma_{0,2}$ = 340 МПа, $\sigma_в$ = 470 МПа, ε = 28 %) соответствует образцам, вырезанным из зоны *2* в направлении, параллельном 3D-печати. Образцы, вырезанные в вертикальном направлении относительно 3D-печати из зоны *3*, демонстрируют самые низкие микротвердость и механические характеристики ($\sigma_{0,2}$ = 260 МПа, $\sigma_в$ = 425 МПа, ε = 20 %).

***Ключевые слова:*** аддитивная технология, WAAM, GMAW, конструкционная сталь, микроструктура, механические свойства, термоциклирование

***Благодарности:*** Работа выполнена в рамках государственного задания Института физики прочности и материаловедения Сибирского отделения РАН, тема номер FWRW-2021-0009.

***Для цитирования:*** Власов И.В., Гордиенко А.И., Кузнецова А.Е., Семенчук В.М. Исследование структуры и анизотропии механических свойств стального изделия, полученного методом послойной электродуговой проволочной 3D-печати. *Известия вузов. Черная металлургия*. 2023;66(6):709–717. https://doi.org/10.17073/0368-0797-2023-6-709-717

## Introduction

Over the past few decades, there has been active development in additive manufacturing of products and the restoration of machine parts using this technology [1]. Additive technologies are in high demand in aviation, the space industry, medicine, and mechanical engineering, and their application is economically feasible for manufacturing prototypes and small-batch production. These technologies are unique and indispensable, particularly for producing parts with complex internal geometry, where the addition of internal stiffeners, the creation of channel systems inside the product, or the manufacturing of parts with minimal loss of expensive raw materials is essential [2]. Currently, various technologies for additive manufacturing of metal parts can be distinguished, including powder-based methods such as selective laser melting, direct laser deposition, and plasma-transferred arc hardfacing, as well as wire-based methods like electron beam wire-feed additive manufacturing and wire and arc additive manufacturing (WAAM) [3].

The WAAM process in a shielding gas environment (GMAW) is the most common, high-performance, cost-effective, and simple technology. This process offers rapid deposition rates of about 4 – 9 kg/h [4] and enables the creation of complex dimensional structures.

The technology of material deposition with a consumable electrode in the environment of shielding inert (MIG) or active (MAG) gases allows the deposition of a wide range of metals, including layer-by-layer deposition of difficult-to-machine alloys such as titanium [5; 6]. In some cases, subsequent heat treatment is required to obtain specified mechanical properties. Each layer in the 3D printing process undergoes multiple thermal heatings that attenuate when moving away from the place of a new layer deposition. All layers are unique as heat accumulates in the wall while heat removal is insufficient [7]. Consequently, the thermal history is shaped, leading to structural-phase transformations and alterations in internal stresses [8]. Uncontrolled thermal impact can pose a significant challenge for alloys requiring multi-stage heat treatment [9].

Another critical issue is the anisotropy of mechanical properties. The growth of columnar crystals during 3D printing, directed heat removal during cooling, the formation of layer boundaries, and the varying thermal stresses experienced by each layer result in heterogeneous mechanical properties in different cross-sections of the product [10]. This anisotropy in mechanical properties significantly complicates the process of designing and obtaining volumetric items with specified parameters.

The objective of this study was to investigate the features of structure formation during 3D printing with structural steel wire and its impact on the distribution of mechanical properties in different sections of the product.

## Materials and methods

A copper-coated ER70S-6 wire with a diameter of 1.2 mm was utilized for layer-by-layer 3D printing. As a substrate, we employed steel of 09G2S grade with a similar chemical composition, designed for the production of parts and elements in welded structures. The substrate was 10 mm thick and was selected to minimize thermal distortion during the 3D printing process. The chemical composition of the materials is provided in Table 1.

Metal wire deposition was carried out using a system comprising a FANUC AM-100iD multi-axis mechanized manipulator (Fig. 1, *a*) integrated with an EWM Titan XQ R 400 welding machine. The wire was deposited in GMAW mode by the MAG method, employing a mixture of carbon dioxide and argon in a ratio of 82 % Ar and 18 % $CO_2$. The optimal 3D printing parameters were pre-selected based on the synergistic curves provided by the manufacturer. This selection aimed to ensure stable arcing, minimal spattering, and the deposition of even layers.

Table 1

**Chemical composition of 09G2S substrate and ER70S-6 wire**

*Таблица 1*. **Химический состав материала подложки 09Г2С и проволоки ER70S-6**

| Material | Element content, wt. % | | | | | | | |
|---|---|---|---|---|---|---|---|---|
| | C | Si | Mn | Ni | Cr | Cu | P/S/N | Fe |
| 09G2S | up to 0.12 | 0.5 – 0.8 | 1.3 – 1.7 | up to 0.30 | up to 0.30 | up to 0.30 | up to 0.01 | ≈96.8 |
| ER70S-6 | 0.06 – 0.10 | 0.9 – 1.1 | 1.6 – 1.8 | up to 0.02 | up to 0.02 | up to 0.02 | up to 0.01 | ≈96.4 |

The most common structural element is the vertical wall, which was produced using 3D printing by depositing layers, each 100 mm long, in 50 passes. Layers were deposited at regular intervals (30 s) with a slight horizontal shift (2 mm) to increase the width of the wall. The welding torch was tilted at a 10° angle against the substrate, moved "backhand". The distance between the torch tip and the workpiece was approximately 10 – 12 mm.

The scheme for cutting samples from the wall is illustrated in Fig. 1, *b*. To conduct microstructural studies, a cross-section of the wall (highlighted in gray in Fig. 1, *b*) was fabricated, encompassing the substrate itself. This facilitated additional analysis of the microstructure in the heat-affected zone. The structural analysis of the samples was conducted using the Carl Zeiss Axiovert 25 microscope and LEO EVO 50 scanning electron microscope at the Nanotech Center for Collective Use of the Institute of Strength Physics and Materials Science, Siberian Branch, RAS. The ferrite grain size was determined using the method of counting intersections of grain boundaries (GOST 5639 – 82). Tensile samples were extracted from both the substrate and the wall, in both horizontal (from the top and bottom of the wall) and vertical directions relative to the 3D printing. The working part of the double-bladed shaped samples had dimensions of 4.0×1.5×40 mm. Static tensile tests were conducted on an Instron 5582 electromechanical machine with a crosshead travel speed of 0.6 mm/min. Microhardness was assessed using a PTM-3 device with a load on the Vickers pyramid of 0.98 N (100 g).

## Research results

### *Microstructural studies*

Following 3D printing in the GMAW print mode, the wall was successfully formed. The geometric characteristics of the wall include a height of 66 mm, a width ranging from 9.7 to 10.4 mm; and a 2 mm recess in the substrate.

Macroanalysis of the outer surface of the wall revealed that in the lower part, the boundaries between the layers are smooth and clear (Fig. 1, *c*). However, towards the top of the wall (approximately from its middle), undulating layer boundaries are formed.

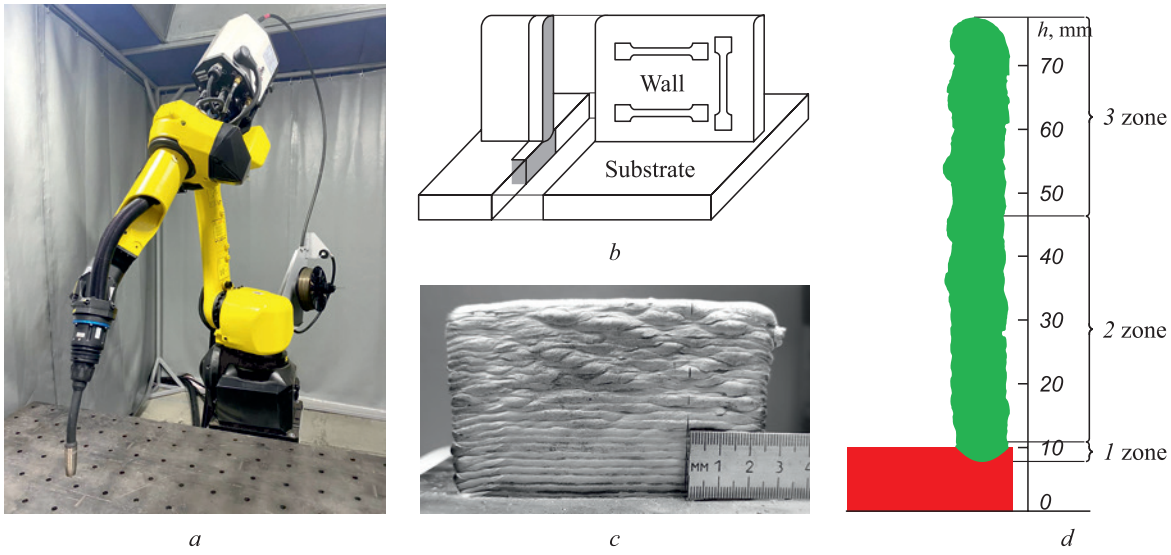


Fig. 1. Photograph of the FANUC ARC Mate-100iD multi-axis robot (*a*), samples cutting scheme (*b*), the wall photograph (*c*), the wall zones scheme (*d*)

Рис. 1. Фотография многоосевого робота FANUC ARC Mate-100iD (*a*), схема вырезки образцов (*b*), фотография стенки (*c*) и схема зон в стенке (*d*)

The 09G2S steel substrate exhibited a ferrite-perlite structure with pronounced banding in the rolling direction (Fig. 2, *a*). The average ferrite grain size was 18 ± 1 μm. In the heat-affected zone, the steel structure transitions from bainitic to ferrite-pearlitic (Fig. 2, *b*).

In the cross-section of the printed wall, three distinct zones can be identified, as illustrated in Fig. 1, *d*. The dimensions of zones *1*, *2*, and *3* were 3 mm (4 %), 35 mm (52 %), and 30 mm (44 %), respectively. It is worth noting that the sum of all zones exceeds the wall height due to zone *1* incorporating a portion of the melted substrate (Fig. 1, *c*).

Zone *1*, located at the base of the wall and the boundary layer with the substrate, is approximately 3 mm in height. It consists of large elongated columnar-shaped grains (Fig. 2, *d*). Allotriomorphic ferrite formed along the boundaries of former austenitic grains, with acicular ferrite developing inside the grains.

Zone *2* situated in the middle part of the wall, is approximately 35 mm in height and is characterized by ferrite grains with pearlite inclusions (Fig. 2, *e*). The average ferrite grain size in this zone varies from 11 ± 1 μm in the lower part of zone *2* to 16.3 ± 2 μm in the upper part, relative to the wall height.

Zone *3*, located in the upper part of the wall, is approximately 30 mm in height and comprises non-equiaxial ferrite grains, Widmanstätten ferrite, separate regions with acicular ferrite, and a pearlitic component (Fig. 2, *f*). The average size of ferrite grains in this zone is significantly larger, measuring 29.8 ± 2 μm.

At the microstructural level, the boundaries between the zones within the wall are not distinctly defined. The transitions between them are seamless and often occupy a substantial portion of the overall area.

The pearlite component and its distribution in the wall structure were examined in greater detail using a scanning

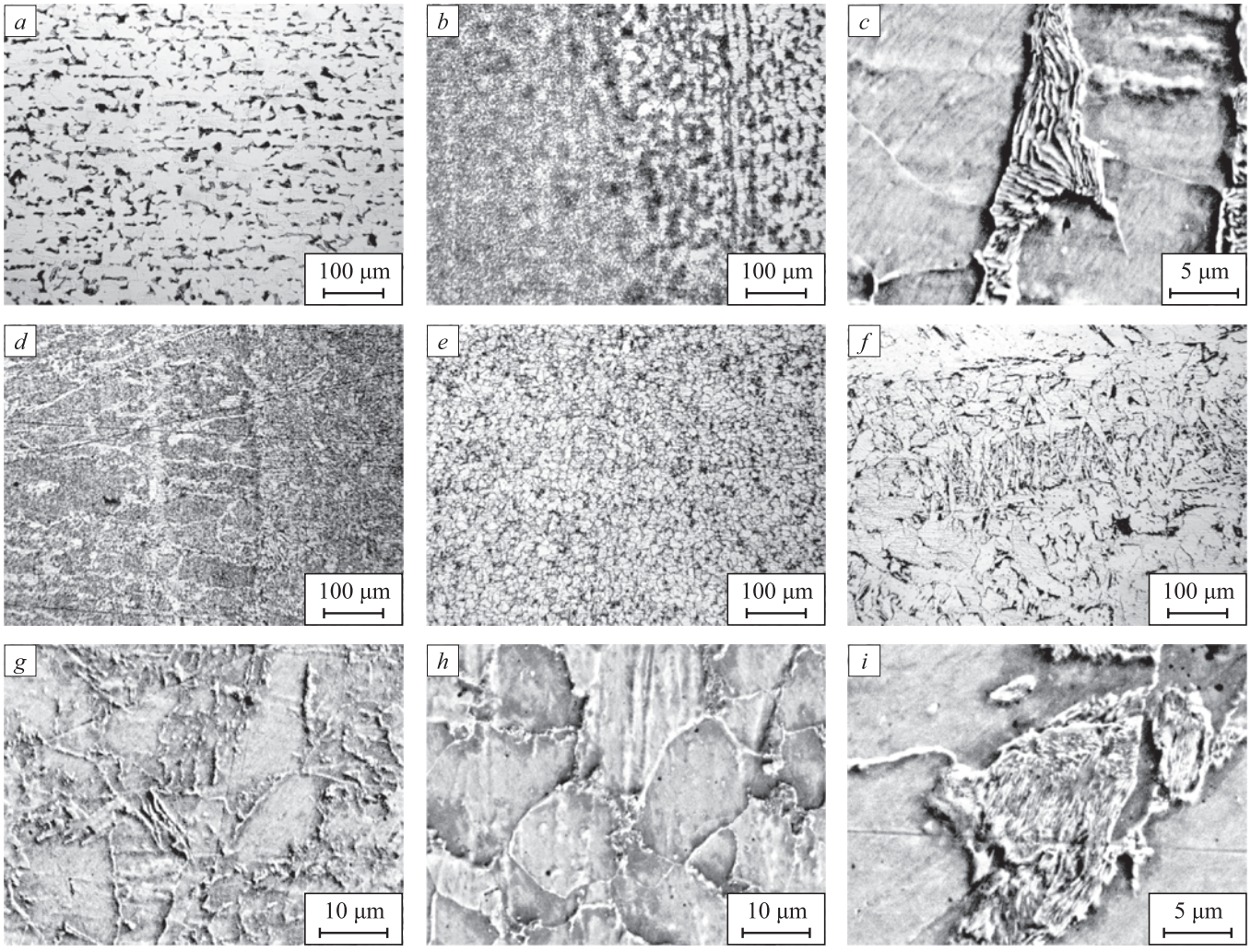


Fig. 2. Optical (*a*, *b*, *d* – *f*) and SEM (*c*, *g* – *i*) photographs of the substrate microstructure (*a* – *c*), the wall base (zones *1*) (*d*, *g*), the wall middle part (zones *2*) (*e*, *h*), the wall top parts (zone *3*) (*f*, *i*)

Рис. 2. Оптические (*a*, *b*, *d* – *f*) и РЭМ (*c*, *g* – *i*) фотографии микроструктуры подложки (*a* – *c*), основания стенки (зоны *1*) (*d*, *g*), средней части стенки (зоны *2*) (*e*, *h*), верхней части стенки (зоны *3*) (*f*, *i*)

electron microscope (Fig. 2, *c*, *h* – *i*). In the 09G2S steel substrate, lamellar pearlite with an interlamellar spacing of about 0.4 ± 0.04 μm was identified (Fig. 2, *c*). As the fusion boundary with the wall was approached, granular pearlite formed in the heat-affected zone. This granular pearlite is likely a result of insufficient austenitization during the short-term heating of the substrate, leading to an inhomogeneous carbon concentration in austenite.

No areas of pearlite were found in zone *1*. Instead, individual cementite particles and thin interlayers were observed near the boundaries of former austenitic grains and acicular ferrite (Fig. 2, *h*). In zone *2*, granular pearlite was observed, distributed along the ferrite grain boundaries (Fig. 2, *i*).

In zone *3*, the distribution of the pearlite component is heterogeneous. As one moves away from zone *2*, the proportion of granular pearlite in the structure decreases, and lamellar pearlite is formed instead (Fig. 2, *i*). The interlamellar spacing in the lamellar pearlite in zone *3* is 0.25 ± 0.03 μm, corresponding to the sorbite structure. In the upper part of the wall, within a distance of up to 3 mm from its top, the proportion of the pearlitic component decreases.

## Microhardness measurement

Microhardness measurements were conducted on the cross-section of the wall (Fig. 3, *a*). The origin on the abscissa corresponds to the rear part of the substrate (as depicted in Fig. 1, *d*). The microhardness of the substrate material was recorded as 1.6 GPa. In the heat-affected zone (~7 mm), microhardness initially decreased to 1.35 GPa and then returned to the initial values of the substrate material microhardness. As the fusion boundary is approached, microhardness increases in zone *1*. The acicular ferrite structure in zone *1* exhibits the highest microhardness values, reaching approximately 1.8 GPa. Given the limited length of this zone (Fig. 3, *a*), the graph only displays a portion of the measured points.

In zone *2* and partially in zone *3*, microhardness gradually decreases, with a more intensive reduction and greater spread of values observed in zone *3*. As the upper boundary of the wall is approached, microhardness increases from 1.3 to 1.5 GPa.

## Static tensile tests

Static tensile tests were conducted on samples cut in both horizontal (from the bottom and top of the wall) and vertical directions relative to 3D printing (Fig. 1, *b*). The need to test samples from the lower (zone *2*) and upper (zone *3*) parts of the wall arises from differences in both the macrogeometry of the layers (presence of undulating layer boundaries in zone *3*) and the microstructure in zones *2* and *3*.

In this study, the substrate and reference data on the mechanical properties of the ER70S-6 wire served as the baseline for evaluating the mechanical properties of the wall. The samples cut in the vertical and horizontal directions (from zone *3*) relative to 3D printing exhibit the lowest strength characteristics, even when compared to the substrate material (Fig. 3, *b*; Table 2). Simultaneously, the values of yield strength and tensile strength are close, but the plasticity of the samples from the vertical section is lower. Samples from the lower part of the wall (zone *2*) exhibit higher strength properties and are closer to the reference values of the wire's mechanical properties.

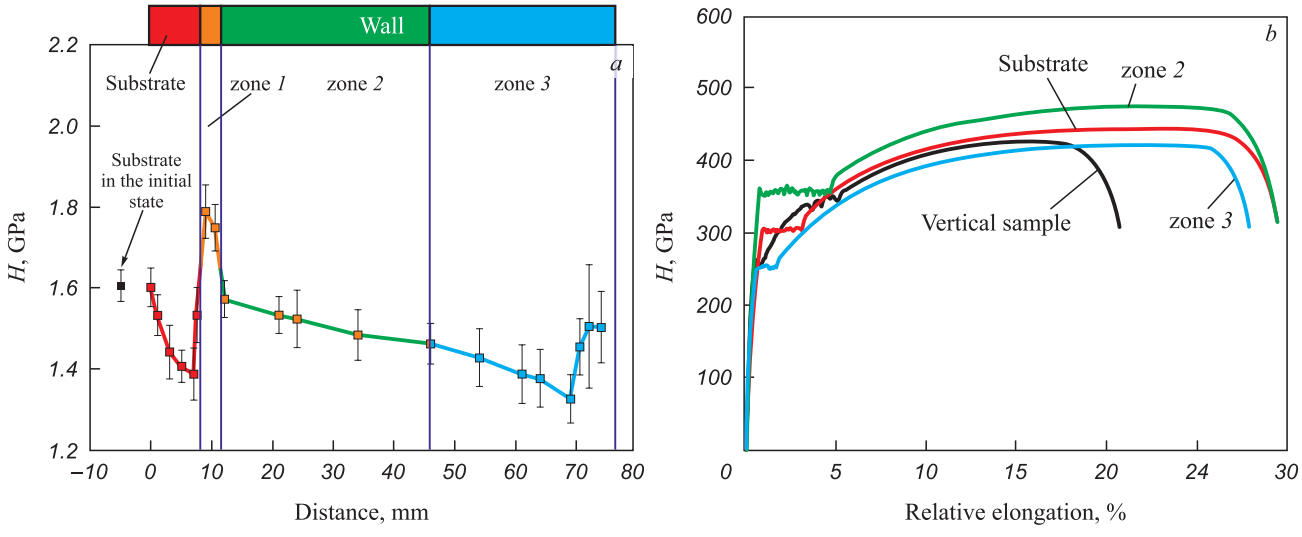


Fig. 3. Microhardness of the wall cross-section measured by its height (*a*), graphs of static tension (*b*)

Рис. 3. Микротвердость в поперечном сечении стенки, измеренная по ее высоте (*b*), диаграммы статического растяжения (*б*)

Table 2

**Results of static tensile test**

*Таблица 2*. **Результаты испытания на статическое растяжение**

| State | Part of the wall | $\sigma_{0.2}$, MPa | $\sigma_u$, MPa | ε, % |
|---|---|---|---|---|
| 09G2S substrate | – | 280 ± 7 | 440 ± 8 | 28 ± 3 |
| ER70S-6 (reference data) | – | – | 480 – 550 | 22 – 30 |
| GMAW | upper (zone *3*) | 260 ± 9 | 422 ± 11 | 26 ± 2 |
| | lower (zone *2*) | 340 ± 10 | 472 ± 10 | 28 ± 3 |
| | vertical section | 265 ± 11 | 428 ± 12 | 20 ± 2 |

Samples cut from zone *2* and the substrate demonstrate a wide yield plateau, whereas samples from zone *3* and the vertical wall section have a much smaller yield plateau. The samples from the vertical wall section fail at the weakest point of the sample corresponding to zone *3*, aligning with the calculated tensile strength in these regions of the wall.

## Results and discussion

Layer-by-layer printing of products induces cyclic heating and multiple phase transformations of underlying layers [11]. With an increase in the number of 3D printing passes, heat accumulates in the wall, and the cooling rate decreases. Over time, during the deposition of a new layer, excessive spreading and distortion occur due to heat accumulation in the wall. This "critical" heat accumulation begins approximately in the middle of the wall, where undulating layer boundaries are clearly visualized. A similar effect observed in 3D wall printing is discussed in [9].

The structure in zone *1* originated from the specific conditions during deposition of the first layers on the substrate. The 3D printing of the wall initiated at room temperature and was performed on a substrate mounted on a solid metal table. This setup significantly enhances heat removal for the initial wall layers, resulting in a high crystallization rate and a significant thermal gradient, facilitating the epitaxial growth of austenitic grains (Fig. 2, *d*) [12]. The formation of allotriomorphic ferrite along the boundaries of former austenitic grains suggests the occurrence of partial diffusion processes. However, acicular ferrite is formed internally, representing a structure of intermediate bainitic transformation, typical in welds [13]. A similar pattern of structure formation during 3D printing of walls is discussed in [7; 14 – 16].

For subsequent layers, heat removal was reduced, both due to substrate heating and a decrease in the contact area with the substrate. Consequently, during 3D printing, with the deposition of each new layer, the underlying layers experience overheating, resulting in recrystallization. Dispersed polygonal ferrite grains and granular pearlite are also formed (Fig. 2, *i*). Granular pearlite is formed due to cyclic heating of layers and insufficient holding time, limiting the time for adequate austenite homogenization.

The upper part of the wall (zone 3), being formed at higher heating temperatures affecting the underlying layers, reduced cooling rates, and sufficient homogenization of austenite, exhibits a predominantly ferrite-sorbitic structure with a small proportion of Widmanstatten and acicular ferrite. Similar results were demonstrated in [17; 18]. However, as the number of layers increases, and hence the heat build-up in the wall, the size of ferrite grains also increases (up to 29.8 ± 2 μm). The very last layers of the wall, due to direct contact with the atmosphere, cool at a higher rate and do not recrystallize as a result of reheating from the following layers [19], resulting in fewer sorbitic regions and a larger proportion of the bainitic component (Widmanstatten and acicular ferrite). This accounts for the less pronounced yield plateau of samples from zone 3 and the vertical wall section. Previous studies have shown that when more than 20 % of the bainite phase is present in the structure of low-carbon steel, the yield plateau in the tension graph completely disappears [20]. Another reason for the shorter yield plateau may be the coarse-grained structure, as fine-grained steels are known to have a longer yield plateau and higher yield strength due to a larger number of contact resistances at grain boundaries compared to coarse-grained steels. The inhomogeneous deformation on the parabolic part of the load curve of the sample from the vertical section may be related to its having an inhomogeneous structure, as it was cut from the wall region containing zones *2* and *3*.

Changes in microstructure along the wall height correlate with with variations in microhardness (Fig. 3, *a*). Microhardness decreases in the heat-affected zone of the substrate material due to several reasons. As the first layers form with short-term substrate heating, the material undergoes tempering, and granular pearlite is formed. The microhardness in zone *1* increases (up to about 1.8 GPa) due to the formation of the acicular ferrite structure. Residual stresses resulting from abrupt

heat removal [19] can also contribute to the increase in microhardness.

In zone *2*, microhardness gradually decreases as the ferrite-perlite structure forms, and the grain sizes increase from 11 ± 1 to 16.3 ± 2 μm due to heat accumulation during layer deposition and a lower cooling rate. Microhardness in zone *3* further decreases (to 1.3 GPa) owing to an increase in the average grain size to 29.8 ± 2 μm. Closer to the top of the wall, corresponding to the last deposited layers, microhardness increases (from 1.3 to 1.5 GPa) due to a higher cooling rate and an increase in the proportion of Widmanstatten and acicular ferrite. The boundary of this transition corresponds to a depth of 4 mm from the top of the wall (zone *3*) and is accompanied by a large spread of microhardness values. This is because structures with very different microhardness values are formed, such as large ferrite grains and regions of acicular ferrite.

Thus, the most uniform level of microhardness values and the most optimal mechanical characteristics are observed in zone *2*. As the wall sections are formed, the main issues causing increased microhardness (zone *1*) or, on the contrary, decreased values of this parameter (zone *3*) are the excessively high cooling rate due to the rapid heat removal to the substrate or severe overheating in the upper part of the wall due to low heat removal. Possible solutions to these problems may include, firstly, substrate preheating aimed at reducing the cooling rate in the first layers, and secondly, an increase in the time interval before depositing each layer to allow the previously formed layers to cool to the specified temperature.

## Conclusions

We investigated the structure and mechanical properties of the steel wall produced using the electric arc additive technology (WAAM) with ER70S-6 wire on the substrate made of 09G2S steel.

Due to the rapid heat removal to the substrate during the initial stages of 3D printing, large austenitic grains with a columnar shape are formed in the structure of the wall base (zone *1*). Along the grain boundaries, allotriomorphic ferrite is released during rapid cooling, and within them, bainite transformation occurs, leading to the formation acicular ferrite. This type of structure is characterized by the highest microhardness values (up to 1.8 GPa).

The middle part of the wall (zone *2*) consists of ferrite grains (11 ± 1 to 16.3 ± 2 μm in size) with inclusions of granular pearlite. This dispersed structure is formed through recrystallization during cyclic heating and a decrease in the cooling rate caused by heat accumulation during multiple 3D printing passes. The formation of this structure results in lower microhardness in zone *2* (up to 1.3 GPa) compared to microhardness in zone *1*. The increased values of accumulated heat and overheating in the upper zones of the wall lead to excessive "spreading" of the forming layers and formation of undulating boundaries (zone *3*).

High temperatures and low cooling rates result in the formation of a coarse-grained structure (with a grain size up to 29.8 ± 2 μm), including sections of ferrite and sorbite with inclusions of Widemanstatten and acicular ferrite. Consequently, the microhardness decreases to 1.3 GPa in this zone.

Static tensile tests revealed anisotropy in the mechanical properties of the wall material in different directions relative to 3D printing. The best mechanical properties were recorded in the lower part of the wall (zone *2*) for the samples cut in the horizontal direction ($\sigma_{0.2}$ = 340 MPa, $\sigma_u$ = 470 MPa). The samples cut in the vertical direction relative to 3D printing from zone *3* exhibited the worst strength characteristics ($\sigma_{0.2}$ = 260 MPa, $\sigma_u$ = 425 MPa).

## References / Список литературы

1. Gibson I., Rosen D., Stucker B. *Additive Manufacturing Technologies: 3D Printing, Rapid Prototyping, and Direct Digital Manufacturing*. NY: Springer New York; 2015:498. https://doi.org/10.1007/978-1-4939-2113-3
2. Senthil T.S., Babu S.R., Puviyarasan M., Dhinakaran V. Mechanical and microstructural characterization of functionally graded Inconel 825-SS316L fabricated using wire arc additive manufacturing. *Journal of Materials Research and Technology*. 2021;15:661–669. https://doi.org/10.1016/j.jmrt.2021.08.060
3. Jafari D., Vaneker T.H.J., Gibson I. Wire and arc additive manufacturing: Opportunities and chellenges to control the quality and accuracy of manufactured parts. *Materials & Design*. 2021;202:109471. https://doi.org/10.1016/j.matdes.2021.109471
4. Buchanan C., Gardner L. Metal 3D printing in construction: A review of methods, research, applications, opportunities and challenges. *Engineering Structures*. 2019;180:332–348. http://doi.org/10.1016/j.engstruct.2018.11.045
5. Lin Z., Song K., Yu X. A review on wire and arc additive manufacturing of titanium alloy. *Journal of Manufacturing Processes*. 2021;70:24–45. https://doi.org/10.1016/j.jmapro.2021.08.018
6. Wu B., Ding D., Pan Z., Cuiuri D., Li H., Han J., Fei Z. Effects of heat accumulation on the arc characteristics and metal transfer behavior in wire arc additive manufacturing of Ti6Al4V. *Journal of Materials Processing Technology*. 2017;250:304–312. http://doi.org/10.1016/j.jmatprotec.2017.07.037
7. Shamsujjoha M., Licavoli J., Lin B., Harma E., Patterson R., Timmermann T., Groeneveld M., McLeod L., Sanders P. Tailoring microstructure of wire arc additively manufactured C–Mn–Si steel with post process heat treatment. *Materials Science and Engineering: A*. 2021;825:141921. https://doi.org/10.1016/j.msea.2021.141921

**8.** Astafurova E.G., Astafurov S.V., Revunova K.A., Mel'nikov E.V., Moskvina V.A., Panchenko M.V., Maier G.G., Rubtsov V.E., Kolubaev E.A. Regularities of structure formation in chromium-manganese vanadium-containing steel with a high concentration of C + N = 1,9 wt. % in electron beam additive manufacturing. *Fizicheskaya mezomekhanika*. 2021;24(3):5–16. (In Russ.). https://doi.org/10.24412/1683-805X-2021-3-5-16

Астафурова Е.Г., Астафуров С.В., Ревунова К.А., Мельников Е.В., Москвина В.А., Панченко М.В., Майер Г.Г., Рубцов В.Е., Колубаев Е.А. Закономерности формирования структуры в хромомарганцевой ванадийсодержащей стали с высокой концентрацией атомов внедрения C + N = 1,9 мас. % при электронно-лучевом аддитивном производстве. *Физическая мезомеханика*. 2021;24(3):5–16. https://doi.org/10.24412/1683-805X-2021-3-5-16

**9.** Huang C., Kyvelou P., Zhang R., Ben Britton T., Gardner L. Mechanical testing and microstructural analysis of wire arc additively manufactured steels. *Materials & Design*. 2022;216:110544. https://doi.org/10.1016/j.matdes.2022.110544

**10.** Sun L., Jiang F., Huang R., Yuan D., Guo C., Wang J. Anisotropic mechanical properties and deformation behaviour of low-carbon high-strength steel component fabricated by wire and arc additive manufacturing. *Materials Science and Engineering: A*. 2020;787:139514. http://dx.doi.org/10.1016/j.msea.2020.139514

**11.** Panchenko O., Kladov I., Kurushkin D., Zhabrev L., Ryl'kov E., Zamozdra M. Effect of thermal history on microstructure evolution and mechanical properties in wire arc additive manufacturing of HSLA steel functionally graded components. *Materials Science and Engineering: A*. 2022;851:143569. https://doi.org/10.1016/j.msea.2022.143569

**12.** Razumov I.K., Gornostyrev Yu.N., Katsnelson M.I. Towards the ab initio based theory of phase transformations in iron and steel. *Physics of Metals and Metallography*. 2017; 118(4):362–388. https://doi.org/10.1134/S0031918X16130032

Разумов И.К., Горностырев Ю.Н., Кацнельсон М.И. К теории фазовых превращений в железе и стали на основе первопринципных подходов. *Физика металлов и металловедение*. 2017;118(4):380–408. https://doi.org/10.7868/S001532301704009X

**13.** Lan L., Kong X., Qiu C., Zhao D. Influence of microstructural aspects on impact toughness of multi-pass submerged arc welded HSLA steel joints. *Materials & Design*. 2016;90:488–498. https://doi.org/10.1016/j.matdes.2015.10.158

**14.** Anand M., Kumar Das A. Grain refinement in wire-arc additive manufactured Inconel 82 alloy through controlled heat input. *Journal of Alloys and Compounds*. 2022; 929:166949. https://doi.org/10.1016/j.jallcom.2022.166949

**15.** Yehorov Y., Da Silva L.J., Scotti A. Exploring the use of switchback for mitigating homoepitaxial unidirectional grain growth and porosity in WAAM of aluminium alloys. *The International Journal of Advanced Manufacturing Technology*. 2019;104(1-4):1581–1592. https://doi.org/10.1007/s00170-019-03959-w

**16.** Basak A., Das S. Epitaxy and microstructure evolution in metal additive manufacturing. *Annual Review of Materials Research*. 2016;46:125–149. https://doi.org/10.1146/annurev-matsci-070115-031728

**17.** Aldalur E., Veiga F., Suárez A., Bilbao J., Lamikiz A. High deposition wire arc additive manufacturing of mild steel: Strategies and heat input effect on microstructure and mechanical properties. *Journal of Manufacturing Processes*. 2020;58:615–626. https://doi.org/10.1016/j.jmapro.2020.08.060

**18.** He J., Feng X., Wang X., Guan X. Fatigue performance and acoustic emission behavior of remanufactured low-carbon steel made by wire and arc additive manufacturing. *International Journal of Fatigue*. 2022;165:107190. https://doi.org/10.1016/j.ijfatigue.2022.107190

**19.** Rani K.U., Kumar R., Mahapatra M.M., Mulik R.S., Świerczyńska A., Fydrych D., Pandey C. Wire arc additive manufactured mild steel and austenitic stainless steel components: Microstructure, mechanical properties and residual stresses. *Materials*. 2022;15(20):7094. https://doi.org/10.3390/ma15207094

**20.** Efron L.I. *Metals Science in Big Metallurgy: Pipe Steels*. Moscow: Metallurgizdat; 2012:694. (In Russ.).

Эфрон Л.И. *Металловедение в большой металлургии: Трубные стали*. Москва: Металлургиздат; 2012:694.

## Information about the Authors / Сведения об авторах

***Il'ya V. Vlasov,*** *Cand. Sci. (Eng.), Research Associate of the Laboratory of Physical Mesomechanics and Non-Destructive Testing,* Institute of Strength Physics and Materials Science, Siberian Branch Russian Academy of Sciences
***ORCID:*** 0000-0001-9110-8313
***E-mail:*** viv@ispms.ru

***Илья Викторович Власов,*** *к.т.н., научный сотрудник лаборатории физической мезомеханики и неразрушающих методов контроля,* Институт физики прочности и материаловедения Сибирского отделения РАН
***ORCID:*** 0000-0001-9110-8313
***E-mail:*** viv@ispms.ru

***Antonina I. Gordienko,*** *Cand. Sci. (Eng.), Research Associate of the Laboratory of Physical Mesomechanics and Non-Destructive Testing,* Institute of Strength Physics and Materials Science, Siberian Branch Russian Academy of Sciences
***ORCID:*** 0000-0002-4361-8906
***E-mail:*** mirantil@ispms.ru

***Антонина Ильдаровна Гордиенко,*** *к.т.н., научный сотрудник лаборатории физической мезомеханики и неразрушающих методов контроля,* Институт физики прочности и материаловедения Сибирского отделения РАН
***ORCID:*** 0000-0002-4361-8906
***E-mail:*** mirantil@ispms.ru

***Anastasya E. Kuznetsova,*** *Postgraduate, Junior Researcher of the Laboratory of Structural Design and Advanced Materials,* Institute of Strength Physics and Materials Science, Siberian Branch Russian Academy of Sciences
***ORCID:*** 0000-0001-6966-8402
***E-mail:*** aekuznetsova@ispms.ru

***Анастасия Евгеньевна Кузнецова,*** *аспирант, младший научный сотрудник лаборатории структурного дизайна перспективных материалов,* Институт физики прочности и материаловедения Сибирского отделения РАН
***ORCID:*** 0000-0001-6966-8402
***E-mail:*** aekuznetsova@ispms.ru

***Vyacheslav M. Semenchuk,*** *Junior Researcher of the Laboratory of Local Metallurgy in Additive Manufacturing Technologies,* Institute of Strength Physics and Materials Science, Siberian Branch Russian Academy of Sciences
***ORCID:*** 0000-0002-7215-0505
***E-mail:*** svm_70@ispms.ru

***Вячеслав Максимович Семенчук,*** *младший научный сотрудник лаборатории локальной металлургии в аддитивных технологиях,* Институт физики прочности и материаловедения Сибирского отделения РАН
***ORCID:*** 0000-0002-7215-0505
***E-mail:*** svm_70@ispms.ru

## Contribution of the Authors / Вклад авторов

***I. V. Vlasov*** – formation of the main concept, goals and objectives; writing the text, literary review, data analysis.

***A. I. Gordienko*** – results processing, data analysis, revising the text.

***A. E. Kuznetsova*** – conducting experimental studies, results processing, data analysis.
***V. M. Semenchuk*** – selection of additive manufacturing modes, results discussion.

***И. В. Власов*** – формирование основной концепции, цели и задач исследования; написание текста статьи, литературный обзор публикаций по теме, анализ экспериментальных данных.
***А. И. Гордиенко*** – обработка результатов и анализ данных, доработка текста.
***А. Е. Кузнецова*** – проведение экспериментальных исследований, обработка результатов и анализ данных.
***В. М. Семенчук*** – подбор режимов проведения аддитивнго формования, обсуждение полученных результатов.

Received 27.04.2023
Revised 13.06.2023
Accepted 11.09.2023

Поступила в редакцию 27.04.2023
После доработки 13.06.2023
Принята к публикации 11.09.2023

**MATERIALS SCIENCE / МАТЕРИАЛОВЕДЕНИЕ**

**UDC** 538.913
**DOI** 10.17073/0368-0797-2023-6-718-724



*Original article*
*Оригинальная статья*

# Interaction of cracks with grain boundaries in iron bicrystals

**D. S. Kryzhevich ✉, A. V. Korchuganov, K. P. Zol'nikov**

**Institute of Strength Physics and Materials Science, Siberian Branch of the Russian Academy of Sciences** (2/4 Akademicheskii Ave., Tomsk 634055, Russian Federation)

✉ kryzhev@ispms.ru

***Abstract***. Molecular dynamic modelling of seed cracks evolution in iron bicrystals with inclined grain boundaries under uniaxial expansion was carried out. The process of seed crack evolution can be divided into four stages. At the first stage, in the interval of elastic deformations, the seed crack is stationary, and the stresses increase linearly, reaching a maximum value of ~7.0 GPa. At the same time, the atomic volume and stresses at the crack tip before its opening grow significantly faster than the average for the sample. At the second stage, the crack begins to spread into the grain volume. The process of crack propagation leads to an abrupt stress release due to relaxation processes in the areas adjacent to the crack banks and the emission of defects from the crack tip. After reaching the grain boundary, the crack stops and blunts. At the third stage, the crack remains in the grain boundary, and the sample stresses experience significant oscillations, which is caused by the emission of various defects both from the grain boundary and from other interfaces. The emission of defects from the crack tip can cause local migration of the grain boundary, which is formation of a bend on the initially flat surface of the grain boundary. When defects cease to be emitted from the crack tip, the voltage and atomic volume in this region increase rapidly. At the fourth stage, the crack begins to spread into the second grain. It was found that a boundary with a large grain misorientation angle is a more effective barrier restraining crack propagation. Initiation of the seed crack propagation in material is always preceded by an abrupt increase in atomic volume and stresses at the crack tip.

***Keywords:*** molecular dynamics, crack, excess atomic volume, iron, uniaxial tension

***Acknowledgements:*** The work was performed within the framework of the state task of the Institute of Strength Physics and Materials Science, Siberian Branch of Russian Academy of Sciences, project No. FWRW-2021-0002.

***For citation:*** Kryzhevich D.S., Korchuganov A.V., Zol'nikov K.P. Interaction of cracks with grain boundaries in iron bicrystals. *Izvestiya. Ferrous Metallurgy*. 2023;66(6):718–724. https://doi.org/10.17073/0368-0797-2023-6-718-724

# Взаимодействие трещины с границей зерен в бикристаллах железа

**Д. С. Крыжевич ✉, А. В. Корчуганов, К. П. Зольников**

**Институт физики прочности и материаловедения Сибирского отделения РАН** (Россия, 634055, Томск, пр. Академический, 2/4)

✉ kryzhev@ispms.ru

***Аннотация***. Проведено молекулярно-динамическое моделирование эволюции затравочных трещин в бикристаллах железа с наклонными границами зерен при одноосном растяжении. Показано, что процесс эволюции затравочной трещины можно разбить на четыре этапа. На первом этапе в интервале упругих деформаций затравочная трещина неподвижна, а напряжения увеличиваются по линейному закону, достигая максимального значения ~7,0 ГПа. При этом атомный объем и напряжения в вершине трещины перед ее раскрытием растут существенно быстрее, чем в среднем по образцу. На втором этапе трещина начинает распространяться в объем зерна. Процесс распространения трещины приводит к скачкообразному сбросу напряжения за счет релаксационных процессов в областях, прилегающих к берегам трещины, и эмиссии дефектов из вершины трещины. Достигнув границы зерен, трещина останавливается и затупляется. На третьем этапе трещина остается в границе зерен, а напряжения образца испытывают существенные осцилляции, что вызвано эмиссией различных дефектов как из границы зерен, так и из других интерфейсов. Эмиссия дефектов из вершины трещины может вызвать локальную миграцию границы зерен, которая представляет собой формирование изгиба на изначально плоской поверхности границы зерен. Когда из вершины трещины перестают испускаться дефекты, то напряжение и атомный объем в этой области быстро увеличиваются. На четвертом этапе трещина начинается распространяться во второе зерно. Обнаружено, что граница с большим углом разориентации зерен является более эффективным барьером, сдерживающим распространение трещины. Показано, что инициированию распространения затравочной трещины в материале всегда предшествует скачкообразный рост атомного объема и напряжений в вершине трещины.

***Ключевые слова:*** молекулярная динамика, трещина, избыточный атомный объем, железо, одноосное растяжение

***Благодарности:*** Работа выполнена в рамках государственного задания Института физики прочности и материаловедения Сибирского отделения РАН, тема номер FWRW-2021-0002.

***Для цитирования:*** Крыжевич Д.С., Корчуганов А.В., Зольников К.П. Взаимодействие трещины с границей зерен в бикристаллах железа. *Известия вузов. Черная металлургия*. 2023;66(6):718–724. https://doi.org/10.17073/0368-0797-2023-6-718-724

## Introduction

Numerous studies have been dedicated to investigating the fracture behavior of iron at the microscopic level. The primary research objective was to ascertain how the fracture processes in the material are influenced by internal structural features such as defects, nanoparticles, and grain sizes [1 – 4], along with the application of various loading schemes involving boundary conditions and loading rates [5], as well as different interatomic potentials [6]. Grain boundaries (GBs) play an important role in initiating and propagating fractures within the material. The interaction between cracks and grain boundaries is determined by several parameters, which can be categorized into two groups [7]. The first group encompasses the type and rate of the applied load, crack parameters, in particular, length and distance from the crack to the grain boundary, which influence stress concentration at the crack tip, serving as a driving force for dislocation emission and motion. The second group comprises grain boundary parameters, defining the resistance level to crack propagation. Two predominant models are commonly employed to describe the interaction between cracks and grain boundaries. The first model, developed and detailed in [8; 9], attributes the resistance of a grain boundary to crack propagation solely to the orientation of an adjacent grain. This orientation determines the positions of slip planes in the second grain and the emission of dislocations in the corresponding slip systems. In the second model [10; 11], the slip plane in the adjacent grain is considered differently. Specifically, the crack must alter the slip plane in the mating grain as it crosses the grain boundary. This model introduces two additional parameters determining the resistance value for crack propagation: the grain boundary surface energy characteristic of different types of grain boundaries and the grain boundary tilt angle concerning the surface.

Crack propagation and fracture represent intricate phenomena involving the rupture of atomic bonds and the emission of dislocations from the crack tip. The linear theory of elasticity posits that stress fields at the crack tip are singular [12]. Atomistic modeling of fracture processes offers a way to eliminate singularity and compute accurate stress fields [13; 14]. In the context of brittle material under loading mode *I*, we utilized molecular dynamics to calculate stresses, local temperature at the crack tip, and the emission of dislocations from the crack. Previous works [15; 16] demonstrated that the initiation of partial dislocations at the crack tip under shear load is significantly influenced by temperature. Additionally, loading modes *I*, *II*, *III*, or their combinations in an iron single crystal markedly affect crack behavior [13]. However, the plasticity at the crack tip is determined by the crystallographic orientation of the sample.

For the study of fracture evolution in materials with a grain structure, it is crucial to identify specific features of the interaction between cracks and grain boundaries. Experimental investigation of crack interaction in materials with specific grain boundaries is challenging. Molecular dynamics, however, provides an effective method for exploring crack interaction with any grain boundaries. Despite its efficacy, there are limited studies on iron bicrystals, with the notable exception of the work [17]. This study was devoted to the fracture resistance of symmetric tilt grain boundaries in iron bicrystals with a seed crack, revealing an inverse relationship between crack delay time at the grain boundary and the grain boundary energy.

The aim of the present work is molecular dynamics modeling of the peculiarities of interaction between cracks propagating in the brittle mode and tilt boundaries in iron bicrystals under uniaxial tension. We investigated the influence of grain boundaries on the retardation and arrest of propagating cracks, peculiarities of grain boundary migration when interacting with the crack, as well as the special features of changes in the excess atomic volume and stress at the crack tip during its evolution and interaction with grain boundaries in iron bicrystals.

## Методы исследования

The simulated iron bicrystals comprised approximately 950,000 atoms and exhibited parallelepiped shapes with edge dimensions of 27×40×10 nm (Fig. 1). In Fig. 1, the edges of the grains on the right consistently followed the directions *X* [1$\bar{2}$0], *Y* [210], *Z* [001]. Notably, the grain on the left side of the bicrystal was subjected to a rotation about the *Z*-axis, with angles of either 10 or 20°. In the simulated samples, the initial temperature was set at 10 K. Free surfaces were set along the *X*-axis, and periodic boundary conditions were applied along the *Z*-axis. Non-deformable grips, consisting of three surface atomic planes with a normal along the *Y*-axis, were configured and moved in opposite directions along the *Y*-axis at 2.5 m/s each, simulating uniaxial tension in the sample.

The interatomic interaction in iron was characterized by a multiparticle potential developed within the frame-

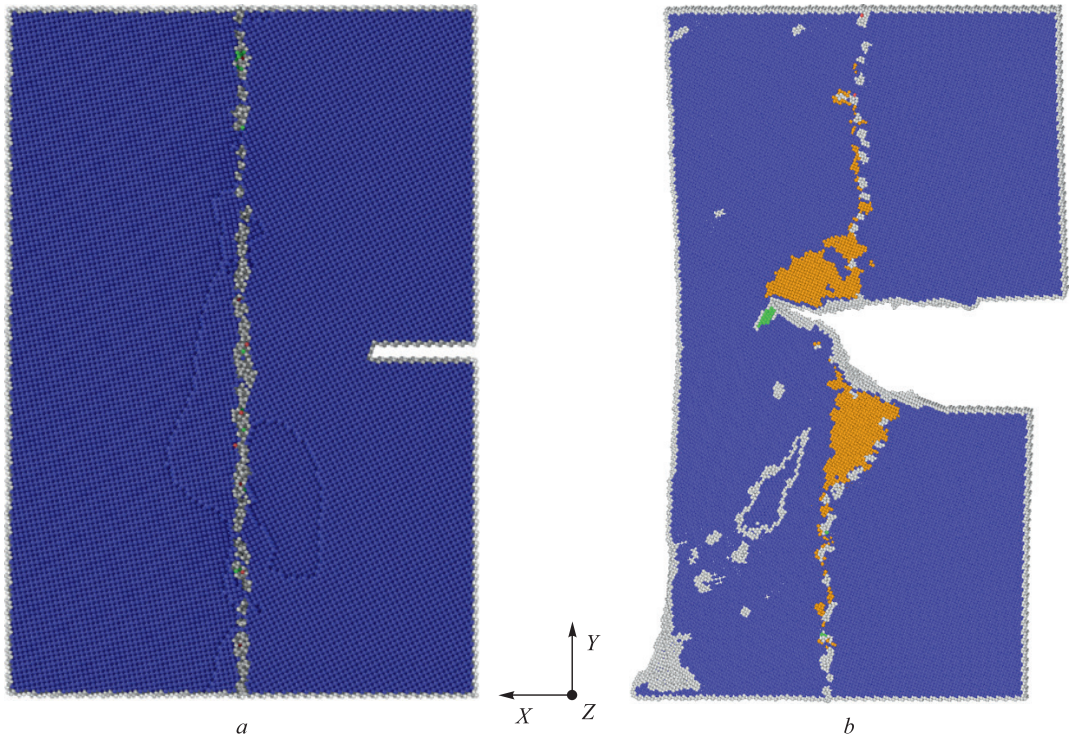


Fig. 1. Initial structure of a Fe bicrystal with grain misorientation 10° (*a*) and structure of the sample deformed by 16.3 % (*b*) (green, blue and gray atoms have the nearest neighbors with FCC, BCC and uncertain symmetry, respectively; orange – atoms across which the grain boundary passes)

Рис. 1. Исходная структура бикристалла железа с разориентацией зерен 10° (*a*) и структура образца, деформированного на 16,3 % (*b*) (зеленым, синим, серым и оранжевым показаны атомы с ГЦК, ОЦК, неопределенной симметрией ближайшего окружения и атомы, через которые проходит ГЗ)

work of the Finnis–Sinclair approximation of the embedded atom method [18]. The initial distribution of atomic velocities in the sample conformed to the Maxwell distribution, with the initial direction of atomic velocities determined using a random number generator. The integration step was set at 1 fs. Atomic volumes were computed based on the construction of Voronoi polyhedra. To identify local structural changes in the loaded sample, the Common Neighbor Analysis pattern for each atom was employed [19]. The tilt angle of the local lattice relative to the axis [100] was determined using the Polyhedral Template Matching (PTM) algorithm [20]. Visualization of the simulated crystallite structure was accomplished using the OVITo software [21].

To compute the excess volume at the crack tip, a simulated cylinder with a radius $R = 1.2$ nm was employed. The crack tip was designated as one of the atoms on the crack surface with the maximum coordinate along the $X$-axis, and the cylinder's axis aligned with the $Z$-axis. To determine the atomic volume at the crack tip, the cylinder was systematically shifted along the $X$- and $Y$-axes, covering a range from $-R$ to $+R$ relative to the crack tip atom, with an increment of $0.1R$. The total volume of atoms within the cylinder was calculated as the sum of Voronoi cell volumes, and the maximum value was selected. The excess atomic volume was defined as the disparity between the Voronoi cell volume and the equilibrium atomic volume at the given temperature. The average excess volume at the crack tip was computed based on the excess volumes of atoms within the cylinder with the maximum volume.

To calculate grain boundary around each atom, the tilt angle of the local lattice from the $X$-axis was determined using the PTM algorithm. Atoms deviating from the chosen axis by more than half the value of the grain misorientation angle were considered part of the second grain, while the remaining atoms constituted the first grain. Through the loading process, atoms transitioning from one grain to another were identified. The sample volume ($dV$) through which the grain boundary migrated relative to its initial position was determined as the total atomic volume of these migrating atoms (Fig. 1, *b*). The parameter for GB migration in the $X$-axis direction was determined using the formula: $L_{GB} = dV/S_X$ where $S_X$ is the cross-sectional area of the sample deformed by the plane perpendicular to the $X$-axis.

## Results of the crack behavior modeling

The stress-strain dependencies for bicrystals with misoriented grain boundaries of 10 and 20° are presented in Fig. 2. Notably, the sample with a 20° grain misorientation

fractures at a considerably higher strain, approximately 26 %. Despite the difference in fracture strain, the qualitative behavior of the curves for these two grain boundaries is generally similar. The deformation curves in Fig. 2 reveal that the crack propagation process in bicrystals unfolds in four distinct stages. Focusing on the detailed analysis of the fracture evolution in the sample with a 10° grain misorientation, the first stage occurs in the elastic deformation range of 0 – 4.8 %. During this stage, the seed crack remains stationary, and stresses increase linearly, reaching a maximum value of around 7.0 GPa. The accumulated internal energy in this deformation range is sufficient to rupture interatomic bonds at the crack tip. Moving to the second stage, within the deformation range of 4.8 – 5.2 %, the crack initiates propagation in the first grain. As the crack advances, a stacking fault is emitted from the crack tip, reaching the grain boundary ahead of the crack (Fig. 3, *a*). The dislocation is emitted into the second grain from the portion of the grain boundary reached by the stacking fault. The process of crack propagation results in an abrupt release of stress due to relaxation processes in the regions adjacent to the crack edges and the emission of defects from both the crack tip and the grain boundary. Upon reaching the grain boundary, the crack comes to a halt and undergoes blunting (Fig. 3, *b*, *c*). During the third stage, the crack remains within the grain boundary, and the sample stresses may undergo significant oscillations. These oscillations are attributed to the emission of various defects from both the grain boundary and the free surface of the second grain (Fig. 3, *c*). Notably, the emission of defects from the crack tip during this stage leads to local grain boundary migration in the vicinity of the crack, as clearly depicted in Fig. 3, *b* and *c*. During the third stage of crack evolution, it is noteworthy that stresses distribute unevenly across the sample as interfaces emit a substantial number of defects. The overall sample stress tends to decrease with increasing strain. However, if defects cease to be emitted from the crack tip, the stress in this specific region starts to rapidly grow, contrary to the decreasing trend observed in the entire sample. The onset of the fourth stage involves crack propagation into the second grain (Fig. 3, *d*), leading to an abrupt release of stress throughout the entire sample. Importantly, it should be emphasized that a boundary with a significant grain misorientation angle acts as a more effective barrier, restraining crack propagation into the adjacent grain and resulting in larger strain values.

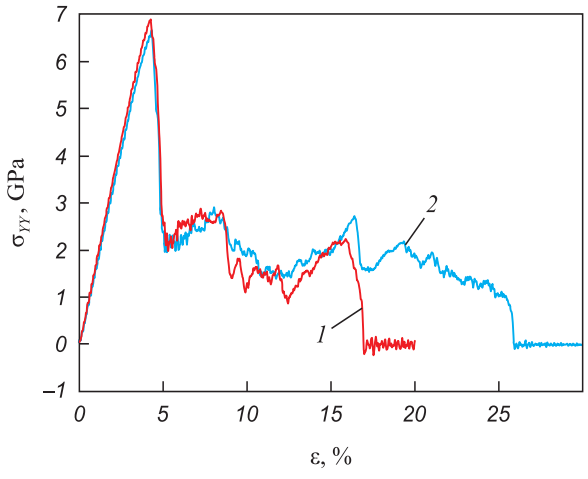


Fig. 2. Stress-strain dependences for the samples with misoriented grain boundaries 10° (*1*) and 20° (*2*)

Рис. 2. Зависимость напряжений от деформации для образцов с разориентацией границ зерен 10° (*1*) и 20° (*2*)

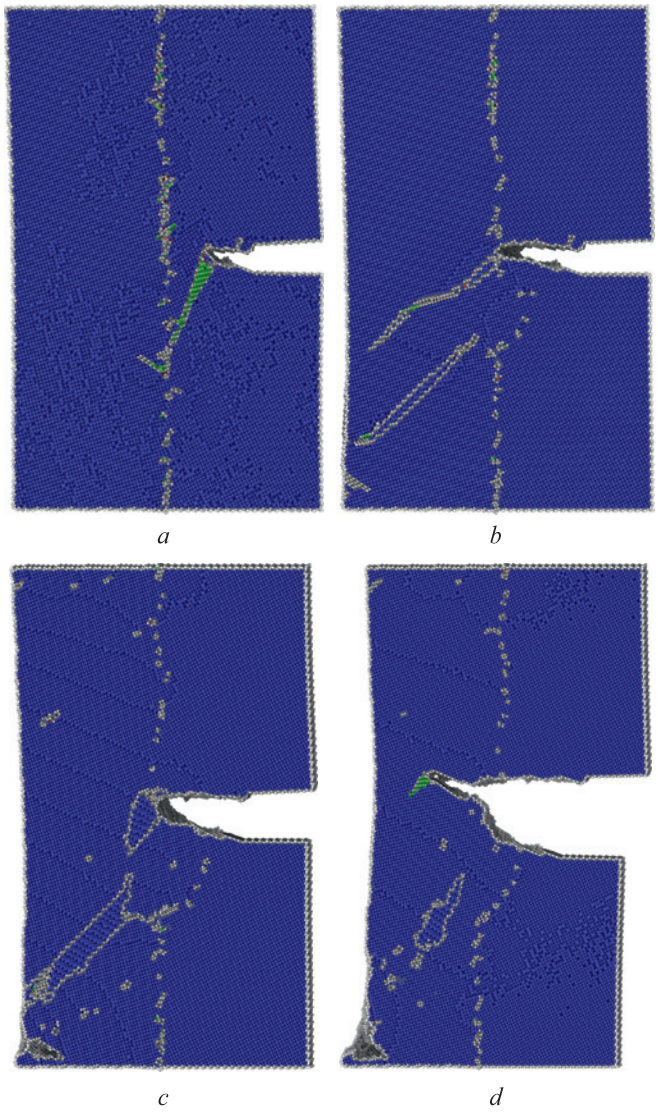


Fig. 3. Structure of the sample with grain misorientation 10° at the strains 4.57 (*a*), 4.83 (*b*), 8.75 (*c*) and 16.52 (*d*) (green, blue and gray atoms have the nearest neighbors with FCC, BCC and uncertain symmetry, respectively)

Рис. 3. Структура образца с разориентацией зерен 10° при деформациях 4,57 (*a*), 4,83 (*b*), 8,75 (*c*) и 16,52 % (*d*) (зеленым, синим и серым показаны атомы с ГЦК, ОЦК и неопределенной симметрией ближайшего окружения соответственно)

The simulation results demonstrate a clear correlation between changes in crack length and variations in stress and volume at the crack tip, as illustrated in Fig. 4. The distinct stages of crack opening are evident, with the crack propagating in discrete steps within the simulated bicrystal. It's important to note that the stress release and subsequent increase during the first stage of crack evolution are associated with the nucleation and growth of a twin at the crack tip. The atomic volume experiences a rapid increase during the first stage, reaching an absolute maximum just before the crack opening (Fig. 4). The crack opening during the second stage results in a sharp drop in atomic volume and an abrupt stress release. In the third stage, a flat region on the curve is observed, reflecting the dependence of crack length on stress at a strain of approximately 9.0 %. This is associated with the crack opening along the boundary of a small twin formed near the grain boundary. Before the onset of the fourth stage, both atomic volume and stresses at the crack tip increase rapidly and then decrease as the crack opens into the second grain.

The simulation results further reveal that the interaction of the crack with the grain boundary initiates active migration of the latter (Fig. 5). This migration is most pronounced in a narrow strain range from 4.5 to 4.6 %, during which the distance between the crack and the grain boundary diminishes from several lattice constants to zero. In this case, the grain boundary undergoes substantial curvature, with the portion above the crack plane migrating towards the first grain, while the part below it shifts in the opposite direction (Fig. 1, *b*). As the strain approaches 8.5 %, when the crack remains within the grain boundary, migration slows down significantly. The abrupt cracking of the grain boundary caused by crack propagation at 8.5 % results in the migration of the grain boundary back towards its initial position. The grain boundary migration parameter exhibits oscillations, corresponding to the emission of structural defects from the grain boundary (Fig. 5). The growth rate of structural defects is highest when the crack tip approaches the grain boundary in the strain range of 4.0 – 4.5 % (Fig. 6). The grain boundary migration induced by the interaction with cracks is consistent with experimental findings obtained through transmission electron microscopy [22; 23].

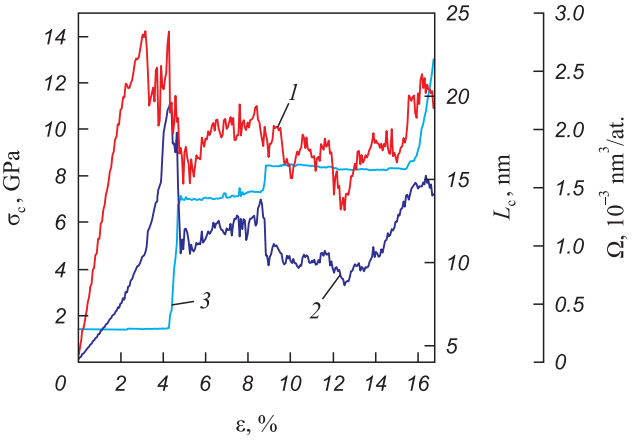


Fig. 4. Dependences of stress (*1*) and atomic volume (*2*) at the crack tip and length (*3*) on tensile strain for the sample with grain misorientation 10°

Рис. 4. Зависимости напряжения (*1*), атомного объема (*2*) в вершине трещины и длины трещины (*3*) от величины растяжения для образца с разориентацией зерен 10°

## CONCLUSIONS

The calculations have revealed that grain boundaries with a larger angle of misorientation in the iron bicrystal significantly retard crack propagation, leading to a prolonged presence of cracks in the intergranular

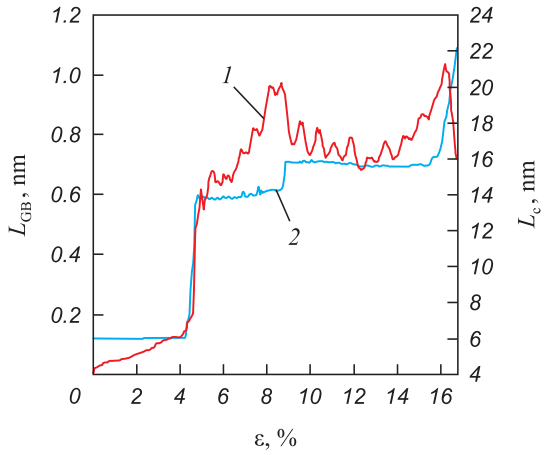


Fig. 5. Dependence of grain boundary migration parameter (*1*) and crack length (*2*) on strain

Рис. 5. Зависимость параметра миграции ГЗ (*1*) и длины трещины (*2*) от деформации

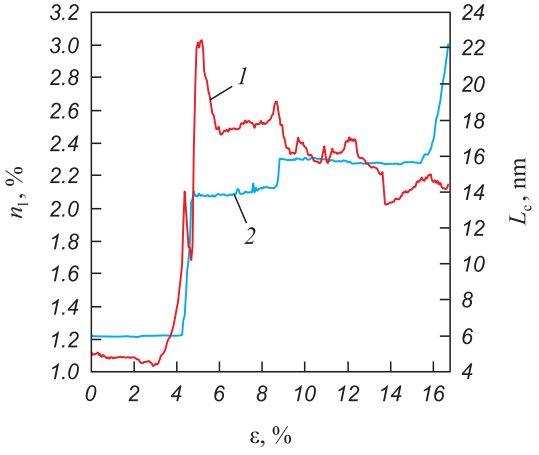


Fig. 6. Dependence of fraction of atoms in structural defects (*1*) and crack length (*2*) on strain

Рис. 6. Зависимость доли атомов, принадлежащих различным дефектам структуры (*1*), и длины трещины (*2*) от деформации

region. In a bicrystal with a greater grain misorientation, the crack propagates a considerable distance along the grain boundary before transitioning into the second grain. It was observed that the initiation of seed crack propagation in the material is consistently preceded by an abrupt increase in atomic volume and stresses at the crack tip. The commencement of crack propagation invariably results in a sharp decrease in stress and atomic volume at the crack tip in the simulated bicrystals. Following the arrest of the crack by the grain boundary, both atomic volume and stress at the crack tip experience a subsequent increase. The interaction of the propagating crack with the grain boundary induces the migration of the grain boundary. Notably, grain boundaries exhibit the most active migration when the crack tip region is in contact with the grain boundary, particularly in the strain range where the crack tip comes in contact with the grain boundary.

## Список литературы / References


1. Uhnáková A., Machová A., Hora P., Červená O. Growth of a brittle crack (001) in 3D bcc iron crystal with a Cu nano-particle. *Computational Materials Science*. 2014;83:229–234. http://dx.doi.org/10.1016/j.commatsci.2013.10.037
2. Farkas D. Atomistic simulations of metallic microstructures. *Current Opinion in Solid State and Materials Science*. 2013;17(6):284–297. https://doi.org/10.1016/J.COSSMS.2013.11.002
3. Liu T., Groh S. Atomistic modeling of the crack–void interaction in α-Fe. *Materials Science and Engineering: A*. 2014;609:255–265. https://doi.org/10.1016/J.MSEA.2014.05.005
4. Latapie A., Farkas D. Molecular dynamics investigation of the fracture behavior of nanocrystalline α-Fe. *Physical Review B*. 2004;69:134110. https://doi.org/10.1103/PhysRevB.69.134110
5. Tanaka M., Tarleton E., Roberts S.G. The brittle–ductile transition in single-crystal iron. *Acta Materialia*. 2008;56(18):5123–5129. https://doi.org/10.1016/J.ACTAMAT.2008.06.025
6. Gordon P.A., Neeraj T., Luton M.J. Atomistic simulation of dislocation nucleation barriers from cracktips in α-Fe. *Modelling and Simulation in Materials Science and Engineering*. 2008;16:045006. https://doi.org/10.1088/0965-0393/16/4/045006
7. Schaef W., Marx M., Vehoff H., Heckl A., Randelzhofer P. A 3-D view on the mechanisms of short fatigue cracks interacting with grain boundaries. *Acta Materialia*. 2011;59(5):1849–1861. https://doi.org/10.1016/j.actamat.2010.11.051
8. Tanaka K., Akiniwa Y., Nakai Y., Wei R.P. Modelling of small fatigue crack growth interacting with grain boundary. *Engineering Fracture Mechanics*. 1986;24(6):803–819. https://doi.org/10.1016/0013-7944(86)90266-3
9. Navarro A., de los Rios E.R. Short and long fatigue crack growth: A unified model. *Philosophical Magazine A*. 1988;57(1):15–36. https://doi.org/10.1080/01418618808204496
10. Zhai T., Wilkinson A.J., Martin J.W. A crystallographic mechanism for fatigue crack propagation through grain boundaries. *Acta Materialia*. 2000;48(20):4917–4927. https://doi.org/10.1016/S1359-6454(00)00214-7
11. Zhai T., Jiang X.P., Li J.X., Garratt M.D., Bray G.H. The grain boundary geometry for optimum resistance to growth of short fatigue cracks in high strength Al-alloys. *International Journal of Fatigue*. 2005;27(10-12):1202–1209. https://doi.org/10.1016/J.IJFATIGUE.2005.06.021
12. Lemaitre J., Chaboche J.-L. *Mechanics of Solid Materials*. Cambridge University Press; 1990:584. https://doi.org/10.1017/CBO9781139167970
13. Ringdalen Vatne I., Stukowski A., Thaulow C., Østby E., Marian J. Three-dimensional crack initiation mechanisms in bcc-Fe under loading modes I, II and III. *Materials Science and Engineering: A*. 2013;560:306–314. https://doi.org/10.1016/J.MSEA.2012.09.071
14. Konovalenko I.S., Kryzhevich D.S., Zol'nikov K.P., Psakhie S.G. Atomic mechanisms of local structural rearrangements in strained crystalline titanium grain. *Technical Physics Letters*. 2011;37(10):946–948. https://doi.org/10.1134/S1063785011100233
15. Zhang Y.W., Wang T.C., Tang Q.H. Simulation of nucleation and emission of dislocations by molecular-dynamics method. *Journal of Applied Physics*. 1995;77(6):2393–2399. https://doi.org/10.1063/1.358764
16. Zhang Y.W., Wang T.C., Tang Q.H. The effect of thermal activation on dislocation processes at an atomistic crack tip. *Journal of Physics D: Applied Physics*. 1995;28:748–754. https://doi.org/10.1088/0022-3727/28/4/018
17. Pezeshki S.S., Silani M., Talaei M.S., Ziaei-Rad S. An atomistic perspective into the fracture behaviour of Fe-bicrystal. *Molecular Simulation*. 2020;46(13):966–974. https://doi.org/10.1080/08927022.2020.1795165
18. Mendelev M.I., Han S., Son W.-j., Ackland G.J., Srolovitz D.J. Simulation of the interaction between Fe impurities and point defects in V. *Physical Review B*. 2007;76:214105. https://doi.org/10.1103/PhysRevB.76.214105
19. Honeycutt D.J., Andersen H.C. Molecular dynamics study of melting and freezing of small Lennard-Jones clusters. *The Journal of Physics Chemistry*. 1987; 91(19):4950–4963. https://doi.org/10.1021/j100303a014
20. Larsen P.M., Schmidt S., Schiøtz J. Robust structural identification via polyhedral template matching. *Modelling and Simulation in Materials Science and Engineering*. 2016;24(5):055007. https://doi.org/10.1088/0965-0393/24/5/055007
21. Stukowski A. Visualization and analysis of atomistic simulation data with OVITO–the Open Visualization Tool. *Modelling and Simulation in Materials Science and Engineering*. 2010;18(1):015012. https://doi.org/10.1088/0965-0393/18/1/015012
22. Legros M., Gianola D.S., Hemker K.J. In situ TEM observations of fast grain-boundary motion in stressed nanocrystalline aluminum films. *Acta Materialia*. 2008;56(14):3380–3393. https://doi.org/10.1016/j.actamat.2008.03.032
23. Rupert T.J., Gianola D.S., Gan Y., Hemker K.J. Experimental observations of stress-driven grain boundary migration. *Science*. 2009;326(5960):1686–1690. https://doi.org/10.1126/science.1178226

## Сведения об авторах / Information about the Authors

***Дмитрий Сергеевич Крыжевич,*** *к.ф.-м.н., научный сотрудник лаборатории компьютерного конструирования материалов,* Институт физики прочности и материаловедения Сибирского отделения РАН
***ORCID:*** 0000-0002-1423-3724
***E-mail:*** kryzhev@ispms.ru

***Александр Вячеславович Корчуганов,*** *к.ф.-м.н., научный сотрудник лаборатории компьютерного конструирования материалов,* Институт физики прочности и материаловедения Сибирского отделения РАН
***ORCID:*** 0000-0002-3765-5911
***E-mail:*** avkor@ispms.ru

***Константин Петрович Зольников,*** *д.ф.-м.н., главный научный сотрудник лаборатории компьютерного конструирования материалов,* Институт физики прочности и материаловедения Сибирского отделения РАН
***ORCID:*** 0000-0001-8988-1040
***E-mail:*** kost@ispms.ru

***Dmitrii S. Kryzhevich,*** *Cand. Sci. (Phys.-Math.), Research Associate of the Laboratory of Computer-Aided Design of Materials,* Institute of Strength Physics and Materials Science, Siberian Branch of Russian Academy of Sciences
***ORCID:*** 0000-0002-1423-3724
***E-mail:*** kryzhev@ispms.ru

***Aleksandr V. Korchuganov,*** *Cand. Sci. (Phys.-Math.), Research Associate of the Computer-Aided Design of Materials,* Institute of Strength Physics and Materials Science, Siberian Branch of Russian Academy of Sciences
***ORCID:*** 0000-0002-3765-5911
***E-mail:*** avkor@ispms.ru

***Konstantin P. Zol'nikov,*** *Dr. Sci. (Phys.-Math.), Chief Researcher of the Laboratory of Computer-Aided Design of Materials,* Institute of Strength Physics and Materials Science, Siberian Branch of Russian Academy of Sciences
***ORCID:*** 0000-0001-8988-1040
***E-mail:*** kost@ispms.ru

## Вклад авторов / Contribution of the Authors

***Д. С. Крыжевич*** – написание основного текста статьи, планирование и проведение экспериментов.
***А. В. Корчуганов*** – написание введения, описание методов исследования, проведение экспериментов.
***К. П. Зольников*** – написание основного текста статьи, планирование экспериментов, анализ и подбор литературных источников.

***D. S. Kryzhevich*** – writing the text, planning and performing experiments.
***A. V. Korchuganov*** – writing of the sections Introduction and Methods, performing experiments.
***K. P. Zol'nikov*** – writing of the text, planning experiments, analysis and selection of literary sources.

Поступила в редакцию 26.06.2023
После доработки 06.07.2023
Принята к публикации 29.09.2023

Received 26.06.2023
Revised 06.07.2023
Accepted 29.09.2023

**МАТЕРИАЛОВЕДЕНИЕ / MATERIALS SCIENCE**

**UDC** 669.018.25:539.219:539.25
**DOI** 10.17073/0368-0797-2023-6-725-732



*Original article*
*Оригинальная статья*

# Structural-phase transformations of 12 % chromium ferritic-martensitic steel EP-823

**K. V. Spiridonova[1], I. Yu. Litovchenko[1], N. A. Polekhina[1], V. V. Linnik[2], T. A. Borisenko[3], V. M. Chernov[4], M. V. Leont'eva-Smirnova[4]**

[1] **Institute of Strength Physics and Materials Science, Siberian Branch of the Russian Academy of Sciences** (2/4 Akademicheskii Ave., Tomsk 634055, Russian Federation)
[2] **National Research Tomsk State University** (36 Lenina Ave., Tomsk 634050, Russian Federation)
[3] **Institute of Solid State Chemistry and Mechanochemistry, Siberian Branch of the Russian Academy of Sciences** (18 Kutateladze Str., Россия, Novosibirsk 630128, Russian Federation)
[4] **JSC "A.A. Bochvar High-Technology Scientific-Research Institute of Inorganic Materials"** (5a Rogova Str., Moscow 123098, Russian Federation)

kseni_ya_almaeva@mail.ru

***Abstract***. The features of phase transformations of 12 % chromium ferritic-martensitic steel EP-823 under heating and cooling conditions in the temperature range from 30 to 1100 °C were studied by the methods of high-temperature X-ray diffraction analysis (XRD) *in situ* and differential scanning calorimetry (DSC). According to XRD *in situ* data, upon heating, the temperatures of the beginning and end of the ($\alpha \rightarrow \gamma$) transformation of ferrite (martensite – austenite) are $Ac_1 \approx 880$ °C, $Ac_3 \approx 1000$ °C, respectively. Upon cooling, a diffusion ($\gamma \rightarrow \alpha$) transformation occurs with critical points – $Ar_1 \approx 860$°C (beginning temperature) and $Ar_3 \approx 840$ °C (end temperature). According to DSC data, during heating, the critical points of the ($\alpha \rightarrow \gamma$) transformation are $Ac_1 \approx 840$ °C and $Ac_3 \approx 900$ °C. During cooling, a martensitic ($\gamma \rightarrow \alpha$) transformation is realized with critical points of the beginning of $M_s = 344$ °C and the end of $M_f = 212$ °C of this transformation. The XRD *in situ* analysis revealed no precipitation of carbide phases under heating and cooling conditions of steel EP-823. Position of the critical points of phase transformations depends on the research method (XRD *in situ* or DSC), which is determined by the difference in effective (taking into account the time for shooting in the XRD method) heating-cooling rate. The effect of elemental composition on the position of critical points of phase transformations and the formation of structural-phase states of ferritic-martensitic steels is discussed. It is shown that the increased content of ferrite-stabilizing elements (Cr, Mo, Nb) in composition of EP-823 steel, compared with other steels of the same class, expands the region of existence of the ferrite phase, which can contribute to an increase in the temperature of $Ac_1$.

***Keywords:*** ferritic-martensitic steel EP-823, structural-phase transformations, high-temperature X-ray diffraction analysis *in situ*, differential scanning calorimetry, quenching, traditional heat treatment

***Acknowledgements:*** The work was performed within the framework of the state task of the Institute of Strength Physics and Materials Science, Siberian Branch of Russian Academy of Sciences, project No. FWRW-2021-0008. The research was carried out with the equipment of Tomsk Regional Core Shared Research Facilities Center of National Research Tomsk State University (center was supported by the Ministry of Science and Higher Education of the Russian Federation).

***For citation:*** Spiridonova K.V., Litovchenko I.Yu., Polekhina N.A., Linnik V.V., Borisenko T.A., Chernov V.M., Leont'eva-Smirnova M.V. Structural-phase transformations of 12 % chromium ferritic-martensitic steel EP-823. *Izvestiya. Ferrous Metallurgy*. 2023;66(6):725–732.
https://doi.org/10.17073/0368-0797-2023-6-725-732

# Структурно-фазовые превращения 12 % хромистой феррито-мартенситной стали ЭП-823

**К. В. Спиридонова[1], И. Ю. Литовченко[1], Н. А. Полехина[1], В. В. Линник[2], Т. А. Борисенко[3], В. М. Чернов[4], М. В. Леонтьева-Смирнова[4]**

[1] **Институт физики прочности и материаловедения Сибирского отделения РАН** (Россия, 634055, Томск, пр. Академический, 2/4)
[2] **Национальный исследовательский Томский государственный университет** (Россия, 634050, Томск, пр. Ленина, 36)
[3] **Институт химии твердого тела и механохимии Сибирского отделения РАН** (Россия, 630128, Новосибирск, ул. Кутателадзе, 18)
[4] **АО «Высокотехнологический научно-исследовательский институт неорганических материалов им. акад. А.А. Бочвара»** (Россия, 123098, Москва, ул. Рогова, 5а)

kseni_ya_almaeva@mail.ru

***Аннотация***. Методами высокотемпературного рентгеноструктурного анализа (РСА) *in situ* и дифференциальной сканирующей калориметрии (ДСК) исследованы особенности фазовых превращений 12 % хромистой феррито-мартенситной стали ЭП-823 в условиях нагрева и охлаждения в температурном интервале от 30 до 1100 °С. По данным РСА *in situ* при нагреве температуры начала $Ac_1$ и конца $Ac_3$ α → γ-превращения (феррит – аустенит) составляют 880 и 1000 °С соответственно. При охлаждении реализуется диффузионное γ → α-превращение с критическими точками $Ar_1 \approx 860$ °С (температура начала) и $Ar_3 \approx 840$ °С (температура конца). Согласно данным ДСК при нагреве критические точки α → γ-превращения: $Ac_1 \approx 840$ °С, $Ac_3 \approx 900$ °С. При охлаждении реализуется мартенситное γ → α-превращение в интервале температур от $M_н = 344$ °С до $M_к = 212$ °С. Методом РСА *in situ* выделения карбидных фаз в условиях нагрева и охлаждения стали ЭП-823 не обнаружено. Положение критических точек фазовых превращений зависит от метода исследований (РСА *in situ* или ДСК), что определяется различием в эффективной (с учетом времени на съемку в методе РСА) скорости нагрева/охлаждения. Обсуждается влияние элементного состава и особенностей микроструктуры на положение критических точек фазовых превращений феррито-мартенситных сталей. Показано, что увеличенное по сравнению с другими сталями того же класса содержание феррит-стабилизирующих элементов (Cr, Mo, Nb) в составе стали ЭП-823 расширяет область существования ферритной фазы, что может способствовать повышению температуры $Ac_1$.

***Ключевые слова:*** феррито-мартенситная сталь ЭП-823, структурно-фазовые превращения, высокотемпературный рентгеноструктурный анализ *in situ*, дифференциальная сканирующая калориметрия, закалка, традиционная термическая обработка

***Благодарности:*** Работа выполнена в рамках государственного задания Института физики прочности и материаловедения Сибирского отделения РАН, тема номер FWRW-2021-0008. Исследования выполнены с использованием оборудования Томского регионального центра коллективного пользования Томскго государственного университета.

***Для цитирования:*** Спиридонова К.В., Литовченко И.Ю., Полехина Н.А., Линник В.В., Борисенко Т.А., Чернов В.М., Леонтьева-Смирнова М.В. Структурно-фазовые превращения 12 % хромистой феррито-мартенситной стали ЭП-823. *Известия вузов. Черная металлургия*. 2023;66(6):725–732. https://doi.org/10.17073/0368-0797-2023-6-725-732

## Introduction

Generation IV fast neutron nuclear reactors with lead or lead-bismuth coolant are currently in development [1 – 5]. The 12 % chromium ferriticmartensitic steel EP-823 is considered one of key materials for manufacturing fuel element cans in Russian nuclear reactors [6 – 9]. This steel is distinctive for its elevated silicon content, providing excellent corrosion resistance, particularly when in contact with liquid metal coolant [7].

The physical and mechanical properties of steel EP-823 underwent comprehensive scrutiny in the late 20th century [7]. Researchers explored the microstructure and mechanical properties of the steel after various treatments, including traditional heat treatment (THT), stepwise heat treatment (STT), and hightemperature thermomechanical treatment (HTMT)) [7 – 9]. They analyzed hardening mechanisms [10], investigated creep resistance, studied thermophysical properties, temperature dependencies of elastic modulus, and internal friction characteristics [11; 12]. Additionally, they examined short-term and long-term mechanical properties after high-dose neutron irradiation [13 – 15]. The findings demonstrated that this steel is on par with other 12 % chromium ferritic-martensitic steels concerning physical-mechanical, heat-resistant, corrosion, and radiation properties [16].

Although steel EP-823 has been a subject of scientific interest for a considerable period, detailed studies on phase transitions during its heating and cooling, utilizing Differential Scanning Calorimetry (DSC) and high-temperature *X*-ray Diffraction (XRD) *in situ* methods, have not been conducted before. The use of these two methods allows us to complement the obtained results and determine the dependence of critical points on the effective heating (cooling) rate. The data on the values of critical points of steel phase transitions are crucial for determining the temperature intervals suitable for practical appli-

cations of the steel and for developing high-temperature thermomechanical treatments.

## Materials and methods

The elemental composition of ferritic-martensitic steel EP-823 is as follows [6 – 8], wt. %: C 0.14; Cr 11.56; Mn 0.58; Mo 0.74; Nb 0.40; V 0.34; W 0.68; Ni 0.68; N 0.03; Si 1.09; Ce 0.10; Ti 0.01; B 0.006; Al 0.02.

To investigate the phase transformations of the steel during heating and cooling, we employed high-temperature *X*-ray diffraction analysis (XRD) *in situ* on the D8 Advance diffractometer with HTK 1200 N high-temperature chamber using Cu$K_\alpha$-radiation in a helium protective atmosphere. This method involved the following steps:

– heating from 30 to 1100 °C (shooting at 30 °C, from 30 to 800 °C without shooting, from 800 to 1000 °C – shooting with a step of 20 °C, heating from 1000 to 1100 °C without shooting, shooting at 1100 °C);

– exposure at 1100 °C for 40 min to obtain a uniform solid solution, followed by shooting;

– subsequent cooling from 1100 to 30 °C (from 1100 to 900 °C without shooting, from 900 to 600 °C – shooting with a step of 20 °C, from 600 to 30 °C without shooting, shooting at 30 °C).

The study utilized plates measuring 1 mm in thickness and 15 mm in diameter as samples. The range of 2θ angles was set at 40 – 80°, with a shooting step of Δ2θ approximately 0.02°. The heating and cooling rates were maintained at 12 °C/min, and the shooting time at each temperature was 7 min. The XRD method was employed to investigate the steel samples post-quenching in water at $T = 1100$ °C (1 h holding time). The temperature intervals for shooting were chosen based on previously obtained results for steel of the same class [16].

Critical points of phase transformations were determined using differential scanning calorimetry (DSC) during continuous heating (from 20 to 1100 °C) at a rate of 10 °C/min and cooling (from 1100 to 20 °C) of the samples in a protective argon atmosphere using a NETZSCH STA 409 PC device. The inflection temperatures on the DSC curves were identified as the beginning and end of the phase transformation. The mass of the samples ranged from 90 to 100 mg. DSC studies were conducted on steel samples after traditional heat treatment (THT), involving quenching in water from a temperature of 1100 °C (1 h holding time) and subsequent tempering at 720 °C (for 3 h).

## Results and discussion

The study [9] provided a comprehensive analysis of the microstructure and phase composition of ferritic-martensitic steel EP-823 using Scanning Electron Microscopy (SEM) in the Electron Back-Scatter Diffraction (EBSD) mode and Transmission Electron Microscopy (TEM). The primary structural features crucial for discussing the peculiarities of its phase transitions during heating and cooling are outlined below.

The microstructure of steel after quenching reveals martensitic lamellae with a high density of dislocations (up to $10^{15}$ m$^{-2}$), ferrite grains, a minimal quantity of coarse and fine particles of *MeX* type (where *Me* is Nb, Mo; *X* – C, N), as well as coarse particles of $Me_{23}C_6$ type (where *Me* – Fe, Cr). In the tempering conditions following quenching (THT mode), the main structural elements (martensitic lamella and ferrite grains) are retained. The density of dislocations decreases, while the density of coarse ($Me_{23}C_6$ type) and fine (*MeX* type) particles significantly increases compared to the state after quenching.

After THT (Fig. 1), former austenitic grains in steel EP-823 exhibit sizes up to 60 μm. A small number of δ-ferrite grains were also evident. Within the former austenitic grains, martensite blocks are observed, clustering together with predominantly high-angle misorientations between adjacent blocks (Fig. 1, *b*, *c*). Low-angle misorientation boundaries (Fig. 1, *c*) represent the boundaries of the martensitic lamellae forming the blocks. The average size of martensite blocks and ferrite grains, as per the EBSD method, is 3.1 μm [9]. Fig. 1, *c* displays coarse (submicron, micron) particles of *MeX* type.

Transmission Electron Microscopy data [9] indicate that the average width of martensitic lamellae is approximately 300 nm. $Me_{23}C_6$ carbides are situated along the boundaries of martensitic lamellae and ferrite grains, with sizes ranging from 50 to 250 nm. Fine carbonitrides of *MeX* type (5 – 20 nm in size) are positioned on dislocations, anchoring them. These particles are predominantly liberated during steel tempering. Coarse particles of the same type appear to have originated from metallurgical operations and remain unchanged in size under heat treatment conditions.

Fig. 2 presents *X*-ray line profiles of steel EP-823 (after quenching) obtained through heating and cooling in the temperature range 30 – 1100 – 30 °C. At room temperature (30 °C), in the initial state, this exhibits a typical *X*-ray diffraction pattern of ferrite-martensitic steel with a BCC lattice. Upon heating, the *X*-ray peaks shift towards smaller 2θ angles due to the thermal expansion of the crystal lattice. The analysis of *X*-ray profiles at different temperatures reveals that the α → γ transition initiates at $T = 880$ °C ($Ac_1$) and completes at $T = 1000$ °C ($Ac_3$). The intercritical temperature interval ($Ac_3 – Ac_1$) is approximately 120 °C. Besides the γ and α phase reflections, *X*-ray diffraction patterns during heating exhibit reflections from $Fe_3O_4$ and $Cr_2O_3$ oxides. Evidently, an oxide layer forms on the sample surface due to the pre-

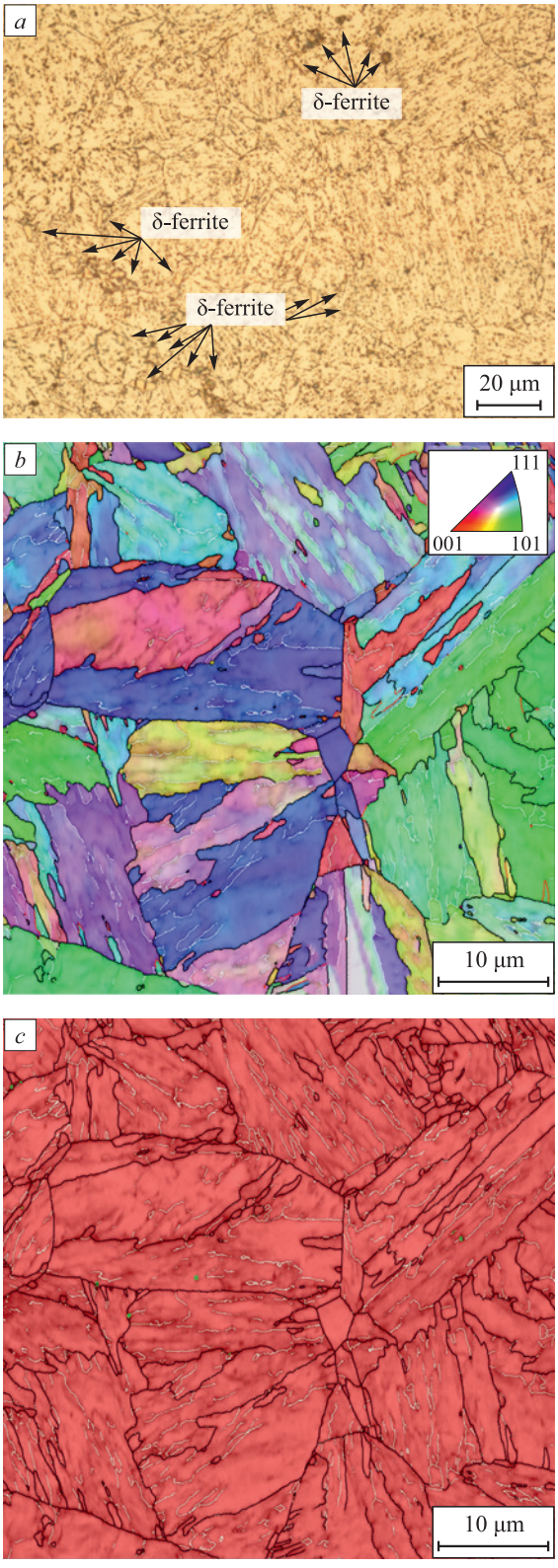


Fig. 1. Images of steel microstructure after traditional heat treatment: *a* – optical image; *b*, *c* – SEM EBSD: *b* – orientation map; *c* – phase map (BCC-Fe – red, *MeX* particles – green, high-angle – black, low-angle – white lines)

Рис. 1. Изображения микроструктуры стали после ТТО: *a* – оптическое изображение; *b* и *c* – РЭМ ДОРЭ; *b* – ориентационная карта; *c* – фазовая карта (ОЦК-Fe указано красным цветом, частицы *MeX* зеленым цветом, высоко- и малоугловые границы – черными и белыми линиями)

sence of residual oxygen in the argon protective atmosphere.

Upon cooling, the diffusive transformation from austenite (γ) to ferrite (α) begins at $Ar_1$ = 860 °C and concludes at $Ar_3$ = 840 °C. In the high-temperature region, as the temperature decreases, reflections from oxide phases ($Fe_3O_4$, $Cr_2O_3$) intensify, signifying an increase in their volume fraction. Notably, the $Fe_3O_4$ (400) and $Cr_2O_3$ (024) reflections closely match those of γ-Fe (111) and γ-Fe (200), respectively. However, at $T$ = 30 °C, there are no reflections from austenite. Oxide reflections are observed under shooting conditions at 30 °C after the heating – holding – cooling cycle.

*X*-ray diffraction patterns do not exhibit peaks from carbide ($Me_{23}C_6$) and carbonitride (*MeX*) particles. The XRD method is unlikely to identify these particles due to their small volume fraction (up to several percent). In [9] it is noted that after THT, the volume fraction of fine particles of *MeX* type in steel EP-823 is ≈0.6 % and that of coarse particles of $Me_{23}C_6$ type is about 5.5 %. In the state after quenching, the volume fractions of these particles are lower than the indicated values.

Fig. 3 presents the results of the investigation of α → γ and γ → α transformations in steel EP-823 obtained by the DSC method during continuous heating and cooling. During heating (Fig. 3, *a*), two dips are observed on the DSC curve. One of them is associated to the phase α → γ transformation, where the points $Ac_1$ = 839 °C and $Ac_3$ = 902 °C. When the study is conducted using this method, the intercritical temperature interval ($Ac_3$ – $Ac_1$) is 63 °C. According to sources [16; 17], the second dip at temperatures 645 – 734 °C is attributed to the magnetic transformation of ferromagnetic α-Fe into paramagnetic α-Fe.

Upon cooling, a peak corresponding to a martensitic transformation (γ → α) is observed on the DSC curve. This transformation occurs between $M_s$ = 344 °C and $M_f$ = 212 °C. Additionally, the DSC curve shows a slight inflection in the temperature range of 700 – 668 °C. In [16], it is noted that inflections at such temperatures are characteristic of the diffusive transformation of austenite to ferrite. The cooling rate during the DSC study is likely to have been high enough. Under such cooling conditions, diffusion-free (martensitic) transformation is realized, while diffusion transformation is practically suppressed.

The table displays the values of critical points for the phase transitions of steel EP-823 determined during continuous heating and cooling using XRD *in situ* and DSC methods. The comparison reveals that the difference in the values of the points $Ac_1$ and $Ac_3$ for the two methods is about 40 – 100 °C, with the difference in the values of the intercritical interval being 57 °C. These

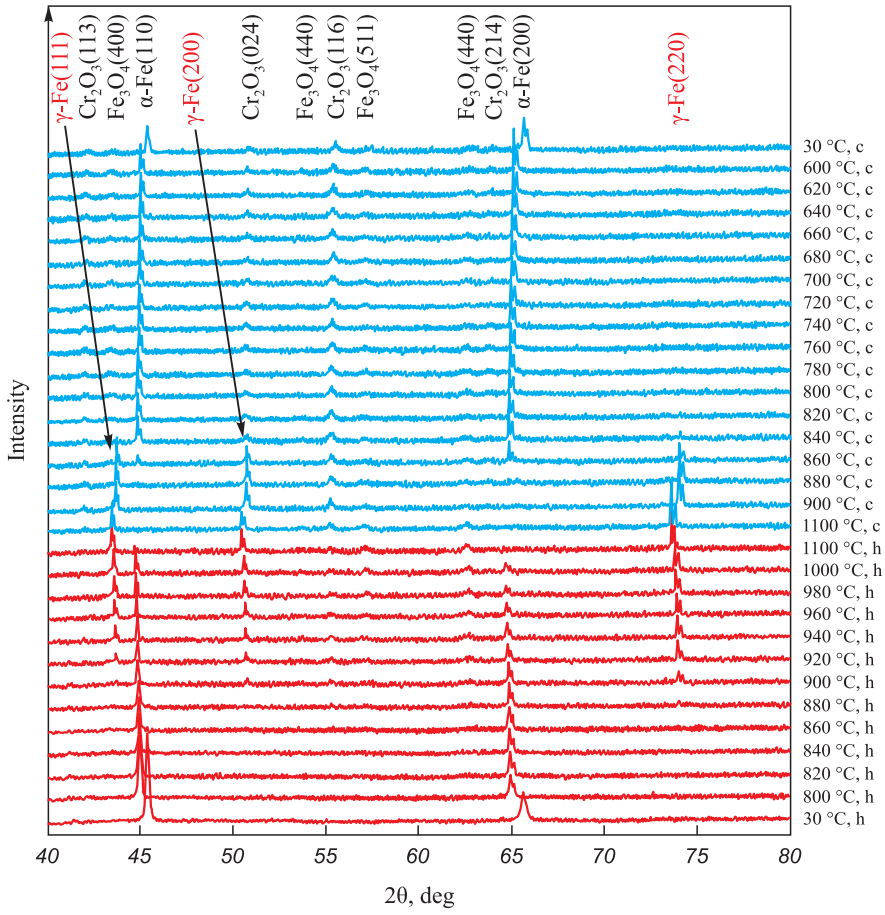


Fig. 2. Profiles of X-ray diffraction lines of steel EP-823 (heating from 30 to 1100 °C, holding at 1100 °C for 40 min, cooling down to 30 °C)

Рис. 2. Профили рентгеновских дифракционных линий стали марки ЭП-823 (нагрев от 30 до 1100 °C, выдержка при 1100 °C в течение 40 мин, охлаждение до 30 °C)

peculiarities are associated with the specific nature of each method, including the variance in effective heating (cooling) rates, taking into account the shooting time when the XRD method is employed. With the application of the DSC method, the effective heating rate is higher, causing the α → γ transformation to commence at lower temperatures, resulting in a shorter intercritical interval compared to the XRD *in situ* method.

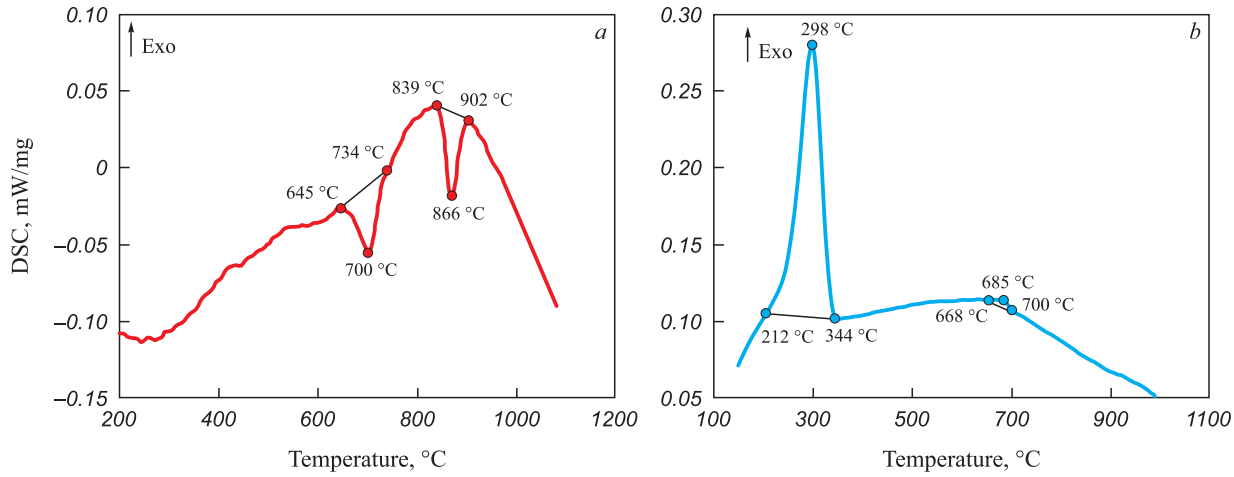


Fig. 3. DSC curves of steel EP-823 during heating (*a*) and cooling (*b*)

Рис. 3. ДСК кривые стали ЭП-823 при нагреве (*a*) и охлаждении (*b*)

**Values of critical points of phase transitions of steel EP-823, determined during continuous heating and cooling**

**Значения критических точек фазовых переходов стали ЭП-823, определенные при непрерывном нагреве и охлаждении**

| Research method | Heating | | Cooling | | | |
|---|---|---|---|---|---|---|
| | $Ac_1$, °C | $Ac_3$, °C | $Ar_1$, °C | $Ar_3$, °C | $M_s$, °C | $M_f$, °C |
| XRD, *in situ* | 880 | 1000 | 860 | 840 | – | – |
| DSC | 839 | 902 | – | – | 344 | 212 |

Comparing the critical points of phase transitions obtained in this investigation (refer to the Table) with experimental and calculated results from prior studies [16; 18 – 20] on various 9 – 12 % chromium ferrito-martensitic steels, we can draw the conclusion that our results are comparable. In the majority of the considered steels, the α → γ transformation during heating occurs within the temperature range of approximately 800 – 900 °C; however, it may be completed at a higher temperature (1000 °C), as observed in the case of steel EP-823 examined through the XRD in situ method in this study (see the Table). Diffusive transformation during cooling takes place in a temperature range close to the aforementioned one. The martensitic transformation in the majority of 9 – 12 % chromium ferrite-martensitic steels is observed within the temperature range of approximately 450 – 200 °C.

Differences in the position of critical points are contingent on the elemental composition of steels and the rates of heating and cooling. An elevation in the content of ferrite-stabilizing elements (Cr, Mo, Nb) in the steel composition expands the ferrite phase region, potentially contribute to the to the increase in temperature at $Ac_1$. The presence of dispersed carbide particles of $Me_{23}C_6$, binding carbon, deplets the solid solution in carbon and can consequently contribute to the expansion of the temperature range required for ferrite existence. The temperature and holding time in the austenitic region determine the homogeneity of the austenite solid solution and the size of the initial austenitic grain, influencing the martensitic transformation. During cooling, the reduction in the size of the austenitic grain contributes to the decrease $M_s$ and $M_f$ points values [17].

## Conclusions

We have identified the critical points of structural-phase transformations during the heating and cooling of 12 % chromium ferrite-martensitic steel EP-823 using *in situ X*-ray diffraction analysis and differential scanning calorimetry.

According to the *X*-ray research, during continuous heating, the temperatures for the beginning and end of the α → γ transformation are $Ac_1$ = 880 °C and $Ac_3$ = 1000 °C, respectively. During cooling, the beginning and end of the γ → α-transformation are $Ar_1$ = 860 °C and $Ar_3$ = 840 °C. Based on differential scanning calorimetry data: $Ac_1$ = 839 °C, $Ac_3$ = 902 °C; martensitic transformation during cooling occurs in the interval between $M_s \approx 340$ °C and $M_f \approx 210$ °C. The Curie point for the investigated steel is in the temperature range of 645 – 734 °C.

The positions of critical points obtained by different methods vary due to the difference in effective heating (cooling) rates, taking into account the shooting time when the *X*-ray method is used. As the heating rate increased, the temperature of the beginning of the α → γ transformation decreased by ≈40 °C, and the intercritical temperature interval narrowed. In case of accelerated cooling (during the DSC study), diffusive γ → α transformation is suppressed, and martensitic transformation is realized.

## References / Список литературы

1. Cabet C., Dalle F., Gaganidze E., Henry J., Tanigawa H. Ferritic-martensitic steels for fission and fusion applications. *Journal of Nuclear Materials*. 2019;523:510–537. https://doi.org/10.1016/j.jnucmat.2019.05.058
2. Yvon P. *Structural Materials for Generation IV Nuclear Reactors*. Amsterdam, Netherlands: Elsevier; 2017:664.
3. Odette R.G., Zinkle S.J. *Structural Alloys for Nuclear Energy Applications*. Amsterdam, Netherlands: Elsevier; 2019:655.
4. Zinkle S.J., Ghoniem N.M. Operating temperature windows for fusion reactor structural materials. *Fusion Engineering and Design*. 2000;51-52:55–71. https://doi.org/10.1016/S0920-3796(00)00320-3
5. Kurtz R.J., Odette G.R. Chapter 3 – Overview of reactor systems and operational environments for structural materials in fusion reactors. In: *Structural Alloys for Nuclear Energy Applications*. Amsterdam, Netherlands: Elsevier; 2019:51–102. https://doi.org/10.1016/B978-0-12-397046-6.00003-4
6. Maloy S.A., Natesan K., Holsomb D.E., Fazio C., Yvon P. Chapter 2 – Overview of reactor systems and operational environments for structural materials in GEN-IV fission reactors. In: *Structural Alloys for Nuclear Energy Applications*. Amsterdam, Netherlands: Elsevier; 2019:23–49. https://doi.org/10.1016/B978-0-12-397046-6.00002-2
7. Ioltukhovskii A.G., Lanskaya K.A., Belomyttsev Yu.S., Saratovskii L.N. Choice of heat treatment modes of 12 % chromium steel EP823 in relation to operating conditions of fuel assembly covers of BN-600 reactor. *Voprosy atomnoi nauki i tekhniki. Ser. Atomnoe materialovedenie*. 1985;(2(19)): 65–70. (In Russ.).

   Иолтуховский А.Г., Ланская К.А., Беломытцев Ю.С., Саратовский Л.Н. Выбор режимов термообработки 12 %-ной хромистой стали ЭП-823 применительно к условиям работы чехлов ТВС реактора БН-600. *Вопросы атомной науки и техники. Сер. Атомное материаловедение*. 1985;(2(19)):65–70.

**8.** Polekhina N.A., Litovchenko I.Yu., Almaeva K.V., Akkuzin S.A., Linnik V.V., Moskvichev E.N., Chernov V.M., Naumenko I.A., Saifutdinova M.S., Leontieva-Smirnova M.V. Special features of the surface layer structure of ferritic-martensitic EP-823-Sh steel after prolonged exposure to the flowing lead at 630 °C under low oxygen concentration. *Journal of Nuclear Materials*. 2022;572:154039. https://doi.org/10.1016/j.jnucmat.2022.154039

**9.** Litovchenko I., Almaeva K., Polekhina N., Akkuzin S., Linnik V., Moskvichev E., Chernov V., Leontyeva-Smirnova M. The microstructure and mechanical properties of ferritic-martensitic steel EP-823 after high-temperature thermomechanical treatment. *Metals*. 2022;12(1):79. https://doi.org/10.3390/met12010079

**10.** Almaeva K.V., Litovchenko I.Yu., Polekhina N.A., Linnik V.V. Mechanisms of hardening of 12 % chromium ferritic-martensitic steel EP-823. *Izvestiya. Ferrous Metallurgy*. 2022;65(12):887–894. (In Russ.). https://doi.org/10.17073/0368-0797-2022-12-887-894

Алмаева К.В., Литовченко И.Ю., Полехина Н.А., Линник В.В. Механизмы упрочнения 12 %-ой хромистой ферритно-мартенситной стали ЭП-823. *Известия вузов. Черная Металлургия*. 2022;65(12):887–894. https://doi.org/10.17073/0368-0797-2022-12-887-894

**11.** Belomyttsev M.Yu., Molyarov V.G. Creep resistance of ferritic-martensitic steel 16Cr12MoWSiVNbB (EP-823). *Izvestiya. Ferrous Metallurgy*. 2019;62(4):290–302. (In Russ.). https://doi.org/10.17073/0368-0797-2019-4-290-302

Беломытцев М.Ю., Моляров В.Г. Исследование сопротивления ползучести феррито-мартенситной стали 16Х12МВСФБР (ЭП-823). *Известия вузов. Черная Металлургия*. 2019;62(4):290–302. https://doi.org/10.17073/0368-0797-2019-4-290-302

**12.** Kruglov A.B., Kruglov V.B., Struchalin P.G., Kharitonov V.S. Study of thermophysical properties of EP-823 steel in the temperature range of 200–900 °C. *Bulletin of the Lebedev Physics Institute*. 2015;42(9):264–267. https://doi.org/10.3103/S1068335615090031

**13.** Porollo S.I., Veremeev A.M., Konobeev Yu.V., Ivanov A.A., Shulepin S.V. Study of the long-term strength of neutron-irradiated austenitic and ferrite-martensite steel. *Atomic Energy*. 2018;124(2):98–104. https://doi.org/10.1007/s10512-018-0381-x

**14.** Maloy S.A., Romero T., James M.R. Tensile testing of EP-823 and HT-9 after irradiation in STIP II. *Journal of Nuclear Materials*. 2006;356(1-3):56–61. http://dx.doi.org/10.1016/j.jnucmat.2006.05.003

**15.** Grachev A.F., Zherebtsov A.A., Zabud'ko L.M., Zvir E.A., Kryukov F.N., Nikitin O.N., Skupov M.V., Ivanov Yu.A., Porollo S.I. Results of investigations of BREST-type reactor fuel rods with mixed uranium-plutonium nitride fuel, irradiated in BOR-60 and BN-600. *Atomic Energy*. 2019;125(5):314–321. https://doi.org/10.1007/s10512-019-00487-4

**16.** Polekhina N.A., Litovchenko I.Yu., Almaeva K.V., Bulina N.V., Korchagin M.A., Tyumentsev A.N., Chernov V.M., Leontyeva-Smirnova M.V. Features of phase transformations of low-activation 12 %-chromium ferritic-martensitic steel EK-181. *Russian Physics Journal*. 2020;62(12):2314–2318. https://doi.org/10.1007/s11182-020-01982-z

**17.** Lanskaya K.A. *High-Chromium Heat-Resistant Steels*. Moscow: Metallurgiya; 1976:216. (In Russ.).

Ланская К.А. *Высокохромистые жаропрочные стали*. Москва: Металлургия; 1976:216.

**18.** Raju S., Ganesh B.J., Rai A.K., Mythili R., Saroja S., Raj B. A study on martensitic phase transformation in 9Cr–1W–0.23V–0.063Ta–0.56Mn–0.09C–0.02N (wt. %) reduced activation steel using differential scanning calorimetry. *Journal of Nuclear Materials*. 2010;405(1):59–69. http://dx.doi.org/10.1016/j.jnucmat.2010.07.036

**19.** Lu Sh., Liang T., Li Y., Li D., Rong L., Li Y. Microstructure and mechanical properties of simulated heat-affected zones of EP-823 steel for ADS/LFR. *Journal of Materials Science and Technology*. 2015;31(8):864–871. http://dx.doi.org/10.1016/j.jmst.2014.08.015

**20.** Ma T., Hao X., Wang P. Effect of heat treatments on microstructural evolution and tensile properties of 15Cr12MoVWN ferritic/martensitic steel. *Metals*. 2020;10(9):1271. http://dx.doi.org/10.3390/met10091271

## Information about the Authors / Сведения об авторах

***Kseniya V. Spiridonova,*** *Cand. Sci. (Phys.-Math.), Junior Researcher of the Laboratory of Materials Science of Shape Memory Alloys,* Institute of Strength Physics and Materials Science, Siberian Branch of Russian Academy of Sciences
***ORCID:*** 0000-0002-9181-4362
***E-mail:*** kseni_ya_almaeva@mail.ru

***Igor' Yu. Litovchenko,*** *Dr. Sci. (Phys.-Math.), Assist. Prof, Head of the Laboratory of Materials Science of Shape Memory Alloys,* Institute of Strength Physics and Materials Science, Siberian Branch of Russian Academy of Sciences
***ORCID:*** 0000-0002-5892-3719
***E-mail:*** litovchenko@ispms.ru

***Nadezhda A. Polekhina,*** *Cand. Sci. (Phys.-Math.), Research Associate of the Laboratory of Materials Science of Shape Memory Alloys,* Institute of Strength Physics and Materials Science, Siberian Branch of Russian Academy of Sciences
***ORCID:*** 0000-0001-9076-5469
***E-mail:*** nadejda89tsk@yandex.ru

***Ксения Викторовна Спиридонова,*** *к.ф.-м.н., младший научный сотрудник лаборатории материаловедения сплавов с памятью формы,* Институт физики прочности и материаловедения Сибирского отделения РАН
***ORCID:*** 0000-0002-9181-4362
***E-mail:*** kseni_ya_almaeva@mail.ru

***Игорь Юрьевич Литовченко,*** *д.ф.-м.н., доцент, заведующий лабораторией материаловедения сплавов с памятью формы,* Институт физики прочности и материаловедения Сибирского отделения РАН
***ORCID:*** 0000-0002-5892-3719
***E-mail:*** litovchenko@ispms.ru

***Надежда Александровна Полехина,*** *к.ф.-м.н., научный сотрудник лаборатории материаловедения сплавов с памятью формы,* Институт физики прочности и материаловедения Сибирского отделения РАН
***ORCID:*** 0000-0001-9076-5469
***E-mail:*** nadejda89tsk@yandex.ru

***Valeriya V. Linnik,*** *Postgraduate,* National Research Tomsk State University
***ORCID:*** 0000-0001-8975-1553
***E-mail:*** lera.linnik.1999@mail.ru

***Tat'yana A. Borisenko,*** *Junior Researcher of the Laboratory of Materials for Additive Technologies,* Institute of Solid State Chemistry and Mechanochemistry, Siberian Branch of the Russian Academy of Sciences
***ORCID:*** 0000-0003-0341-8755
***E-mail:*** tanya.borisenko.97@mail.ru

***Vyacheslav M. Chernov,*** *Dr. Sci. (Phys.-Math.), Prof., Chief Researcher,* JSC "A.A. Bochvar High-Technology Scientific-Research Institute of Inorganic Materials"
***ORCID:*** 0000-0002-9558-3055
***E-mail:*** VMChernov@bochvar.ru

***Mariya V. Leont'eva-Smirnova,*** *Cand. Sci. (Eng.), Assist. Prof., Head of Department,* JSC "A.A. Bochvar High-Technology Scientific-Research Institute of Inorganic Materials"
***E-mail:*** MVLeonteva-Smirnova@bochvar.ru

***Валерия Васильевна Линник,*** *аспирант,* Национальный исследовательский Томский государственный университет
***ORCID:*** 0000-0001-8975-1553
***E-mail:*** lera.linnik.1999@mail.ru

***Татьяна Андреевна Борисенко,*** *младший научный сотрудник лаборатории материалов для аддитивных технологий,* Институт химии твердого тела и механохимии Сибирского отделения РАН
***ORCID:*** 0000-0003-0341-8755
***E-mail:*** tanya.borisenko.97@mail.ru

***Вячеслав Михайлович Чернов,*** *д.ф.-м.н, профессор, главный научный сотрудник,* АО «Высокотехнологический научно-исследовательский институт неорганических материалов имени академика А.А. Бочвара»
***ORCID:*** 0000-0002-9558-3055
***E-mail:*** VMChernov@bochvar.ru

***Мария Владимировна Леонтьева-Смирнова,*** *к.т.н., доцент, руководитель отдела,* АО «Высокотехнологический научно-исследовательский институт неорганических материалов имени академика А.А. Бочвара»
***E-mail:*** MVLeonteva-Smirnova@bochvar.ru

## Contribution of the Authors

***K. V. Spiridonova*** – analysis of data obtained by XRD *in situ* and DSC methods, writing the text.
***I. Yu. Litovchenko*** – scientific guidance, formation of the article concept, editing of the text.
***N. A. Polekhina*** – formation of the article concept, editing the text.

***V. V. Linnik*** – preparation of the samples for XRD *in situ* and DSC analysis, analysis of the results.
***T. A. Borisenko*** – conducting XRD *in situ* analysis.
***V. M. Chernov*** – editing the text.
***M. V. Leont'eva-Smirnova*** – editing the text.

## Вклад авторов

***К. В. Спиридонова*** – анализ данных, полученных методами РСА *in situ* и ДСК; написание текста статьи.
***И. Ю. Литовченко*** – научное руководство, разработка концепции статьи, редактирование текста статьи.
***Н. А. Полехина*** – разработка концепции статьи, редактирование текста статьи.
***В. В. Линник*** – подготовка образцов для исследований методами РСА *in situ* и ДСК, анализ результатов.
***Т. А. Борисенко*** – проведение исследования методом РСА *in situ*.
***В. М. Чернов*** – редактирование текста статьи.
***М. В. Леонтьева-Смирнова*** – редактирование текста статьи.

Received 28.07.2023
Revised 22.08.2023
Accepted 11.09.2023

Поступила в редакцию 28.07.2023
После доработки 22.08.2023
Принята к публикации 11.09.2023

**Innovation in metallurgical industrial and laboratory equipment, technologies and materials** / **Инновации в металлургическом промышленном и лабораторном оборудовании, технологиях и материалах**

**UDC** 621.74.045
**DOI** 10.17073/0368-0797-2023-6-733-742



*Original article*
*Оригинальная статья*

# Simulation of a new process of mixing liquid metal in CCM mold with rotating cooling jacket with vertical ribs

**V. I. Odinokov, A. I. Evstigneev, E. A. Dmitriev, V. A. Karpenko**

**Komsomolsk-on-Amur State University** (27 Lenina Ave., Komsomolsk-on-Amur, Khabarovsk Territory 681013, Russian Federation)

diss@knastu.ru

***Abstract***. The article proposes a new technology of filling the CCM mold with liquid metal and mixing it. The original patented device consists of a closed bottom nozzle and a rotating jacket. Experimental studies of liquid metal flow in a mold are long, complex and time-consuming, therefore, in the work was used mathematical modeling by numerical method. The objects of research are the hydrodynamic and thermal flows of liquid metal during the new process of steel casting into a CCM mold of rectangular cross-section, and the result is a spatial mathematical model that describes the flows and temperatures of liquid metal in the mold. To simulate the processes occurring during the metal flow in the mold, the authors used a specially created software package. The theoretical calculations are based on the fundamental equations of hydrodynamics, the equations of mathematical physics (equation of thermal conductivity taking into account mass transfer) and a proven numerical method. The area under study is divided into elements of finite dimensions, for each element a formulated system of equations is written in a difference form. The result is the velocity and temperature fields of the metal flow in the mold volume. According to the developed numerical schemes and algorithms, a calculation program was compiled. The paper considers an example of calculating the steel casting into a mold of rectangular cross-section and flow diagrams of liquid metal over various mold sections. Vector flows of liquid metal in various mold sections are clearly presented for different rotary speed of the rotating jacket. The authors identified the areas of intense turbulence and presented the results of the problem numerical solution in graphical form by diagrams of the velocity fields of liquid metal flows and their temperature over various mold sections.

***Keywords:*** modeling, mold, liquid metal, filling, melt flow, mathematical model, numerical scheme, algorithm, flow rate

***For citation:*** Odinokov V.I., Evstigneev A.I., Dmitriev E.A., Karpenko V.A. Simulation of a new process of mixing liquid metal in CCM mold with rotating cooling jacket with vertical ribs. *Izvestiya. Ferrous Metallurgy*. 2023;66(6):733–742.
https://doi.org/10.17073/0368-0797-2023-6-733-742

# Моделирование нового процесса перемешивания жидкого металла в кристаллизаторе установки непрерывной разливки стали при вращающейся рубашке с вертикальными ребрами

**В. И. Одиноков, А. И. Евстигнеев, Э. А. Дмитриев, В. А. Карпенко**

**Комсомольский-на-Амуре государственный университет** (Россия, 681013, Хабаровский край, Комсомольск-на-Амуре, пр. Ленина, 27)

diss@knastu.ru

***Аннотация***. Предложена новая технология процесса заполнения кристаллизатора установки непрерывной разливки стали (УНРС) жидким металлом и его перемешивания. Приведена оригинальная запатентованная конструкция устройства, состоящая из глуходонного стакана и вращающейся рубашки. Экспериментальные исследования течения жидкого металла в кристаллизаторе продолжительны, сложны и трудоемки, поэтому в работе применяется математическое моделирование численным методом. Представлены основные результаты исследований течения расплава в объеме кристаллизатора. Объектами исследований являются гидродинамические и тепловые потоки жидкого металла нового процесса разливки стали в кристаллизатор прямоугольного сечения УНРС, а результатом – пространственная математическая модель, описывающая потоки и температуры жидкого металла в кристаллизаторе. Для моделирования процессов, проте-

кающих при течении металла в кристаллизаторе, авторы используют специально созданный программный комплекс. В основе теоретических расчетов лежат основополагающие уравнения гидродинамики, уравнения математической физики (уравнение теплопроводности с учетом массопереноса) и апробированный численный метод. Исследуемая область разбивается на элементы конечных размеров, для каждого элемента в разностном виде формулируется система уравнений. Результат решения – поля скоростей и температур потока металла в объеме кристаллизатора. По разработанным численным схемам и алгоритмам составлена программа расчета. Приведен пример расчета разливки стали в кристаллизатор прямоугольного сечения, схемы потоков жидкого металла по различным сечениям кристаллизатора. Наглядно представлены векторные потоки жидкого металла в различных сечениях кристаллизатора при разных числах оборотов вращающейся рубашки. Выявлены области интенсивной турбулентности. Результаты численного решения задачи представлены в графической форме схемами полей скоростей потоков жидкого металла и их температуры по различным сечениям кристаллизатора.

***Ключевые слова:*** моделирование, кристаллизатор, жидкий металл, заполнение, потоки расплава, математическая модель, численная схема, алгоритм, скорость течения

***Для цитирования:*** Одиноков В.И., Евстигнеев А.И., Дмитриев Э.А., Карпенко В.А. Моделирование нового процесса перемешивания жидкого металла в кристаллизаторе установки непрерывной разливки стали при вращающейся рубашке с вертикальными ребрами. *Известия вузов. Черная металлургия*. 2023;66(6):733–742. https://doi.org/10.17073/0368-0797-2023-6-733-742

## Introduction

There is an increasing interest in refining the techniques for managing the flow and blending of liquid metal in Continuous Casting Molds (CCM), including the tools needed for these processes.

Experimental analysis of liquid metal movement within molds is notably complex and demands significant time, prompting a shift towards mathematical modeling, particularly through numerical methods, for these studies.

The strategies for enhancing the distribution and integration of liquid metal in CCM are well-documented in numerous national and international studies, highlighting the impact on ingot quality.

The traditional method [1 – 5] for ensuring that liquid metal washes the mold walls more evenly to achieve a uniform structure around the ingot's perimeter involves the following approach: the metal from the tundish is introduced into the mold through the holes of a closed-bottom submerged nozzle. These holes are positioned at angles of 180° relative to each other.

Innovative techniques for directing liquid metal from the nozzle into the mold have been developed. These methods vary the angle and positioning of nozzle openings [6], employ eccentrically located holes [7], use multiple nozzles [8], apply electromagnetic stirring within the mold [9], and introduce metal through deflectors [10].

Additional studies [11 – 13] introduce novel approaches and practical findings on optimizing the introduction and amalgamation of liquid metal into the CCM [11 – 13].

Researchers are actively developing models for the mathematical analysis of liquid metal flow and steel solidification in molds, using techniques such as digital modeling [14], examining the role of secondary flow in rotary electromagnetic stirring during continuous casting [15], studying metal flow inside the CCM [16; 17], investigating turbulent flow and particle transport [18], and creating models for metal solidification [19 – 21] and heat transfer during solidification [22 – 24].

They have also developed mathematical models for various liquid metal supply methods into the mold, allowing for the evaluation of specific devices' efficiency [7; 8].

Yet, there's a notable gap in the mathematical modeling of these processes, especially using numerical methods, limiting the innovation of new technologies for liquid metal supply and mixing in CCMs.

Despite past achievements, the design and modeling of melt supply and mixing processes and devices are not thoroughly explored, highlighting the importance of such research.

Therefore, it's crucial to develop new melt supply and mixing processes and their mathematical models. This will enable the prediction of new devices' performance and efficiency early in the design stage.

This paper introduces innovative technologies for casting liquid metal into the mold, utilizing rotational effects for improved mixing.

The goal is to establish a mathematical model that captures the hydrodynamic processes in the CCM mold with this new steel supply method. It aims to demonstrate the advantages of controlled rotation for liquid metal supply and mixing over the conventional free rotation of the submerged nozzle during steel casting.

We describe and analyze a novel process for liquid metal supply and mixing in the CCM mold [25], which, unlike previous methods [26; 27], offers extensive control over mixing speed. This control is crucial for achieving higher quality continuous ingots.

Fig. 1 illustrates the design of a specific device. Metal is transferred from the tundish (*1*) into the mold (*5*) via a closed-bottom submerged nozzle (*2*), which is equipped with off-center holes (*4*). A refractory jacket (*3*) featuring ribs (*6*) is fitted around the submerged nozzle's outer surface, just above its discharge holes, with a small gap in between. This jacket is linked to a rotating mechanism, comprised of an axial bearing (*7*), a gearbox (*8*), and an electric motor (*9*).

The process in question is dynamic, yet it's modeled as if it were steady under certain simplifying assump-

tions. The submerged nozzle and the rotating refractory jacket share the same square shape at their outlets. Thus, as the jacket rotates, its edges stir the liquid metal within the mold.

The rotation direction causes one side of the refractory jacket's square edge to push the metal outward, while the opposite side draws it in. In this model, the submerged nozzle is considered to be fixed, with metal movement in and out of the jacket's edges depending on the rotation speed and the square dimensions of the jacket. This idealized scenario is thoroughly explained in [1], allowing the process to be viewed as steady for the purpose of this analysis. It's important to note that the formation of a solid metal crust on the mold edges is not accounted for in this model.

The medium, which is liquid metal, is considered incompressible. Let's consider the equations of hydrodynamics. The following equations are valid for the flow of a Newtonian, viscous, incompressible fluid when the process is stationary:

$$\sigma_{ij,j} + F_i^* = I_i^*;\ I_i^* = \rho\left(\dot{v}_i + v_k \frac{\partial v_i}{\partial x_k}\right); \quad (1)$$

$$\sigma_{ij} - \sigma\delta_{ij} = 2\mu\xi_{ij};\ \xi_{ij} = \frac{1}{2}\left(v_{i,j} + v_{j,i}\right); \quad (2)$$

$$v_{i,i} = 0;\ i = 1, 2, 3; \quad (3)$$

$$\frac{d\theta}{d\tau} = a\Delta\theta;\ \frac{d\theta}{d\tau} = v_i \frac{\partial\theta}{\partial x_i};\ i = 1,\ 2,\ 3, \quad (4)$$

here $\sigma_{ij}$ are the components of the stress tensor; $\xi_{ij}$ are the components of the strain rate tensor; $\delta_{ij}$ is Kronecker's delts; $p$ is the pressure at a given point ($p = -\sigma$); $\sigma$ is the hydrostatic stress; $\mu$ is the viscosity coefficient, (g·s)/cm$^2$; $v_i$ is the velocity projections along the coordinate axes $x_i (i = 1, 2, 3)$; $\rho$ is the density of the liquid metal; $F_i^*$ is the projection of the specific volume force on the coordinate axis $x_i (i = 1, 2, 3)$; $\tau$ is time; $\Delta$ is the Laplace operator; $\theta$ is the temperature; $a = \lambda/(c\gamma)$ is the temperature-conductivity ratio; $\lambda$ is the heat transfer coefficient; $c$ is the specific heat capacity; $\gamma$ is the density, all of which are considered constants in this context.

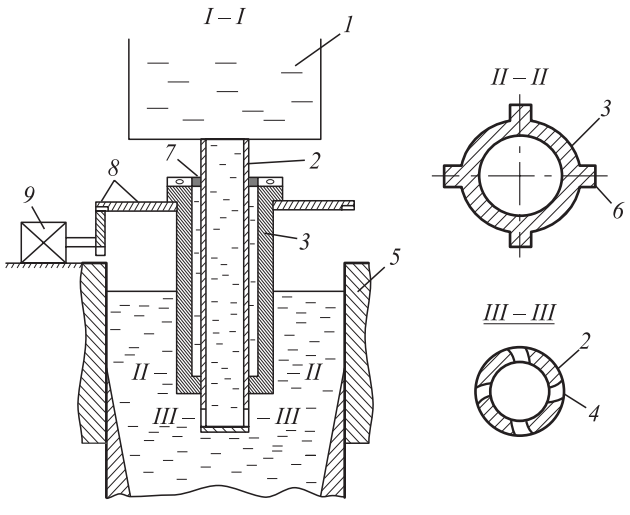


Fig. 1. Scheme of a device for supply and mixing of steel in the mold with rotating jacket with vertical ribs

Рис. 1. Схема устройства для подачи и перемешивания стали в кристаллизаторе с вращающейся рубашкой с вертикальными ребрами

For the stationary process:

$$\dot{v}_i = \frac{\partial v_i}{\partial\tau} = 0.$$

The thermal conductivity equation considers mass transfer and the condition of stationarity.

Fig. 2 illustrates the computational scheme for the process being examined.

The boundary conditions of the problem are defined as follows (Fig. 2):

$$\begin{gathered}
\sigma_{11}\big|_{\Gamma_2} = p_1;\ (\sigma_{12} = \sigma_{13})\big|_{\Gamma_i} = 0;\ i = 1 \div 3; \\
(\sigma_{21} = \sigma_{23})\big|_{\Gamma_i} = 0;\ i = 5 \div 8; \\
(\sigma_{31} = \sigma_{32})\big|_{\Gamma_i} = 0;\ i = 9 \div 11; \\
(\sigma_{21} = \sigma_{23})\big|_{\Gamma_8'} = 0;\ (\sigma_{31} = \sigma_{32})\big|_{\Gamma_8''} = 0; \\
v_2\big|_{\Gamma_5} = v^*; \\
v_3\big|_{\Gamma_8''} = V_t; \\
v_2\big|_{\Gamma_8'} = V_t; \\
v_1\big|_{\Gamma_1} = v_u; \\
v_1\big|_{\Gamma_3} = 0; \\
v_2\big|_{\Gamma_i} = 0;\ i = 6 \div 8; \\
v_3\big|_{\Gamma_i} = 0;\ i = 9 \div 11.
\end{gathered} \quad (5)$$

The boundary conditions were applied to solve the thermal conductivity equation (4):

$$\begin{gathered}
\theta\big|_{\Gamma_i} = \theta_i^*;\ i = 1 \div 10; \\
q\big|_{\Gamma_i} = q_i^*;\ i = 6,\ 7,\ 9,\ 10;
\end{gathered} \quad (6)$$

here $v_u$ is the speed at which the ingot is pulled (Fig. 2); $v_2^*$ is the speed of liquid metal exiting through the holes of the submerged nozzle; the given functions of metal temperature distribution on surfaces $\Gamma_i$ are denoted as $\theta_i^*$; while $q_i^*$ refers to the heat flows through surfaces $\Gamma_i$ obtained from experimental data; the preset temperature of the metal exiting through the hole $\Gamma_5$ is specified as $\theta_5^*$.

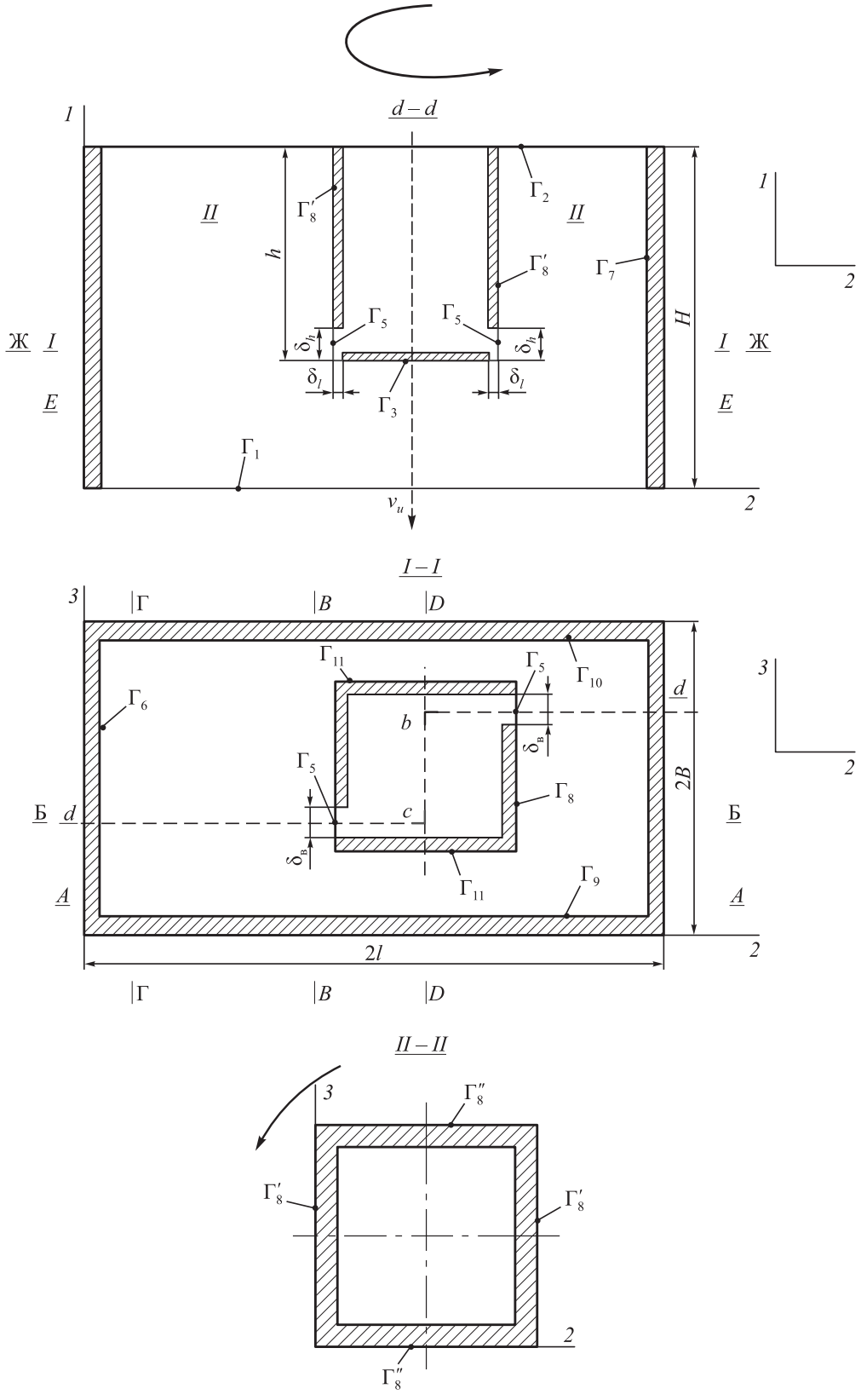


Fig. 2. Formalized design scheme of metal casting into the mold

Рис. 2. Формализованная расчетная схема процесса разливки металла в кристаллизатор

The numerical scheme and algorithm for solving the system of equations (1) – (4) under the boundary conditions (5), (6) are described in detail in [28], utilizing a numerical method that has been extensively tested.

Below, we present the results of the numerical solution for the problem across different sections of the mold, along with an analysis of these results.

## Results of numerical calculation

We set the mold dimensions as follows: $H = 100$ cm; $B = 12.5$ cm; $l = 100$ cm; $h = 20$ cm; $b = 7.5$ cm; $\delta_h = 8.5$ cm; $\delta_B = 1.5$ cm; $\delta_1 = 1.5$ cm; $v_u = 1$ m/min = 1.66 cm/s. For the stationary process, the value $v^*$ was determined from the equality of the second volumes:

$$v_u Bl = v^* \delta_n \delta_B \Rightarrow v^* = \frac{v_u Bl}{\delta_n \delta_B}.$$

The temperature of the liquid steel flowing out of the hole ($\Gamma_5$) was set to $\theta^*\big|_{\Gamma_5} = 1600$ °C. The temperature on the surfaces of the submerged nozzle (Fig. 2) $\Gamma_i$ ($i$ = 3, 8, 8′, 11) was determined from experimental data to be $\theta^*\big|_{\Gamma_i} = 1550$ °C, $i$ = 3, 8, 8′, 11. On the surface $\Gamma_2$ (Fig. 2) there is a liquid slag "jacket" with a temperature of $\theta^*\big|_{\Gamma_2} = 1550$ °C.

Constants are defined as follows $\lambda = 0.29$ W/(cm·s); $c = 444.47$ J/(kg·s); $\gamma = 7.8$ g/cm$^3$. The viscosity factor $\mu = 2.1 \cdot 10^{-4}$ (kg·s)/m$^2$ used in equations (2) was adopted based on [29].

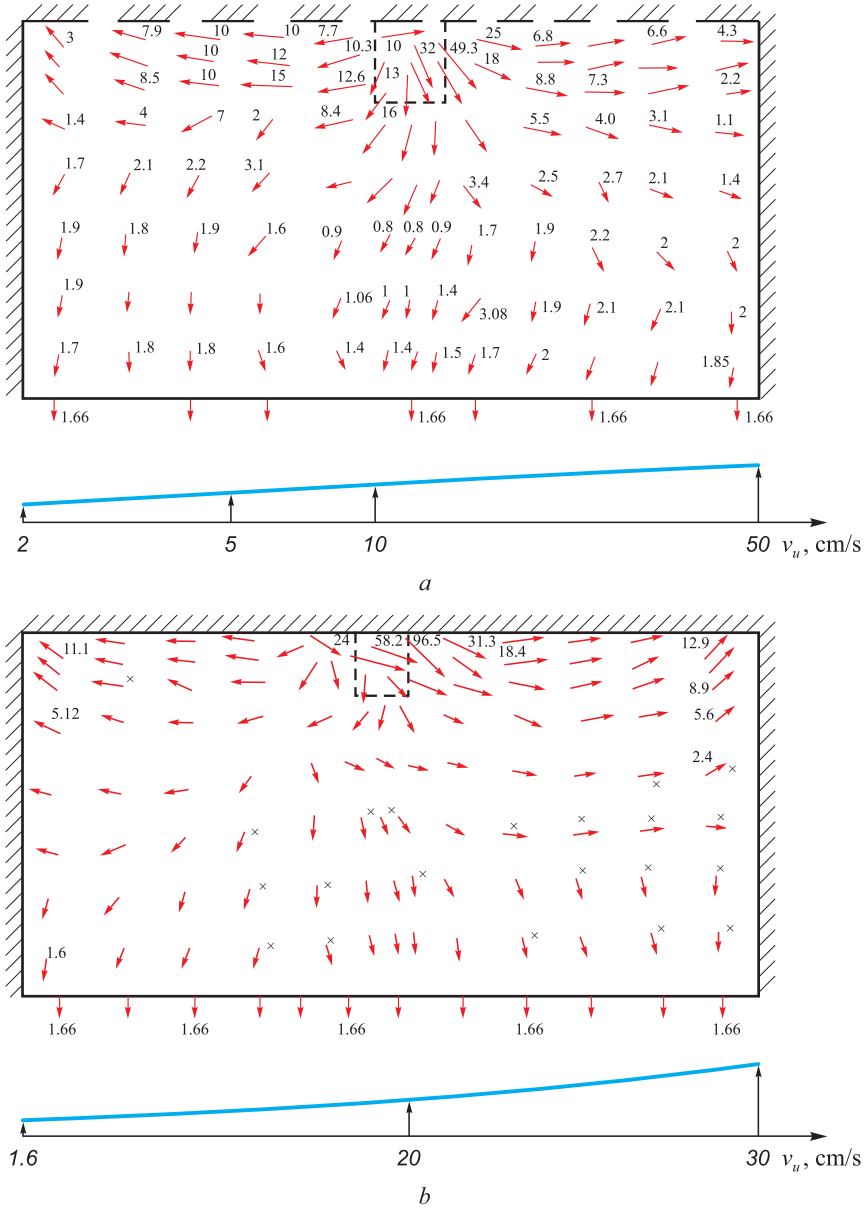


Fig. 3. Velocity field of metal flows in the mold cross-section $A - A$ at $n = 30$ (*a*) and 50 rpm (*b*)

Рис. 3. Поле скоростей потоков течения металла в кристаллизаторе в сечении $A - A$ при $n = 30$ (*a*) и 50 об/мин (*b*)

Fig. 3 illustrates the metal flows in the cross-section $A - A$ as the jacket rotates at speed ($n$) of 30 and 50 rpm. The low patterns are comparable, yet the intensity of the flows increases at $n$ = 50 rpm (Fig. 3, *b*). In cross-section $A - A$, metal flow near the submerged nozzle appears chaotic. Areas where the metal temperature exceeds the crystallization point are indicated by asterisks in Fig. 3, *b*, highlighting regions of higher thermal variance. This suggests a more uneven distribution of temperature within the metal flows across this cross-section.

In Fig. 4 the metal flows in the vertical cross-section $B-B$, which captures the area where metal exits the submerged nozzle, are depicted. This figure compares the flow dynamics at rotational speeds of 30 and 50 rpm, with all flow vectors predominantly pointing downwards. Consistent with expectations, flow intensity is higher at the increased rotational speed of 50 rpm.

Fig. 5, *a*, presents the metal flows in cross-section $D - D$ (Fig. 2) when the jacket rotates at 30 rpm and at 50 rpm. At $n$ = 30 rpm (Fig. 5, *a*), small vortices are observed beneath the submerged nozzle, specifically at its center. However, at the higher speed of 50 rpm, these vortices disappear. The metal flow rate near the side edges of the mold is significantly higher than that under the submerged nozzle.

In Fig. 6, the metal flows are illustrated in the horizontal cross-section $E - E$, with the jacket rotating at speeds of 30 and 50 rpm.

The flow vectors show little difference in terms of motion patterns and velocities. At a rotational speed of 50 rpm, Fig. 7 illustrates the metal flows in the horizontal section of the submerged nozzle as it moves through the outlets (cross-section Ж – Ж). The pattern of metal flow is similar to that observed in cross-section $E - E$ (Fig. 6), albeit more intense.

When the rotation speed reaches 50 rpm, the metal can penetrate into the slag cushion along the narrow mold walls. Fig. 8 displays the motion field of the liquid metal (cross-section Г′ – Г′). In this case, the liquid metal moves upward, covering half of the vertical plane of the mold's

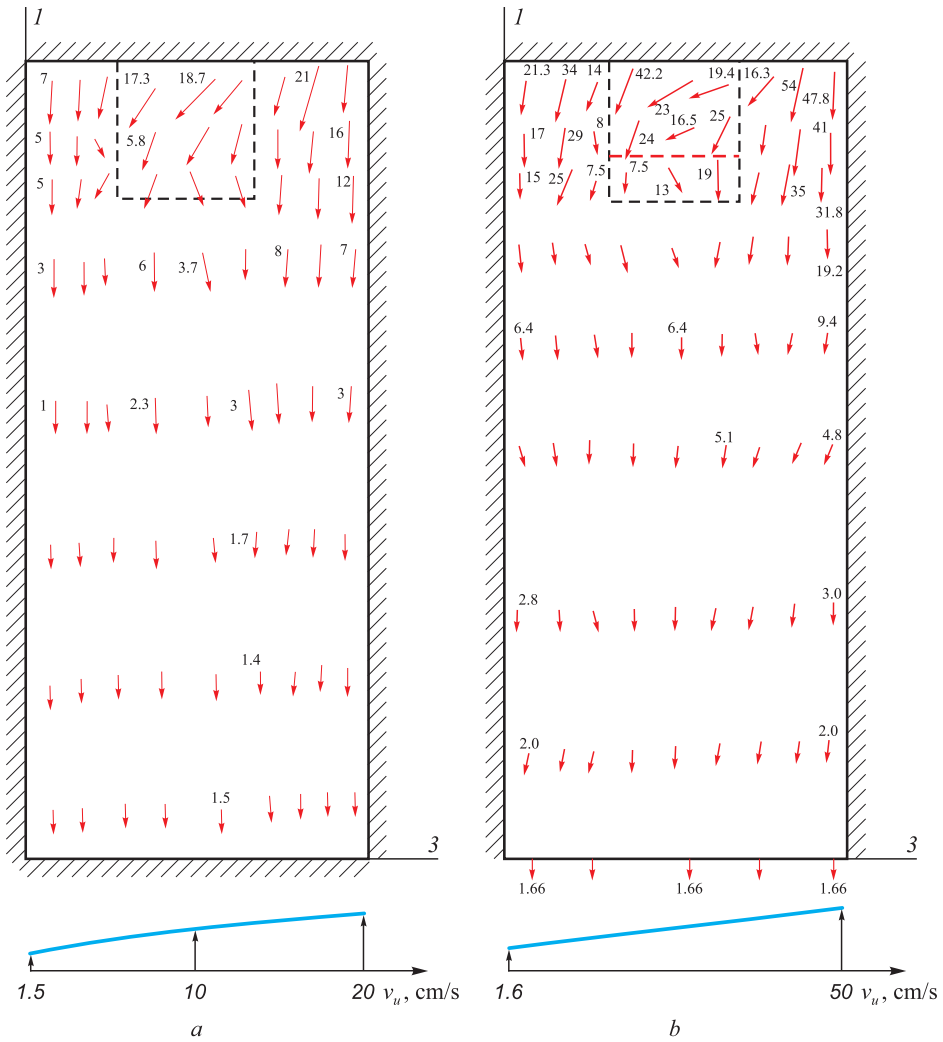


Fig. 4. Velocity field of metal flows in the mold cross-section $B - B$ at $n$ = 30 (*a*) and 50 rpm (*b*)

Рис. 4. Поле скоростей потоков течения металла в кристаллизаторе в сечении $B - B$ при $n$ = 30 (*a*) и 50 об/мин (*b*)

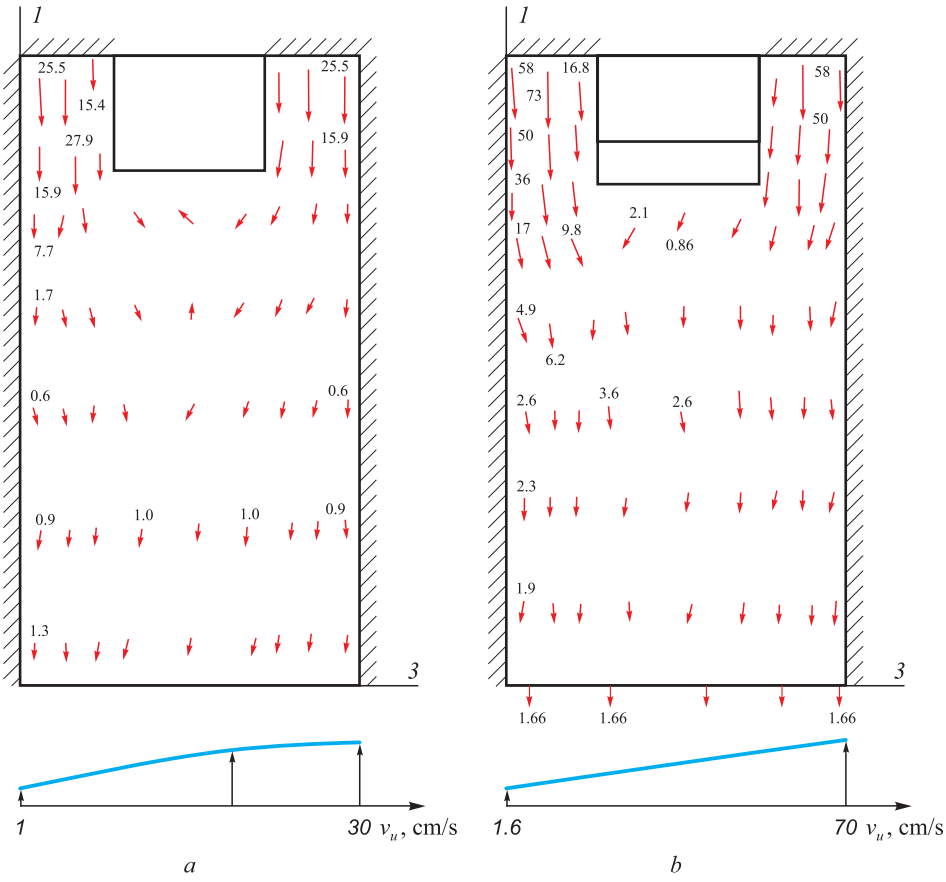


Fig. 5. Velocity field of metal flows in the mold cross-section $D – D$ at $n$ = 30 (*a*) and 50 rpm (*b*)

Рис. 5. Поле скоростей потоков течения металла в кристаллизаторе в сечении $D – D$ при $n$ = 30 (*a*) и 50 об/мин (*b*)

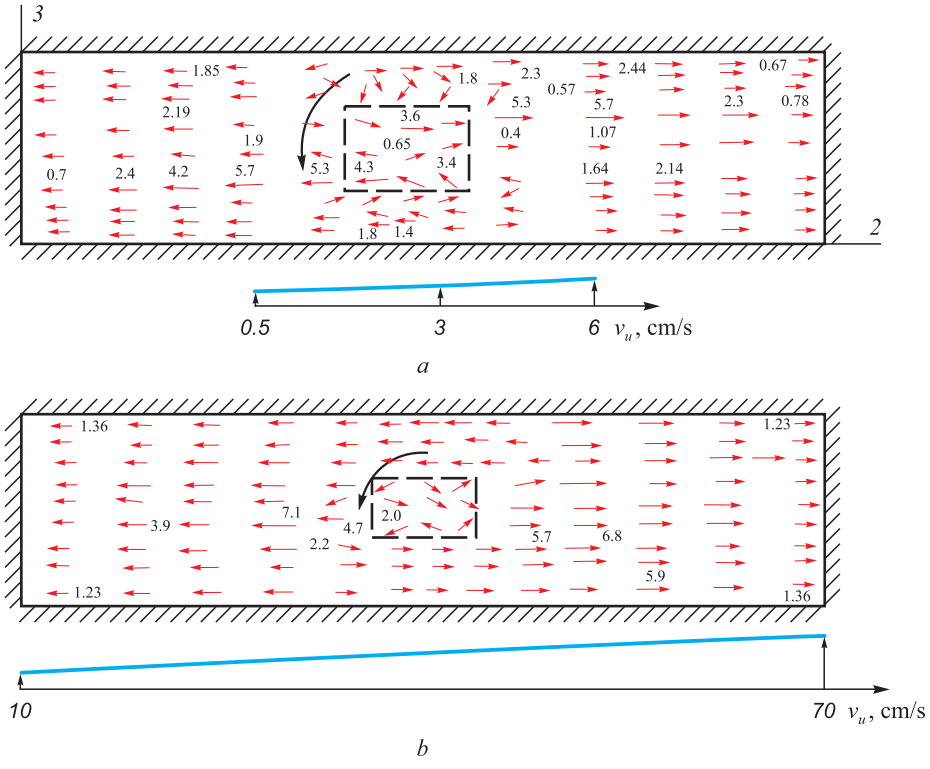


Fig. 6. Velocity field of metal flows in the mold cross-section $E – E$ at $n$ = 30 (*a*) and 50 rpm (*b*)

Рис. 6. Поле скоростей потоков течения металла в кристаллизаторе в сечении $E – E$ при $n$ = 30 (*a*) и 50 об/мин (*b*)

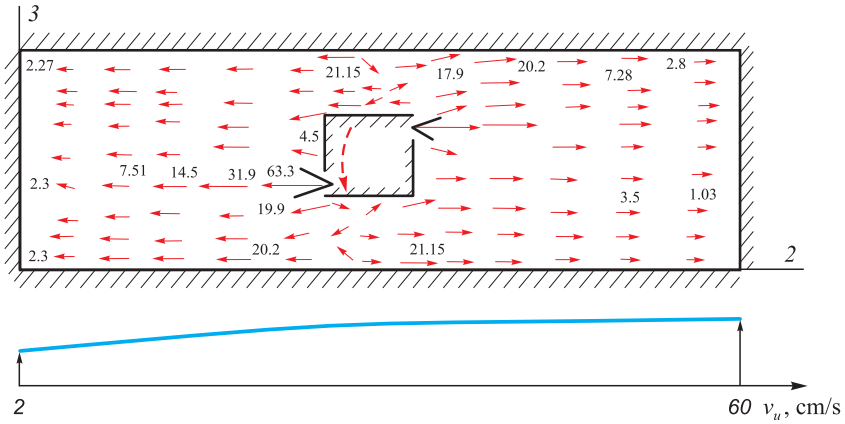


Fig. 7. Velocity field of metal flows in the mold cross-section Ж – Ж at $n$ = 50 rpm

Рис. 7. Поле скоростей потоков течения металла в кристаллизаторе в сечении Ж – Ж при $n$ = 50 об/мин

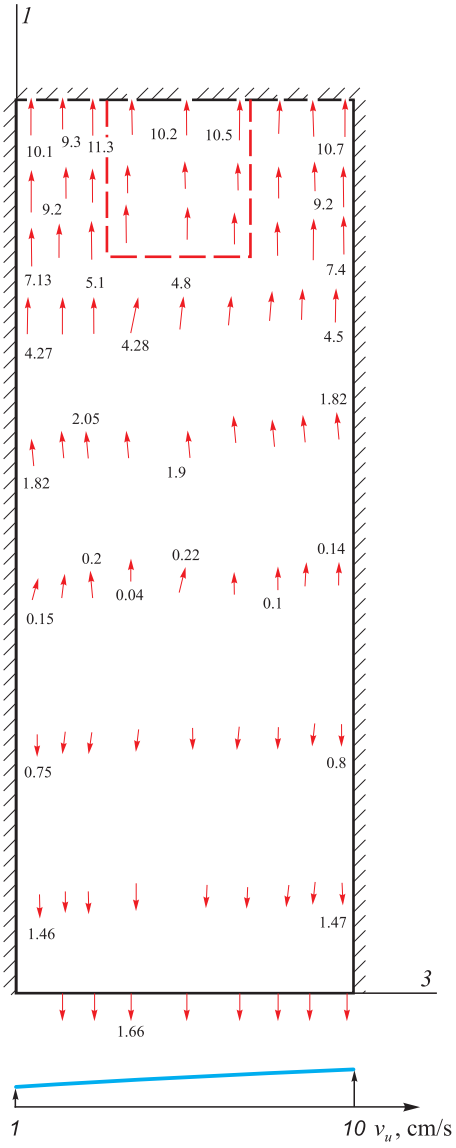


Fig. 8. Velocity field of metal flows
in the mold cross-sectionn Г′ – Г′ at $n$ = 50 rpm

Рис. 8. Поле скоростей потоков течения металла
в кристаллизаторе в сечении Г′ – Г′ при $n$ = 50 об/мин

side wall, and accelerates at the slag jacket, reaching a speed of 10 cm/s. In the cross-section $D$ – $D$, metal moves swiftly downward from the slag jacket (Fig. 5, *b*). This rapid movement suggests the potential formation of vortices beneath the slag jacket. Such vorticity in the metal flow is not necessarily benign. It raises the concern that slag could become entrapped within the continuous ingot, negatively impacting the quality of the ingot.

## Conclusions

The theoretical study produced numerical results:

– in cases of forced mixing of liquid metal within a rectangular cross-section mold, the mold walls are intensively washed, significantly aiding in the transfer of heat from the liquid metal to the mold walls;

– within the mold, particularly in its upper section, there is observed accelerated movement of liquid metal flows;

– on narrow mold walls, liquid metal is propelled (even at 30 rpm) towards the slag jacket area, potentially allowing some of the slag to mix into the continuously cast ingot. To prevent this issue, the submerged nozzle equipped with the rotating jacket can be positioned deeper into the mold. This adjustment requires an increase in mold height.

## References / Список литературы

**1.** Dyudkin D.A., Kisilenko V.V., Smirnov A.N. *Production of Steel. Vol. 4. Continuous Casting of Metal*. Moscow: Teplotekhnik; 2009:528. (In Russ.).

Дюдкин Д.А., Кисиленко В.В., Смирнов А.Н. *Производство стали. Т. 4. Непрерывная разливка металла*. Москва: Теплотехник; 2009:528.

**2.** Efimov V.A. *Casting and Crystallization of Steel*. Moscow: Metallurgiya; 1976:552. (In Russ.).

Ефимов В.А. *Разливка и кристаллизация стали*. Москва: Металлургия; 1976:552.

**3.** Akimenko A.D., Girskii V.E., Gus'kov A.I. Influence of methods of metal supply to a mold on formation of axial zone in a square ingot. *Stal'*. 1973;(5):408–409. (In Russ.).

Акименко А.Д., Гирский В.Е., Гуськов А.И. Влияние способов подвода металла в кристаллизатор на формирование осевой зоны квадратного слитка. *Сталь*. 1973;(5):408–409.

4. Odinokov V.I., Dmitriev E.A., Evstigneev A.I. Numerical modeling of the process of filling the CCM mold with metal. *Izvestiya. Ferrous Metallurgy*. 2017;60(6):493–498. (In Russ.). https://doi.org/10.17073/0368-0797-2017-6-493-499

   Одиноков В.И., Дмитриев Э.А., Евстигнеев А.И. Численное моделирование процесса заполнения металлом кристаллизатора УНРС*. *Известия вузов. Черная металлургия*. 2017;60(6):493–498. https://doi.org/10.17073/0368-0797-2017-6-493-499

5. *Proceedings of the Int. Symp. on Electromagnetic Processing of Materials. October 25–28, 1994*, *Nagoya, Japan*. ISIJ; 1994:580.

6. Stulov V.V., Matysik V.A., Novikov T.V., Shcherbakov S.V., Chistyakov I.V., Plotnikov A.P. *Development of a New Method for Casting Slab Blanks in CCM*. Vladivostok: Dal'nauka; 2008:156. (In Russ.).

   Стулов В.В., Матысик В.А., Новиков Т.В., Щербаков С.В., Чистяков И.В., Плотников А.П. *Разработка нового способа разливки слябовых заготовок на МЛНЗ*. Владивосток: Дальнаука; 2008:156.

7. Odinokov V.I., Dmitriev E.A., Evstigneev A.I. Mathematical modeling of metal flow in crystallizer at its supply from submersible nozzle with eccentric holes. *Izvestiya. Ferrous Metallurgy*. 2018;61(8):606–612. (In Russ.). https://doi.org/10.17073/0368-0797-2018-8-606-612

   Одиноков В.И., Дмитриев Э.А., Евстигнеев А.И. Математическое моделирование процесса течения металла в кристаллизаторе при его подаче из погружного стакана с эксцентричными отверстиями. *Известия вузов. Черная металлургия*. 2018;61(8):606–612. https://doi.org/10.17073/0368-0797-2018-8-606-612

8. Kuberskii S.V., Semiryagin S.O., Fedorov O.V. *Calculations of Technological and Design Parameters of CCM: Tutorial*. Alchevsk: DONSTU; 2006:146. (In Russ.).

   Куберский С.В., Семирягин С.О., Федоров О.В. *Расчеты технологических и конструктивных параметров МЛНЗ: Учебное пособие*. Алчевск: ДОНГТУ; 2006:146.

9. Smirnov A.A., Niskovskikh V.M., Kulikov V.I. Investigation of electromagnetic mixing of metal in slab CCM by modeling method. In: *Improving the Structures, Research and Calculation of CCM: Coll. of Sci. Papers*. Moscow: VNIIMETMASh; 1987:85–90. (In Russ.).

10. Odinokov V.I., Evstigneev A.I., Dmitriev E.A. Numerical modelling of metal filling in CCM mold completed with deflector. *Izvestiya. Ferrous Metallurgy*. 2019;62(10):747–755. (In Russ.). https://doi.org/10.17073/0368-0797-2019-10-747-755

    Одиноков В.И., Евстигнеев А.И., Дмитриев Э.А. Численное моделирование процесса заполнения металла кристаллизатора с отражателем УНРС. *Известия вузов. Черная металлургия*. 2019;62(10):747–755. https://doi.org/10.17073/0368-0797-2019-10-747-755

11. Nartst Kh.-P., Kellerer S., Shtakhelberger K., Merval'd K., Fedeshpil' K., Val' G. Innovative solutions and practical results of continuous slab casting technology. *Chernye metally*. 2003;(11):34–38. (In Russ.).

    Нарцт Х.-П., Келлерер С., Штахельбергер К., Мёрвальд К., Федершпиль К., Валь Г. Новаторские решения и практические результаты технологии непрерывного литья слябов. *Черные металлы*. 2003;(11):34–38.

12. Vimmer F., Tene X., Pekshtainer L. High-speed casting of small-grade billets on CCM with Diamond mold. *Stal'*. 1999;(6):22–26. (In Russ.).

    Виммер Ф., Тене Х., Пекштайнер Л. Высокоскоростное литье мелкосортовых заготовок на МНЛЗ с кристаллизатором «Дайэмоулд». *Сталь*. 1999;(6):22–26.

13. Aikhinger A., Frauenkhuber K., Khedl' X., Merval'd K. Modern equipment for high-performance continuous casting. *Stal'*. 2000;(3):25–28. (In Russ.).

    Айхингер А., Фрауэнхубер К., Хедль Х., Мервальд К. Новейшее оборудование для высокопроизводительной непрерывной разливки. *Сталь*. 2000;(3):25–28.

14. Oler K., Odental' Kh.-Yu., Pfaifer G., Lemanovich I. Digital modeling of metal flow and solidification in CCM for casting thin slabs. *Chernye metally*. 2002;(8):22–30. (In Russ.).

    Олер К., Оденталь Х.-Ю., Пфайфер Г., Леманович И. Цифровое моделирование процессов течения и затвердевания металла в МНЛЗ для литья тонких слябов. *Черные металлы*. 2002;(8):22–30.

15. Davidson P.A., Boysan F. The importance of secondary flow in the rotary electromagnetic stirring of steel during continuous casting. *Applied Scientific Research*. 1987;44(1–2):241–259. http://doi.org/10.1007/BF00412016

16. Thomas B.G., Mika L.J., Najjar F.M. Simulation of fluid flow inside a continuous slab casting machine. *Metallurgical Transactions B*. 1990;21(2):387–400. http://doi.org/10.1007/BF02664206

17. Thomas B.G., Zhang L. Mathematical modeling of fluid flow in continuous casting. *ISIJ International*. 2001;41(10):1181–1193. http://doi.org/10.2355/isijinternational.41.1181

18. Yuan Q., Shi T., Vanka S.P., Thomas B.G. Simulation of turbulent flow and particle transport in the continuous casting of steel. In: *Computational Modeling of Materials Minerals and Metals*. Warrendale, PA; 2002:491–500.

19. Larreq M., Sagues C., Wanin M. Vodele mathematique de la solidification eu coulee continue tenant compte de la convection al`interface solide-liquide. *Revue de Metallurgie*. 1978;75(6):337–352.

20. Ozava M., Okano S., Matsuno J. Influence des contitions du jet de coulee sur la formation de la peau solidifiee eu lingotiere de brames de colee con-tinue. *Tetsu-to-Hagane*. 1976;62(4):86.

21. Kohn A., Morillon Y. Etnde mathematique de la solidification des lingots en acier mi-dur. *Revue de Metallurgie*. 1966;63(10):779–790.

22. Ho K., Pehlke R. Modelling of steel solidification using the general finite difference method. In: *5th Int. Iron and Steel Congress. Proceedings of the 6th Process Technol. Conf. (Apr. 6–9, 1986)*. Warrendale; 1986;6:853–866.

23. Mizikar E. Mathematical heat transfer model for solidification of continuous cast steel slabs. *Transactions of the Metallurgical Society of AIME*. 1967;239(11):1747.

24. Szekely J., Stanek V. On heat transfer and liquid mixing in the continuous casting of steel. *Metallurgical Transactions*. 1970;1(1):119. https://doi.org/10.1007/BF02819250

25. Odinokov V.I., Evstigneev A.I., Dmitriev E.A., Aleksandrov A.Yu., Karpenko V.A. *A device for feeding and mixing*

*steel in CCM mold*. Pat. RF 2764446. *Byulleten' izobretenii*. 2022;(2). (In Russ.).

Патент №2764446 РФ. *Устройство для подачи и перемешивания стали в кристаллизаторе установки непрерывной разливки* / Одиноков В.И., Евстигнеев А.И., Дмитриев Э.А., Александров А.Ю., Карпенко В.А.; заявл. 20.05.2021; опубл. 17.01.2022. Бюл. № 2.

**26.** Odinokov V.I., Dmitriev E.A., Evstigneev A.I., Kuznetsov S.A., Gornakov A.I. Improvement of devices for filling CCM mold by liquid metal. *Metallurg*. 2021;(4):33–35. (In Russ.). https://doi.org/10.52351/00260827_2021_04_33

Одиноков В.И., Дмитриев Э.А., Евстигнеев А.И., Кузнецов С.А., Горнаков А.И. Совершенствование устройств по заполнению кристаллизатора УНРС жидким металлом. *Металлург*.2021;(4):33–35. https://doi.org/10.52351/00260827_2021_04_33

**27.** Odinokov V.I., Evstigneev A.I., Dmitriev E.A., Aleksandrov S.Yu., Karpenko V.A. Improvement of devices for feeding and mixing of liquid metal in continuous casting mould. *Zagotovitel'nye proizvodstva v mashinostroenii*. 2022;20(3):99–103. (In Russ.). https://doi.org/10.36652/1684-1107-2022-20-3-99-102

Одиноков В.И., Евстигнеев А.И., Дмитриев Э.А., Александров С.Ю., Карпенко В.А. Совершенствование устройств для подачи и перемешивания жидкого металла в кристаллизаторе установки непрерывного литья стали. *Заготовительные производства в машиностроении*. 2022;20(3): 99–103. https://doi.org/10.36652/1684-1107-2022-20-3-99-102

**28.** Odinokov V.I., Evstigneev A.I., Dmitriev E.A., Karpenko V.A. Mathematical modeling of mixing liquid metal in CCM mold. *Matematicheskoe modelirovanie i chislennye metody*. 2023;(3):18–41. (In Russ.).

Одиноков В.И., Евстигнеев А.И., Дмитриев Э.А., Карпенко В.А. Математическое моделирование процесса перемешивания жидкого металла в кристаллизаторе установке непрерывной разливки стали. *Математическое моделирование и численные методы*. 2023;(3):18–41.

**29.** Kim W.S., Chair T.S. A simplified phenomenological theory of viscosity for liquid metals. *Bulletin of the Korean Chemical Society*. 2001;22(1):43–45.

## Information about the Authors / Сведения об авторах

***Valerii I. Odinokov,*** *Dr. Sci. (Eng.), Prof., Chief Researcher of the Department of Research Activities,* Komsomolsk-on-Amur State University
***ORCID:*** 0000-0003-0200-1675
***E-mail:*** 79122718858@yandex.ru

***Aleksei I. Evstigneev,*** *Dr. Sci. (Eng.), Prof., Chief Researcher of the Department of Research Activities,* Komsomolsk-on-Amur State University
***ORCID:*** 0000-0002-9594-4068
***E-mail:*** diss@knastu.ru

***Eduard A. Dmitriev,*** *Dr. Sci. (Eng.), Assist. Prof., Rector,* Komsomolsk-on-Amur State University
***ORCID:*** 0000-0001-8023-316X
***E-mail:*** rector@knastu.ru

***Vladimir A. Karpenko,*** *Candidates for a Degree of Cand. Sci. (Eng.),* Komsomolsk-on-Amur State University
***ORCID:*** 0009-0003-7137-0789
***E-mail:*** volodya.karpenko.89@mail.ru

***Валерий Иванович Одиноков,*** *д.т.н., профессор, главный научный сотрудник Управления научно-исследовательской деятельностью,* Комсомольский-на-Амуре государственный университет
***ORCID:*** 0000-0003-0200-1675
***E-mail:*** 79122718858@yandex.ru

***Алексей Иванович Евстигнеев,*** *д.т.н., профессор, главный научный сотрудник Управления научно-исследовательской деятельностью,* Комсомольский-на-Амуре государственный университет
***ORCID:*** 0000-0002-9594-4068
***E-mail:*** diss@knastu.ru

***Эдуард Анатольевич Дмитриев,*** *д.т.н., доцент, ректор,* Комсомольский-на-Амуре государственный университет
***ORCID:*** 0000-0001-8023-316X
***E-mail:*** rector@knastu.ru

***Владимир Анатольевич Карпенко,*** *соискатель степени к.т.н.,* Комсомольский-на-Амуре государственный университет
***ORCID:*** 0009-0003-7137-0789
***E-mail:*** volodya.karpenko.89@mail.ru

## Contribution of the Authors / Вклад авторов

***V. I. Odinokov*** – scientific guidance, analysis of the research results, editing and correction of the final version of the article.

***A. I. Evstigneev*** – formation of the article concept, setting the goal and objectives of the study, analysis of the research results, writing the text.

***E. A. Dmitriev*** – conducting calculations, analysis, writing and correction of the text.

***V. A. Karpenko*** – conducting calculations, analysis, preparation of references, processing of graphic material, design of materials.

***В. И. Одиноков*** – научное руководство, анализ результатов исследований, редактирование и корректировка финальной версии статьи.

***А. И. Евстигнеев*** – формирование концепции статьи, определение цели и задачи исследования, анализ результатов исследования, подготовка текста.

***Э. А. Дмитриев*** – проведение расчетов, их анализ, подготовка и корректировка текста.

***В. А. Карпенко*** – проведение расчетов, их анализ, подготовка библиографического списка, обработка графического материала, оформление материалов.

Received 27.06.2023
Revised 12.07.2023
Accepted 14.07.2023

Поступила в редакцию 27.06.2023
После доработки 12.07.2023
Принята к публикации 14.07.2023

**PHYSICO-CHEMICAL BASICS OF METALLURGICAL PROCESSES** / **ФИЗИКО-ХИМИЧЕСКИЕ ОСНОВЫ МЕТАЛЛУРГИЧЕСКИХ ПРОЦЕССОВ**

**UDC** 669.168
**DOI** 10.17073/0368-0797-2023-6-743-749



*Original article*
*Оригинальная статья*

# Influence of basicity on physical properties of slags of the $CaO - SiO_2 - 18\ \% Cr_2O_3 - 6\ \% B_2O_3 - 3\ \% Al_2O_3 - 8\ \% MgO$ system

**A. A. Babenko, R. R. Shartdinov, A. G. Upolovnikova, A. N. Smetannikov, D. A. Lobanov, A. V. Dolmatov**

**Institute of Metallurgy, Ural Branch of the Russian Academy of Sciences** (101 Amundsena Str., Yekaterinburg 620016, Russian Federation)

rr.shartdinov@gmail.com

***Abstract***. Influence of basicity on viscosity, crystallization onset temperature, phase composition, and structure of slags of the $CaO-SiO_2-18\ \% Cr_2O_3-6\ \% B_2O_3-3\ \% Al_2O_3-8\ \% MgO$ system in the basicity range ($B = CaO/SiO_2$) from 1.0 up to 2.5 was studied using vibrational viscometry, thermodynamic modeling, and Raman spectroscopy. It was established that the physical properties of slags depend on the balance of polymerization degree and phase composition. Acid slags with a basicity of 1.0 belong to the category of "long" slags and are characterized by an increased proportion of high-temperature phases up to 34.1 %. However, despite the fact that the proportion of high-temperature phases is 1.6 times higher compared to the proportion of low-temperature ones, they are characterized by a simpler silicate structure, providing a viscosity of no more than 0.25 Pa·s at a crystallization onset temperature of 1530 °C. An increase in basicity of slags of the studied oxide system (up to 2.5), along with an increase in the proportion of high-temperature phases (by almost 5.9 times), is accompanied by formation of a more complex silicate structure. The resulting four-coordination structural elements [$CrO_4$] and [$AlO_4$] are embedded in the silicate structure and complicate it, which increases the polymerization degree. Thus, at basicity of 2.5, due to a high proportion of high-temperature phases in the slag and development of polymerization process, slag crystallization onset temperature increases to 1700 °C and its viscosity reaches 1.0 Pa·s at a temperature of 1670 °C.

***Keywords:*** AOD-slag, boron oxide, chromium oxide, structure, viscosity, phase composition, crystallization onset temperature

***Acknowledgements:*** The work was performed according to the state assignment of the Institute of Metallurgy, Ural Branch of the Russian Academy of Sciences using the equipment of the Shared Access Center "Composition of Compounds" of Institute of High Temperature Electronics, Ural Branch of the Russian Academy of Sciences.

***For citation:*** Babenko A.A., Shartdinov R.R., Upolovnikova A.G., Smetannikov A.N., Lobanov D.A., Dolmatov A.V. Influence of basicity on physical properties of slags of the $CaO - SiO_2 - 18\ \% Cr_2O_3 - 6\ \% B_2O_3 - 3\ \% Al_2O_3 - 8\ \% MgO$ system. *Izvestiya. Ferrous Metallurgy*. 2023;66(6): 743–749. https://doi.org/10.17073/0368-0797-2023-6-743-749

# Влияние основности на физические свойства шлаков системы $CaO - SiO_2 - 18\ \% Cr_2O_3 - 6\ \% B_2O_3 - 3\ \% Al_2O_3 - 8\ \% MgO$

**А. А. Бабенко, Р. Р. Шартдинов, А. Г. Уполовникова, А. Н. Сметанников, Д. А. Лобанов, А. В. Долматов**

**Институт металлургии Уральского отделения РАН** (Россия, 620016, Свердловская обл., Екатеринбург, ул. Амудсена, 101)

rr.shartdinov@gmail.com

***Аннотация***. В работе исследовано влияние основности на вязкость, температуру начала кристаллизации, фазовый состав и структуру шлаков системы $CaO-SiO_2-18\ \% Cr_2O_3-6\ \% B_2O_3-3\ \% Al_2O_3-8\ \% MgO$ в диапазоне основности от 1,0 до 2,5 методами вибрационной вискозиметрии, термодинамического моделирования и рамановской спектроскопии. Физические свойства шлаков зависят от баланса процессов полимеризации и формирования фазового состава. Кислые шлаки основностью 1,0 относятся к категории «длинных» шлаков и характеризуются повышенной (до 34,1 %) долей высокотемпературных фаз. Однако, несмотря на то, что доля высокотемпературных фаз в 1,6 раза выше по сравнению с долей низкотемпературных фаз, они характеризуются более простой силикатной структурой, обеспе-

чивая при температуре начала кристаллизации 1530 °С вязкость не более 0,25 Па·с. Рост основности (до 2,5) шлаков изучаемой оксидной системы, наряду с повышением (примерно в 5,9 раза) доли высокотемпературных фаз, сопровождается формированием более сложной силикатной структуры. Образующиеся четырехкоординационные структурные элементы [$CrO_4$] и [$AlO_4$] встраиваются в кремний-кислородную решетку и усложняют ее, что повышает степень полимеризации. Таким образом, при основности 2,5, в связи с высокой долей высокотемпературных фаз в шлаке и развитием процесса полимеризации, температура начала кристаллизации шлака возрастает до 1700 °С, а его вязкость достигает 1,0 Па·с при температуре 1670 °С.

***Ключевые слова:*** АКР-шлак, оксид бора, оксид хрома, структура, вязкость, фазовый состав, температура начала кристаллизации

***Благодарности:*** Работа выполнена по государственному заданию Института металлургии Уральского отделения РАН с использованием оборудования ЦКП «Состав вещества» Института высокотемпературной электрохимии Уральского отделения РАН.

***Для цитирования:*** Бабенко А.А., Шартдинов Р.Р., Уполовникова А.Г., Сметанников А.Н., Лобанов Д.А., Долматов А.В. Влияние основности на физические свойства шлаков системы CaO – $SiO_2$ – 18 % $Cr_2O_3$ – 6 % $B_2O_3$ – 3 % $Al_2O_3$ – 8 % MgO. *Известия вузов. Черная металлургия*. 2023;66(6):743–749. https://doi.org/10.17073/0368-0797-2023-6-743-749

## Introduction

In the contemporary field of low-carbon stainless steel production, argon-oxygen decarburization (AOD) technology predominates, entailing phases of oxidation and reduction. The reduction phase slags, rich in chromium oxide, present significant challenges in chromium reduction and steel desulfurization due to their high viscosity and refractory nature. To mitigate these issues, calcium fluoride is traditionally added as a fluxing agent during the reduction phase [1]. However, this addition poses drawbacks, including aggressive wear on the refractory lining, alterations in slag composition over time, and the formation of environmentally detrimental volatile fluorides [2]. Therefore, researchers have to find a way to replace it. One of the solutions can be the use of boron oxide. In response to these challenges, boron oxide emerges as a promising alternative, attributed to its beneficial impact on slag viscosity and crystallization temperature [3 – 5]. Nonetheless, the specific influence of boron oxide on the physical properties of chromium-containing slags remains largely underexplored.

This study employs vibrational viscometry, thermodynamic modeling of phase composition (HSC Chemistry 6.12 (Outokumpu)), and Raman spectroscopy to investigate the effects of varying basicity ($B = CaO/SiO_2$) from 1.0 to 2.5 – mirroring the composition at the commencement of the AOD process reduction period – on the viscosity η, crystallization onset temperature ($t_{cr}$), phase composition and structure of slags in the CaO – $SiO_2$ – 18 % $Cr_2O_3$ – – 6 % $B_2O_3$ – 3 % $Al_2O_3$ – 8 % MgO system [6].

## Materials and methods

To study the physical properties of slags within the six-component oxide system CaO – $SiO_2$ – 18 % $Cr_2O_3$ – – 6 % $B_2O_3$ – 3 % $Al_2O_3$ – 8 % MgO, experimental slags were synthesized with compositions detailed in Table 1.

These slags were produced in a resistance furnace using molybdenum crucibles under an argon atmosphere, employing analytical-reagent grade oxides pre-calcinated at 800 °C (with $B_2O_3$ calcinated at 100 °C) for 2 to 3 h.

The viscosity measurements for these slags were conducted utilizing a vibrating viscometer [7] within molybdenum crucibles in an argon flow, with temperature monitoring achieved through a tungsten-rhenium thermocouple. The slags' crystallization onset temperatures were ascertained based on Frenkel's theory of viscous flow. This involved plotting graphs in the coordinates $\ln\eta - 1/T$, with the crystallization temperature identified at the inflection point of these curves [8].

Thermodynamic modeling of the phase composition for the experimental slag samples was performed using the HSC Chemistry 6.12 software package (Outokumpu) [9].

The structure of slag samples was investigated using a Raman microscope spectrometer (U 1000) quipped with a 532 nm excitation wavelength laser. The acquired spectra span a wave number range of 200 to 1600 $cm^{-1}$. The spectrum lines observed can be unequivocally linked to the vibrational movements of the molecules within the slag sample. An analysis of the slag's structure is facilitated through examination of the oscillation frequency, as well as the intensity and contour of these spectrum lines [10].

## Results and discussion

Fig. 1 illustrates the relationship between slag viscosity, temperature, and basicity. Fig. 2 presents these relationships

Table 1

**Composition of experimental slags**

*Таблица 1*. **Состав экспериментальных шлаков**

| Slag | Content, % | | | | | | *B* | $t_{cr}$, °C |
|---|---|---|---|---|---|---|---|---|
| | CaO | $SiO_2$ | $Cr_2O_3$ | MgO | $Al_2O_3$ | $B_2O_3$ | | |
| *1* | 32.5 | 32.5 | 18.0 | 8.0 | 3.0 | 6.0 | 1.0 | 1530 |
| *2* | 39.0 | 26.0 | 18.0 | 8.0 | 3.0 | 6.0 | 1.5 | 1552 |
| *3* | 43.3 | 21.7 | 18.0 | 8.0 | 3.0 | 6.0 | 2.0 | 1614 |
| *4* | 46.4 | 18.6 | 18.0 | 8.0 | 3.0 | 6.0 | 2.5 | 1700 |

within the coordinates $\ln\eta - 1/T$, facilitating the determination of the crystallization temperature (Table 1).

Table 2 outlines the phase composition modeling results for the slag samples tested. Based on their melting temperatures, all phases have been categorically divided into three groups: low-temperature (1130 – 1280 °C), medium-temperature (1460 – 1600 °C), and high-temperature (1710 – 2852 °C).

Raman spectroscopy results of the experimental slag samples, with basicities of 1.0 and 2.5 (slags *1* and *4*, respectively) and a constant content of chromium oxide (18 %) and boron oxide (6.0 %), are depicted in Fig. 3. Table 3 correlates the wave numbers to the peaks of structural elements observed.

Peaks within the wave number ranges of 470 to 660 and 250 to 400 $cm^{-1}$ are associated with symmetric stretching and bending vibrations of Si–O–Si linkages. Peaks at 550 $cm^{-1}$, found within these ranges, are attributed to Al–O–Al and Cr–O–Cr connections. As slag basicity increases, these peaks, including the Si–O–Si linkages, become less distinct.

Variations in the wave number region of 800 to 1200 $cm^{-1}$ indicate that with an increase in basicity to 2.5, Raman spectrum peaks corresponding to $[CrO_4]$ and $Q^3_{Al}$ appear at wave numbers 873 and 780 $cm^{-1}$. This suggests the presence of these structural components in slags with elevated basicity, recognized as slag polymerizers [14; 19].

Fig. 3 lacks peaks corresponding to three-coordination boron $[BO_3]$, indicating that within the slag structure, boron oxide is represented by four-coordination boron $[BO_4]$. The $[BO_4]$ tetrahedra tend to create bonds with silicon atoms, complicating the structure, but at the same time, reducing its uniformity and strength [20 – 22]. Reduction in the slag viscosity when such oxide is used as a fluxing agent can be attributed to weakening of the structure and formation of low-melting compounds.

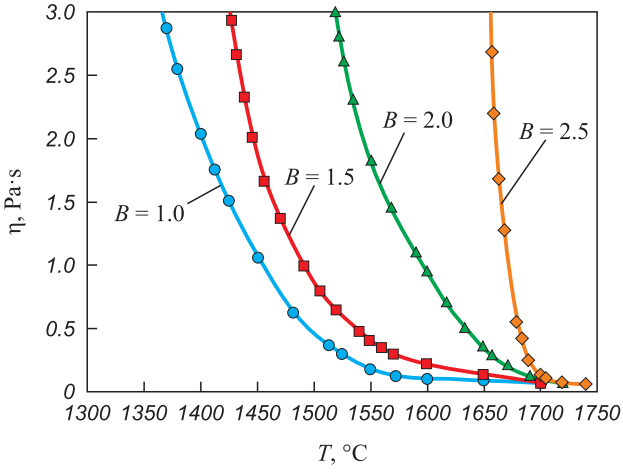


Fig. 1. Dependence of viscosity on temperature and basicity of slags of the studied oxide system

Рис. 1. Зависимость вязкости от температуры и основности шлаков изучаемой оксидной системы

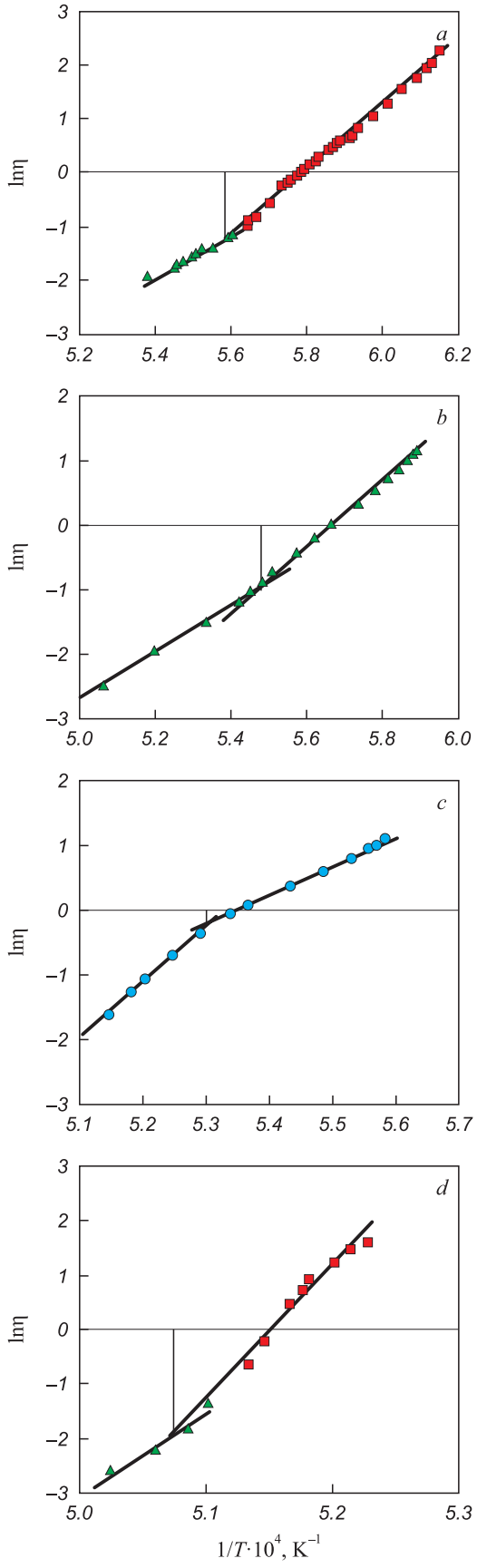


Fig. 2. Dependence of viscosity logarithm of ($\ln\eta$) on inverse absolute temperature ($1/T$) for slags *1 – 4* (*a – d*)

Рис. 2. Зависимость логарифма вязкости ($\ln\eta$) от обратной абсолютной температуры ($1/T$) шлаков *1 – 4* (*a – d*)

Table 2

**Phase composition of experimental slags at 1600 °C**

*Таблица 2*. **Фазовый состав экспериментальных шлаков при 1600 °С**

| Phase composition | Melting temperature, °C | Content, %, in the slag | | | |
|---|---|---|---|---|---|
| | | *1* | *2* | *3* | *4* |
| Low-temperature phases | | | | | |
| CB | 1130 | 4.3 | 2.8 | 1.4 | 0.4 |
| 2CB | 1280 | 8.3 | 10.1 | 10.7 | 8.4 |
| CM2S | 1391 | 9.2 | 5.6 | 2.0 | 0.3 |
| Total | | 21.8 | 18.5 | 14.1 | 9.1 |
| Medium-temperature phases | | | | | |
| 2CM2S | 1454 | 3.0 | 3.4 | 2.7 | 1.0 |
| 3CB | 1460 | 0.7 | 1.7 | 3.9 | 8.9 |
| 3C2S | 1460 | 5.6 | 7.5 | 8.1 | 6.0 |
| CMS | 1503 | 7.7 | 9.9 | 10.9 | 8.4 |
| CS | 1540 | 15.9 | 13.1 | 9.0 | 4.6 |
| CA2S | 1550 | 3.6 | 1.8 | 0.4 | 0.02 |
| MS | 1557 | 5.8 | 4.0 | 2.0 | 0.5 |
| 3CM2S | 1575 | 1.2 | 2.5 | 4.3 | 4.9 |
| CA | 1600 | 0.4 | 0.9 | 1.9 | 3.2 |
| Total | | 43.9 | 44.8 | 43.2 | 37.52 |
| High-temperature phases | | | | | |
| S | 1710 | 4.9 | 2.2 | 0.7 | 0.1 |
| A | 2040 | 1.4 | 1.8 | 1.7 | 1.0 |
| 2CS | 2130 | 6.3 | 9.6 | 14.6 | 21.9 |
| C | 2570 | 0.2 | 0.4 | 0.7 | 2.2 |
| M | 2852 | 1.4 | 2.0 | 3.1 | 4.8 |
| Cr | 2435 | 12.8 | 10.3 | 6.8 | 3.0 |
| CCr | 2100 | 7.1 | 10.6 | 15.4 | 20.5 |
| Total | | 34.1 | 36.9 | 43.0 | 53.5 |

Note (phase designations):
CB – $CaO \cdot B_2O_3$; 2CB – $2CaO \cdot B_2O_3$ ;
3CB – $3CaO \cdot B_2O_3$; CS – $CaO \cdot SiO_2$; 2CS – $2CaO \cdot SiO_2$;
3C2S – $3CaO \cdot 2SiO_2$; C – CaO; CM2S – $CaO \cdot MgO \cdot 2SiO_2$;
CMS – $CaO \cdot MgO \cdot SiO_2$; 2CM2S – $2CaO \cdot MgO \cdot 2SiO_2$;
3CM2S – $3CaO \cdot MgO \cdot 2SiO_2$; S – $SiO_2$; MS – $MgO \cdot SiO_2$;
M – MgO; CA2S – $CaO \cdot Al_2O_3 \cdot 2SiO_2$; A – $Al_2O_3$;
CA – $CaO \cdot Al_2O_3$; Cr – $Cr_2O_3$; CCr – $CaO \cdot Cr_2O_3$.

The polymerization degree of slag is primarily influenced by the high-frequency silicate region, spanning wave numbers 800 to 1200 $cm^{-1}$, which correspond to $[SiO_4]$ tetrahedrons. To gain a more nuanced understanding of the slag's structural intricacies, we performed deconvolution of the obtained Raman spectra using the Gaussian method [23] (Fig. 4). This process facilitated the representation of the slag's polymerization degree through the quantification of the average number of bridging oxygen (BO) molecules, calculated by the formula:

$$BO = 0 \cdot Q_{Si}^0 + 1 \cdot Q_{Si}^1 + 2 \cdot Q_{Si}^2 + 3 \cdot Q_{Si}^3 + 4 \cdot Q_{Si}^4, \quad (1)$$

where $Q_{Si}^n$ is $[SiO_4]$ with *n* number of bridging oxygen.

Calculations of the average amount of bridging oxygen (BO) are presented in Table 4.

Acid slags with a basicity of 1.0 (Fig. 1, slag *1*) categorized as "long" slags, are shown to possess a heightened proportion of high-temperature phases, reaching up to 34.1 % (Table 2). However, despite the fact that the proportion of high-temperature phases is 1.6 times higher compared to that of low-temperature phases, slags with a basicity of 1.0 have a simpler silicate structure. The average amount of bridging oxygen BO does not exceed 0.55, likely because chromium oxide behaves more like a base in the acidic slag environment [24; 25]. The depolymerizing impact on the silicon-oxygen lattice results in a majority (0.64) of the silicate structural elements being composed of $[SiO_4]$ units devoid of bridging oxygen. This simpler structure, particularly in slags with a basicity of 1.0, ensures relatively high fluidity at a crystallization temperature of 1530 °C, despite having a 1.6-fold greater proportion of high-temperature phases. At and above the crystallization temperature, the viscosity of the slag remains below 0.25 Pa·s.

Table 3

**Correspondence of wave numbers and structures**

*Таблица 3*. **Соответствие волновых чисел и структур**

| Elements | Wave number, $cm^{-1}$ | Structures | References |
|---|---|---|---|
| $Q_{Si}^0$ | 850 – 880 | without bridging oxygen in $[SiO_4]$ | [11; 12] |
| $Q_{Si}^1$ | 900 – 920 | with 1 bridging oxygen in $[SiO_4]$ | |
| $Q_{Si}^2$ | 950 – 980 | with 2 bridging oxygen in $[SiO_4]$ | |
| $Q_{Si}^3$ | 1040 – 1060 | with 3 bridging oxygen in $[SiO_4]$ | |
| $Q_{Si}^4$ | 1060, 1190 | with 4 bridging oxygen in $[SiO_4]$ | |
| Si–O–Si | 500 – 650 | deformation vibrations Si – $O^0$ | [13] |
| Al–O–Al | 550 | stretch vibrations Al – $O^0$ | [14] |
| Cr–O–Cr | 520 – 540 | stretch vibrations Cr – $O^0$ | [15] |
| $[CrO_4]$ | 873 | stretch vibrations Cr – $O^0$ | [16] |
| $[BO_3]$ | 1350 – 1530 | stretch vibrations B – $O^-$ in $[BO_3]^-$ | [17; 18] |
| $[BO_4]$ | 900 – 920 | stretch vibrations B – $O^0$ in $[BO_4]$ | [18] |
| $Q_{Al}^3$ | 780 | with 3 bridging oxygen in $[AlO_4]$ | [14] |

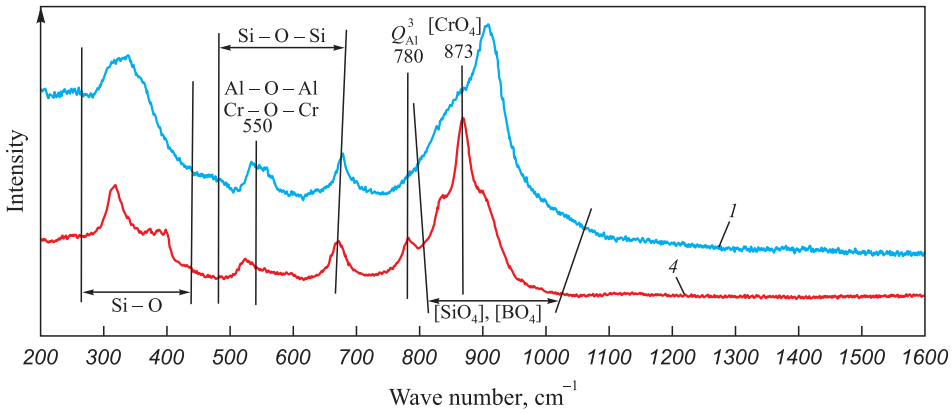


Fig. 3. Raman spectra of slags *1* and *4*

Рис. 3. Рамановские спектры шлаков *1* и *4*

As the basicity of the slags within this oxide system increases, the trend of a rising proportion of high-temperature phases and a declining proportion of low-temperature ones continues (as indicated in Table 2). For instance, a slag with a basicity of 2.5 (slag *4*, Fig. 1) is classified as belonging to the "short" slags category (Table 2), with its high-temperature phase proportion escalating to 53.5 %. This increase is largely attributable to the phases $2CaO \cdot SiO_2$ (21.9 %) and $CaO \cdot Cr_2O_3$ (20.5 %), alongside a reduction in low-temperature phases to 9.1 %, due to diminished proportions of $CaO \cdot B_2O_3$ and $CaO \cdot MgO \cdot 2SiO_2$ to 0.4 and 0.3 %, respectively. Concurrently, despite the enhanced basicity and the integration of the [$BO_4$] structural element, the presence of chromium and aluminum oxides, acting as acidic oxides [14; 19; 20], leads to a heightened polymerization degree of the slag. The incorporation of four-coordination chromium [$CrO_4$] and aluminum [$AlO_4$] into the silicon-oxygen framework intensifies its complexity. Consequently, the average number of bridging oxygen (BO) rises to 0.73, predominantly because a significant portion (0.52) of the silicate structural elements consists of [$SiO_4$] with one bridging oxygen. This intricate silicate structure, alongside an approximately 5.9-fold increase in the proportion of high-temperature phases compared to low-temperature ones, contributes to a rise in the crystallization temperature to 1700 °C and viscosity levels reaching 1.0 Pa·s or more at temperatures of 1670 °C and below.

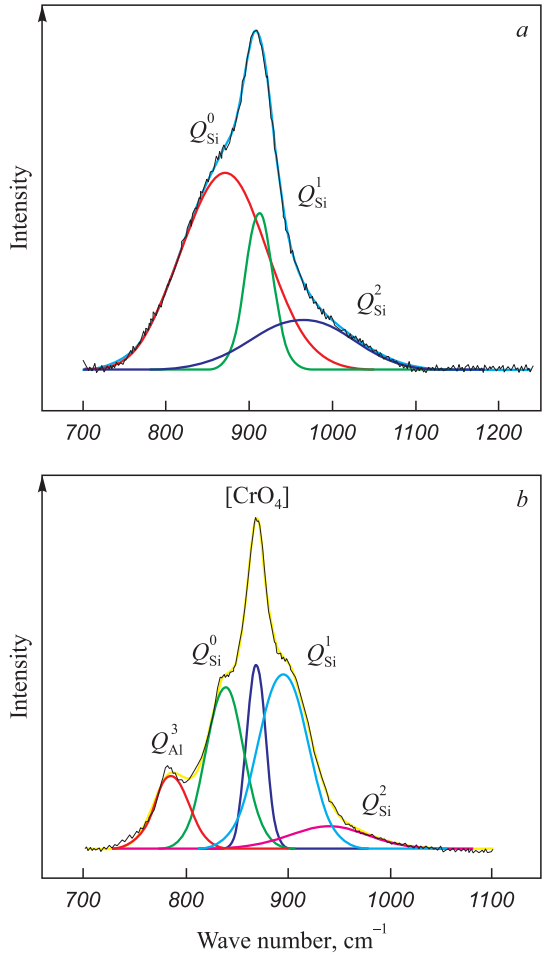


Fig. 4. Results of deconvolution of slags *1* (*a*) and *4* (*b*)

Рис. 4. Результаты деконволюции шлаков *1* (*a*) и *4* (*b*)

## Conclusions

Our research has revealed new details about how the basicity of slags in the $CaO–SiO_2–18\ \%\ Cr_2O_3–$

Table 4

**Fractions of silicate structural elements**

*Таблица 4.* **Количество силикатных структурных элементов**

| Slag | *B* | Number of structural elements, shares | | | | BO |
|---|---|---|---|---|---|---|
| | | $Q^0_{Si}$ | $Q^1_{Si}$ | $Q^2_{Si}$ | $Q^3_{Si}$ | |
| *1* | 1.0 | 0.64 | 0.17 | 0.19 | 0 | 0.55 |
| *4* | 2.5 | 0.37 | 0.52 | 0.11 | 0 | 0.73 |

– 6 % $B_2O_3$ – 3 % $Al_2O_3$ – 8 % MgO system impacts their phase composition, structure, viscosity, and the temperature at which they begin to crystallize.

We've found that the physical properties of slags hinge on the interaction between polymerization processes and their phase makeup:

– at a basicity level of 1.0, chromium oxide acts in a way that simplifies the slag's structure, resulting in a bridging oxygen (BO) value of 0.55. This simple structure leads to a low viscosity of 0.25 Pa·s at the temperature where crystallization starts, which is 1530 °C, even though there's a high presence of high-temperature phases;

– on the contrary, when the basicity reaches 2.5, the degree of polymerization in the slag increases (BO = 0.73). This is because $Cr_2O_3$ starts to show acidic properties, as seen by the formation of the [$CrO_4$] structural unit in the slag. Along with this, there's a significant increase in high-temperature phases, by about 1.57 times. This combination leads to a more complex structure, pushing the slag's viscosity up to 1.0 Pa·s at 1670 °C and raising the temperature at which crystallization begins to 1700 °C.

## References / Список литературы


1. Kalicka Z., Kawecka-Cebula E., Pytel K. Application of the Iida model for estimation of slag viscosity for $Al_2O_3$–$Cr_2O_3$–CaO–$CaF_2$. *Archives of Metallurgy and Materials*. 2009;54(1):179–187.
2. Dyudkin D.A., Kisilenko V.V. *Production of Steel. In 3 vols. Vol. 3. Extra-Furnace Metallurgy of Steel*. Moscow: Teplotekhnik; 2010:544. (In Russ.).

   Дюдкин Д.А., Кисиленко В.В. *Производство стали. В 3-х томах. Т. 3. Внепечная металлургия стали*. Москва: Теплотехник; 2010:544.
3. Wang H.M., Li G.R., Li B., Zhang X.J., Yan Y.Q. Effect of $B_2O_3$ on melting temperature of cao-based ladle refining slag. *Journal of Iron and Steel Research International*. 2010;17(10):18–22. https://doi.org/10.1016/S1006-706X(10)60177-X
4. Wang H.M., Zhang T.W., Zhu H., Yan Y.Q., Zhao Y.N. Effect of $B_2O_3$ and $CaF_2$ on viscosity of ladle refining slag. *Advanced Materials Research*. 2011;295–297:2647. https://doi.org/10.4028/www.scientific.net/AMR.295-297.2647
5. Babenko A.A., Shartdinov R.R., Upolovnikova A.G., Smetannikov A.N., Gulyakov V.S. Physical properties of slags of CaO – $SiO_2$ – $B_2O_3$ system containing 15 % of $Al_2O_3$ and 8 % of MgO. *Izvestiya. Ferrous Metallurgy*. 2019;62(10):769–773. (In Russ.). https://doi.org/10.17073/0368-0797-2019-10-769-773

   Бабенко А.А., Шартдинов Р.Р., Уполовникова А.Г., Сметанников А.Н., Гуляков В.С. Физические свойства шлаков системы CaO – $SiO_2$ – $B_2O_3$, содержащей 15 % $Al_2O_3$ и 8 % MgO. *Известия вузов. Черная металлургия*. 2019;62(10):769–773. https://doi.org/10.17073/0368-0797-2019-10-769-773
6. Tokovoi O.K. *Argon-Oxygen Refining of Stainless Steel*. Chelyabinsk: South Ural State University; 2015:250. (In Russ.).

   Токовой О.К. *Аргонокислородное рафинирование нержавеющей стали*. Челябинск: ИЦ ЮУрГУ; 2015:250.
7. Shtengel'meier S.V., Prusov V.A., Bogachev V.A. Improvement of the viscosity measurement technique with a vibrating viscometer. *Zavodskaya laboratoriya*. 1985;51(9):56–57. (In Russ.).

   Штенгельмейер С.В., Прусов В.А., Богачев В.А. Усовершенствование методики измерения вязкости вибрационным вискозиметром. *Заводская лаборатория*. 1985;51(9):56–57.
8. Voskoboinikov V.G., Dunaev N.E., Mikhalevich A.G, Kukhtin T.I., Shtengel'meier S.V. *Properties of Liquid Blast Furnace Slags*. Moscow: Metallurgiya; 1975:180. (In Russ.).

   Воскобойников В.Г., Дунаев Н.Е., Михалевич А.Г., Кухтин Т.И., Штенгельмейер С.В. *Свойства жидких доменных шлаков*. Москва: Металлургия; 1975:180.
9. Roine A. *HSC 6.0 Chemistry Reactions and Equilibrium Software with Extensive Thermochemical Database and Flowshut*. Pori: Outokumpu Research Oy; 2006:448.
10. Böcker J. *Spektroskopie: Instrumentelle Analytik mit Atom- und Molekülspektrometrie*. Würzburg: Vogel Communications Group GmbH & Co. KG; 1997:519. (In Germ.).

    Бёккер Ю. *Спектроскопия* / Пер. Л.Н. Казанцева. Москва: РИЦ Техносфера, 2009:528.
11. McMillan P. Structural studies of silicate glasses and melts-applications and limitations of Raman spectroscopy. *American Mineralogist*. 1984;69(6):622–644.
12. Matson D.W., Sharma S.K., Philpotts J.A. The structure of high-silica alkali-silicate glasses. A Raman spectroscopic investigation. *Journal of Non-Crystalline Solids*. 1983;58(2–3):323–352. https://doi.org/10.1016/0022-3093(83)90032-7
13. McMillan P.F., Poe B.T., Gillet P.H., Reynard B. A study of $SiO_2$ glass and supercooled liquid to 1950 K via high-temperature Raman spectroscopy. *Geochimica et Cosmochimica Acta*. 2001;58(17):3653–3662. https://doi.org/10.1016/0016-7037(94)90156-2
14. Kim T.S., Park J.H. Structure-viscosity relationship of low-silica calcium aluminosilicate melts. *ISIJ International*. 2014;54(9):2031–2038. https://doi.org/10.2355/isijinternational.54.2031
15. Dines T.J., Inglis S. Raman spectroscopic study of supported chromium (VI) oxide catalysts. *Physical Chemistry Chemical Physics*. 2003;5(6):1320–1328. https://doi.org/10.1039/b211857b
16. Weckhuysen B.M., Wachs I.F. Raman spectroscopy of supported chromium oxide catalysts. Determination of chromium–oxygen bond distances and bond orders. *Journal of the Chemical Society, Faraday Transactions*. 1996;92(11):1969–1973. https://doi.org/10.1039/FT9969201969
17. Kim Y., Morita K. Relationship between molten oxide structure and thermal conductivity in the CaO–$SiO_2$–$B_2O_3$ system. *ISIJ International*. 2014;54(9):2077–2083. https://doi.org/10.2355/isijinternational.54.2077
18. Cochain B., Neuville D.R., Henderson G.S., McCammon C.A., Pinet O., Richet P. Effects of the iron content and redox state on the structure of sodium borosilicate glasses: A Raman, Mössbauer and boron K-Edge XANES spectroscopy study. *Journal of the American Ceramic Society*. 2012;95(3):962–971. https://doi.org/10.1111/j.1551-2916.2011.05020.x
19. Li Q., Gao J., Zhang Y., An Z., Guo Z. Viscosity measurement and structure analysis of $Cr_2O_3$-bearing CaO–$SiO_2$–MgO–$Al_2O_3$ slags. *Metallurgical and Materials Transactions B*. 2017;48:346–356. https://doi.org/10.1007/s11663-016-0858-8

**20.** Xu R.Z., Zhang J.L., Wang Z.Y., Jiao K.X. Influence of $Cr_2O_3$ and $B_2O_3$ on viscosity and structure of high alumina slag. *Steel Research International*. 2017;88(4):1600241. https://doi.org/10.1002/srin.201600241

**21.** Sun Y., Zhang Z. Structural roles of boron and silicon in the CaO–$SiO_2$–$B_2O_3$ glasses using FTIR, Raman, and NMR spectroscopy. *Metallurgical and Materials Transactions B*. 2015;46:1549–1554. https://doi.org/10.1007/s11663-015-0374-2

**22.** Cai Z., Song B., Li L., Liu Zh., Cui X. Effects of $B_2O_3$ on viscosity, structure, and crystallization of mold fluxes for casting rare earth alloyed steels. *Metals*. 2018;8(10):737. https://doi.org/doi:10.3390/met8100737

**23.** Mysen B.O., Virgo D., Scarfe C.M. Relations between the anionic structure and viscosity of silicate melts – a Raman spectroscopic study. *American Mineralogist*. 1980;65(7):690–710.

**24.** Forsbacka L., Holappa L., Kondratiev A., Jak E. Experimental study and modelling of viscosity of chromium containing slags. *Steel Research International*. 2007;78(9):676–684. http://dx.doi.org/10.1002/srin.200706269

**25.** Wu T., Zhang Y., Yuan F., An Z. Effects of the $Cr_2O_3$ content on the viscosity of CaO–$SiO_2$–10 Pct $Al_2O_3$–$Cr_2O_3$ quaternary slag. *Metallurgical and Materials Transactions B*. 2018;49:1719–1731. https://doi.org/10.1007/s11663-018-1258-z

## Information about the Authors / Сведения об авторах

***Anatolii A. Babenko,*** *Dr. Sci. (Eng.), Prof., Chief Researcher,* Institute of Metallurgy, Ural Branch of the Russian Academy of Sciences
***ORCID:*** 0000-0003-0734-6162
***E-mail:*** babenko251@gmail.com

***Ruslan R. Shartdinov,*** *Junior Researcher of the Laboratory of Steel and Ferroalloys,* Institute of Metallurgy, Ural Branch of the Russian Academy of Sciences
***ORCID:*** 0000-0003-0852-1161
***E-mail:*** rr.shartdinov@gmail.com

***Alena G. Upolovnikova,*** *Cand. Sci. (Eng.), Senior Researcher of the Laboratory of Steel and Ferroalloys,* Institute of Metallurgy, Ural Branch of the Russian Academy of Sciences
***ORCID:*** 0000-0002-6698-5565
***E-mail:*** upol.ru@mail.ru

***Artem N. Smetannikov,*** *Junior Researcher of the Laboratory of Steel and Ferroalloys,* Institute of Metallurgy, Ural Branch of the Russian Academy of Sciences
***ORCID:*** 0000-0001-9206-0905
***E-mail:*** artem.smetannikov.89@mail.ru

***Daniil A. Lobanov,*** *Cand. Sci. (Eng.), Research Associate,* Institute of Metallurgy Ural Branch of the Russian Academy of Sciences
***ORCID:*** 0009-0007-5659-1208
***E-mail:*** summerdanny@yandex.ru

***Aleksei V. Dolmatov,*** *Cand. Sci. (Chem.), Senior Researcher of the Laboratory of Metallurgical Melts,* Institute of Metallurgy, Ural Branch of the Russian Academy of Science
***ORCID:*** 0000-0002-6632-9533
***E-mail:*** dolmatov.imet@gmail.com

***Анатолий Алексеевич Бабенко,*** *д.т.н., профессор, главный научный сотрудник,* Институт металлургии Уральского отделения РАН
***ORCID:*** 0000-0003-0734-6162
***E-mail:*** babenko251@gmail.com

***Руслан Рафикович Шартдинов,*** *младший научный сотрудник лаборатории стали и ферросплавов,* Институт металлургии Уральского отделения РАН
***ORCID:*** 0000-0003-0852-1161
***E-mail:*** rr.shartdinov@gmail.com

***Алена Геннадьевна Уполовникова,*** *к.т.н., старший научный сотрудник лаборатории стали и ферросплавов,* Институт металлургии Уральского отделения РАН
***ORCID:*** 0000-0002-6698-5565
***E-mail:*** upol.ru@mail.ru

***Артем Николаевич Сметанников,*** *младший научный сотрудник лаборатории стали и ферросплавов,* Институт металлургии Уральского отделения РАН
***ORCID:*** 0000-0001-9206-0905
***E-mail:*** artem.smetannikov.89@mail.ru

***Даниил Андреевич Лобанов,*** *к.т.н., научный сотрудник,* Институт металлургии Уральского отделения РАН
***ORCID:*** 0009-0007-5659-1208
***E-mail:*** summerdanny@yandex.ru

***Алексей Владимирович Долматов,*** *к.х.н., старший научный сотрудник лаборатории металлургических расплавов,* Институт металлургии Уральского отделения РАН
***ORCID:*** 0000-0002-6632-9533
***E-mail:*** dolmatov.imet@gmail.com

## Contribution of the Authors / Вклад авторов

***A. A. Babenko*** – scientific guidance, data analysis, writing and editing the text.
***R. R. Shartdinov*** – conducting the experiment, data processing and analysis, writing and editing the text.
***A. G. Upolovnikova*** – modeling, data analysis, editing the text.

***A. N. Smetannikov*** – conducting the experiment, data analysis.
***D. A. Lobanov*** – conducting the experiment, data analysis.
***A. V. Dolmatov*** – data processing and analysis.

***А. А. Бабенко*** – руководство, анализ результатов, написание статьи, редактирование статьи.
***Р. Р. Шартдинов*** – проведение эксперимента, обработка и анализ результатов, написание статьи, редактирование статьи.
***А. Г. Уполовникова*** – моделирование, анализ результатов, редактирование статьи.
***А. Н. Сметаников*** – проведение эксперимента, анализ результатов.
***Д. А. Лобанов*** – проведение эксперимента, анализ результатов.
***А. В. Долматов*** – обработка и анализ результатов.

Received 14.04.2023
Revised 06.07.2023
Accepted 11.09.2023

Поступила в редакцию 14.04.2023
После доработки 06.07.2023
Принята к публикации 11.09.2023

ON THE MATERIALS OF THE INTERNATIONAL CONFERENCE "SCIENTIFIC AND PRACTICAL SCHOOL FOR YOUNG METALLURGISTS" – 2023

ПО МАТЕРИАЛАМ МЕЖДУНАРОДНОЙ КОНФЕРЕНЦИИ «НАУЧНО-ПРАКТИЧЕСКАЯ ШКОЛА ДЛЯ МОЛОДЫХ МЕТАЛЛУРГОВ» – 2023

**UDC** 621.746.01
**DOI** 10.17073/0368-0797-2023-6-750-759



***Original article***
***Оригинальная статья***

# PHYSICAL MODELING OF THE EFFECT OF REFILLING THE MELT INTO AN INGOT KNOCK-OFF HEAD ON SOLIDIFICATION AND STRUCTURE FORMATION

**S. B. Gamanyuk, D. V. Rutskii, N. A. Zyuban, M. V. Kirilichev, M. S. Nikitin**

**Volgograd State Technical University** (28 Lenina Ave., Volgograd 400005, Russian Federation)

gamanuk@mail.ru

***Abstract***. The paper presents the results of a laboratory study of the effect of refilling the ingot knock-off head with melt in a certain time interval after pouring the ingot body on solidification and structure formation of the model ingot. The research was carried out by the method of physical (cold) modeling for which a laboratory installation (casting form-mold) was developed and manufactured. It allows visually studying the processes occurring during solidification and structure formation on a 19.6-ton model ingot. We used sodium sulfuric acid (crystalline hyposulfite) as a modeling solution. Correspondence of the processes occurring on the model and in real conditions of industrial ingots casting was evaluated using similarity criteria obtained on the basis of dimension theory with analysis of physico-chemical processes occurring during casting and crystallization of the ingot. Casting of the melt into the casting form-mold was downhill. In order to assess changes in the temperature field during casting and crystallization of the ingot in the entire solidification time, we performed thermometry of the mold model surface. Analysis of the conducted studies results showed that refilling the melt before 40 min leads to stimulation of early settling of crystals ("rain of crystals"), which contributes to an increase in the crystallization directivity in vertical direction. It was established that in a conventional ingot up to 40 min solidification proceeds by a sequential mechanism, and after that the crystals begin to settle ("rain of crystals") and the solidification of the ingot passes through a volume-sequential mechanism. Refilling the ingot knock-off head with melt 40 min after pouring the ingot body contributed to the continuation of the sequential mechanism of ingot solidification, which led to the formation of a monolithic defect-free structure in the ingot body and the least development of shrinkage shell in the knock-off head. The results obtained make it possible to develop a technology for differentiated ingots casting when filling their knock-off heads with melt in a certain time interval after pouring the ingot body, which will affect the process of metal structure formation and reduce defective zones.

***Keywords:*** physical simulation, downhill casting, casting form – mold, refilling the ingot knock-off head, solidification, axial zone, large forging ingot

***Acknowledgements:*** The work was supported by the Russian Science Foundation, grant No. 23-29-00973, https://rscf.ru/project/23-29-00973/.

***For citation:*** Gamanyuk S.B., Rutskii D.V., Zyuban N.A., Kirilichev M.V., Nikitin M.S. Physical modeling of the effect of refilling the melt into an ingot knock-off head on solidification and structure formation. *Izvestiya. Ferrous Metallurgy*. 2023;66(6):750–759. https://doi.org/10.17073/0368-0797-2023-6-750-759

# ФИЗИЧЕСКОЕ МОДЕЛИРОВАНИЕ ВЛИЯНИЯ ДОЛИВКИ РАСПЛАВА В ПРИБЫЛЬНУЮ ЧАСТЬ СЛИТКА НА ПРОЦЕСС ЗАТВЕРДЕВАНИЯ И СТРУКТУРООБРАЗОВАНИЕ

**С. Б. Гаманюк, Д. В. Руцкий, Н. А. Зюбан, М. В. Кириличев, М. С. Никитин**

**Волгоградский государственный технический университет** (Россия, 400005, Волгоград, пр. им. В.И. Ленина, 28)

gamanuk@mail.ru

***Аннотация***. В работе представлены результаты лабораторного исследования эффекта доливки прибыльной части слитка расплавом на процесс затвердевания и структурообразование модельного слитка. Доливка производилась через определенный интервал времени

после заливки тела слитка. Исследования проводили методом физического (холодного) моделирования, для которого была разработана и изготовлена лабораторная установка (изложница-кристаллизатор), позволяющая визуально изучать процессы, происходящие при затвердевании и структурообразовании на модели слитка массой 19,6 т. В качестве моделирующего раствора использовали натрий серноватистокислый (кристаллический гипосульфит). Соответствие процессов, происходящих на модели и в реальных условиях отливки промышленных слитков, оценивалось с помощью критериев подобия. Они получены на основе теории размерностей исходя из анализа физико-химических процессов, происходящих при разливке и кристаллизации слитка. Разливка расплава в изложницу-кристаллизатор выполнялась сверху. С целью оценки изменения поля температур при разливке и кристаллизации слитка в течение всего времени затвердевания проводили термометрирование поверхности модели изложницы. Анализ результатов проведенных исследований показал, что доливка расплава до 40 мин приводит к стимулированию раннего оседания кристаллов («дождь кристаллов»), что способствует увеличению направленности кристаллизации в вертикальном направлении. Установлено, что в обычном слитке до 40 мин затвердевание идет по последовательному механизму, а после начинается оседание кристаллов («дождь кристаллов») и затвердевание слитка проходит по объемно-последовательному механизму. Доливка прибыльной части слитка расплавом спустя 40 мин после заливки тела слитка способствовала продолжению последовательного механизма затвердевания слитка. Это привело к образованию монолитной бездефектной структуры в теле слитка и наименьшему развитию усадочной раковины в объеме прибыли. Полученные результаты обусловливают возможность разработки технологии дифференцированной разливки слитков при наполнении их прибыли расплавом через определенный интервал времени после заливки тела слитка. Это позволит воздействовать на процесс формирования структуры металла и сокращение дефектных зон.

***Ключевые слова:*** физическое моделирование, разливка сверху, изложница-кристаллизатор, доливки прибыльной части слитка, процесс затвердевания, осевая зона, крупный кузнечный слиток

***Благодарности:*** Исследование выполнено за счет гранта Российского научного фонда № 23-29-00973, https://rscf.ru/project/23-29-00973/.

***Для цитирования:*** Гаманюк С.Б., Руцкий Д.В., Зюбан Н.А., Кириличев М.В., Никитин М.С. Физическое моделирование влияния доливки расплава в прибыльную часть слитка на процесс затвердевания и структурообразование. *Известия вузов. Черная металлургия*. 2023;66(6):750–759. https://doi.org/10.17073/0368-0797-2023-6-750-759

## Introduction

The theory and practice of ingot production demonstrate that the solidification time of large ingots spans several days, during which liquation and shrinkage phenomena significantly manifest. These phenomena give rise to chemical and physical heterogeneity within the cast metal, which, if pronounced, may persist even after forging. Consequently, this can result in the rejection of billets either during manufacturing or during delivery trials, leading to losses for the enterprise.

Currently, numerous methods have been developed to enhance metal quality, primarily focusing on process improvements during smelting and casting. However, despite advancements, the benefits achieved during smelting can be compromised during the casting and solidification of large ingots, each weighing no less than 14 tons.

Studies [1 – 3] demonstrate that challenges in achieving structural quality and uniform mechanical properties throughout the height and radius of forgings stem from varying solidification conditions across different parts of the ingot. Additionally, shrinkage processes, significant liquation of impurities in the steel composition, and the shape and size of the ingot contribute to these difficulties.

The significant influence of ingot geometrical parameters on the development of the axial zone is widely acknowledged. Specifically, parameters such as the height to average diameter ratio $H/D$ [4 – 7], conicity [8 – 10], and the type of the ingot (shortened, normal, elongated) are recognized as predominant factors.

The formation of axial porosity is closely linked to shrinkage phenomena, which are, in turn, influenced by temperature conditions and thermophysical processes during ingot casting and crystallization. Consequently, the method and speed of metal casting are crucial determinants in the formation of axial defects in the ingot [11 – 13].

To enhance the quality of large ingots, it's imperative to explore effective methods that influence the solidification process. Understanding the mechanisms and conditions leading to the formation of localized defect areas, which contribute to the development of macro-defects resistant to deformation removal, is essential. Analyzing the solidification features of large ingots is intricate, requiring consideration of numerous factors impacting crystallization phenomena.

One approach to studying solidification processes in large ingots is through physical (cold) modeling, utilizing casting form models [14 – 16]. This method enables the visual assessment of solid and solid-liquid phase advancement kinetics alongside convective mixing of the modeling melt and internal defect development. It's important to note that physical modeling provides qualitative insights into the influence of casting process factors on structure formation nuances and defect zone development.

The conditions outlined in [2; 3; 17] suggest that refilling the knock-off head is justified when the ratio of crystallization interval value to temperature gradient value meets the criterion $\Delta T_{cr}/\delta T \geq 1$. Researchers in [18] demonstrated that refilling the knock-off head with hot melt can significantly impact ingot structural zone formation conditions, elevating the $\delta T$ parameter to values prompting a return to sequential solidification, resulting in a denser dendritic structure.

The aim of this research is to investigate the impact of refilling the knock-off head with melt on the solidification process and structure formation of the model ingot. Refilling is executed at specific time intervals following casting of the ingot body.

## Materials and methods

In this study, we employed the physical (cold) ingot modeling method, for which we designed and fabricated a laboratory installation (casting form-mold) [16]. Using this installation, we visually examined the processes occurring during solidification and structure formation of model ingots. The geometric parameters of both real industrial and model ingots are detailed in Table 1.

As a modeling solution, we utilized sodium thiosulfate (crystalline hyposulfite) – $Na_2S_2O_3 \cdot 5H_2O$ was used as a modeling solution. The solidification onset temperature ranged from 48 to 52 °C. To evaluate the correspondence between the processes observed in the model and those in real industrial ingot casting conditions, we employed similarity criteria, including Froude (Fr), Reynolds (Re), Weber (We), Biots (Bi), and Fourier homochronicity (Fo). These criteria were derived from dimensional analysis of physical and chemical processes during ingot casting and crystallization. Additionally, we utilized the solidification criterion (phase transfer) *N*, describing the ratio of phase transfer heat to cooling heat [4; 19].

Calculation of the similarity criteria (Bi, N, Fo, Fr, We) as outlined in [4] demonstrated (see Table 2) that their values for both model and real conditions differed by no more than one order of magnitude, indicating correspondence between the studied processes [19].

The direct shadow method, also known as the schlieren method, was employed to examine the hydrodynamic characteristics of liquid motion at the end of casting into the casting form – mold, as well as the behavior of convective flows (both downward and upward) in the melt during the solidification process. This method facilitated visualization and quantification of the nature and rate of change of convective flows during the solidification of model ingots.

The direct shadow method (Fig. 1), involves generating a parallel beam of light *2* using a light source and collecting lens *1*, which is then directed to "shine through" the object under examination (casting form – mold) *4*. When encountering inhomogeneity, the rays deflected by it form an image projected onto a screen *5*. To ensure the light beam's parallelism, in this study, the light was directed to a straight mirror *3* whose size matches that of the mold. Light *2* reflected by the mirror *3* from the source *1*, while passing through the solidifying ingot model within the casting form – mold *4*, reveals the image of inhomogeneity on the screen *5*, which was captured using a high-resolution digital video camera *6*. The video recordings obtained were utilized to calculate the velocities of convective flows immediately after casting and during the solidification of the model ingot. To calcu-

Table 1

**Geometrical parameters of industrial and model ingots**

*Таблица 1*. **Геометрические параметры промышленного и модельного слитков**

| Ingot parameters | Sample ingot (19.6 t) | Model |
|---|---|---|
| Height to average diameter ratio, *H*/*D* | 2.15 | 2.3 |
| Ingot body conicity, $K_{in.b}$, % | 4.1 | 4.4 |
| Feeder head conicity, $K_{head}$, % | 14.7 | 14.7 |
| Ingot body volume, $V_{in.b}$, % | 77.4 | 79.7 |
| Volume of knock-off head, $V_{head}$, % | 18.0 | 15.7 |
| Volume of bottom part of ingot, $V_{bot}$, % | 4.6 | 4.5 |

Table 2

**Values of similarity criteria in the sample and model**

*Таблица 2*. **Значения критериев подобия в образце и модели**

| Ingot type | Similarity criterion | | | | |
|---|---|---|---|---|---|
| | Bi | *N* | Fo | Fr | We |
| Model ingot | $1.02 \cdot 10^{-8}$ | 0.52 | $1.083 \cdot 10^{-4}$ | $2.80 \cdot 10^{-6}$ | $7.56 \cdot 10^{-4}$ |
| Sample ingot | $1.73 \cdot 10^{-7}$ | 4.01 | $6.340 \cdot 10^{-4}$ | $3.67 \cdot 10^{-5}$ | $5.83 \cdot 10^{-3}$ |

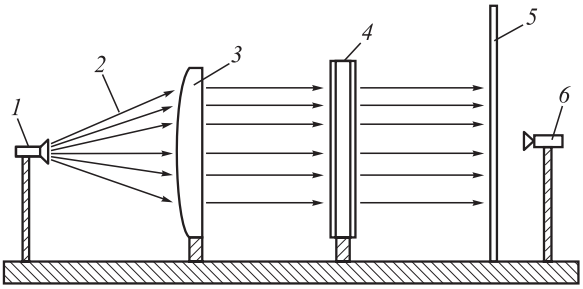


Fig. 1. Layout of installation for studying the solidification and structure formation of a model ingot:
*1* – light source; *2* – light beam; *3* – direct mirror;
*4* – casting form-mold; *5* – screen;
*6* – high–resolution digital video camera

Рис. 1. Схема установки для исследования процесса затвердевания и структурообразования модельного слитка:
*1* – источник света; *2* – пучок света; *3* – прямое зеркало;
*4* – изложница-кристаллизатор; *5* – экран;
*6* – цифровая видеокамера высокого разрешения

late these velocities, a grid with square side dimensions of 25 mm was applied to the screen.

The melt was poured into the casting form – mold from above, and the experimental conditions' specifics are detailed in Table 3.

Four model ingots were cast using the physical (cold) modeling method to simulate the ingot solidification process. One ingot followed classical technology (referred to as an ordinary ingot), while the others had the head cast after different time intervals: 7, 19 and 40 min after casting the ingot body (referred to as experimental ingots or refilling of the head after 7, 19 and 40 min). Refilling of the knock-off head of experimental ingots was performed with melt temperature 5 °C "colder" than the melt used for casting the ingot body. At the time of refilling, the solidified solid phase area in the body of experimental ingots (zone of columnar crystals) amounted to 16.7, 23.5 and 43.4 %, respectively (Table 1). Throughout the ingot modeling process, the geometric parameters of casting remained constant (Table 1).

During modeling, the advancing solidification front was analyzed in two components: horizontal solidification, where the solid phase sequentially grows from the walls to the center of the casting form, and vertical solidification vertical solidification, where the solid phase advances from the walls to the center along the axis of the casting form.

Following the casting of the melt into the casting form-mold, the thickness of the solidified layer was measured every 5 min vertically from the bottom to the center of the casting form along the axis and at three levels along the height of the ingot (bottom section, middle height, and sub-knock-off head horizon).

At the end of the solidification process, the structural zones of model ingots and their volume fractions were measured, and the length and average width of the axial zone were determined. The impact of the time interval for refilling the knock-off head with melt on the crystallization rate and the dynamics of solid phase growth in model ingots in both vertical and horizontal solidification directions, as well as on the total solidification time, was assessed.

To evaluate changes in the temperature field during casting and crystallization of the ingot, thermometry of the casting form model surface was conducted throughout the solidification period. Initially, after casting completion, the crystallizing melt was photographed every 5 min for 30 min, followed by intervals of 20 min. Thermometry was performed using a thermal camera Testo 875i, and the thermal images obtained were processed using TestoIRSoft software. As the thermal camera allows only surface thermometry without direct measurement of melt temperature, the dynamics of melt temperature change were assumed to mirror the dynamics of surface temperature change of the casting form model, providing a qualitative insight into the temperature field variations.

## Results and discussion

The data processing resulted in the preparation of curves illustrating the solid phase growth rate in both vertical and horizontal solidification directions for various ingot casting techniques (Fig. 2).

Analysis of the results revealed that for an ordinary ingot (Fig. 2, *a*) and an ingot with head refilling after 7 min (Fig. 2, *b*), between 10 and 73 min, constituting 5 to 38 % of the total solidification time, structure formation follows a volume-sequential mechanism. This mechanism arises due to the settling of crystal fragments from the "mirror" of the melt in the head and near

Table 3

**Characteristics of the experimental conditions**

*Таблица 3*. **Характеристика условий проведения эксперимента**

| Indicator | Technology of model ingot casting | | | |
|---|---|---|---|---|
| | ordinary ingot | head refilling after 7 min | head refilling after 19 min | head refilling after 40 min |
| Temperature of melt casting of the ingot body, $T_{cas.in.b}$, °C | 75 | 75 | 75 | 75 |
| Temperature of melt casting of the head, $T_{cas.head}$, °C | 75 | 70 | 70 | 70 |
| Time of melt casting of the ingot body, $\tau_{in.b.}$, s | 42 | 37 | 42 | 46 |
| Time of melt casting of the head, $\tau_{head}$, s | 45 | 27 | 42 | 38 |
| Time before melt refilling of the head, $\tau_{ref.\ head}$, min:s | – | 7:00 | 19:00 | 40:00 |
| Cooling liquid temperature, $T_{cool.liq.}$, °C | 11 | 11 | 11 | 11 |
| Weight of ingot body/head, $M_{in}$ /$m_{head}$, g | 550/150 | 550/150 | 550/150 | 550/150 |
| Solidification time, $\tau_{sol.}$, min | 205 | 220 | 238 | 258 |

the solidification front. These fragments sink to the lower part of the ingot, forming a cone-shaped settling zone. The descending crystals enhance the vertical solidification rate, thereby increasing the orientation of ingot solidification. Consequently, this phenomenon results in reduced development of axial friability and chemical heterogeneity in the ingot [1]. Subsequent solidification of the ingot proceeds in the horizontal direction via a sequential mechanism.

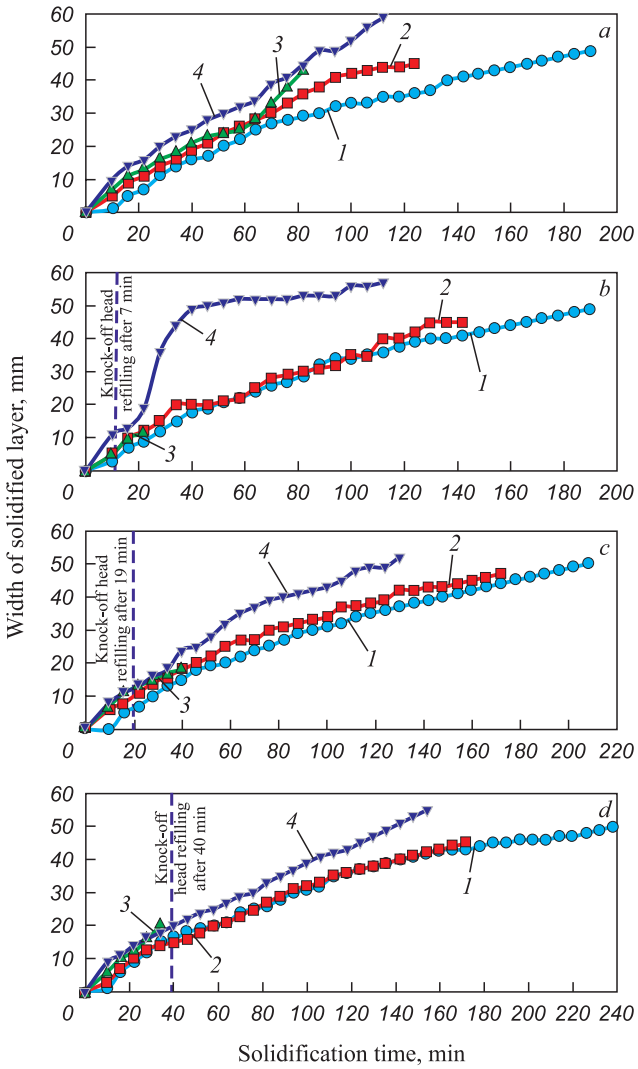


Fig. 2. Curves of solid phase growth in height and cross section of model ingots obtained by physical modeling:
*a* – ordinary ingot; *b* – refilling the knock-off head after 7 min;
*c* – refilling the knock-off head after 19 min;
*d* – refilling the knock-off head after 40 min;
*1* – sub-knock-off head horizon; *2* – mid-height;
*3* – lower section; *4* – vertical solidification

Рис. 2. Кривые нарастания твердой фазы по высоте и сечению модельных слитков, полученные методом физического моделирования:
*a* – обычный слиток; *b* – доливка прибыли спустя 7 мин;
*c* – доливка прибыли спустя 19 мин;
*d* – доливка прибыли спустя 40 мин;
*1* – подприбыльный горизонт; *2* – середина высоты;
*3* – нижнее сечение; *4* – вертикальное затвердевание

It's noteworthy that in the experimental ingot, the "rain of crystals" commenced immediately after refilling the head with melt and persisted for over 50 min, whereas in the ordinary ingot, crystal settling began only after 40 min and lasted for 30 min. Furthermore, during the initial 40 min of solidification in the experimental ingot (21 % of the total solidification time), the width of the solid phase in the vertical direction was twice that of the ordinary ingot. This suggests that refilling the head with "cold" melt (at 70 °C) into the "hot" melt (at 75 °C), with only 7 min elapsed since casting the ingot body, resulted in an increased temperature gradient and the emergence of crystallization centers. Consequently, this contributed to the formation of a dense "rain" of crystals and accelerated the advancement of the solidification front in the vertical direction. Additionally, the introduction of a portion of melt induced forced convection, leading to the displacement of crystals from the crystallization front into the settling cone zone.

In the ingot with head refilling after 19 min (Fig. 2, *c*) solidification occurred according to the volume-sequential mechanism from 32 to 79 min (15 to 38 % of the total solidification time) due to crystal settling.

For the ingot with head refilling after 40 min (Fig. 2, *d*), solidification occurred via the sequential mechanism from the walls to the ingot axis, without the "rain of crystals" phenomenon typically observed in ingots of this experimental series.

Thermometry of the casting form model surface during solidification of an ordinary ingot revealed (Figs. 3, *a*; Fig. 4, *a*) that during the initial half of the ingot solidification time, the thermal center was located in the sub-knock-off head horizon. Subsequently, it shifted to the ingot mid-height, and by the end of solidification, it returned to the sub-knock-off head horizon. This observation aligns with existing concepts regarding the solidification process of large ingots [1; 2].

For the ingot with head refilling after 7 min (Fig. 3, *b*; Fig. 4, *b*), the thermal center remained consistent, moving only from the middle to 2/3 of the ingot height throughout the solidification process, eventually settling at the sub-knock-off head horizon by the end of solidification. Similarly, for the ingot with head refilling after 19 min (Fig. 3, *c*; Fig. 4, *c*), the thermal center remained at the ingot mid-height throughout solidification, eventually shifting to the sub-knock-off head horizon at the end. In contrast, for the ingot with head refilling after 40 min (Fig. 3, *d*; Fig. 4, *d*), the thermal center was initially located at 2/3 of the ingot height, moving to the sub-knock-off head horizon after melt refilling and remaining there until the end of solidification.

It's evident that melt refilling influenced the dynamics of thermal processes during ingot crystallization.

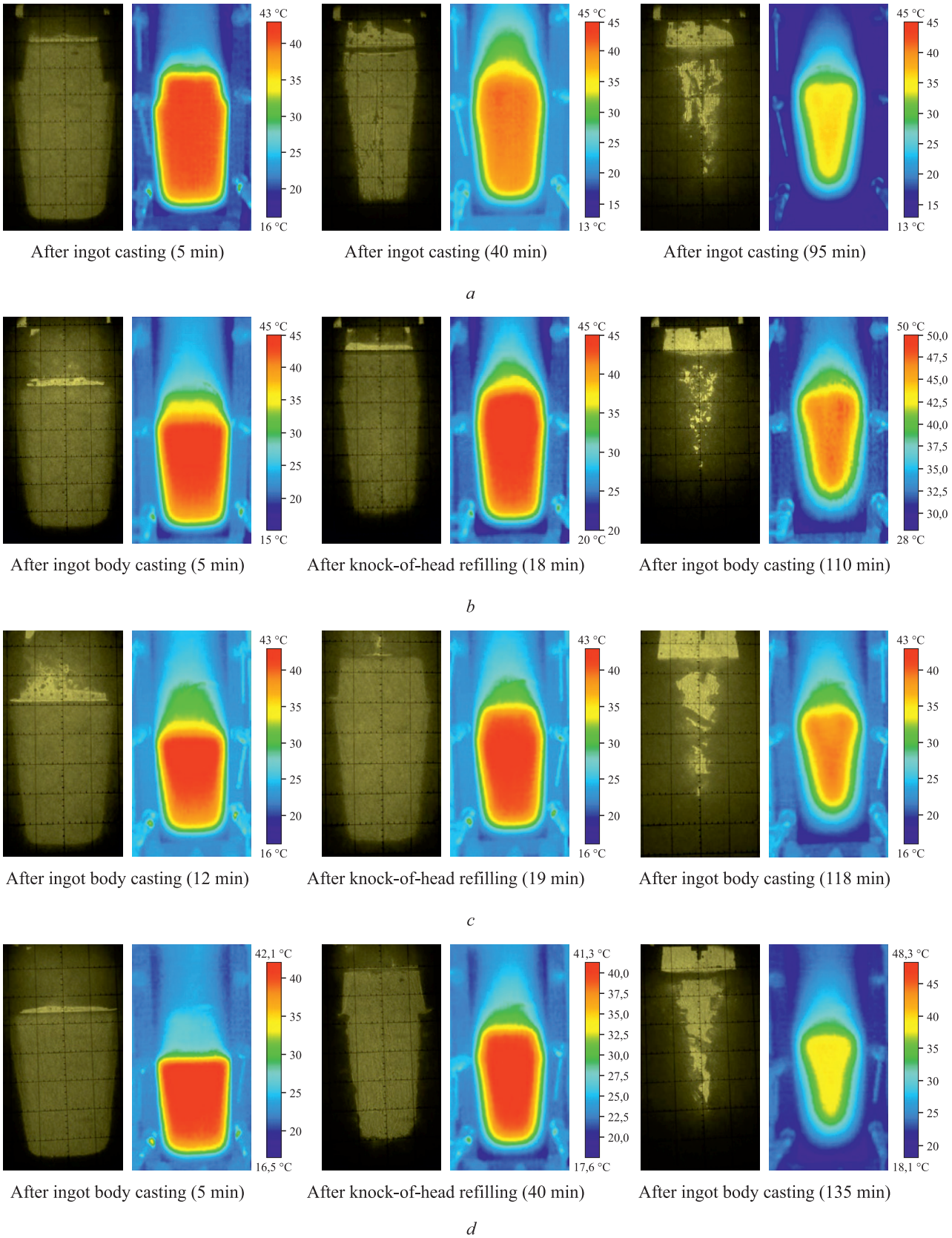


Fig. 3. Dynamics of the thermal center movement during solidification of model ingots:
*a* – ordinary ingot; *b* – refilling the knock-off head after 7 min; *c* – refilling the knock-off head after 19 min;
*d* – refilling the knock-off head after 40 min

Рис. 3. Динамика перемещения теплового центра при затвердевании модельных слитков:
*a* – обычный слиток; *b* – доливка прибыли спустя 7 мин; *c* – доливка прибыли спустя 19 мин;
*d* – доливка прибыли спустя 40 мин

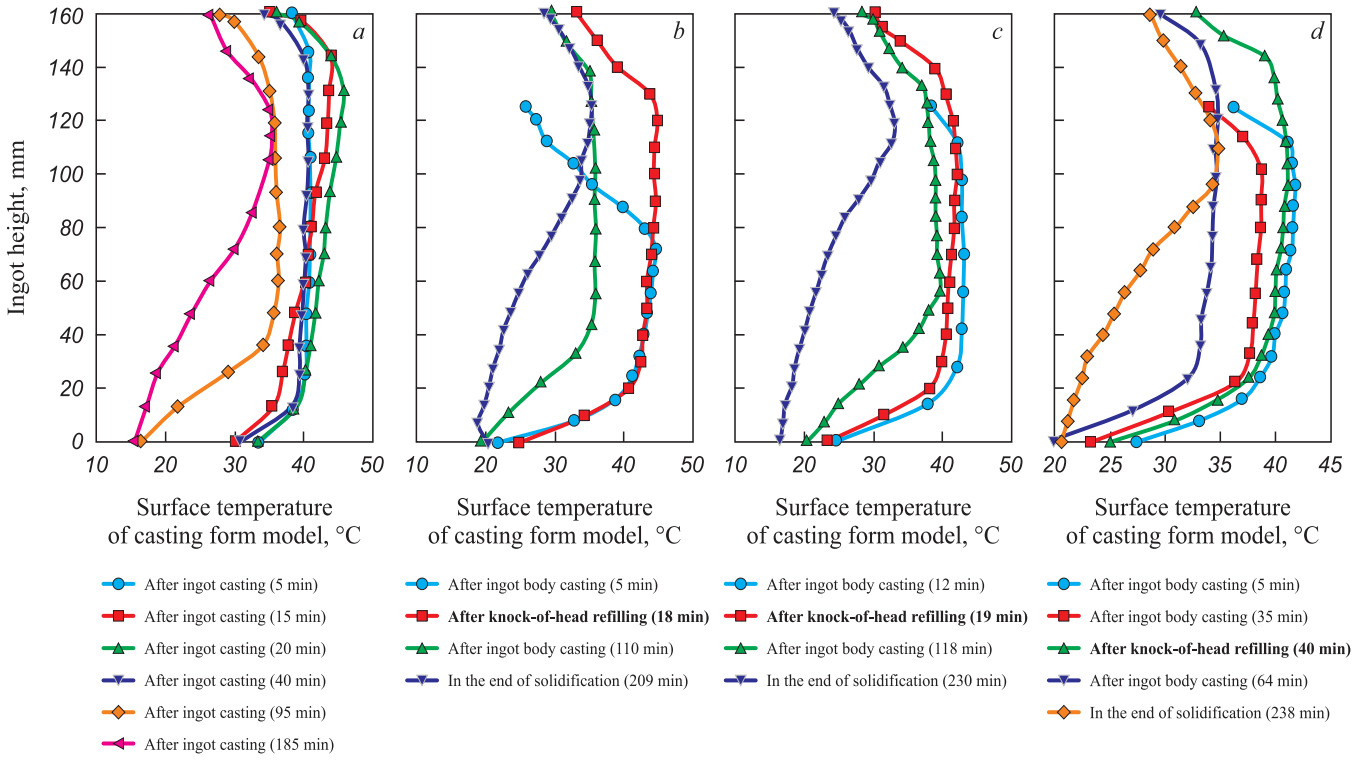


Fig. 4. Change in surface temperature of the casting form model in height of the model ingots
(based on the processing of thermal vision images using Testo IRSoft software):
*a* – ordinary ingot; *b* – refilling the knock-off head after 7 min; *c* – refilling the knock-off head after 19 min;
*d* – refilling the knock-off head after 40 min

Рис. 4. Изменение температуры поверхности модели изложницы по высоте модельных слитков
(на основании обработки тепловизионных изображений с помощью программного обеспечения Testo IRSoft):
*a* – обычный слиток; *b* – доливка прибыли спустя 7 мин; *c* – доливка прибыли спустя 19 мин;
*d* – доливка прибыли спустя 40 мин

Analysis of structural zone development in model ingots (Table 4, Fig. 5) revealed that three ingots (Fig. 5, *a* – *c*) exhibited the development of a settling cone zone. Two ingots (Fig. 5, *a*, *b*) were characterized by the penetration of a shrinkage hole from the head to the ingot body, which is evidently an ingot defect.

Visual inspection of the macrostructure of the cast ingots revealed that the ingot with head refilling conducted after 40 min (Fig. 5, *d*) exhibited a dense and defect-free structure.

This suggests that refilling the head with melt 40 min after casting the ingot body influenced the ingot crystallization mechanism, causing it to solidify via the sequential mechanism from the ingot walls to the axis, without the occurrence of the "rain of crystals" phenomenon. This process promoted the growth of columnar crystals toward

Table 4

**Volume fractions of structural zones in the model ingots**

*Таблица 4*. **Объемные доли структурных зон модельных слитков**

| Area of structural zones of model ingots, % | Technology of model ingot casting | | | |
|---|---|---|---|---|
| | ordinary ingot | head refilling after 7 min | head refilling after 19 min | head refilling after 40 min |
| Columnar crystals (before head refilling) | – | 16.7 | 23.5 | 43.4 |
| Columnar crystals | 65.2 | 22.4 | 47.3 | 56.6 |
| Omnidirectional crystals | 28.6 | 42.5 | 25.2 | – |
| Settling cone | 6.2 | 18.4 | 4.0 | – |
| Shrinkage hole | 32.8 | 41.4 | 36.3 | 24.0 |

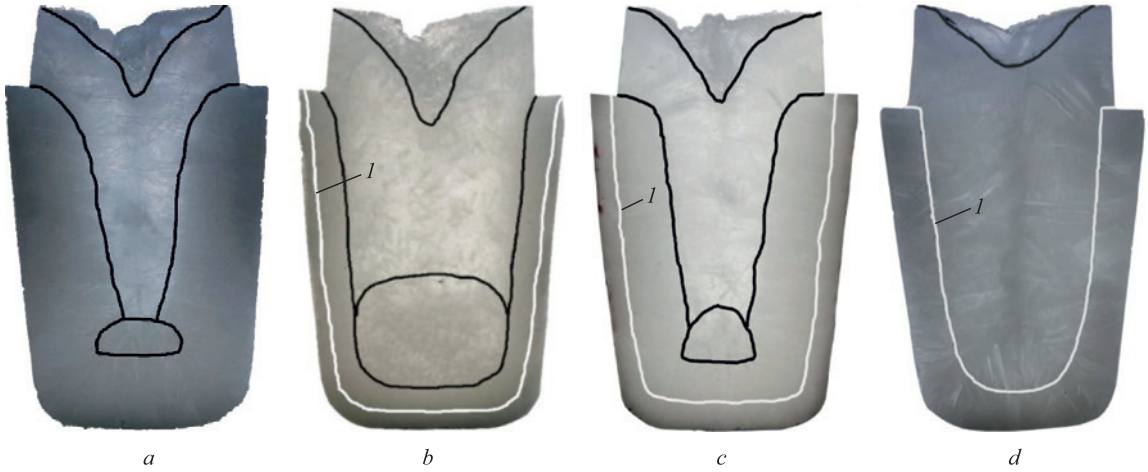


Fig. 5. Macrostructure of the model ingots:
*1* – boundary of the solidified solid phase layer in the ingot body before refilling the knock-off head with the melt;
*a* – ordinary ingot; *b* – refilling the knock-off head after 7 min; *c* – refilling the knock-off head after 19 min;
*d* – refilling the knock-off head after 40 min

Рис. 5. Макроструктура модельных слитков:
*1* – граница затвердевшего слоя твердой фазы в теле слитка перед доливкой в прибыльную часть расплава;
*a* – обычный слиток; *b* – доливка прибыли спустя 7 мин; *c* – доливка прибыли спустя 19 мин; *d* – доливка прибыли спустя 40 мин

the ingot axis, resulting in minimal development of a shrinkage hole and ultimately yielding a defect-free structure.

## Conclusions

It has been observed that in an ordinary ingot, solidification proceeds via a sequential mechanism up to 40 min, after which crystals begin to settle (“rain of crystals”), transitioning the solidification process to a volume-sequential mechanism. However, refilling the knock-off head with melt 40 min after casting the ingot body sustained the sequential mechanism of ingot solidification. This resulted in the formation of a monolithic, defect-free structure in the ingot body and minimized the development of shrinkage holes in the head volume.

Melt refilling within the initial 40 min stimulates early crystal settling (“rain of crystals”), enhancing crystallization orientation in the vertical direction.

Thermometry of the casting form-mold surface during ingot solidification revealed the influence of melt refilling of the head on the dynamics of thermal processes occurring during crystallization.

These findings provide insight into the development of differentiated casting technology for ingots, wherein the head is filled with melt at specific intervals after casting the ingot body. This approach can effectively influence the metal structure formation process and reduce defect zones.

## References / Список литературы

1. Skoblo S.Ya., Kazachkov E.A. *Ingots for Large Forgings*. Moscow: Metallurgiya; 1973:247.

   Скобло С.Я., Казачков Е.А. *Слитки для крупных поковок*. Москва: Металлургия; 1973:247.
2. Smirnov A.N., Makurov S.L., Safonov V.M., Tsuprun A.Yu. *Large Ingot*. Donetsk: Veber; 2009:279.

   Смирнов А.Н., Макуров С.Л., Сафонов В.М., Цуприн А.Ю. *Крупный слиток*. Донецк: Вебер; 2009:279.
3. Zhul’ev S.I., Zyuban N.A., Rutskii D.V. *Steel Ingots: Quality and New Technologies*. Volgograd: VolgSTU; 2016:176. (In Russ.).

   Жульев С.И., Зюбан Н.А., Руцкий Д.В. *Стальные слитки: проблемы качества и новые технологии*. Волгоград: ВолгГТУ; 2016:176.
4. Gamanyuk S.B. *Investigation of a large forging steel ingot of modified geometry in order to improve the quality of metal forgings: Cand. Tech. Sci. Diss*. Volgograd; 2012. (In Russ).

   Гаманюк С.Б. *Исследование крупного кузнечного стального слитка измененной геометрии с целью повышения качества металла поковок: Дисертация ... кандата технических наук*. Волгоград, 2012.
5. Jiaqi W., Paixian F., Hongwei L., Dianzhong L., Yiyi L. Shrinkage porosity criteria and optimized design of a 100-ton 30Cr2Ni4MoV forging ingot. *Materials & Design*. 2012;35:446–456. https://doi.org/10.1016/j.matdes.2011.09.056
6. Zhang C.-J., Bao Y.-P., Wang M. Influence of casting parameters on shrinkage porosity of a 19 ton steel ingot. *Metallurgia Italiana*. 2016;108(1):37–44.
7. Yu Z., Zhang H., Wang X., Wu X. Study on heat transfer characteristics during solidification of 18-ton steel ingot with large ratio of height to diameter. *Metallurgia Italiana*. 2020;112(5):37–47.
8. Tashiro K., Watanabe S., Kitagawa I., Tamura I. Influence of mould design on the solidification and soundness of heavy forging ingots. *Transactions of the Iron and Steel Institute of Japan*. 1983;23(4):312–321. https://doi.org/10.2355/isijinternational1966.23.312

**9.** Romashkin A.N., Malginov A.N., Tolstyh D.S., Ivanov I.A., Doub V.S. The ingot geometry effect on the axial shrinkage. *Computer Research and Modeling*. 2015;7(1):107–112. (In Russ.). https://doi.org/10.20537/2076-7633-2015-7-1-107-112

Ромашкин А.Н., Мальгинов А.Н., Толстых Д.С., Иванов И.А., Дуб В.С. Влияние геометрии слитка на объем осевой рыхлости в нем. *Компьютерные исследования и моделирование*. 2015;7(1):107–112. https://doi.org/10.20537/2076-7633-2015-7-1-107-112

**10.** Zhang C., Bao Y., Wang M., Guo B. Influence of casting parameters on the shrinkage porosity of a 40-ton steel ingot by numerical simulation. In: *Proceedings of the 6th Int. Congress on the Science and Technology of Steelmaking, 2015*. 2015:543–546.

**11.** Zhang C., Loucif A., Jahazi M., Morin J.-B. FE modelling and prediction of macrosegregation patterns in large size steel ingots: Influence of filling rate. *Metals*. 2022;12(1):29. https://doi.org/10.3390/met12010029

**12.** Zhang C., Loucif A., Jahazi M., Tremblay R., Lapierre L.-P. On the effect of filling rate on positive macrosegregation patterns in large size cast steel ingots. *Applied Sciences (Switzerland)*. 2018;8(10):1878. https://doi.org/10.3390/app8101878

**13.** Marx K., Rödi S., Schramhauser S., Seemann M. Optimization of the filling and solidification of large ingots. *Metallurgia Italiana*. 2014;106(11–12):11–19.

**14.** Ludwig A., Stefan-Kharicha M., Kharicha A., Wu M. Massive formation of equiaxed crystals by avalanches of mushy zone segments. *Metallurgical and Materials Transaction A*. 2017;48:2927–2930. https://doi.org/10.1007/s11661-017-4008-y

**15.** Stefan-Kharicha M., Kharicha A., Mogeritsch J., Wu M., Ludwig A. Review of ammonium chloride-water solution properties. *Journal of Chemical & Engineering Data*. 2018;63(9):3170–3183. https://doi.org/10.1021/acs.jced.7b01062

**16.** Gamanyuk S.B., Zyuban N.A., Rutskii D.V., Palatkin S.V. *Device for studying the crystallization process of ingots in a mold*. Patent RF no. 169365. *Bulliten' izobretenii*. 2017:(8). (In Russ.).

Пат. 169365 РФ, B22D7/08. *Устройство для исследования процесса кристаллизации слитков в изложнице* / Гаманюк С.Б., Зюбан Н.А., Руцкий Д.В., Палаткин С.В. Заявлено 24.05.2016; опубликовано 15.03.2017; Бюллетень № 8.

**17.** Efimov V.A., Eldarkhanov A.S. *Modern Technologies for Casting and Crystallization of Alloys*. Moscow: Mashinostroenie; 1998:359. (In Russ.).

Ефимов В.А., Эльдарханов А.С. *Современные технологии разливки и кристаллизации сплавов*. Москва: Машиностроение; 1998:359.

**18.** Gorunov A.I., Naumenko V.V., Rutskii D.V. Effect of refilling the knock-off head on solidification and structure formation of 38KhN3MFA steel ingot. *News of the Volgograd State Technical University. Series "Problems of materials science, welding and strength in mechanical engineering". Issue 2: Interuniver. Coll. of Sci. Papers*. 2008;10:157–159. (In Russ.).

Горунов А.И., Науменко В.В., Руцкий Д.В. Влияние доливки прибыльной части на процесс затвердевания и структурообразования слитка стали 38ХН3МФА. *Известия Волгоградского государственного технического университета. Серия «Проблемы материаловедения, сварки и прочности в машиностроении». Выуск. 2: Межвузовский сборник научных статей*. 2008;10:157–159.

**19.** El'darkhanov A.S., Efimov V.A., Nuradinov A.S. *Processes of Castings Formation and Their Modeling*. Moscow: Mashinostroenie; 2001:208.

Эльдарханов А.С., Ефимов В.А., Нурадинов А.С. *Процессы формирования отливок и их моделирование*. Москва: Машиностроение; 2001:208.

## Information about the Authors / Сведения об авторах

***Sergei B. Gamanyuk,*** *Cand. Sci. (Eng.), Assist. Prof. of the Chair "Materials Technology",* Volgograd State Technical University
***E-mail:*** gamanuk@mail.ru

***Dmitrii V. Rutskii,*** *Cand. Sci. (Eng.), Assist. Prof., Head of the Chair "Materials Technology",* Volgograd State Technical University
***E-mail:*** drutskii@vstu.ru

***Nikolai A. Zyuban,*** *Dr. Sci. (Eng.), Prof. of the Chair "Materials Technology",* Volgograd State Technical University
***E-mail:*** tecmat@vstu.ru

***Mikhail V. Kirilichev,*** *Head of the Laboratory of the Chair "Materials Technology",* Volgograd State Technical University
***E-mail:*** tecmat@vstu.ru

***Maks S. Nikitin,*** *Postgraduate of the Chair "Materials Technology",* Volgograd State Technical University
***E-mail:*** tecmat@vstu.ru

***Сергей Борисович Гаманюк,*** *к.т.н., доцент кафедры «Технология материалов»,* Волгоградский государственный технический университет
***E-mail:*** gamanuk@mail.ru

***Дмитрий Владимирович Руцкий,*** *к.т.н., доцент, заведующий кафедрой «Технология материалов»,* Волгоградский государственный технический университет
***E-mail:*** drutskii@vstu.ru

***Николай Александрович Зюбан,*** *д.т.н., профессор кафедры «Технология материалов»,* Волгоградский государственный технический университет
***E-mail:*** tecmat@vstu.ru

***Михаил Владимирович Кириличев,*** *заведующий лабораторией кафедры «Технология материалов»,* Волгоградский государственный технический университет
***E-mail:*** tecmat@vstu.ru

***Макс Станиславович Никитин,*** *аспирант кафедры «Технология материалов»,* Волгоградский государственный технический университет
***E-mail:*** tecmat@vstu.ru

## Contribution of the Authors / Вклад авторов

***S. B. Gamanyuk*** – analysis of literary sources, processing of the research results, writing the text, preparation of references.

***D. V. Rutskii*** – setting the research goals and objectives, formation of the article concept, editing of the final text.

***N. A. Zyuban*** – scientific guidance, analysis of the research results.

***M. V. Kirilichev*** – conducting research, processing of the research results.

***M. S. Nikitin*** – conducting research, processing of the research results.

***С. Б. Гаманюк*** – анализ литературных источников, обработка результатов исследований, написание основного текста статьи, подготовка библиографического списка.

***Д. В. Руцкий*** – определение цели и задачи исследования, формирование концепции статьи, редактирование финальной версии статьи.

***Н. А. Зюбан*** – научное руководство, анализ результатов исследований.

***М. В. Кириличев*** – проведение исследований, обработка результатов исследований.

***М. С. Никитин*** – проведение исследований, обработка результатов исследований.

Received 10.10.2023
Revised 31.10.2023
Accepted 11.11.2023

Поступила в редакцию 10.10.2023
После доработки 31.10.2023
Принята к публикации 11.11.2023

ON THE MATERIALS OF THE INTERNATIONAL CONFERENCE "SCIENTIFIC AND PRACTICAL SCHOOL FOR YOUNG METALLURGISTS" – 2023

ПО МАТЕРИАЛАМ МЕЖДУНАРОДНОЙ КОНФЕРЕНЦИИ «НАУЧНО-ПРАКТИЧЕСКАЯ ШКОЛА ДЛЯ МОЛОДЫХ МЕТАЛЛУРГОВ» – 2023

**UDC** 669.162.142:622.78
**DOI** 10.17073/0368-0797-2023-6-760-767



***Original article***
***Оригинальная статья***

# Production of refining alumina-containing fluxes by sintering from technogenic raw materials

**V. V. Aksenova ✉, A. V. Pavlov, G. M. Markov**

**National University of Science and Technology "MISIS"** (4 Leninskii Ave., Moscow 119049, Russian Federation)

✉ axenovaviki@gmail.com

***Abstract***. Modern Russian steelmaking plants use predominantly alumina-containing materials for liquefying lime in a ladle-furnace unit, which replaced fluorspar. Alumina-containing materials currently available on the market cannot be used directly in steelmaking without preliminary preparation (refining, heat treatment or briquetting), or are simply unsuitable for ladle processing of steel. This work describes laboratory studies on the production of refining alumina-containing fluxes by sintering in units such as machines for pellets firing or producing agglomerate (in the temperature range of 1200 – 1500 °C) from clean metallurgical waste (fine dust from the production of alumina and burnt lime), meeting the requirements of steelmaking plants by chemical composition and mechanical properties. A comparison was made of sintering technological schemes with the introduction of hydrated lime and a mixture of hydrated lime and calcium carbonate in a 1:1 ratio as a source of CaO. We determined that the maximum permissible CaO content in sintered briquettes when using a mixture of hydrated lime and calcium carbonate in the charge, which does not lead to hydration destruction in air, is in the range of 2.3 – 3.6 %, depending on the holding temperature. The maximum permissible content of $Al_2O_3$ in sintered briquettes when using hydrated lime in the charge, which does not lead to hydration destruction in air, is in the range of 9.5 – 31.7 %, depending on the holding temperature. In existing fuel units it is possible to obtain fluxes by sintering only when using hydrated lime as a source of CaO, because adding calcium carbonate to the charge (9 – 22 %) requires an increase in holding temperature (above 1500 °C) or holding time (more than 25 min).

***Keywords:*** ladle-furnace, alumina dust, refining fluxes, alumina-containing materials, calcium aluminates, sintering, hydration destruction

***For citation:*** Aksenova V.V., Pavlov A.V., Markov G.M. Production of refining alumina containing fluxes by sintering from technogenic raw materials. *Izvestiya. Ferrous Metallurgy*. 2023;66(6):760–767. https://doi.org/10.17073/0368-0797-2023-6-760-767

# Получение рафинировочных глиноземсодержащих флюсов методом спекания из техногенного сырья

**В. В. Аксенова ✉, А. В. Павлов, Г. М. Марков**

**Национальный исследовательский технологический университет «МИСИС»** (Россия, 119049, Москва, Ленинский пр., 4)

✉ axenovaviki@gmail.com

***Аннотация***. Современные сталеплавильные предприятия России для разжижения извести на агрегате ковш-печь применяют преимущественно глиноземсодержащие материалы, которые пришли взамен плавиковому шпату. Доступные сейчас на рынке глиноземсодержащие материалы не могут быть использованы напрямую в сталеплавильном производстве без предварительной подготовки (рафинирования, термообработки или брикетирования), либо просто непригодны для ковшевой обработки стали. В данной работе описаны лабораторные исследования по получению рафинировочных глиноземсодержащих флюсов методом спекания в агрегатах по типу машин для обжига окатышей или производства агломерата (в температурном интервале 1200 – 1500 °C) из чистых отходов металлургического производства (мелкодисперсная пыль производства глинозема и обожженной извести), отвечающих требованиям сталеплавильных предприятий по химическому составу и механическим свойствам. Проведено сравнение технологических схем спекания с введением в качестве источника CaO гидратированной извести и смеси гидратированной извести и карбоната кальция в соотношении 1:1. Предельно допустимое содержание CaO в спеченных брикетах при использовании в шихте смеси гидратированной извести и карбоната кальция, не приводящее к гидратационному разрушению на воздухе, находится в диапазоне 2,3 – 3,6 % в зависимости от температуры выдержки. Предельно допустимое содержание $Al_2O_3$ в спеченных брикетах при использовании в шихте гидратированной извести, не приводящее к гидратационному разрушению на воздухе, находится в диапазоне 9,5 – 31,7 % в зависимости от температуры выдержки. В существующих топливных агрегатах возможно получить флюсы методом спекания только при использовании в качестве источника CaO гидратированной извести, так как добавление карбоната кальция в шихту (9 – 22 %) требует увеличения температуры выдержки (выше 1500 °C) или ее продолжительности (более 25 мин).

***Ключевые слова:*** агрегат ковш-печь, глиноземная пыль, рафинировочные флюсы, глиноземсодержащие материалы, алюминаты кальция, спекание, гидратационное разрушение

***Для цитирования:*** Аксенова В.В., Павлов А.В., Марков Г.М. Получение рафинировочных глиноземсодержащих флюсов методом спекания из техногенного сырья. *Известия вузов. Черная металлургия*. 2023;66(6):760–767. https://doi.org/10.17073/0368-0797-2023-6-760-767

## Introduction

The fluxes and slag-forming materials used in metallurgy exert significant influence on production technology, as well as the chemical composition and quality of smelted steel. The quantity of detrimental impurities (such as sulfur, phosphorus, and gases like oxygen, hydrogen, and nitrogen) is contingent upon the type of additives employed, which constitutes a fundamental determinant in achieving high-quality steel.

In the ladle-furnace unit (LFU) utilized for steel processing, lime serves as the primary slag-forming material, boasting a melting point exceeding 2500 °C. To lower the slag's melting point during extraction, flux is introduced alongside lime to induce liquefaction. In the past, fluorspar was widely employed for slag liquefaction in LFUs; however, its usage has recently been minimized or entirely phased out due to various adverse factors including its short-term efficacy, diminishment of lining resistance in the slag belt zone, and environmental concerns [1 – 3].

Alumina-containing fluxes, surpassing fluorspar in several aspects, emerge as a promising alternative to fluorine-based materials. These alumina-containing materials can be employed either independently or in conjunction with fluorspar, even for steel grades designated as "aluminum-free" [4]. Notably, aluminothermal slags derived from ferrovanadium and aluminothermal chromium production have gained significant traction as alumina-containing fluxes. However, a major drawback lies in their market scarcity due to the limited production of ferroalloys via aluminothermal reduction. Additionally, other available alumina-containing materials often require preliminary treatment (such as refining, heat treatment, or briquetting) before they can be utilized in steelmaking, or they may prove unsuitable for the ladle processing of steel [5 – 7].

When procuring fluxes, steelmaking plants impose criteria concerning both chemical composition and mechanical properties. Fluxes are expected to be supplied in the form of lumps or briquettes, with overall dimensions ranging from 10 to 50 mm. The fine fraction (0 – 5 mm) should not exceed 10 % of the total mass, while moisture content is to be kept below 1 % in summer and up to 6.5 % in winter. Consumers may also specify requirements regarding the strength properties of briquettes/lumps. A summarized outline of the chemical composition requirements for alumina-containing fluxes is presented in Table 1.

The required quantity of alumina-containing flux for processing in the LFU is determined through the balance equation of aluminum utilization in ladle processing:

$$Al_{sec} = Al_{res} + Al_{deox} + Al_{air} + Al_{sl} + Al_{evap},$$

where $Al_{res}$ is residual aluminum, $Al_{deox}$ is deoxidation aluminum, $Al_{air}$ is air oxygen-oxidized aluminum, $Al_{sl}$ is furnace slag-oxidized aluminum, and $Al_{evap}$ is evaporated aluminum.

A portion of $Al_2O_3$ needed for lime liquefaction is generated through the interaction of aluminum with dissolved oxygen in steel, while another portion results from combustion on the slag surface and subsequent deoxidation. The remaining portion is introduced in the form of flux to facilitate free-running slag. Despite its technological efficiency, aluminum is deemed economically impractical due to its high cost as a source of $Al_2O_3$. According to the balance equation, it's estimated that aluminum consumption is distributed as follows: $Al_{res}$ – 15 %; $Al_{deox}$ – 18 %; $Al_{air}$ – 38 %; $Al_{sl}$ – 28 %; $Al_{evap}$ – 1 %.

Given the current industrial environmental constraints and stringent steel quality requirements, developing alumina-containing flux production technology in an environmentally sustainable and cost-effective manner emerges as an urgent challenge.

## Materials and methods

An essential consideration in flux production via sintering is the meticulous selection of charge materials. Firstly, these materials must not introduce harmful impurities that resist removal during heat treatment and could potentially contaminate the processed steel. Secondly, they should be relatively amenable to briquetting, as sintering technology involves the heat treatment of lump material. Thirdly, availability on the market is crucial.

The recycling of metallurgical waste to yield marketable products has gained significant traction in recent times. Among such wastes is the dust collected from the filters of roasting furnaces. This paper focuses on the processing of dust originating from alumina calcination and limestone roasting furnaces.

Alumina calcination involves the dehydration of aluminum hydroxide at elevated temperatures. Aluminothermal slag, utilized in rotary tube furnaces or fluidized-bed furnaces at temperatures reaching up to 1200 °C, represents the final stage in the $Al_2O_3$ production process chain. Inevitably, during the calcination processes in

Table 1

**Consolidated requirements for the chemical composition of alumina-containing fluxes imposed by metallurgical enterprises in Russia**

*Таблица 1.* **Сводные требования к химическому составу глиноземсодержащих флюсов, предъявляемые металлургическими предприятиями России**

| Element | Content in steelmaking flux, % | | Features of use in the LFU |
|---|---|---|---|
| | min | max | |
| min, % | | | |
| $Al_2O_3$ | 50 | 80 | Reduces the melting point of CaO |
| max, % | | | |
| CaO | 20 | 30 | Forms a low-melt eutectic with $Al_2O_3$ |
| MgO | 8 | 20 | |
| $Fe_2O_3$ | 2 | 6 | Worsens the desulfiding process |
| MnO | 1.5 | 2.0 | Limitation on the use of corundum production slags and alumina-containing ores without refining |
| $SiO_2$ | 3 | 15 | |
| $P_{tot} + S_{tot}$ | 0.02 | 0.30 | Transfer to metal and require additional refining |
| $Cr_2O_3$ | 2 | 10 | Form carbides, worsen further processing |
| $TiO_2$ | 1 | 5 | Restriction on the use of aluminothermal slags from ferrotitanium and chromium metal production |
| $V_2O_5 + Nb_2O_5$ | 1 | 1 | Recovered and converted to metal<br>Restriction on the use of aluminothermal slags from ferrovanadium and ferroniobium production |
| $Na_2O + K_2O$ | 1 | 8 | Restriction on the use of slag from secondary aluminum production |

various units, nanoscale dust is generated. Research cited in [8] indicates that the size of dust nanoparticles falls within the range of 50 – 300 nm. Approximately 14 % of the fine alumina dust is carried away from the furnace by flue gas during calcination, which is then directed to multicyclones and electric filters [9]. However, this dust, containing nanoparticles, is unsuitable for use in the classical technology of electrolytic decomposition of $Al_2O_3$ due to its hygroscopic nature, leading to excessive hydrogen content in aluminum metal. Nonetheless, this material finds applicability in the iron industry as a source of $Al_2O_3$ in steelmaking fluxes.

When selecting a source of CaO for flux production via sintering, one should consider a chain of chemical transformations: $CaCO_3 \rightarrow CaO \rightarrow Ca(OH)_2 \rightarrow CaCO_3$.

Fine-dispersed carbonate rocks, burnt, or slaked lime can serve as a source of CaO, each carrying its own set of advantages and disadvantages. Limestone ($CaCO_3$) necessitates no preliminary preparation before briquetting. However, during sintering, its decomposition into CaO and $CO_2$ absorbs heat (178 kJ/mol). Burnt lime (CaO), on the other hand, doesn't undergo significant mass loss during sintering due to the absence of crystal hydrate moisture. Yet, its slaking during briquetting releases heat (65 kJ/mol), which is not conducive to the process. Slaked lime ($Ca(OH)_2$) offers several advantages over the aforementioned materials:

– it requires no preliminary preparation and can hydrate in air during storage;

– it facilitates convenient briquetting as it doesn't generate heat when interacting with water;

– heat absorption during its decomposition into CaO and $H_2O$ (65 kJ/mol) during sintering is almost 3 times less than the heat absorbed during the decomposition of $CaCO_3$.

In industrial settings, burnt lime is typically obtained by calcinating carbonate rocks in shaft or rotary furnaces at temperatures ranging from 1000 to 1250 °C [10]. Analogous to alumina calcination, this process generates micro-sized dust particles (6 – 60 μm), which are typically collected in bag filters or electric filters [11]. While this dust shares a similar composition with the burnt material, its smaller particle size renders it more prone to rapid hydration in the air during storage. Nonetheless, this fine dust can also serve as raw material for the production of sintered alumina-lime fluxes.

An integral aspect of working with dispersed materials involves their preparation for heat treatment. In this study, cold briquetting was employed. Drawing from suc-

cessful experiments involving porous alumina-containing materials [12], a binder based on polyacrylamide was utilized. This binder exhibits low consumption (0.6 % of the mass of the briquetted raw material) and is completely removed at sintering temperatures.

The production technology of alumina-lime fluxes, designed to withstand hydration and subsequent destruction during sintering, from pure components encompasses the following operations:

– production of briquettes from pure components;

– heating the material to the holding temperature;

– maintaining a constant temperature during holding;

– cooling in ambient air.

In laboratory settings, sintering was conducted in a resistance furnace equipped with a graphite heater. The technologies employed in ore pellet roasting and agglomerate production served as the foundation for flux production. The temperature range for laboratory experiments was selected in accordance with the existing process characteristics of fuel units. Literature data indicates that the maximum roasting temperature for iron ore pellets is around 1400 °C [13 – 17], while for chromite pellets, it ranges from 1400 to 1500 °C [18 – 22]. Hence, the temperature holding interval ranged from 1200 to 1500 °C. During laboratory experiments, the average heating rate was maintained at 20 °C, and the duration of holding at a constant temperature ranged from 15 to 25 min. Following heat treatment, the sintered briquettes were cooled in ambient air, after which their mass and geometric parameters were measured. Subsequently, the briquettes were stored in air, at a temperature of 21 °C and a relative humidity of 50 %, to monitor any changes in mass. Weighing and recording the mass change of the briquettes were conducted once every seven days until the mass stabilized.

Two series of experiments were conducted utilizing different sources of CaO: a mixture of hydrated lime and calcium carbonate in a 1:1 ratio (series *1*) and hydrated lime along (series *2*). The proportion of $Al_2O_3$ in the briquettes before sintering varied from 50 to 80 % in both cases, with increment of 5 %. The chemical composition of the raw materials is provided in Table 2.

## Results and discussion

After the briquettes had cooled in air, an external evaluation of their post-sintering state was conducted. Based on their appearance, the heat-treated briquettes were categorized into four conventional groups (Fig. 1).

The STATISTICA software package was employed to process the results and identify factors influencing the hydration destruction of sintered briquettes. The dependent variable was the percentage of mass gain during storage in air, while the independent variables included the temperature of sintering (°C), sintering time (min), composition of initial briquettes (%), change in density and volume of briquettes during sintering (%), and

Table 2

**Chemical composition of raw materials**

*Таблица 2*. **Химический состав исходных материалов**

| Material | $Al_2O_3$ dust | | | CaO dust | | | | |
|---|---|---|---|---|---|---|---|---|
| Element | $Al_2O_3$ | $Fe_2O_3$ | $Na_2O + K_2O$ | CaO | MgO | $SiO_2$ | P | S |
| Content, % | 99.53 | 0.01 | 0.45 | 98.76 | 0.50 | 0.70 | 0.01 | 0.03 |

*a* *b* *c* *d*

Fig. 1. Appearance of heat-treated briquettes:
*a* – sintered; *b* – semi-melted; *c* – melted; *d* – collapsed/cracked

Рис. 1. Внешний вид термообработанных брикетов:
*a* – спеченные; *b* – оплавленные; *c* – расплавившиеся; *d* – разрушившиеся/треснувшие

$\Delta m_{hydr} = 6.5334 - 0.0041 t_{hold} + 0.7228(\%\ Ca(OH)_{2\ (s)})$ $\Delta m_{hydr} = 1.3671 + 0.0135(\%\ Al_2O_{3\ (s)}) - 0.001 t_{hold}$

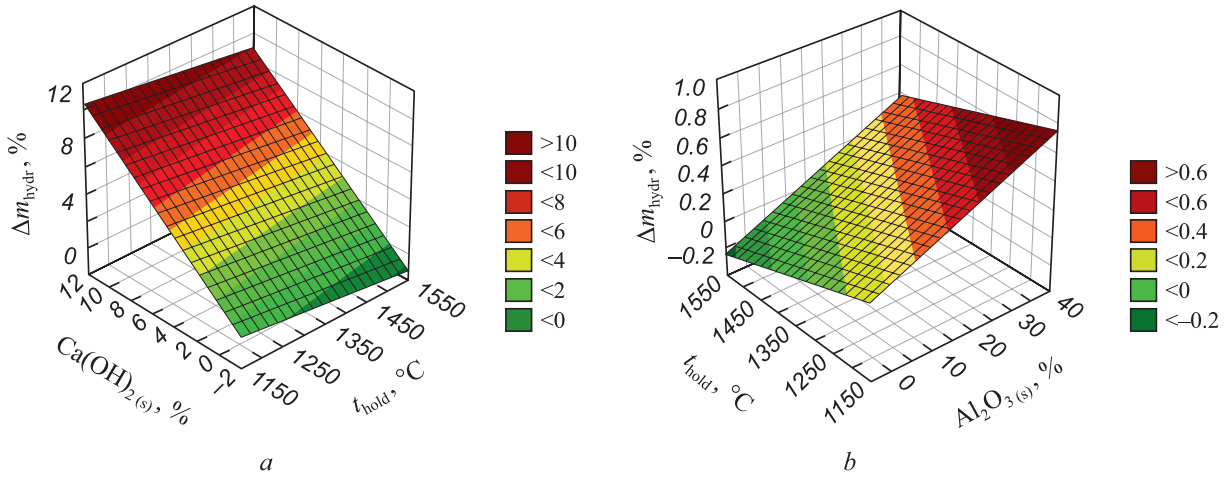


*a* *b*

Fig. 2. Influence of holding temperature, $Ca(OH)_2$ and $Al_2O_3$ content in sintered materials on change in mass:
*a* – when using a mixture of $CaCO_3$ and $Ca(OH)_2$; *b* – when using $Ca(OH)_2$

Рис. 2. Влияние температуры выдержки, содержания $Ca(OH)_2$ и $Al_2O_3$ в спеченных материалах на изменение массы:
*a* – при использовании смеси $CaCO_3$ и $Ca(OH)_2$; *b* – при использовании $Ca(OH)_2$

phase composition of sintered briquettes after holding in air (%). Fig. 2 illustrates the primary factors influencing the hydration destruction of briquettes for the two series of experiments.

In addition to quantitative evaluation, qualitative assessment of the visual state of briquettes during air storage was conducted. For experiments in series *1*, the initial signs of hydration degradation, accompanied by mass gain, were observed as early as the 7th day of air storage, with the mass gain concluding on the 56th day of observation. For the experiments in series 2, the first indicators of hydration degradation were observed only on the 28th day of air storage, with the mass gain ceasing on the 100th day of observation. The results of *X*-ray structural analysis of sintered briquettes that remained intact during air storage are presented in Table 3.

The results of the comprehensive evaluation by regression equations, determining the maximum permissible content of free CaO and $Al_2O_3$ in sintered briquettes for two laboratory series, are presented in Table 4.

It has been established that in series *1*, where the process of calcium aluminate formation coincides with the decomposition of calcium carbonate and calcium hydroxide, it is necessary to elevate the temperature

Table 3

**X-ray structural analysis of sintered briquettes not collapsed during storage in air**

*Таблица 3*. **Рентгеноструктурный анализ спеченных брикетов, не разрушившихся при хранении на воздухе**

| Series number | Share of $Al_2O_3$ in briquette before sintering, % | Holding temperature, °C | Holding time, min | $Al_2O_3$, % | $CaO{\cdot}Al_2O_3$, % | $12CaO{\cdot}7Al_2O_3$, % | $CaO{\cdot}2Al_2O_3$, % | $3CaO{\cdot}Al_2O_3$, % | $CaO{\cdot}6Al_2O_3$, % |
|---|---|---|---|---|---|---|---|---|---|
| *1* | 50 | 1500 | 15 | 0 | 9.10 | 90.90 | 0 | 0 | 0 |
| *1* | 75 | 1500 | 15 | 22.90 | 25.10 | 0 | 38.20 | 0 | 13.80 |
| *2* | 50 | 1200 | 15 | 0 | 0 | 78.30 | 0 | 21.70 | 0 |
| *2* | 50 | 1200 | 25 | 0 | 0 | 65.90 | 0 | 34.10 | 0 |
| *2* | 70 | 1400 | 20 | 14.00 | 53.40 | 15,30 | 16.10 | 1.20 | 0 |
| *2* | 55 | 1400 | 20 | 4.40 | 3.40 | 92.30 | 0 | 0 | 0 |
| *2* | 50 | 1400 | 20 | 0 | 2.50 | 97.50 | 0 | 0 | 0 |
| *2* | 50 | 1500 | 25 | 0 | 0 | 86.30 | 0 | 13.70 | 0 |
| *2* | 80 | 1500 | 25 | 26.90 | 25.90 | 0 | 40.60 | 6.50 | 0 |

Table 4

**Ultimate content of CaO and $Al_2O_3$ in sintered briquettes**

*Таблица 4*. **Предельное содержание CaO и $Al_2O_3$ в спеченных брикетах**

| Series number | Limit content of elements in briquette, % | Holding temperature, °C | | | | | | |
|---|---|---|---|---|---|---|---|---|
| | | 1200 | 1250 | 1300 | 1350 | 1400 | 1450 | 1500 |
| *1* | CaO ($Ca(OH)_2$) | 2.3 (3.0) | 2.5 (3.3) | 2.6 (3.5) | 2.9 (3.8) | 3.1 (4.1) | 3.6 (4.7) | 3.6 (4.7) |
| *2* | $Al_2O_3$ | 9.5 | 13.2 | 16.9 | 20.6 | 24.3 | 28.0 | 31.7 |

(>1500 °C) and/or extend the holding time (>25 min) to ensure the completion of all structural transformations. Conversely, series *2* demonstrates that hydration-resistant materials can be produced at relatively low temperatures (starting from 1200 °C) within the specified time interval (15 – 25 min).

## Conclusions

The maximum allowable content of CaO in sintered briquettes, which prevents the destruction of the sintered material during air storage (in the case of using a mixture of hydrated lime and calcium carbonate as a source of CaO), falls within the range of 2.3 to 3.6 %, depending on the holding temperature during sintering, corresponding to a mass gain of 3.8 %.

The maximum allowable content of $Al_2O_3$ in sintered briquettes, which avoids the destruction of the sintered material during air storage (in the case of using hydrated lime as a source of CaO), ranges from 9.5 to 31.7 %, depending on the holding temperature during sintering, corresponding to a mass gain of 0.3 %.

Given the existing fuel units, fluxes can only be produced when hydrated lime (series *2*) is utilized as a source of CaO. This is because when a mixture of hydrated lime combined with calcium carbonate (series *1*) is used as a source of CaO, a holding temperature exceeding 1500 °C is required, which is unattainable with the existing fuel units, or by extending the holding time to over 25 min.

The most favorable source of CaO for flux production via the sintering method is the hydrated dust from limestone roasting furnaces. This is attributed to the fact that during sintering, its heat absorption is three times lower than that of limestone.

## References / Список литературы

1. Sheshukov O.Yu., Mikheenkov M.A., Nekrasov I.V., Metelkin A.A., Egiazar'yan D.K. Optimization of the slag composition in ladle treatment of steel for increasing the resistance of refractories and promoting slag reuse. *Metallurgist*. 2018;62:723–728. https://doi.org/10.1007/s11015-018-0714-y

2. Larionov L.M., Kondratyev V.V., Kuzmin M.P. Ways of using carbon-containing waste from aluminum production. *iPolytech Journal*. 2017;21(4(123)):139–146. (In Russ.). https://doi.org/10.21285/1814-3520-2017-4-139-146

Ларионов Л.М., Кондратьев В.В., Кузьмин М.П. Пути использования углеродсодержащих отходов алюминиевого производства. *Вестник Иркутского государственного технического университета*. 2017;21(4(123)):139–146. https://doi.org/10.21285/1814-3520-2017-4-139-146

3. Sarkar S., Anand V., Ranjan R., Borra C.R., Sahoo P.P. Elimination of fluorspar use and reduction in lime consumption at ladle furnace by reutilizing alumina-rich ladle furnace slag. *Journal of Sustainable Metallurgy*. 2022;8(1):398–408. https://doi.org/10.1007/s40831-022-00492-1

4. Sheshukov O.Yu., Nekrasov I.V., Miheenkov M.A., Egiazar'yan D.K., Lobanov D.A., Neugodnikov O.V., Ivanov B.A. Experience in the use of aluminous aluminumcontaining flux during ladle processing of "aluminum-free" steels. *Novye ogneupory (New Refractories)*. 2017;(3):75–77. (In Russ.). https://doi.org/10.17073/1683-4518-2017-3-75-77

Шешуков О.Ю., Некрасов И.В., Михеенков М.А., Егиазарьян Д.К., Лобанов Д.А., Неугодников О.В., Иванов Б.А. Опыт использования глиноземистого алюминийсодержащего флюса при ковшевой обработке «безалюминиевых» сталей. *Новые огнеупоры*. 2017;(3):75–77. https://doi.org/10.17073/1683-4518-2017-3-75-77

5. Viklund-White C., Johansson H., Ponkala R. Utilization of spent refractories as slag formers in steelmaking. In: *Proceedings of the 6th Int. Conf. on Molten Slags, Fluxes and Salts*. Stockholm, Sweden; 2000:12–17.

6. Ramaswamy P., Gomes S.A., Ravichander N.P. Utilization of aluminum dross: Refractories from industrial waste. *IOP Conference Series: Materials Science and Engineering*. 2019;577(1):012101. https://doi.org/10.1088/1757-899X/577/1/012101

7. Paramguru R.K., Rath P.C., Misra V.N. Trends in red mud utilization – A review. *Mineral Processing & Extractive Metallurgy Review*. 2004;26(1):1–29. https://doi.org/10.1080/08827500490477603

8. Davydov S.Ya., Apakashev R.A., Koryukov V.N. The collection of nanoscale particles in alumina production. *Novye ogneupory (New Refractories)*. 2016;(2):12–15. (In Russ.).

Давыдов С.Я., Апакашев Р.А., Корюков В.Н. Улавливание наноразмерной фракции частиц глиноземного производства. *Новые огнеупоры*. 2016;(2):12–15.

9. Davydov S.Ya., Apakashev R.A., Koryukov V.N. The recycling of the alumina calciner kiln dust containing nanopartic-

les. *Novye ogneupory (New Refractories)*. 2014;(8):10–13. (In Russ.).

Давыдов С.Я., Апакашев Р.А., Корюков В.Н. Утилизация пыли печей кальцинации глинозема, содержащей наночастицы. *Новые огнеупоры*. 2014;(8):10–13.

10. Nesterov A.N., Datukashvili D.O. Production of high-calcium lime in Russia. *Stroitel'nye materialy*. 2017;(3):52–59. (In Russ.).

Нестеров А.В., Датукашвили Д.О. Производство кальциевой извести в России. *Строительные материалы*. 2017;(3):52–59.

11. Mantula V.D., Shaparenko A.V., Pavlyuchenko A.M., Fadeev A.V., Lyzhnik G.V. Application of bag filters in gas cleaning of limekiln and dolomite processes. *Ehkologiya i promyshlennost'*. 2017;(1(50)):29–35. (In Russ.).

Мантула В.Д., Шапаренко А.В., Павлюченко А.М., Фадеев А.В., Лыжник Г.В. Применение рукавных фильтров в газоочистках агрегатов известково-обжигового и доломитного производств. *Экология и промышленность*. 2017;(1(50)):29–35.

12. Aksenova V.V., Alimbaev S.A., Pavlov A.V., Mustafin R.M. Briquetting of porous alumina-containing materials with organic binders. *Izvestiya. Ferrous Metallurgy*. 2021;64(5):323–329. (In Russ.).
https://doi.org/10.17073/03680797-2021-5-323-329

Аксенова В.В., Алимбаев С.А., Павлов А.В., Мустафин Р.М. Брикетирование пористых глиноземсодержащих материалов на органических связующих. *Известия вузов. Черная Металлургия*. 2021;64(5):323–329.
https://doi.org/10.17073/0368-0797-2021-5-323-329

13. Zhang Y.B., Chen X.J., Su Z.J., Liu S., Chen F., Wu N.Y., Jiang T. Improving properties of fluxed iron ore pellets with high-silica by regulating liquid phase. *Journal of Iron and Steel Research International*. 2021;29:1381–1392.
https://doi.org/10.1007/s42243-021-00665-4

14. Fan X.H., Gan M., Jiang T., Yuan L.S., Chen X.L. Influence of flux additives on iron ore oxidized pellets. *Journal of Central South University of Technology*. 2010;17(4):732–737.
https://doi.org/10.1007/s11771-010-0548-7

15. Li G., Jiang T., Zhang Y., Tang Z. Recrystallization of $Fe_2O_3$ during the induration of iron ore oxidation pellets. *Recrystallization*. 2012;13:329–350.
https://doi.org/10.5772/32738

16. Umadevi T., Lobo N.F., Desai S., Mahapatra P.C., Sah R., Prabhu M. Optimization of firing temperature for hematite pellets. *ISIJ International*. 2013;53(9):1673–1682.
https://doi.org/10.2355/isijinternational.53.1673

17. Forsmo S.P.E., Forsmo S.E., Samskog P.O., Björkman B.M.T. Mechanisms in oxidation and sintering of magnetite iron ore green pellets. *Powder Technology*. 2008;183(2):247–259.
https://doi.org/10.1016/j.powtec.2007.07.032

18. Timofeeva A.S., Kozhukhov A.A., Nikitchenko T.V. Study of iron ore pellets hardening mechanisms in the process of burning. *Ferrous Metallurgy. Bulletin of Scientific, Technical and Economic Information*. 2020;76(11):1107–1112. (In Russ.).
https://doi.org/10.32339/0135-5910-2020-11-1107-1112

Тимофеева А.С., Кожухов А.А., Никитченко Т.В. Исследование механизмов упрочнения железорудных окатышей в процессе обжига. *Черная металлургия. Бюллетень научно-технической и экономической информации*. 2020;76(11):1107–1112.
https://doi.org/10.32339/0135-5910-2020-11-1107-1112

19. Akberdin A.A., Kim A.S., Zinyakova O.N. Improvement of production technology of chromite pellets. *Izvestiya. Ferrous Metallurgy*. 2014;57(9):24–28. (In Russ.).
https://doi.org/10.17073/0368-0797-2014-9-24-28

Акбердин А.А., Ким А.С., Зинякова О.Н. Совершенствование технологии производства хромитовых окатышей. *Известия вузов. Черная Металлургия*. 2014;57(9):24–28.
https://doi.org/10.17073/0368-0797-2014-9-24-28

20. Kim A.S., Akberdin A., Isagulov A., Sultangaziev R. Relationship between phase formation processes and the quality of chromite pellets during hardening firing. *Proceedings of the University*. 2019;(4):24–27. (In Russ.).

Ким А.С., Акбердин А., Исагулов А., Султангазиев Р. Взаимосвязь процессов фазообразования и качества хромитовых окатышей при упрочняющем обжиге. *Труды Университета*. 2019;(4):24–27.

21. Akberdin A.A., Kim A.S., Akberdin R.A. Agglomeration of refractory chromite ore. *Proceedings of INFACON XIII – 13th Int. Ferroalloys Congress: Efficient Technologies in Ferroalloy Industry*. 2020:1–4.

## Сведения об авторах / Information about the Authors

***Виктория Владимировна Аксенова,*** *аспирант кафедры металлургии стали, новых производственных технологий и защиты металлов,* Национальный исследовательский технологический университет «МИСИС»
***ORCID:*** 0009-0001-2611-2057
***E-mail:*** axenovaviki@gmail.com

***Александр Васильевич Павлов,*** *д.т.н., профессор кафедры металлургии стали, новых производственных технологий и защиты металлов,* Национальный исследовательский технологический университет «МИСИС»
***ORCID:*** 0000-0003-3773-9469
***E-mail:*** pav-gnts@misis.ru

***Георгий Михайлович Марков,*** *младший научный сотрудник,* Национальный исследовательский технологический университет «МИСИС»
***ORCID:*** 0000-0001-7285-7888
***E-mail:*** markov.sci@gmail.com

***Viktoriya V. Aksenova,*** *Postgraduate of the Chair of Metallurgy of Steel, New Production Technologies and Metal Protection,* National University of Science and Technology "MISIS"
***ORCID:*** 0009-0001-2611-2057
***E-mail:*** axenovaviki@gmail.com

***Aleksandr V. Pavlov,*** *Dr. Sci. (Eng.), Prof. of the Chair of Metallurgy of Steel, New Production Technologies and Metal Protection,* National University of Science and Technology "MISIS"
***ORCID:*** 0000-0003-3773-9469
***E-mail:*** pav-gnts@misis.ru

***Georgii M. Markov,*** *Junior Researcher,* National University of Science and Technology "MISIS"
***ORCID:*** 0000-0001-7285-7888
***E-mail:*** markov.sci@gmail.com

## Вклад авторов / Contribution of the Authors

***В. В. Аксенова*** – планирование и проведение экспериментов, определение химического состава исходных материалов методом волнодисперсионной рентгенофлуоресцентной спектрометрии, обработка полученных экспериментальных данных, подготовка текста статьи.
***А. В. Павлов*** – определение цели исследования, планирование и организация экспериментов, обсуждение результатов и выводов.
***Г. М. Марков*** – определение фазового состава спеченных образцов методом рентгенодифрактометрии.

***V. V. Aksenova*** – planning and conducting experiments, determination of chemical composition of the starting materials by wave-dispersive X-ray fluorescence spectrometry, processing the experimental data obtained, writing the text.

***A. V. Pavlov*** – setting the research goal, planning and organization of experiments, discussion of results and conclusions.
***G. M. Markov*** – determination of phase composition of sintered samples by X-ray diffraction.

Поступила в редакцию 10.10.2023
После доработки 31.10.2023
Принята к публикации 11.11.2023

Received 10.10.2023
Revised 31.10.2023
Accepted 11.11.2023

**UDC** 621.73
**DOI** 10.17073/0368-0797-2023-6-768-774



***Original article***
***Оригинальная статья***

# Modeling the pattern of metal flow during forming of forgings from a flat billet

**K. N. Solomonov[1], L. I. Tishchuk[1], S. M. Gorbatyuk[2], S. A. Snitko[3], O. N. Chicheneva[2]**

[1] **Voronezh Branch of the Rostov State Transport University** (75a Uritskogo Str., Voronezh 394026, Russian Federation)
[2] **National University of Science and Technology "MISIS"** (4 Leninskii Ave., Moscow 119049, Russian Federation)
[3] **Donetsk National Technical University** (58 Artema Str., Donetsk, Donetsk People's Republic 283001, Russian Federation)

konssol@list.ru

***Abstract***. Parts made of the billets with a thin web and stiffeners are manufactured at metallurgical enterprises in special workshops equipped with powerful hydraulic presses. Often their production is accompanied by the defects that worsen the product macrostructure. In this regard, new techniques are relevant that allow modeling the processes of forming of forgings with stiffeners. The processes of metal treatment by pressure are difficult to create a mathematical model describing the stress-strain state of plastic forming of metal. One of the ways to solve the problem of modeling the pattern of metal flow and the spatial diagram of contact pressures is the "theory of thin layer flow", based on assumptions that simplify the initial system of differential equations. Then the problem is reduced to a purely geometric one and can be solved within the framework of the "sandy analogy" using the proposed methodology. The paper presents the results of computer and physical modeling of the forming of stamped forgings with contour stiffeners. The experiment was carried out in industrial conditions on the precipitation of flat billets made of AK6 alloy on a hydraulic press with a deformation force of 150 MN. It is shown that the proposed software package can have a different functional purpose: express analysis of the pattern of metal flow and calculation of the shape of the billet at the stages of its deformation. This allows, by sorting through values of the geometric parameters of the stamp engraving, to obtain different patterns of metal flow and profiles of stiffeners and choose from them those that guarantee the most uniform filling of the stamp cavities with metal under the stiffeners, which ensures defect-free production of the product.

***Keywords:*** stamping, metal flow, mathematical modeling, physical modeling, software, forming

***For citation:*** Solomonov K.N., Tishchuk L.I, Gorbatyuk S.M., Snitko S.A., Chicheneva O.N. Modeling the pattern of metal flow during forming of forgings from a flat billet. *Izvestiya. Ferrous Metallurgy*. 2023;66(6):768–774. https://doi.org/10.17073/0368-0797-2023-6-768-774

# Моделирование картины течения металла при формообразовании поковки из плоской заготовки

**К. Н. Соломонов[1], Л. И. Тищук[1], С. М. Горбатюк[2], С. А. Снитко[3], О. Н. Чиченева[2]**

[1] **Филиал Ростовского государственного университета путей сообщения в г. Воронеж** (Россия, 394026, Воронеж, ул. Урицкого, 75а)
[2] **Национальный исследовательский технологический университет «МИСИС»** (Россия, 119049, Москва, Ленинский пр., 4)
[3] **Донецкий национальный технический университет** (Россия, Донецкая народная республика, 283001, Донецк, ул. Артема, 58)

konssol@list.ru

***Аннотация***. Детали из заготовок с тонким полотном и ребрами жесткости изготавливаются на металлургических предприятиях в специальных цехах, оборудованных мощными гидравлическими прессами. Нередко их производство сопровождается дефектами, ухудшающими макроструктуру изделия. В связи с этим актуальны новые методики, позволяющие моделировать процессы формообразования поковок с ребрами жесткости. Процессы обработки металлов давлением сложны в создании математической модели, описывающей напряженно-деформированное состояние пластического формообразования металла. Одним из способов решения задачи моделирования картины течения металла и пространственной эпюры контактных давлений является «теория течения тонкого слоя», основанная на допущениях, упрощающих исходную систему дифференциальных уравнений. В этом случае задача сводится к чисто геометрической и может быть

решена в рамках «песчаной аналогии» с помощью предложенной методики. Приведены результаты компьютерного и физического моделирования формообразования штампованной поковки с контурным оребрением. Эксперимент проведен в промышленных условиях по осадке плоских заготовок из сплава АК6 на гидравлическом прессе силой деформирования 150 МН. Показано, что предложенный программный комплекс может иметь различное функциональное назначение: экспресс-анализ картины течения металла и расчет формоизменения заготовки на стадиях ее деформирования. Это позволяет, перебирая значения геометрических параметров гравюры штампа, получать разные картины течения металла и профили ребер жесткости и выбирать из них те, которые гарантируют наиболее равномерное заполнение металлом полостей штампа под ребра жесткости, что обеспечивает бездефектное получение изделия.

***Ключевые слова:*** штамповка, течение металла, математическое моделирование, физическое моделирование, программное обеспечение, формообразование

***Для цитирования:*** Соломонов К.Н., Тищук Л.И., Горбатюк С.М., Снитко С.А., Чиченева О.Н. Моделирование картины течения металла при формообразовании поковки из плоской заготовки. *Известия вузов. Черная металлургия*. 2023;66(6):768–774.
https://doi.org/10.17073/0368-0797-2023-6-768-774

## Introduction

Improving the production efficiency of the domestic industry [1 – 4], heavy engineering in particular [5 – 8], is an urgent concern. Parts composed of billets with thin webs and stiffeners are typically manufactured at metallurgical plants in specialized workshops equipped with high-capacity hydraulic presses. However, their production often encounters defects that degrade the macrostructure of the final product. Hence, novel methods enabling the modeling of the forging processes involving stiffeners are highly relevant. The method devised by the authors could also be effectively applied in the fabrication of rail wheel billets. In the production of forged-rolled rail wheels, a critical operational step involves obtaining billets with minimal asymmetry across all units of the press-rolling line [9; 10 – 13]. This aspect is contingent upon various factors, primarily the stability of the mass and dimensions of the initial billets [14 – 18].

In metal forming processes, creating a mathematical model to describe the stress-strain state of plastic metal forming poses significant challenges. One approach to address this modeling issue concerning the metal flow pattern and the spatial distribution of contact pressures is through the "theory of thin layer flow" [19]. This theory relies on assumptions that simplify the initial system of differential equations, transforming the problem into a purely geometric one. Subsequently, it can be resolved within the context of a "sandy analogy" method developed by the authors [20].

## Main principles of the developed method

The developed method is founded on the following principles [21; 22].

The shortest-normal principle governs the direction of current lines perpendicular to the forging contour, which represents a line of abrupt changes in the layer thickness (incorporating stiffeners or elevations along the forging web). During the initial stage of strain, when the terminal pressures are uniform along the contour, the metal flows orthogonally to the contour, and the quantity of leaked metal at each boundary point is dictated by the length of the current lines.

During strain, the boundary conditions change resulting in unequal contact pressures along the contour. Consequently, the current lines will deviate at an acute angle from the forging contour. However, given that the spatial distribution of contact pressures forms a linear surface, the slope lines (and consequently the current lines) are perpendicular to the level lines of this surface. By projecting the volumetric pattern onto the forging web plane, a hypothetical contour can be introduced where the contact pressures are uniform. Subsequently, the current lines become perpendicular to this hypothetical contour.

Generally, the hypothetical contour is a rather intricate curve. According to the principle of smallest perimeter, a flat billet tends to adopt the shape of a circle in plan. Therefore, it can be assumed that the current lines follow the radii of some circular arc. As a result, the hypothetical contour becomes a circle, and the metal flow path along the forging web becomes radial.

It's worth noting that the radial metal flow path is more versatile than the normal flow path. It can be applied even at the initial stage of strain for a forging with a contour comprising curved line sections. By approximating the contour of the forging with circular arcs, the radial scheme can also be employed initially, when the current lines are perpendicular to the contour.

Consequently, the spatial distribution of contact pressures forms a combination of conical surfaces at any stage of the forging strain, except for the initial one. The terminal contact pressures lie in vertical planes intersecting these surfaces.

Determining the value of the terminal contact pressure at any moment of strain for any arbitrary point on the contour relies on several parameters: the thickness of the forging web, the dimensions of the die cavity, the width of the gutter, and the amount of metal leaked into the cavity. Accounting for all these parameters necessitates the use of rather complex formulas to calculate the terminal contact pressure.

As the spatial distribution of terminal pressure forms a surface of uniform slope, the metal flow interface rep-

resents a geometric locus of points equidistant from the forging contour. The contour itself can be approximated using straight lines and circular arcs. Consequently, constructing the metal flow interface boils down to determining the geometric location of points equidistant from circles and straight lines.

Given that any complex contour can be adequately approximated by straight line segments and circular arcs, it's reasonable to assume that the surface of the spatial distribution of contact pressures comprises flat and conical sections. The intersection lines between them constitute edges, commonly referred to as ridges.

By examining the frontal and profile projections of these edges, we can ascertain the volume of the contact pressure distribution and, correspondingly, the forces needed to deform the metal. The horizontal projection, or plan view, depicts a line representing the metal flow interface, which characterizes the distribution of metal flows on the contact surface.

## New algorithm for building the equidistant

In mechanical engineering, a significant portion of parts, driven by design processability requirements, comprise rotational surfaces and polyhedrons. Consequently, die forging in practice often involves parts derived from flat billets featuring planar elements [23 – 25]. This study focuses on the simplest scenario, addressing the challenge of constructing an equidistant curve for a contour represented by a piecewise linear closed line, namely, a polygon (Fig. 1, *a*).

The equidistant line of two intersecting straight lines corresponds to the bisector of the angle formed by their intersection. Our approach initiates from the smallest angle of the polygon. Thus, the first equidistant line of the contour constitutes the bisector of the angle at vertex *D*. Subsequently, we extend this line by drawing bisectors of the two adjacent angles, intersecting at points *G* and *H*, which mark the termination points of the first equidistant lines at the closest intersection point *G* with the bisectors of the neighboring angles.

Next, we disregard the *DE* contour side. The equidistant lines were formed by the bisectors of the adjacent angles to the *DE* contour side. We proceed until reaching the intersection of contour sides *FE* and *CD*, adjacent to the discarded line.

The dimensionality of the contour has decreased by one: instead of a hexagon, we will now consider a pentagon. Obviously, now the smallest angle in the contour polygon will be the newly obtained angle. The procedure is repeated, but the new equidistant line is drawn not from the contour angle, but from the end point of the last equidistant line – point *G*. Then we again search for the smallest contour angle among the remaining ones (this is the angle at vertex *F*) and repeat the above algorithm until the polygon is reduced actually to a triangle. As we know from geometry, in a triangle the bisectors always intersect in one point, so to complete building the equidistant lines it is sufficient to connect the points where the consecutive actions were stopped. Building is over (the result is shown in Fig. 1, *b*).

This approach can be applied to construct the equidistant line of any polygon. Currently, the algorithm has been implemented in the DELPHI visual programming environment. Additionally, a similar algorithm has been devised for a piecewise-nonlinear multilink contour [26 – 28].

## Computer modeling

Let us explore the capabilities of the developed method and software system through an example of modeling the forming of a stamped forging with contour ribbing (Fig. 2).

To swiftly assess the viability of incorporating a boss (or a cutout) in the given forging, the developed software system [29 – 31] was employed to simulate the metal flow pattern by adjusting the position of the circle center and the radius value. Analysis of the results demonstrates that directing the metal flow towards the boss (or cutout) mitigates the unevenness of metal distribution into the die cavity, thereby confirming its practical applicability.

To conduct the forging forming simulation, we utilized software built upon the developed method.

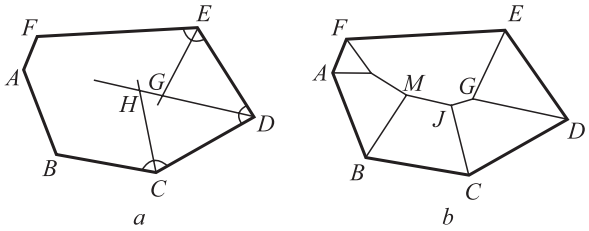


Fig. 1. Equidistant construction scheme

Рис. 1. Схема построения эквидистанты

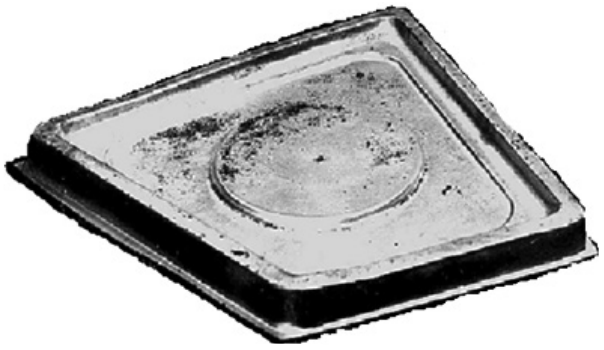

Fig. 2. Stamped forging with technological cutout

Рис. 2. Штампованная поковка с технологическим вырезом

When conducting the modeling, certain requirements must be considered. Only geometric elements that do not impact the design of the final product can be altered. These include parameters such as the width and height of the gutter threshold, the radius of the boss, the initial thickness of the billet, or the upset increment. Notably, the radius of the boss is included in these variables because it will be replaced by a 240 mm diameter hole in the finished part, and the boss will be removed during machining. Throughout the calculation process, the size of the boss functions as a control factor, allowing for the generation of various metal flow patterns along the die impression surface and, consequently, different profiles of the stiffener.

Fig. 3, *a* schematically illustrates the pattern of metal flow along the forging web.

Similarly, it is feasible to derive the metal flow pattern for contours of any complexity, as depicted in Fig. 3, *b*.

## Physical modeling

To validate the results of the analysis regarding the forming of the stamped forging with contour ribbing, an experiment was conducted under industrial conditions involving the stage-by-stage upsetting of flat forged billets (Fig. 4). These billets were composed of AK6 alloy and processed on a hydraulic press with a strain force of 150 MN.

The forging could not be fully formed due to the insufficient capacity of the hydraulic press. At the latest studied stage of upsetting, the boss was already formed in full, while one of the corner areas did not reach the designed height (Fig. 4, *d*).

The central areas of the stiffeners significantly outpaced the corner areas in terms of forming. Consequently, metal flowed over the die cavities beneath the stiffeners in the central areas, resulting in poor macrostructure of the product. This deficiency manifested in an inadequate alignment of metal fibers featuring sharp bends (Fig. 5, *a*), which could potentially lead to undercutting of the stiffener from the flash gutter side.

These observations were corroborated by the utilization of software for modeling various technological alternatives aimed at producing the specified serial forging. As previously noted, the forging could not be stamped in a single pass using the manufacturer's proposed technology.

The analysis of the calculation results has led to recommendations regarding the design of the die and the manufacturing process for producing a series of forgings. Despite the introduction of a large-radius boss, which failed to eliminate the uneven formation of individual stiffeners, thereby risking defects, it is proposed to conduct stamping in two passes using a single final die. This involves cutting a hole in the center of the forging after the first pass.

Stamping conducted in industrial conditions, while incorporating these recommendations, has validated their effectiveness. A hydraulic press with a capacity of up to 100 MN proved sufficient for achieving a high-quality product. Notably, the macrostructure of the stamped forging saw significant improvement, resulting in smooth

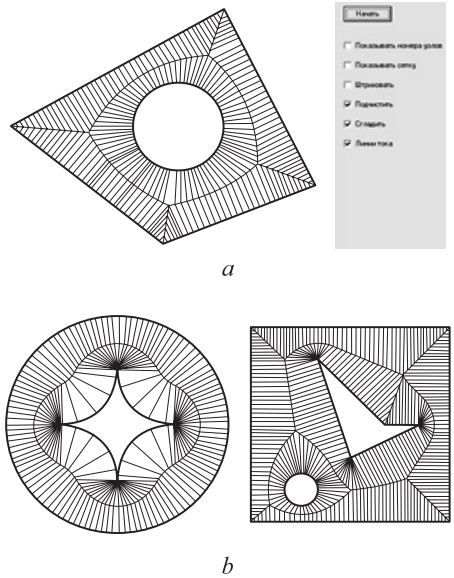


*a*

*b*

Fig. 3. Model of the metal flow pattern

Рис. 3. Модель картины течения металла

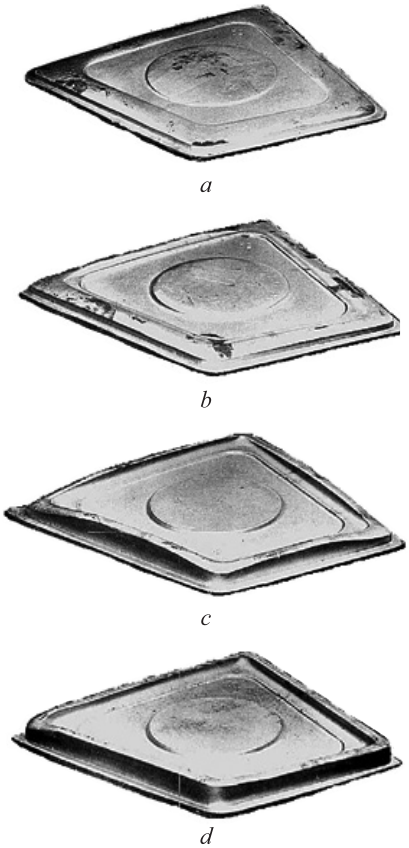

*a*

*b*

*c*

*d*

Fig. 4. Forming of stamped forgings

Рис. 4. Формообразование штампуемой поковки

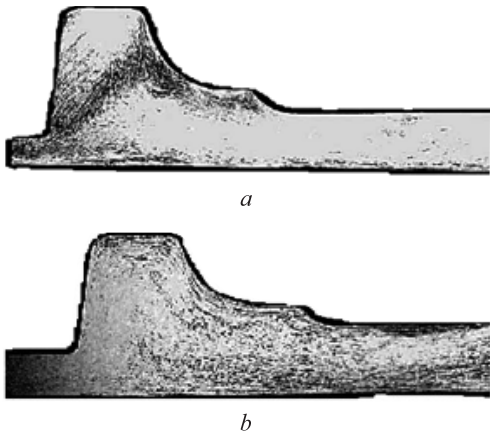

*a*

*b*

Fig. 5. Macrostructure of the forging

Рис. 5. Макроструктура поковки

alignment of metal fibers at the base of the stiffeners (Fig. 5, *b*). This effectively prevents the occurrence of defects such as "shooting-through".

## Conclusions

The software system can serve a diverse functional purpose: facilitating rapid analysis of the metal flow pattern and computation of billet forming across its strain stages. This capability enables users to select various geometrical parameters of the die impression, thereby obtaining different metal flow patterns and stiffener profiles. By prioritizing configurations that ensure the most uniform filling of die cavities with metal beneath the stiffeners, manufacturers can guarantee defect-free production of their products. The outcomes of the presented development can be effectively leveraged to further advance modeling efforts concerning the plastic flow of metal in the metalworking process [32 – 35].

## References / Список литературы

1. Sosenushkin E.N., Kadymov V.A., Yanovskaya E.A. Mathematical modeling of metal flow along planes with free flow into ribs. In: *Machine Tool Construction and Innovative Mechanical Engineering. Problems and Growth Points: Proceedings of the All-Russ. Sci.-Tech. Conf. in the Ufa State Avia. Tech. University*. Ufa: RIK USATU; 2019:337–342. (In Russ.).

   Сосенушкин Е.Н., Кадымов В.А., Яновская Е.А. Математическое моделирование течения металла по плоскостям со свободным затеканием в ребра. *Станкостроение и инновационное машиностроение. Проблемы и точки роста: Материалы Всероссийской научно-технической конференции Уфимского государственного авиационного технического университета*. Уфа: РИК УГАТУ; 2019:337–342.
2. Ushakov I.V., Safronov I.S. Directed changing properties of amorphous and nanostructured metal alloys with help of nanosecond laser impulses. *CIS Iron and Steel Review*. 2021;22:77–81. https://doi.org/10.17580/cisisr.2021.02.14
3. Kondratenko V.E., Devyatiarova V.V., Albul S.V., Kartyshev D.S. Improving methodology for calculating scaffolding formwork of monolithic slabs in building constructions. *IOP Conference Series: Materials Science and Engineering*. 2020;971(5):052037. https://doi.org/10.1088/1757-899x/971/5/052037
4. Bardovsky A.D., Gerasimova A.A., Basyrov I.I. Constructive solutions for upgrading of the drive of processing equipment. *IOP Conference Series: Materials Science and Engineering*. 2020;709(2):022015. https://doi.org/10.1088/1757-899x/709/2/022015
5. Shinkaryov A.S., Ozherelkov D.Yu., Pelevin I.A., Eremin S.A., Anikin V.N., Burmistrov M.A., Chernyshikhin S.V., Gromov A.A., Nalivaiko A.Yu. Laser fusion of aluminum powder coated with diamond particles via selective laser melting: Powder preparation and synthesis description. *Coatings*. 2021;11(10):1219. https://doi.org/10.3390/coatings11101219
6. Kulagin Yu.A., Baranov E.O., Shinkarev A.S., Avatinyan G.A., etc. New aspects of the development of ice and laser technologies for sports of higher achievements. *Kholodil'naya tekhnika*. 2016;(12):36–43. (In Russ.).

   Кулагин Ю.А., Баранов Е.О., Шинкарев А.С., Аватинян Г.А. и др. Новые аспекты развития ледовых и лазерных технологий для спорта высших достижений. *Холодильная техника*. 2016;(12):36–43.
7. Ganzulenko O.Y., Petkova A.P. Simulation and approbation of the marking laser process on metal materials. *Journal of Physics: Conference Series*. 2021;1753(1):012016. https://doi.org/10.1088/1742-6596/1753/1/012016
8. Brunman V.E., Vataev A.S., Volkov A.N., Petkova A.P., Plotnikov D.G. Optimizing pump-drive operation to improve the energy-efficiency of oil extraction. *Russian Engineering Research*. 2017;37(6):479–484. https://doi.org/10.3103/S1068798X17060089
9. Kadymov V.A., Sosenushkin E.N., Yanovskaya E.A. Contact problems of plastic flow in a thin layer: Theory, analysis of solutions, and applications. *Journal of Machinery Manufacture and Reliability*. 2022;51(3):206–215. https://doi.org/10.3103/S1052618822030062
10. Kushnarev A.V., Kirichkov A.A., Shestak V.D., Timofeev V.V., Bogatov A.A. Introduction of wheel production on a new pressing and rolling line. *Steel in Translation*. 2010;40(12):1098–1100. https://doi.org/10.3103/S0967091210120181

    Кушнарев А.В., Киричков А.А., Шестак В.Д., Тимофеев В.В., Богатов А.А. Опыт освоения производства колес на новой прессопрокатной линии. *Сталь*. 2010;(12):44–46.
11. Pogrebnyak R.P. Experimental study of shape of a railway wheel rolled billet. *Proizvodstvo prokata*. 2012;(2):29–33. (In Russ.).

    Погребняк Р.П. Экспериментальное исследование формы прокатной заготовки железнодорожного колеса. *Производство проката*. 2012;(2):29–33.
12. Snitko S.A., Yakovchenko A.V. Influence of the axial reduction conditions on the variation in the thickness of a wheel rim at the initial stage of rolling. *Metallurgist*. 2017;61(5-6):387–393. https://doi.org/10.1007/s11015-017-0505-x

    Снитко С.А., Яковченко А.В. Влияние режима осевого обжатия на разнотолщинность обода колесной заготовки на начальной стадии ее прокатки. *Металлург*. 2017;(5):46–51.

**13.** Kleiner M., Geiger M., Klaus A. Manufacturing of lightweight components by metal forming. *CIRP Annals*. 2003;52(2):521–542. https://doi.org/10.1016/S0007-8506(07)60202-9

**14.** Park C.S., Ku T.W., Kang B.S., Hwang S.M. Process design and blank modification in the multistage rectangular deep drawing of an extreme aspect ratio. *Journal of Materials Processing Technology*. 2004;153–154:778–784. https://doi.org/10.1016/j.jmatprotec.2004.04.306

**15.** Pichuev A.V., Petrov V.L. Equivalent circuit for mine power distribution systems for the analysis of insulation leakage current. *Mining Science and Technology (Russia)*. 2023;8(1):78–86. (In Russ.). https://doi.org/10.17073/2500-0632-2023-01-72

Пичуев А.В., Петров В.Л. Обоснование схемы замещения шахтной подземной электрической сети для анализа режимов утечки тока через изоляцию. *Горные науки и технологии*. 2023;8(1):78–86. https://doi.org/10.17073/2500-0632-2023-01-72

**16.** Sukhorukova M.A., Ivannikov A.L. Vehicle accident risk assessment in mines. *Mining Informational and Analytical Bulletin*. 2020;(6–1):224–232. (In Russ.). https://doi.org/10.25018/0236-1493-2020-61-0-224-232

Сухорукова М.А., Иванников А.Л. Оценка рисков аварий на транспортных средствах на рудниках. *Горный информационно-аналитический бюллетень*. 2020;(6-1):224–232. https://doi.org/10.25018/0236-1493-2020-61-0-224-232

**17.** Tatarnikov N.N., Yusupov V.S., Belelyubsky B.F. Manufacturing of work-rolls with higher geometry and roughness requirements for rolling the thinnest strip. *AIP Conference Proceedings*. 2023;2697:030012. https://doi.org/10.1063/5.0135274

**18.** Kim S.H., Chung S.W., Padmanaban S. Investigation of lubrication effect on the backward extrusion of thin-walled rectangular aluminum case with large aspect ratio. *Journal of Materials Processing Technology*. 2006;180(1–3):185–192. https://doi.org/10.1016/j.jmatprotec.2006.06.003

**19.** Il'yushin A.A. *Plasticity*. Moscow: Gostekhizdat; 1948:376. (In Russ.).

Ильюшин А.А. *Пластичность*. Москва: Гостехиздат; 1948:376.

**20.** Solomonov K.N., Kostarev I.V., Abashkin V.P. *Modeling of Processes of Volumetric Stamping and Forging of Flat Billets*. Moscow: MISIS; 2008:128. (In Russ.).

Соломонов К.Н., Костарев И.В, Абашкин В.П. *Моделирование процессов объемной штамповки и ковки плоских заготовок*. Москва: Издательский дом МИСиС; 2008:128.

**21.** Lisunets N.L., Solomonov K.N., Tsepin M.A. *Volumetric Stamping of Aluminum Billets*. Moscow: Mashinostroenie; 2009:172. (In Russ.).

Лисунец Н.Л., Соломонов К.Н., Цепин М.А. *Объемная штамповка алюминиевых заготовок*. Москва: Машиностроение; 2009:172.

**22.** Chichenev N.A., Chicheneva O.N., Karfidov A.O., Pashkov A.N. Selection of laser processing parameters for hot stamping tools based on mathematical planning of the experiment. *CIS Iron and Steel Review*. 2021;22:37–40. https://doi.org/10.17580/cisisr.2021.02.07

**23.** Kiani-Rashid A.R., Rounaghi S.A. The new methods of graphite nodules detection in ductile cast iron. *Materials and Manufacturing Processes*. 2011;26(2):242–248. https://doi.org/10.1080/10426914.2010.520788

**24.** Di Cocco V., Iacoviello F., Cavallini M. Damaging micromechanisms characterization of a ferritic ductile cast iron. *Engineering Fracture Mechanics*. 2010;77(11):2016–2023. https://doi.org/10.1016/j.engfracmech.2010.03.037

**25.** Milenin A., Petrov P., Petrov M., Krutina E. Numerical model of fracture in magnesium alloys during forming processes. *Steel Research International*. 2012;SPL:847–850.

**26.** Chaus A.S., Soyka J., Pokrovsky A.I. The effect of hot plastic deformation on changes in the microstructure of cast iron with spherical graphite. *The Physics of Metals and Metallography*. 2013;114(1):4–104. https://doi.org/10.1134/S0031918X13010031

**27.** Solomonov K.N., Fedorinin N.I., Tishchuk L.I. Method of constructing a metal flow dividing line during flat billet precipitation. *Vestnik nauchno-tekhnicheskogo razvitiya*. 2016;(2):36–55. (In Russ.).

Соломонов К.Н., Федоринин Н.И., Тищук Л.И. Методика построения линии раздела течения металла в процессах осадки плоских заготовок. *Вестник научно-технического развития*. 2016;(2):36–55.

**28.** Zhang Y.Q., Jiang S.Y., Zhao Y.N., Shan D.B. Isothermal precision forging of complex-shape rotating disk of aluminum alloy based on processing map and digitized technology. *Materials Science and Engineering: A*. 2013;580:294–304. https://doi.org/10.1016/j.msea.2013.05.059

29. Zheng J.H., Lin J.G., Lee J., Pan R., Li C., Davies C.M. A novel constitutive model for multi-step stress relaxation ageing of a pre-strained 7xxx series alloy. *International Journal of Plasticity*. 2018;106:31–47. https://doi.org/10.1016/j.ijplas.2018.02.008

**30.** Maksimov E.A., Shatalov R.L., Krutina E.V. Calculation technique for deformation and energy-power parameters in combined rotary drawing and cross rolling of wheel disks. *Chernye metally*. 2019;(1):34–38. (In Russ.).

Максимов Е.А., Шаталов Р.Л., Крутина Е.В. Методика расчета деформационных и энергосиловых параметров при совмещенной ротационной вытяжке и поперечной прокатке дисков колес. *Черные металлы*. 2019;(1):34–38.

**31.** Chichenev N.A., Gorbatyuk S.M., Naumova M.G., Morozova I.G. Using the similarity theory for description of laser hardening processes. *CIS Iron and Steel Review*. 2020;19:44–47. https://doi.org/10.17580/cisisr.2020.01.09

**32.** Yong P., Shuncheng W., Kaihong Z., Wenjun Q., Hexing C., Haitao Z., Influence of the pressing time during the liquid stamping of the deformable aluminum alloy 6061 on its mechanical. *Special Casting & Nonferrous Alloys*. 2013;33(12):1152–1157.

**33.** Gorbatyuk S., Pashkov A., Chichenev N. Improved copper-molybdenum composite material production technology. *Materials Today: Proceedings*. 2019;11(1):31–35. https://doi.org/10.1016/j.matpr.2018.12.102

**34.** Solomonov K. Development of software for simulation of forming forgings. *Procedia Engineering*. 2014;81:437–443. https://doi.org/10.1016/j.proeng.2014.10.019

**35.** Singh A., Agrawal A. Investigation of surface residual stress distribution in deformation machining process for aluminum alloy. *Journal of Materials Processing Technology*. 2015;225:195–202. https://doi.org/10.1016/j.jmatprotec.2015.05.025

## Information about the Authors

***Konstantin N. Solomonov,*** *Dr. Sci. (Eng.), Prof. of the Chair of Social, Humanitarian, Natural Sciences and General Professional Disciplines,* Voronezh Branch of the Rostov State Transport University
***E-mail:*** konssol@list.ru

***Lyudmila I. Tishchuk,*** *Assist. Prof. of the Chair of Social, Humanitarian, Natural Sciences and General Professional Disciplines,* Voronezh Branch of the Rostov State Transport University
***E-mail:*** liudmila.tishchuk@mail.ru

***Sergei M. Gorbatyuk,*** *Dr. Sci. (Eng.), Prof. of the Chair "Engineering of Technological Equipment",* National University of Science and Technology "MISIS"
***ORCID:*** 0000-0002-4368-5965
***E-mail:*** sgor02@mail.ru

***Sergei A. Snitko,*** *Dr. Sci. (Eng.), Assist. Prof., Head of the Chair "Metal Forming",* Donetsk National Technical University
***ORCID:*** 0000-0002-1099-5801
***E-mail:*** snitko_sa@mail.ru

***Ol'ga N. Chicheneva,*** *Cand. Sci. (Eng.), Assist. Prof.,* National University of Science and Technology "MISIS"
***E-mail:*** chich38@mail.ru

## Сведения об авторах

***Константин Николаевич Соломонов,*** *д.т.н., профессор кафедры социально-гуманитарных, естественно-научных и общепрофессиональных дисциплин,* филиал Ростовского государственного университета путей сообщения в г. Воронеж
***E-mail:*** konssol@list.ru

***Людмила Ивановна Тищук,*** *доцент кафедры социально-гуманитарных, естественно-научных и общепрофессиональных дисциплин,* филиал Ростовского государственного университета путей сообщения в г. Воронеж
***E-mail:*** liudmila.tishchuk@mail.ru

***Сергей Михайлович Горбатюк,*** *д.т.н., профессор кафедры «Инжиниринг технологического оборудования»,* Национальный исследовательский технологический университет «МИСИС»
***ORCID:*** 0000-0002-4368-5965
***E-mail:*** sgor02@mail.ru

***Сергей Александрович Снитко,*** *д.т.н., доцент, заведующий кафедрой «Обработка металлов давлением»,* Донецкий национальный технический университет
***ORCID:*** 0000-0002-1099-5801
***E-mail:*** snitko_sa@mail.ru

***Ольга Николаевна Чиченева,*** *к.т.н., доцент,* Национальный исследовательский технологический университет «МИСИС»
***E-mail:*** chich38@mail.ru

## Contribution of the Authors

***K. N. Solomonov*** – development of a mathematical model, determination of boundary conditions.
***L. I. Tishchuk*** – graphic design of the obtained results.
***S. M. Gorbatyuk*** – analysis and generalization of the obtained modeling results.
***S. A. Snitko*** – formation of the article concept, setting the goal and objectives of the study, writing the text.
***O. N. Chicheneva*** – technical justification of research tasks, justification of process parameters.

## Вклад авторов

***К. Н. Соломонов*** – разработка математической модели, определение граничных условий.
***Л. И. Тищук*** – графическое оформление полученных результатов.
***С. М. Горбатюк*** – анализ и обобщение полученных результатов моделирования.
***С. А. Снитко*** – формирование концепции статьи, определение цели и задачи исследования, подготовка текста.
***О. Н. Чиченева*** – техническое обоснование задач исследования, обоснование параметров процесса.

Received 23.08.2023
Revised 10.10.2023
Accepted 04.11.2023

Поступила в редакцию 23.08.2023
После доработки 10.10.2023
Принята к публикации 04.11.2023

# Указатель статей, помещенных в журнале «Известия высших учебных заведений. Черная металлургия» за 2023 год, том 66

## МЕТАЛЛУРГИЧЕСКИЕ ТЕХНОЛОГИИ



## ЭКОЛОГИЯ И РАЦИОНАЛЬНОЕ ПРИРОДОПОЛЬЗОВАНИЕ



## СТАЛИ ОСОБОГО НАЗНАЧЕНИЯ



## МАТЕРИАЛОВЕДЕНИЕ

## ИННОВАЦИИ В МЕТАЛЛУРГИЧЕСКОМ ПРОМЫШЛЕННОМ И ЛАБОРАТОРНОМ ОБОРУДОВАНИИ, ТЕХНОЛОГИЯХ И МАТЕРИАЛАХ



## ФИЗИКО-ХИМИЧЕСКИЕ ОСНОВЫ МЕТАЛЛУРГИЧЕСКИХ ПРОЦЕССОВ



## ИНФОРМАЦИОННЫЕ ТЕХНОЛОГИИ И АВТОМАТИЗАЦИЯ В ЧЕРНОЙ МЕТАЛЛУРГИИ



## ЭКОНОМИЧЕСКАЯ ЭФФЕКТИВНОСТЬ МЕТАЛЛУРГИЧЕСКОГО ПРОИЗВОДСТВА

## ПО МАТЕРИАЛАМ МЕЖДУНАРОДНОЙ НАУЧНОЙ КОНФЕРЕНЦИИ «ФИЗИКО-ХИМИЧЕСКИЕ ОСНОВЫ МЕТАЛЛУРГИЧЕСКИХ ПРОЦЕССОВ» им. академика А.М. Самарина, Выкса, 10 – 14 октября 2022 г.



## ПО МАТЕРИАЛАМ МЕЖДУНАРОДНОЙ КОНФЕРЕНЦИИ «НАУЧНО-ПРАКТИЧЕСКАЯ ШКОЛА ДЛЯ МОЛОДЫХ МЕТАЛЛУРГОВ»



## В ПОРЯДКЕ ДИСКУССИИ

# Index of articles "Izvestiya. Ferrous Metallurgy" for 2023, vol. 66

## METALLURGICAL TECHNOLOGIES



## ECOLOGY AND RATIONAL USE OF NATURAL RESOURCES



## SUPERDUTY STEEL



## MATERIAL SCIENCE

## INNOVATIONS IN METALLURGICAL INDUSTRIAL AND LABORATORY EQUIPMENT, TECHNOLOGIES AND MATERIALS



## PHYSICO-CHEMICAL BASICS OF METALLURGICAL PROCESSES

## INFORMATION TECHNOLOGIES AND AUTOMATIC CONTROL IN FERROUS METALLURGY



## ECONOMIC EFFICIENCY OF METALLURGICAL PRODUCTION



## MATERIALS OF THE INTERNATIONAL SCIENTIFIC CONFERENCE "PHYSICO-CHEMICALFOUNDATIONS OF METALLURGICAL PROCESSES" named after Academician A.M. Samarin, Vyksa, October 10 – 14, 2022



## BASED ON THE MATERIALS OF THE INTERNATIONAL CONFERENCE "SCIENTIFIC AND PRACTICAL SCHOOL FOR YOUNG METALLURGISTS"



## IN THE ORDER OF DISCUSSION

Над номером работали:

Л.И. Леонтьев, *главный редактор*

Е.В. Протопопов, *заместитель главного редактора*

Е.А. Ивани, *заместитель главного редактора*

Л.П. Бащенко, *заместитель ответственного секретаря*

Е.Ю. Потапова, *заместитель главного редактора по развитию*

О.А. Долицкая, *научный редактор*

Е.М. Запольская, *ведущий редактор*

А.О. Гашникова, *ведущий редактор*

В.В. Расенець, *верстка, иллюстрации*

Г.Ю. Острогорская, *менеджер по работе с клиентами*

---

Подписано в печать 25.12.2023. Формат 60×90 $^{1}/_{8}$. Бум. офсетная № 1.
Печать цифровая. Усл. печ. л. 15,25. Заказ 18897. Цена свободная.

---

Отпечатано в типографии Издательского Дома МИСИС.
119049, Москва, Ленинский пр-кт, д. 4, стр. 1.
Тел./факс: (499) 236-76-17

**Зарегистрирован Федеральной службой по надзору в сфере связи, информационных технологий и массовых коммуникаций. Свидетельство о регистрации ПИ № ФС77-35456.**

**Подписной индекс 70383.**